Neuronal Pathways for Cerebello-Cerebral Communication

Carmen Schäfer

Cover photo: Satellite image of the Netherlands; European Space Agency (ESA) in Katwijk, adapted by Carmen Schäfer

Layout and printed by Optima Grafische Communicatie, Rotterdam, the Netherlands

ISBN 978-94-6361-588-4

Neuronal Pathways for Cerebello-Cerebral Communication

Neuronale paden voor cerebello-cerebrale communicatie

Proefschrift

ter verkrijging van de graad van doctor aan de
Erasmus Universiteit Rotterdam
op gezag van de
rector magnificus

Prof.dr. A.L. Bredenoord
en volgens besluit van het College voor Promoties.

De openbare verdediging zal plaatsvinden op
dinsdag 26 oktober 2021 om 10.30 uur
door

Carmen Bianca Schäfer
geboren te Brackenheim, Duitsland.

Erasmus University Rotterdam

Promotiecommissie

Promotoren:	Prof. Dr. F.E. Hoebeek
	Prof. Dr. C.I. De Zeeuw
Overige leden:	Prof.dr. J.G.G. Borst
	Dr. A.M. Badura
	Prof.dr. C.P.J. de Kock
Copromotor:	Prof. Dr. Z. Gao

OUTLINE THESIS

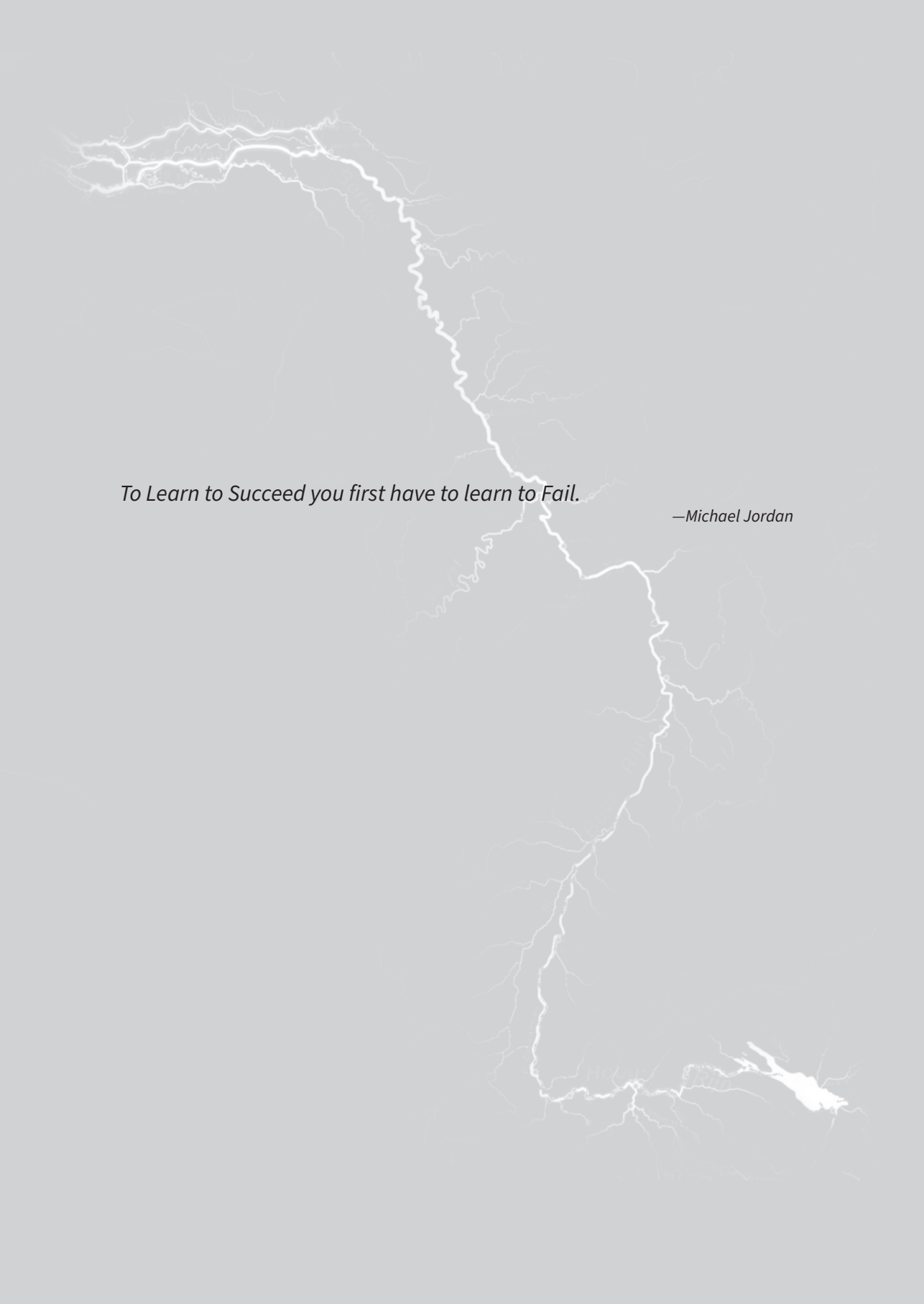

To Learn to Succeed you first have to learn to Fail.

—Michael Jordan

Chapter 1

Introduction

The Organization of the Sensorimotor System

The planning and execution of movements require interaction of multiple brain regions, which are distributed across the central nervous system. These systems coordinate Sprograms that involve the muscular system of the body to execute movements. The sensorimotor systems are hierarchically organized with the peripheral level comprising the spinal cord, the intermediate level involving brain stem systems and the higher-order sensorimotor systems involving sensory and motor cortical systems (Figure 1, Kandel et al. 2012). The components of the sensorimotor system can function independently but also in parallel, as - for example - the spinal cord in itself is capable of inducing automatized and reflexive movements, which can also be triggered by the brainstem or the motor cortex (Lemon, 2008; Esposito *et al.*, 2014; Svoboda & Li, 2017*a*; Arber & Costa, 2018; Ruder *et al.*, 2021). Within this hierarchically organized sensorimotor system, several brain areas serve as functional hubs that fulfill specialized tasks essential for the successful and accurate execution of movements.

At the lowest hierarchical level, the spinal cord consists of local interneuronal circuits, which innervate the muscular system, induce muscle contraction and are capable of inducing reflexive and autonomous movements (Lemon, 2008; Esposito *et al.*, 2014; Ruder *et al.*, 2016, 2021; Arber, 2017). Apart from their autonomous function, spinal interneurons also form the executive station that is targeted by intermediate and higher order brain systems.

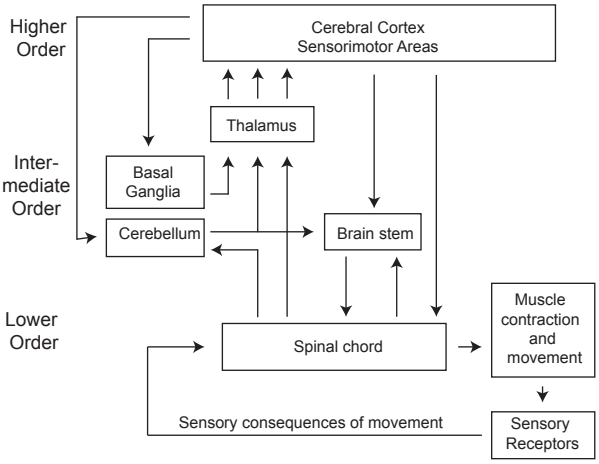

Figure 1 The organization of the sensorimotor system. The sensorimotor system is hierarchically organized into executive centers found in the spinal chord, the brain stem and the cortex, respectively. The thalamus relays any sensory information that is transferred to the cerebral cortex. The cerebellum and basal ganglia connect to brainstem nuclei and the cerebral cortex via the thalamus. Adapted from (Kandel *et al.*, 2012)

The brainstem contains various nuclei such as the vestibular nucleus, the reticular formation, the superior colliculus as well as the red nucleus, which are capable of shaping movements without the involvement of cerebral cortex and innervate downstream executive motor circuits in the spinal cord (Felsen & Mainen, 2008; Esposito *et al.*, 2014; Bouvier *et al.*, 2015; Capelli *et al.*, 2017; Ruder *et al.*, 2021). They are essentially involved in the coordination of posture as well as eye and head movements in response to environmental or self-induced adjustments in position and stability of the body (Lemon, 2008; Kandel *et al.*, 2012).

Higher order sensorimotor processing involves cortical areas such as primary and secondary sensory cortex as well as motor cortical areas such as primary and secondary motor cortices. Within this cortical organization, sensory and motor cortices are strongly interconnected and mainly involved in the execution of complex and voluntary movements that involve motor planning (Brecht *et al.*, 2004; Matyas *et al.*, 2010; Aronoff *et al.*, 2010; Suter & Shepherd, 2015; Chen *et al.*, 2017; Svoboda & Li, 2017*b*). They innervate and influence not only the executive circuits in the spinal cord but also brain stem centers and cerebellum (see **Chapter 7).** All sensory subcortical inputs that give the sensorimotor system feedback concerning environmental changes are relayed via the thalamus to the cortex.

In addition to integrative centers in cerebral cortex, brainstem and spinal cord, the cerebellum and basal ganglia form core components of the sensorimotor system. Amongst other tasks, cerebellum is functionally specialized in calculating the sensory prediction error necessary to adapt and fine-tune ongoing movements during motor learning (Ramnani, 2006; De Zeeuw *et al.*, 2011; Gao *et al.*, 2012, 2018; Brooks *et al.*, 2015), while basal ganglia control voluntary movements by deciding which behavioral motor program to execute (Lee *et al.*, 2020). Both brain centers connect to executive brainstem centers as well as thalamic nuclei via which they modulate cortical systems (Arber & Costa, 2018; Iino *et al.*, 2020; Lee *et al.*, 2020).

Each component of the sensorimotor system receives primary sensory information to adjust and adapt ongoing movements, where exclusively higher order systems are capable of modulating and processing the afferent information arriving from primary sensory relay nuclei. Most interestingly, each of the components of the sensorimotor system is somatotopically organized, which is maintained in the interconnectivity between brain areas and the pathway of axonal tracts. Taking the rodent whisker system as an example, each individual whisker of the rodent snout is individually represented in brain stem nuclei, thalamus as well as sensory and motor cortices, giving space to a beautiful somatotopically organized anatomy (Bosman *et al.*, 2010; Aronoff *et al.*, 2010).

In the following paragraphs I want to introduce the individual components of the sensorimotor system, with specific focuses on the brain areas involved in the integration of cerebellar output into ongoing cortical processing of sensorimotor information.

The Cerebral Cortex

The General Architecture of the Cerebral Cortex

The cortex is subdivided into white matter formed by myelinated axonal tracts and grey matter formed by cell bodies. Within all functional areas the cortex can be subdivided in six main layers, which gives it its laminar shape. Throughout the cortex, divers types of excitatory and inhibitory neurons can be found. I will mainly focus on the excitatory neurons in this thesis. The six cortical layers are formed by intra-telencephalic (IT), projection-type (PT) and cortico-thalamic (CT) neurons (Figure 2A). IT neurons localize to cortical layer two (LII) to four (LIV) as well as to layer five (LV) and six (LVI), while PT neurons can be found in LV and CT neurons in LVI. (Figure 2). Most cortico-cortical and interhemispheric projections to the contralateral cortex are formed by IT-neurons. PT-neurons are the large pyramidal neurons of layer V B and form the main cortical output neurons to subcortical targets (see **Chapter 7**). They send axonal collaterals to multiple subcortical areas, such as brainstem, midbrain, thalamus, ipsilateral cortex and spinal cord. CT neurons in cortical LVI - in contrast - exclusively innervate the thalamus as subcortical target (Figure 2B).

All primary sensory inputs to the cortex arise from the thalamus and are relayed to cortical LIV as well as to LI and LV (Cruikshank *et al.*, 2007, 2012; Kuramoto *et al.*, 2009*a*, 2011; Wimmer *et al.*, 2010; Ohno *et al.*, 2012; Kaneko, 2013). Besides receiving sensory information from primary thalamic relay nuclei, LIV IT cells form mainly local networks

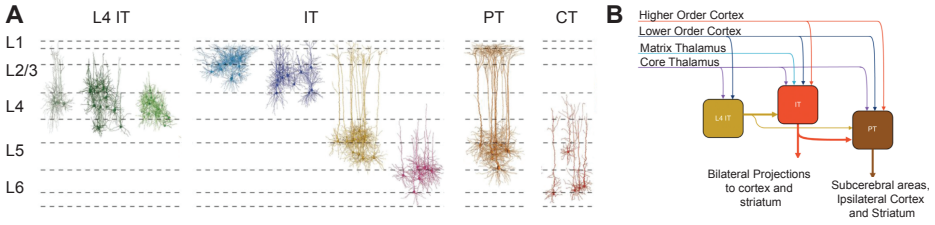

Figure 2 The organization and morphology of cortical networks. A The dendritic morphology of excitatory cortical neurons is depicted and shows intratelencephalic neurons (IT) that localize across layer 1 to 6 and form cortico-cortical connections, projectiontype neurons (PT) that project to subcortical targets and cortico-thalamic neurons (CT) that innervate the thalamus. **B** Within the cortical organization IT and PT neurons integrate information from diverse cortical and thalamic sources. IT neurons transfer their output further downstream to PT neurons, while PT neurons form the final output station of the cortical column and innervate downstream subcortical targets. Adapted from (Harris & Shepherd, 2015).

and densely project to LII/III IT neurons (Figure 2; Douglas & Martin 2004; Harris & Shepherd 2015). Due to the diverse and abundant cortico-cortical connectivity of LII/III IT neurons, sensory information is exchanged and integrated with signals from other cortical areas and then further transferred to LV projection neurons (Figure 3; Harris & Shepherd 2015; Weiler et al. 2009; Petreanu et al. 2009; Suter & Shepherd 2015; Hooks et al. 2011). As a recipient of the extensive input from divers types of IT neurons and the thalamus, PT neurons act as main downstream integrator of local cortical networks (Constantinople and Bruno, 2013; Petreanu et al., 2009; Weiler et al., 2009). CT neurons in cortical LVI have been shown to provide inhibitory control across cortical layers, in addition to providing cortico-thalamic feedback (Olsen *et al.*, 2012; Bortone *et al.*, 2014).

Sensory Cortex

The somatosensory cortex is formed by a set of modules in the neocortex responsible for the processing of touch. For this reason, the sensory cortex is the main recipient of primary sensory information in the cerebrum. In line with the organization described previously, the primary sensory cortex (S1) is subdivided in six layers, with LIV as the primary input layer for sensory information (de Kock & Sakmann, 2009; Meyer *et al*., 2010; Oberlaender *et al*., 2012). Even though S1 processes ex-afferent and tactile information from the whole body, the anatomy and function of the sensory cortex can best be explained on the example of the rodent whisker system. The proprioceptive information of every single whisker of the rodent snout - the principal whisker - is individually represented in a so-called 'barrel column' in layer four of the whisker responsive portion of S1 or the so-called barrel cortex (Aronoff *et al*. 2010b; Bosman *et al*. 2011). Due to the strict somatotopic organization of the barrel field, a single barrel column defines a discrete whisker-specific cytoarchitectonic unit (Welker 1974; Woolsey & Van der Loos 1970). Initially, primary tactile inputs are relayed via thalamo-cortical pathways to LIV as well as to LI and LV A (Cruikshank *et al*., 2007; Wimmer *et al*., 2010; Viaene *et al*., 2011). The dimensions of a single barrel column in the barrel field of S1 is defined by the granularity formed by LIV neurons and the thalamo-cortical innervation arising from the ventroposteromedial (VPM) thalamus, the core relay nucleus for whisker-based information (Wimmer *et al*. 2010; Meyer *et al*. 2010; Oberlaender *et al*. 2012). Functionally, barrel cortex is of essential importance for the perception and processing of whisker inputs, as one of its core functions is to encode the location of whiskers over time (Crochet & Petersen, 2006; de Kock & Sakmann, 2009). After having explained the anatomical organization of the barrel-cortex based on the processing of tactile information from the whiskers, it is important to note that all of S1 is somatotopically organized. Therefore, S1 plays a critical role in processing afferent sensory information from bodyparts such as fore- and hindlimbs and contributes to the integration of sensory and motor signals necessary for the generation of skilled movements.

Motor Cortex

The motor cortex is essentially involved in the planning and execution of voluntary movements. Just like the sensory cortex, the motor cortex is somatotopically organized and traditionally subdivided into the primary motor cortex (M1) and the secondary motor cortex (M2) (Tennant *et al.*, 2011; Chen *et al.*, 2017; Morandell & Huber, 2017). Similar to other cortices, motor cortex receives inputs from cortical and thalamic origins; however, due to the minor presence of LIV these inputs are distributed across layer II/III, LV A as well as upper and lower LV B (Hooks *et al.*, 2013; Luo *et al.*, 2019; Muñoz-castañeda *et al.*, 2020). Sensory inputs from sensory cortices and sensory thalamus target upper motor cortical layers (Ohno *et al.*, 2012; Hooks *et al.*, 2013; Muñoz-castañeda *et al.*, 2020). The cerebellar information, which is transferred via motor thalamus, distributes across LII-V (Kuramoto *et al.*, 2009*a*; Yamawaki & Shepherd, 2015). Axonal fibers that arise from VM mainly innervate cortical LI (Kuramoto *et al.*, 2013). Pyramidal neurons in layer 5B are innervated by projections arising from frontal areas of secondary motor cortex in addition to thalamic inputs (Hooks *et al.*, 2011; Luo *et al.*, 2019; Muñoz-castañeda *et al.*, 2020). Their downstream projection targets distribute across subcortical motor centers such as striatum, superior colliculus, pons, reticular formation and motor thalamus (Winnubst *et al.*, 2019; Muñoz-castañeda *et al.*, 2020). Human motor cortical pyramidal neurons can directly innervate spinal motor neurons in addition to local inter-neuronal networks in the spine, while in rodents no direct projection to spinal motor neurons is found, and movement execution is induced via disynaptic connections in the brainstem (Brecht *et al.*, 2004; Lemon, 2008; Ruder *et al.*, 2016; Arber, 2017). In **Chapter 7** we characterize a novel population of LV projection neuron that innervates the cerebellar nuclei and forms a direct route between the cerebral and the cerebellar cortex. A short-cut for direct cerebro-cerebellar communication within the brain.

The execution and learning of skilled movements requires an intact motor cortex as acute motor cortical inactivation (Guo *et al.*, 2015; Morandell & Huber, 2017; Galiñanes *et al.*, 2018) and motor cortical lesion (Ramanathan *et al.*, 2006) result in deficits in movement execution. Correlating neuronal activity with behavioral performance during movement execution or during the learning and adaptation of skilled movements identifies neuronal subclasses with selective population dynamics. During movement execution, specific phases of motor performance such as motor planning, movement onset and sensory integration are accompanied by selective activity patterns and distinct neuronal response types (Li *et al.*, 2015; Elsayed *et al.*, 2016; Chen *et al.*, 2017; Guo *et al.*, 2017; Lara *et al.*, 2018). These data suggest a functional subdivision across motor cortices, in which neuronal activity related to the detection of objects localizes to posterior-medial motor cortical areas – including the whisker responsive portion (wM1) - while motor preparatory activity appears in the most frontal portion (ALM) of motor

cortex ((Chen et al., 2017; Kim et al., 2016; Li et al., 2015, 2016; Svoboda and Li, 2017a). Within motor cortical layer 5, the movement initiation command is assumed to be mediated by cortico-spinal neurons (CSN) as they form the final stage for cortical output and send direct projections to the brainstem and the spinal cord (Lemon, 2008). More specifically, spatially defined groups of CSNs are assumed to encode distinct aspects of movement associated motor skills, as region-specific manipulations indicate that CSNs from caudal or rostral forelimb motor cortical areas control reaching or grasping (Wang *et al.*, 2017). During the learning of skilled movements subsets of corticospinal neurons in layer V (L5) are selectively active while other subpopulations are selectively active during quiescence (Komiyama *et al.*, 2010; Peters *et al.*, 2014, 2017). This suggests that cortical activity is dynamic during learning and that movements early and late in learning are represented by different activity patterns. Therefore, monitoring the success and error of the outcome of movements is essential for the adaptation of movement and learning processes.

The Thalamus

The thalamus is the most centrally located complex of brain nuclei within the mammalian brain (Jones, 2007). It forms the core relay station of the brain, which distributes incoming information from subcortical sources to their cortical destinations. For this reason the thalamic complex is also called 'The gate to consciousness'. Furthermore, the thalamus also relays cortical informaiton of one region to other cortical regions.

The Thalamic Organization

The nuclei of the thalamus can be subdivided dependent on the sensory modality from which they receive their primary inputs: the medial geniculate nucleus for the auditory system, the lateral geniculate body for the visual system, the ventral-posterior nuclei for the proprioceptive system and the ventral-anterior and lateral nuclei for the motor system (Jones, 2007). On top of inputs from primary subcortical sources, the thalamus receives dense feedback projections from LV and LVI of its cortical target areas, thereby forming cortico-thalamo-cortical loops that distribute and integrate information.

Depending on the cortical innervation pattern, the thalamus is sub-categorized into first and higher order nuclei (Figure 3). First order nuclei receive dense feedback from cortical LVI and are essentially relaying primary sensory inputs to their cortical target areas. Higher order nuclei – in contrast – are additionally innervated by projections from cortical LV, integrate primary sensory inputs with information that flows within the cortico-thalamo-cortical loop and provide a trans-thalamic gate for functional cortico-cortical communication (Figure 3; Sherman 2012; Reichova 2004; Sherman & Guillery 2011; Rovó et al. 2012; Sherman & Guillery 2002).

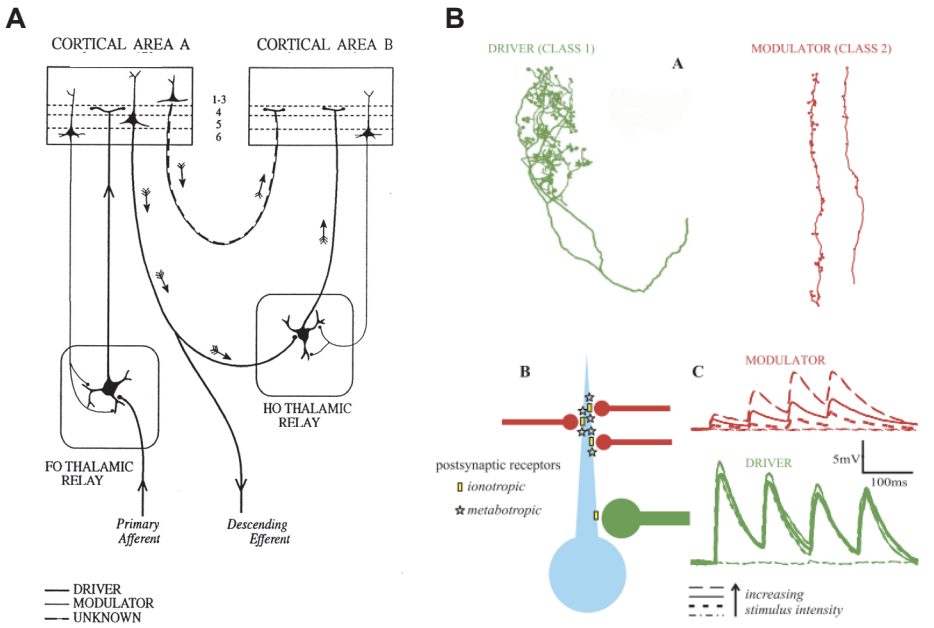

Figure 3 Drivers and modulators in the thalamic organization. A The thalamic system is hierarchically organized, where first order thalamic nuclei receive synaptic inputs from subcortical sources and cortical layer 6 and higher order thalamic nuclei receive additional feedback from cortical layer 5. **B** The characteristics of drivers and modulators in the thalamus are distinct. Adapted from (Sherman & Guillery, 1998, 2011).

In addition to the subdivision into first and higher order nuclei, thalamic neurons can be subdivided into core-type (C-type), matrix-type (M-type) and intralaminar-type (IL-type) neurons (Jones, 2007; Clascá *et al.*, 2012; Phillips *et al.*, 2017). This subdivision is based on the targeting pattern of thalamo-cortical axons as well as cell morphological measures. From a historical perspective, C-type neurons are the most well characterized subtype, as they exclusively and in a topographically organized manner connect to middle layers of cortical target areas (Cruikshank *et al.*, 2007; Kuramoto *et al.*, 2009*b*; Petreanu *et al.*, 2009; Viaene *et al.*, 2011). In contrast M-type neurons and IL-type neurons innervate multiple cortical areas in a more widespread manner and send collaterals to subcortical targets such as the striatum, while innervating cortical layer 1 and 5 (Deschênes *et al.*, 1998; Jones, 1998; Petreanu *et al.*, 2009; Cruikshank *et al.*, 2012; Ohno *et al.*, 2012; Kuramoto *et al.*, 2013). This profile of projection targeting and sub-classification of thalamic nuclei expresses itself also in the transcriptional profile of ion channels and receptor genes in thalamic nuclei across sensory modalities (Phillips *et al.*, 2017).

First and higher order nuclei can be found for every sensory modality, but have been particularly well studied for the rodent whisker system, which now serves as a model

for the proprioceptive system (Bosman et al., 2011, see **Chapter 2** and **3**). After whisker stimulation, subcortical inputs from the trigeminal nucleus are relayed via the lemniscal pathway to the ventral-posterior medial thalamic nucleus (VPM) and via the paralemniscal pathway to the posterior-medial thalamic nucleus (PoM) (Veinante & Deschênes, 1999). The VPM – as the first order thalamic relay nucleus - sends projections to LIV in primary sensory cortex (S1), while PoM – as the higher order thalamic nucleus – sends projections to LV, LI and the sub-columnar space in LIV (Figure 3; Viaene et al. 2011; Wimmer et al. 2010; Pierret et al. 2000). In addition to the subcortical inputs from the trigeminal nucleus, both VPM and PoM receive cortico-thalamic feedback (Deschênes *et al.*, 1998). As previously indicated, cortical LVI projection neurons send feedback projections to both VPM and PoM, while LV exclusively innervates PoM (Figure 3; Bourassa et al. 1995; Liao et al. 2010; Killackey & Sherman 2003; Deschênes et al. 1998; Veinante, Lavallée, et al. 2000; Rouiller & Welker 2001). The widespread feedback from cortical LVI modulates the thalamic membrane potential, while driving input from cortical LV or subcortical sources actively induces thalamic spiking (Theyel *et al.*, 2009; Groh *et al.*, 2013; Mease *et al.*, 2014*b*; Bickford *et al.*, 2015). Therefore, ascending lemniscal and paralemniscal pathways via VPM and PoM, respectively, convey separated streams of proprioceptive information. Upon repetitive 8Hz whisker stimulation and trigeminal neuron activation, VPM neurons respond by modulating the amplitude of their spike output while PoM neurons encode the input via a change in their response latency translating the trigeminal input into a rate code (Ahissar *et al.*, 2000). The systematic separation into first and higher order thalamic nuclei can be extended to the visual, auditory as well as the motor system (Jones, 2007); however, for the motor system and the cerebellar input into thalamus this subdivision has been less well characterized (see **Chapter 5** and **6**).

Excitatory Inputs to the Thalamus

Excitatory inputs, which arise from projection neurons in layer six and layer five as well as subcortical nuclei in the mid- and hindbrain, are forming modulator and driver synapses with distinct and well defined characteristics in the thalamus (Figure 3; Reichova & Sherman 2004; Sherman 2012; Li et al. 2003; Landisman & Connors 2007; Rouiller & Welker 2001; Turner & Salt 1998). Modulators arise from thin axons with small volume synaptic boutons that innervate thalamic neurons on distal dendrites (Hoogland *et al.*, 1991). They activate postsynaptic metabotropic glutamate receptors and induce facilitating responses due to their low release probability (Turner & Salt, 1998; Reichova, 2004; Viaene *et al.*, 2013). The characteristics of driver synapses oppose modulatory synapse properties in every aspect. They innervate proximal dendrites and form large volume terminals with multiple release sites (Hoogland *et al.*, 1991). On the postsynaptic side they activate ionotropic glutamate receptors and their high release probability

induces large amplitude currents that depress during higher frequency activation (Figure 3; Groh et al. 2008; Groh et al. 2013; Seol & Kuner 2015; Pelzer et al. 2017; Gornati et al. 2018; Bickford et al. 2015). Interestingly, not only cortical layer five neurons send drivers to the thalamus, but also synapses originating from subcortical sources show driver characteristics (Turner & Salt, 1998; Groh *et al.*, 2013; Bickford *et al.*, 2015; Gornati *et al.*, 2018). The sub-categorization of the thalamus into first order nuclei innervated by subcortical drivers and modulatory feedback as well as higher order nuclei, which receive additional cortical driver input, lines up with their functional characterization (Figure 3). Within this thalamic organization, strongly depolarizing and driving inputs from primary sensory sources as well as driving feed-forward cortical inputs transfer the main information within the thalamo-cortical circuit.

Inhibitory Inputs to the Thalamus

In addition to excitatory inputs, thalamic circuits receive inhibitory inputs from various sources, which have been categorized in two main types: the thalamic reticular nucleus (TRN), which surrounds the thalamus like a shell, as well as additional extra-thalamic inhibitory centers such as the zona incerta (ZI) and the anterior pretectal area (APT) (Wanaverbecq *et al.*, 2008; Halassa & Acsády, 2016). The inhibition conveyed by the TRN is rather widespread and can, for example during sleep, entrain the complete network state of the thalamo-cortical circuit (Pita-Almenar *et al.*, 2014). In contrast, the inhibition induced by extra-thalamic inhibitory centers exhibits strong and focal feed-forward inhibitory control (Bokor *et al.*, 2005; Wanaverbecq *et al.*, 2008).

The local reticular-thalamic networks are organized in a reciprocal inhibitory-excitatory loop, where TRN neurons inhibit thalamic neurons which in turn excite TRN neurons (Huguenard & McCormick, 2007). TRN neurons are connected via gap-junctions (Landisman *et al.*, 2002), which strengthens the unique capability of TRN neurons to entrain the cortico-thalamic circuit in reverberating network oscillations. Interestingly, LVI cortico-thalamic cells also innervate GABAergic cells in the TRN, which in turn disynaptically innervate thalamic cells. The balance between the relay of disynaptic feedforward inhibition from TRN and the direct monosynaptic excitation from the cortex determines thalamic membrane state and potential fluctuations. Due to the depressing short-term release dynamics of RT synapses in the thalamus, the balance between excitation and inhibition induced by cortical layer 6 shifts towards depolarized membrane potentials when modulated at frequencies of 12Hz, i.e. a frequency that mimics in-vivo layer 6 neuron spiking patterns and facilitates cortico-thalamic synapses (Wanaverbecq *et al.*, 2008; Crandall *et al.*, 2015).

In contrast, the inhibition originating from extra-thalamic centers such as substantia nigra, internal globus pallidus, ventral pallidum, zona incerta (ZI), anterior pretectal nucleus (APT) and the pontine reticular formation conveys strong and temporally precise focal inhibition on thalamic relay cells (Halassa & Acsády, 2016). These inhibitory centers are capable of imposing unidirectional feed-forward inhibition onto thalamic relay neurons, because they are not wired within the thalamo-cortical loop. Synapses formed by extra-thalamic centers form multiple active zones on thick proximal dendrites and are covered by a thick glial sheet that restricts GABA spillover (Barthó *et al.*, 2002; Wanaverbecq *et al.*, 2008; Bodor *et al.*, 2008). This pronounced inhibition is capable to silence action potential generation and subsequently induce thalamic rebound spiking (Bokor *et al.*, 2005). For example, the extra-thalamic inhibition in PoM originates from ZI and APT and is sufficient to effectively modulate PoM spiking rates upon activation of trigeminal nucleus or motor cortex (Lavalle *et al.*, 2005; Urbain & Deschênes, 2007).

Electro-responsiveness of Thalamic Neurons: The Characteristics of Tonic and Burst Spike Induction

Due to the expression of low-voltage activated calcium channels (T-type calcium channel), the thalamus is capable of transfering information via two discrete modes of spiking, namely tonic and burst-spike modes (Murray Sherman, 2001). The transition between tonic or burst-spike modes depends on the instantaneous membrane potential of the thalamic cell, which determines the activation state of the T-type calcium channel and the possible induction of a low-threshold calcium spike (LTS, (Jahnsen & Llinas, 1984*a*, 1984*b*). With membrane potentials more positive than -55mV, the low-voltage activated calcium conductance is inactivated (Jahnsen & Llinás, 1984). The cell responds with a single sodium spike, as long as the cell receives supra-threshold depolarizing inputs (Jahnsen & Llinas, 1984*a*). In contrast, with hyperpolarized membrane potentials starting from below -55mV, the T-type channel is engaged and the cell responds with a LTS and several sodium spikes riding on top. This transition between spiking modes can be physiologically significant. For example, in the whisker responsive part of VPM, the state of the membrane potential determines the shift from burst to tonic spiking during more depolarized states and allows the relay of high-frequency tactile information (Mease *et al.*, 2014*a*). In contrast to the tonic spike transition, a strong burst of action potentials increases signal detectability and the reliability of signal transfer to target areas. For a long time it has been thought that burst firing is restricted to sleep states or pathological conditions. However, in the visual and proprioceptive system it has been shown that the chance of burst firing during awake behavior is dependent on the intensity of the stimulus and that burst firing conveys particular types of information (Weyand *et al.*, 2000; Whitmire *et al.*, 2016).

Cerebellar Innervation in Thalamus – the Motor Thalamus

In Chapter 5 and 6 I focus on the cerebellar and cerebral afferents of the motor thalamus. The cerebellar nuclei densely innervate thalamic nuclei such as the ventro-lateral (VL), ventro-medial (VM) and centro-lateral nucleus (Bentivoglio & Kuypers, 1982; Angaut *et al.*, 1985; Aumann *et al.*, 1994; Teune *et al.*, 2000; Gornati *et al.*, 2018). The VL - as the core and historically well characterized cerebello-recipient nucleus of the motor thalamus – is innervated by large synaptic boutons with multiple release sides (Sawyer *et al.*, 1994*a*; Aumann & Horne, 1996*a*, 1996*b*, 1999). From electrophysiological in-vivo studies in rats and cats, we already know that cerebellar stimulation induces spiking in thalamic neurons localized in VL (Sawyer, Young, et al. 1994; Uno et al. 1970). *In-vivo* optogenetic stimulation shows that cerebellar nuclei activation is capable of activating thalamic neurons and corresponding motor target areas in the cortex and basal ganglia (Cruikshank *et al.*, 2012; Popa *et al.*, 2013; Chen *et al.*, 2014; Proville *et al.*, 2014). Single axon tracing studies provide the anatomical base for these cerebello-thalamo-cortical response patterns, as they show that classical C-type neurons in cerebellar-recipient VL innervate layers 2-5 in motor cortices without forming striatal collaterals (Kuramoto *et al.*, 2009*b*). In contrast, thalamic M-type neurons in VM preferably innervate cortical layer 1 in motor cortical areas, but also other cortical areas such as the orbitofrontal or cingulate cortex as well as the striatum in the basalganglia (Kuramoto *et al.*, 2013).

The Cerebellum

The successful execution and timing of voluntary movements requires motor learning and the continuous updating of motor programs (Marr, 1969; Albus, 1971). The cerebellum has been postulated to contribute to the fine-tuning of motor commands by utilizing either forward or inverse models of sensory feedback errors (de Zeeuw *et al.*, 1988; Simpson *et al.*, 1996; Soetedjo *et al.*, 2008; Brooks *et al.*, 2015; Herzfeld *et al.*, 2015). For the coordination of acquired movements it calculates the sensory consequences of movements and determines the sensory prediction error in relation to the sensory feedback (Hansel *et al.*, 2001; De Zeeuw *et al.*, 2011; Gao *et al.*, 2012; Brooks *et al.*, 2015). As a classic example for cerebellar malfunction, patients that suffer from cerebellar ataxia are incapable to precisely move their fingertip to their nose without deviations.

The highly organized anatomy of the cerebellum is optimized to calculate this sensory prediction error (Ruigrok & Voogd, 2000; Apps & Hawkes, 2009). The cerebellum can be subdivided into the cerebellar cortex, the cerebellar nuclei (CN) and the cerebellar peduncles (inferior, medial and superior), which contain the axons that connect the cerebellum to the rest of the central nervous system. Along the medio-lateral axis the cerebellar cortex can be functionally subdivided into the spinocerebellum and cerebrocerebellum, which regulate body and limb movements and evaluate sensory

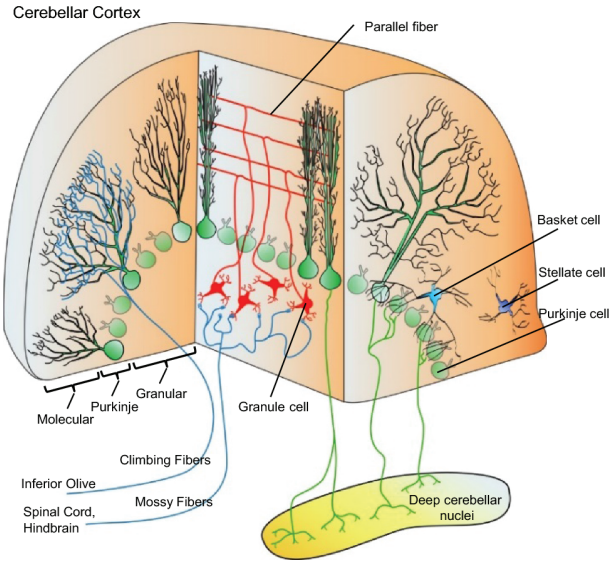

Figure 4 The cerebellar anatomy. The cerebellar anatomy on the microcircuit level depicts the two major inputs via mossy fibers and climbing fibers that innervate granular cells and Purkinje cells, respectively. Climbing fibers arise from the inferior olive and co-innervate the cerebellar nuclei. The granular cells send parallel fibers to Purkinje cells and also innervate Golgi cells. Basket cells and Stellate cells are the interneurons of the molecular layer. Adapted from (Ransdell & Nerbonne, 2018)

information necessary for motor planning. The spinocerebellum receives direct sensory afferents from the sensory spinal cord neurons, while the cerebrocerebellum receives information from the cerebral cortex via the pontine nucleus (Huang *et al.*, 2013; Henschke & Pakan, 2020). The vestibulocerebellum, which is localized in the floccular lobule mediates balance and eye movements and receives its afferents from the vestibular nucleus (Kandel *et al.*, 2012).

The cerebellar cortex has 3 layers, which include the granular layer at the bottom, the Purkinje cell layer and the molecular layer as the top layer within the cerebellar circuitry (Figure 4). The granular layer is formed by billions of granule cells as well as interneurons such as Golgi cells, unipolar bush cells and others. As an impressive fun fact: the number of granule cells in the human brain is estimated to 50 billion, which is about 80 percent of all the neurons that form the brain (Williams & Herrup, 1988). Importantly, all these granule cells send their axons as so called parallel fibers to the molecular layer (Garwicz & Andersson, 1992). The Purkinje cell layer is formed by the alignment of Purkinje cell somata, which send their dendrites into the molecular layer, where they receive dense excitatory inputs from parallel fibers and climbing fibers as

well as inhibition from molecular layer interneurons such as basket and stellate cells (Eccles *et al.*, 1966; Sillitoe *et al.*, 2008).

The two main external inputs to the cerebellar cortex are mossy fiber afferents that provide primary sensory information to granule cells and climbing fiber afferents that originate from the inferior olive (Eccles *et al.*, 1966; Simpson *et al.*, 1996; Huang *et al.*, 2013; Chabrol *et al.*, 2015; Ishikawa *et al.*, 2015; Biswas *et al.*, 2019). Both pathways terminate on Purkinje cells, which respond by firing simple and complex spikes, respectively, and in turn inhibit cerebellar nuclei cells (Fujita et al., 2020; Person and Raman, 2011). Within the mossy fiber pathway the mossy fibers innervate granular cells, which ascend their axons into the molecular layer and bifurcate in parallel fibers. Both the ascending and parallel fiber parts of the granule cell axons synapse onto Purkinje cell dendrite and thereby modulate simple spike firing frequency (Häusser & Clark, 1997; Wulff *et al.*, 2009; Galliano *et al.*, 2013). In contrast, climbing fibers provide direct extensive excitation to the Purkinje cell dendrite and induce the so called complex spike (Sugihara *et al.*, 1999; Schmolesky *et al.*, 2002). According to the Albus-Marr theory the complex spike provides a teaching signal (unconditioned stimulus, US) that encodes the error in motor execution, while the parallel fiber provides the Purkinje cell with contextual information (conditioned stimulus, CS). The combination of both inputs modulates simple spike firing frequency (conditioned response, CR) and provides cellular mechanisms that induce motor learning in classical conditioning paradigms (Marr, 1969; Albus, 1971; Hansel *et al.*, 2001; De Zeeuw *et al.*, 2011; Ten Brinke *et al.*, 2017).

The CN form the final output from the cerebellar cortex. They can be subdivided into lateral, interposed and fastigial nuclei and connect to subcortical targets such as the superior nucleus, the red nucleus, the thalamus and many more (Bentivoglio & Kuypers, 1982; Teune *et al.*, 2000; Fujita *et al.*, 2020; Kebschull *et al.*, 2020). Within the microcircuitry of the CN, the neurotransmitter identity and soma size have been used to identify five major CN cell types (Uusisaari & Knöpfel, 2011; Fujita *et al.*, 2020; Kebschull *et al.*, 2020). Large glutamatergic projection neurons form the cerebellar output to subcortical premotor centers and thalamus, but have recently been shown to also form cerebellar nucleocortical projections (Uusisaari *et al.*, 2007; Gao *et al.*, 2016). Small GABAergic neurons project to the inferior olive and in addition glycinergic as well as small glutamatergic and large GABAergic neurons have been identified (Uusisaari *et al.*, 2007; Uusisaari & Knöpfel, 2010). The Purkinje cell firing pattern essentially inhibits CN cells and thus determines CN spiking activity and pattern (Person & Raman, 2011*a*; Sarnaik & Raman, 2018). In addition to the strong inhibitory inputs from Purkinje cells, CN neurons receive excitatory collaterals from both mossy and climbing fibers (Cicirata *et al.*, 2004; Pijpers *et al.*, 2005). The intrinsic firing frequency of CN neurons ranges between 30 and 160Hz

and is highly irregular during rest (Antziferova et al., 1980; Armstrong and Edgley, 1984; Hoebeek et al., 2010; Ohmae et al., 2013; Person and Raman, 2011; Sarnaik and Raman, 2018); however, during walking the high-frequency spiking pattern of CN neurons becomes more phasic and aligned with the movement execution. This rich spiking pattern most likely encodes the cerebellar prediction error necessary to fine-tune movement execution.

Scope of the Thesis

In this thesis we aim to describe the anatomical and physiological properties of pathways that are involved in the communication between the cerebral cortex and the cerebellum. In more detail, we zoom in on the characteristics of individual pathways that mediate the transfer of information between the motor cortex, the sensory cortex, the thalamus and the cerebellum.

After an initial introduction of the anatomical architecture, cell types and physiological characteristics that form the core of each brain region (**Chapter 1**), we aim to describe the details of the synaptic connectivity between the sensory cortex and sensory thalamus in **Chapter 2**. In particular, we intend to use the cortical driver synapse in sensory thalamus as a model synapse to identify physiological phenotypes in the absence of the presynaptic scaffolding protein Bassoon. In **Chapter 3** we aim to identify hot spots for anatomical convergence between sensory cortex and cerebellar nuclei in the thalamus but also in extra-thalamic areas. After the description of connectivity within the sensory thalamus (**Chapter 2 and 3**), we aspire to describe the anatomical and physiological properties of the cerebellar pathway in the motor thalamus (**Chapter 4 and 5**). In **Chapter 4**, we want to raise the question whether cerebellar output is differentially processed in ventro-lateral, ventro-medial and centro-lateral nuclei of the thalamus. Therefore, we aim for a detailed anatomical and physiological description of the cerebellar synapse and the thalamic neuron in each of the nuclei. Following up on this initial description, we desired to show physiological convergence between the inputs from cerebellar nuclei and feedback from motor cortical layer 6 in ventro-lateral nucleus of the thalamus (**Chapter 5**). We aim to use a dual-optogenetic stimulation approach to co-activate both pathways and to evaluate the effect of their integration on the thalamo-cortical spike transfer. In **Chapter 6**, we aim to describe how deviations from healthy synaptic connectivity induced by hyperactivity of the mTOR signaling pathway and the focal expression of a dominant-active mutation in Ras Homolog Enriched in Brain 1 protein can induce epileptic seizures. We aspire to provide evidence for the anatomical and physiological abnormalities induced by mTOR hyperactivity that can lead to generalized epilepsy. While **Chapters 2-5** are centered around the cortex and/or the cerebellar nuclei sending their projections to the thalamus, we want to use **Chapter 7** to hypothesize on the

existence of undescribed subpopulation of cortico-spinal neurons that innervate the cerebellar nuclei and provide a route for direct communication between the motor cortex and the cerebellar nuclei. We aim to characterize the anatomical embedding of this pathway in the brain circuitry as well as its physiological properties and genetic profile.

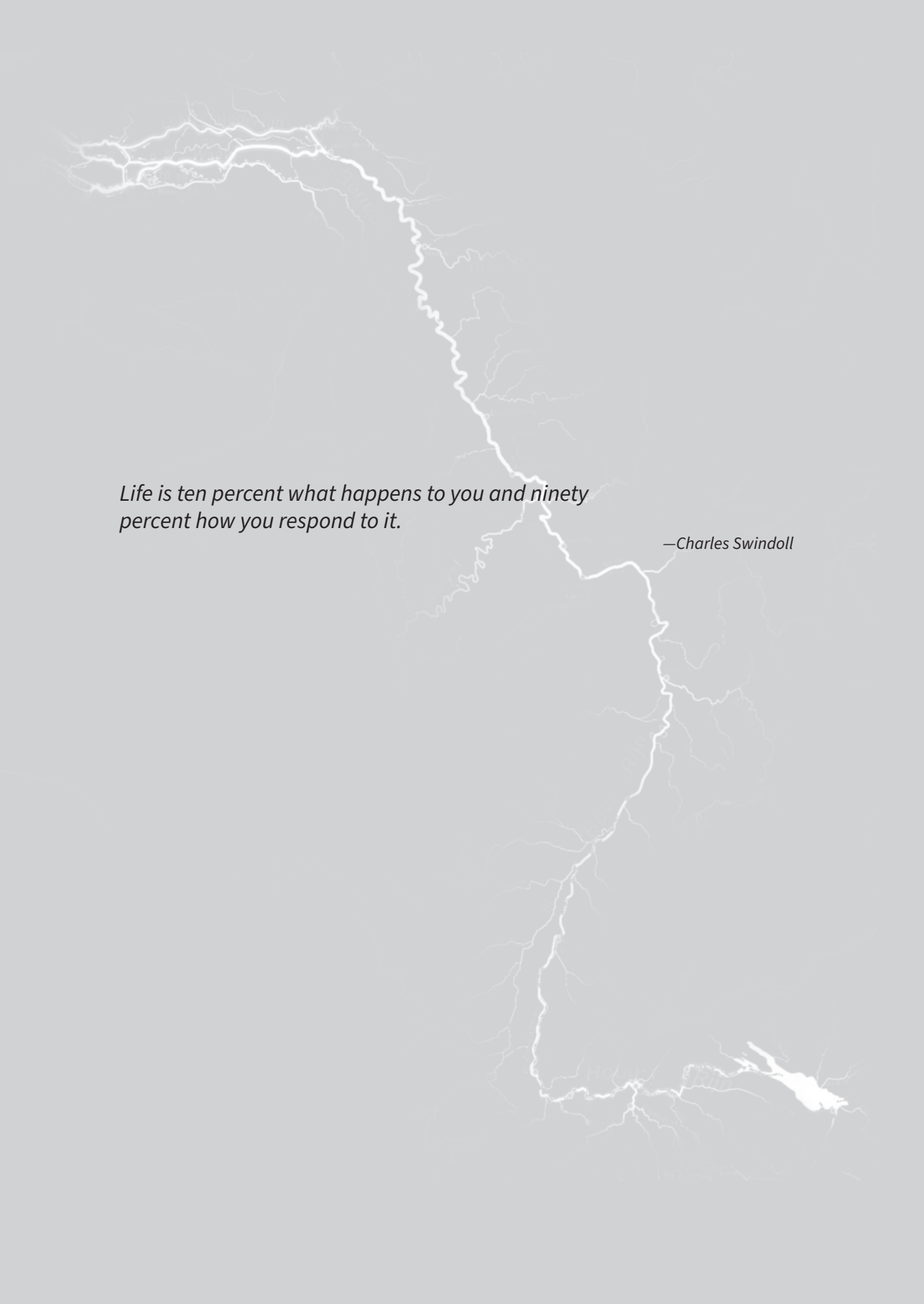

Life is ten percent what happens to you and ninety percent how you respond to it.

—Charles Swindoll

Chapter 2

Synaptic Release in Bassoon Deficient Thalamic Giant Synapses

Carmen B Schäfer
Anna Fejtova
Christoph Körber
Frank Herrmannsdörfer
Eckart D Gundelfinger
Thomas Kuner

ABSTRACT

In synaptic transmission of chemical synapses, the release of neurotransmitter is temporally coupled to the arrival of action potentials. In the presynaptic compartment the docking and fusion of synaptic vesicles takes place at active zones. Bassoon and Piccolo are two homologous active zone multidomain scaffolding proteins, which have been suggested to function in anchoring active zones as well as the reloading of synaptic vesicles. This study aimed at investigating the role of Bassoon during basic and sustained neurotransmission in thalamic giant synapses. We established a conditional Bassoon knockout model in cortical giant synapses of the posterior-medial thalamic nucleus (POm). Immnunohistochemical analysis revealed a 50% reduction of Bassoon expression after incubating with Cre-recombinase for 14 days. We applied a single synapse stimulation paradigm and evaluated synaptic responses to single stimuli as well as trains of stimuli in Bassoon deficient and WT synapses. We found a significant increase in the amplitude of excitatory-postsynaptic currents (EPSCs) whereas EPSC kinetics were similar between WT and Bassoon deficient synapses. During sustained neurotransmission we found an enhancement in short-term synaptic depression defined by a faster depletion of the ready-releasable vesicle pool in the absence of Bassoon. These findings are in line with results found previously and support a role of Bassoon during the reloading of synaptic vesicles to release sites and thus the rapid refilling of the ready-releasable vesicle pool during sustained synaptic transmission.

INTRODUCTION

Synaptic communication ensures the flow of information between neurons and is the base of behavioural responses. For the release of neurotransmitter, the presynaptic site is specialized into active zones (AZ) of exocytosis which appear as electron dense structures and are formed by a tight protein network. The cytomatrix of AZs is made up by scaffolding proteins such as RIMs (Rab3-interacting molecules), Munc13 proteins, ELKS, Liprin-α as well as Piccolo and Bassoon (Schoch & Gundelfinger, 2006; Südhof, 2012). The core protein complex of the AZ is involved in linking presynaptic Ca^{2+} channels, synaptic vesicles and the fusion machinery to each other and the plasma membrane, thereby organizing the release and retrieval of synaptic vesicles from the presynaptic terminal (Gundelfinger & Fejtova, 2012). Thus the precise composition of AZ proteins determines synaptic specification and function.

The largest AZ-specific scaffolding proteins are Piccolo (Cases-Langhoff *et al.*, 1996; Wang *et al.*, 1999; Fenster *et al.*, 2000) and Bassoon (Dieck *et al.*, 1998). Both proteins have a highly redundant protein structure made up by two zinc-finger and three coiled-coil domains localized at their N-terminal and the protein center, respectively. Both proteins form an interaction node in the AZ, as their third coiled-coil region interacts with ELKS (Takao-Rikitsu *et al.*, 2004), but also with Munc-13 (Wang *et al.*, 2009). Bassoon was shown to specifically control the abundance of presynaptic P/Q-type Calcium channels via its interaction with RIM-binding protein (Davydova *et al.*, 2014).

Multiple studies have been conducted to evaluate the function of Piccolo and Bassoon, but both proteins seem to function differently depending on the synapse type. Double knockdown of Piccolo and Basson has been shown to induce alterations in protein ubiquitination which result in synapse degradation accompanied by the loss of multiple AZ proteins such as Munc13, RIM, SNAP25 and Synapsin in hippocampal synapses (Waites *et al.*, 2013). A weaker phenotype is found in Bassoon and Piccolo deficient hippocampal synapses of $Pclo^{\Delta Ex14}$ mice, characterized by decreased numbers of SVs, a lowered density of SVs per terminal, less vesicles closely localizing to the AZ and a reduction in synapses containing vesicle clusters (Mukherjee *et al.*, 2010). In contrast an up-regulation of Piccolo protein levels but no down-regulation of other AZ proteins has been found in Bassoon deficient synapses, indicative of compensatory effects of Piccolo (Altrock *et al.*, 2003; Schulz Mendoza *et al.*, 2014). Characterization of $Bsn^{\Delta Ex4/5}$ hippocampal synapses showed an inactivation of a significant portion of synapses, while the remaining synapses show unaltered release properties (Altrock *et al.*, 2003). In contrast, in high-frequency transmitting mossy-fiber to granule cell synapses (Hallermann *et al.*, 2010) and End-bulb of Held synapses (Schulz Mendoza *et al.*, 2014) an increased synap-

tic depletion and a slower initial phase of recovery have been detected. These results are indicative of a role of Bassoon in speeding the reloading of synaptic vesicles to the AZ during sustained synaptic transmission but not during basic transmission such as in hippocampal synapses.

Here, we created a mutant mouse in which Cre-mediated Bassoon deficiency can be induced on top of a constitutive Piccolo knock-out (KO) (Mukherjee *et al.*, 2010). We studied synaptic transmission in Bassoon deficient cortico-thalamic driver synapses in the posterior medial nucleus (POm) of the thalamus, in which the native Piccolo expression is maintained. This conditional Bassoon knockdown (KD) allows a normal *in vivo* synapse development. We combine high-speed confocal imaging and in vitro electrophysiology to apply a single synapse stimulation paradigm that enables us to evaluate the release phenotype of these Bassoon deficient synapses.

RESULTS

Bassoon turnover

In an initial step, we assessed the required time for the loss of Bassoon from the active zones of PoM giant terminals after cortical injection of Adeno-associated virus (AAV) which expresses iCre-mOrange and induces Bassoon knock-down (Bsn -/-). PoM giant synapses were co-labeled with Synaptophysin-EGFP and cytoplasmic mOrange2, where mOrange2 fluorescence indicates nuclear expression of iCre and thus Bassoon deficiency. A time series of 9, 14 and 21-22 days incubation with Cre was established in $Bsn^{lox/lox}$ and WT animals. Bassoon expression levels were determined by quantifying immunohistochemical signal intensities within the Synaptophysin-EGFP positive presynaptic volumes and Synaptophysin-EGFP positive but Cre negative controle terminals (WT Cre pos.: 6.5 ± 0.2, n = 60; WT Cre neg.: 7.2 ± 0.3, n = 34; 9D Cre pos.: 4.2 ± 0.2, n = 62; 9D Cre neg.: 6.7 ± 0.4, n = 33; 14D Cre pos. 3.9 ± 0.2, n = 64; 14D Cre neg. 6.7 ± 0.6, n = 30; 21D Cre pos. 4.0 ± 0.3, n = 48; 21D Cre neg. 6.7 ± 0.6, n = 33; N = 3; arbitrary units). A ~55% reduction in Bassoon expression level in comparison to WT synapses was found in cre positive terminals after 9, 14 and 21 - 22 days incubation. A ~45% reduction was found, when comparing Cre positive and negative synapses within the same group (Figure 1). In summary, we report a 50% reduction in Bassoon protein levels in Cre positive POm giant synapses after 14 days of incubation, leading us to further evaluate the release phenotype of these Bassoon deficient synapses.

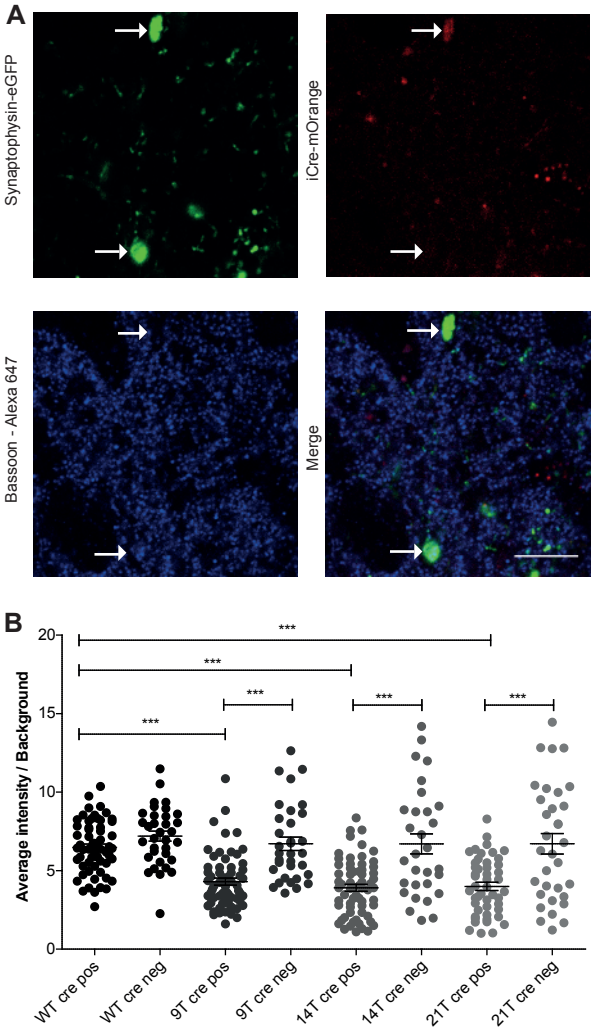

Figure 1. The Bassoon protein turnover. **A** Synaptophysin-EGFP labeled synapses which are iCre-mOrange2 positive and downregulated in Bassoon expression (upper arrow) or iCre-mOrange2 negative and normal Bassoon expression levels (lower arrow) are depicted. The scale bar is 10µm. **B** The Bassoon turnover after 9, 14 and 21 -22 days of iCre incubation in conditional Bsn KD mice and after 14 days in WT mice is quantified. Here, the normalized intensity of Bassoon immunolabeling within the presynaptic volume for iCre positive and negative synapses is shown. The values represent mean ± SEM and are depicted in arbitrary units. n = number of synapses, N = number of animals. ***p-value < 0.001.

Sective Stimulation of Single Corticothalamic Synapses

To gain insight into the basic release properties of WT and Bsn-/- POm giant synapses, we applied a stimulation paradigm targeting single presynaptic terminals. We labeled corticothalamic terminals originating in Layer 5B of barrelcortex and induced their Bassoon deficiency by co-injecting AAV that expresses Synaptophysin-EGFP and/or

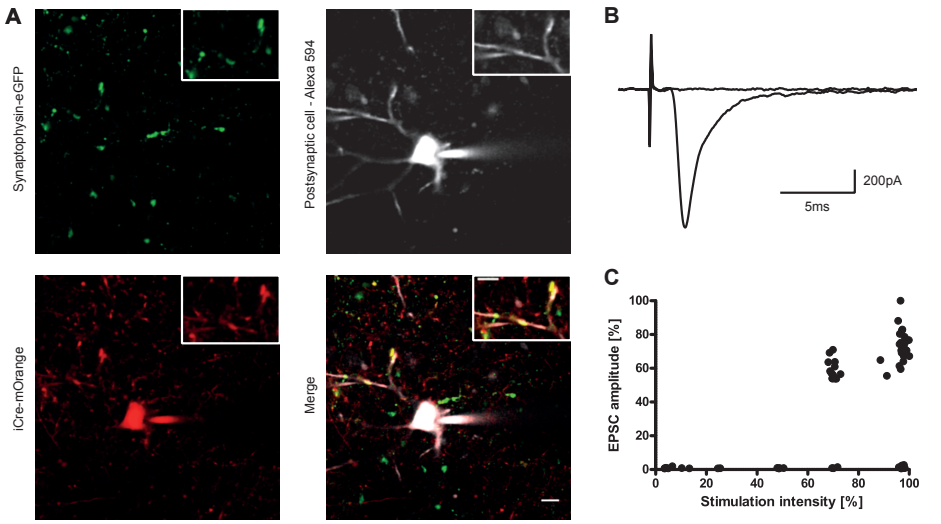

Figure 2. Stimulation of individual Bassoon deficient synapses in the POm. A Synaptophysin-EGFP and iCre-mOrange2 were co-injected to Layer 5B of the barrelcortex to label POm giant synapses and to knockdown Bassoon expression. Multichannel high-speed confocal microscopy was used to detect Synaptophysin-EGFP (green) and mOrange (red) positive synapses as well as the postsynaptic neuron loaded with Alexa 594 (grey) simultaneously. The double-barrel stimulation pipette was loaded with Alexa 594 and positioned within 1µm distance to a Synaptophysin-EGFP and mOrange2 positive synapse contacting the postsynaptic neuron (inlay). Scale bar is 10 µm and 5 µm in the inlay. **B** Representative EPSC evoked in an all-or-none manner. Current traces show the postsynaptic response before and after reaching the stimulation threshold for inducing synaptic release (upper panel). Upon increasing the stimulation intensity an unitary postsynaptic response with a constant amplitude is induced.

iCre-mOrange. AAV injection labeling of cortical synapses with Synaptophysin-EGFP or iCre-mOrange2 positive as well as co-labeled synapses. POm neurons embedded in co-labeld terminals were chosen for whole cell recordings and loaded with Alexa 594. Cortical giant synapses contacting the postsynaptic dendrite were selectively stimulated by positioning a double-barrel stimulation pipette within the proximity of 1µm close to the terminal (Figure 2). Stimulation intensity and duration were gradually increased until a synaptic all-or-none response, was induced. The response was only considered as single synaptic, when the EPSC was defined by a steep risetime and a further increase of stimulation intensity or duration did not evoke higher EPSC amplitudes. Moving the stimulation pipette more than 1µm from the presynaptic terminal resulted in the loss of the synaptic response and assured the local selectivity of the electrical stimulation.

Basal synaptic transmission in Bassoon deficient synapses

The basic synaptic release properties upon single stimuli were evaluated. The amplitudes of EPSCs were significantly higher in Bassoon deficient synapses when compared to WT (WT: -204.1 ± 24.03 pA, n = 8; Bsn-/-: -570.8 ± 123.9 pA, n = 9; p-value = 0.0152,

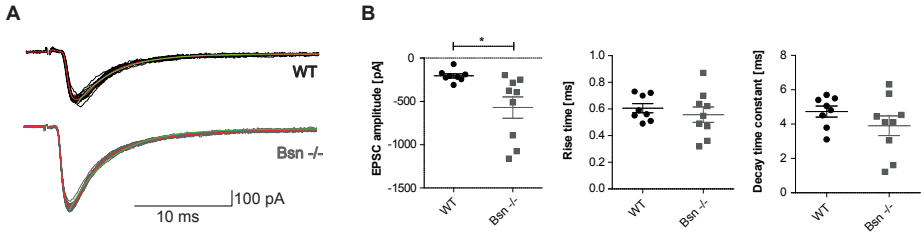

Figure 3. Basic synaptic transmission in WT and Bsn-/- synapses. A EPSCs for WT and Bsn-/- synapses with their corresponding averages (in red) are shown (stimulus artefacts are removed). The single exponential fit on the EPSC decay is shown in green. **B** The average amplitude, rise time and decay time for WT (in black, n = 8) and for Bassoon deficient (in grey, n = 9) synapses are shown.

t-test), whereas no difference in the rise time (WT: 0.61 ± 0.03 ms, n = 8; Bsn-/-: 0.056 ± 0.06 ms, n = 9; p-value = 0.4895, t-test) and decay time (WT: 4.73 ± 0.32 ms, n = 8; Bsn-/-: 3.9 ± 0.57 ms, n = 9; p-value = 0.2383, t-test; Figure 3) was detected.

Presynaptic short-term plasticity in Bassoon deficient synapses

To unravel the protein function of Bassoon during sustained neurotransmission, we applied repititive stimuli at higher frequencies of 10 and 50Hz. For the analysis the average EPSC amplitudes were normalized to the first EPSC in the train and plotted against time for both frequencies. Already for the second EPSC in the train we find a decrease in amplitude when comparing WT and Bassoon deficient synapses at stimulation frequencies of 10Hz (WT: 75.02 ± 5.0 ms, n = 7; Bsn-/-: 48.8 ± 3.6 ms, n = 7; p-value = 0.001, t-test) and 50 Hz (WT: 44.6 ± 5.1 ms, n = 5; Bsn-/-: 13.8 ± 2.6 ms, n = 4; p-value = 0.0159, Mann-Whitney test). During the steady state at 10 Hz the EPSC amplitudes were reduced to 47.7 ± 4.3% in WT and 35.6 ± 3.6% in Bsn (p-value = 0.0553, t-test) and to 9.9 ± 1.9% and 4.5 ± 2.6% at 50 Hz, respectively (p-value = 0.1111, Mann-Whitney test). Therefore, we find that Bassoon deficient synapses show a significantly faster depression in comparison to WT synapses (Figure 4). Our data suggests Bassoon to accelarate the reloading of synaptic vesicles to active zones during high frequency transmission.

Pool properties

To further evaluate the effect of Bassoon deficiency on synaptic release properties, we determined the readily-releasable pool (RRP) size by back-extrapolating the cummulative EPSC amplitudes during steady-state depression at 50Hz (WT: 508.8 ± 135.5 pA, n = 5; Bsn-/-: 865.2 ± 283 pA, n = 5; p-value = 0.2884, t-test; Figure 5) (Schneggenburger *et al.*, 1999; Groh *et al.*, 2008). In a next step, we determined the release probability by calculating the proportion of current that is released with the first stimulus in the 50Hz train (WT: 38.3 ± 6.1 %, n = 5; Bsn-/- 63.6 ± 12.5 %, n = 5; p-value = 0.1069, t-test). We find

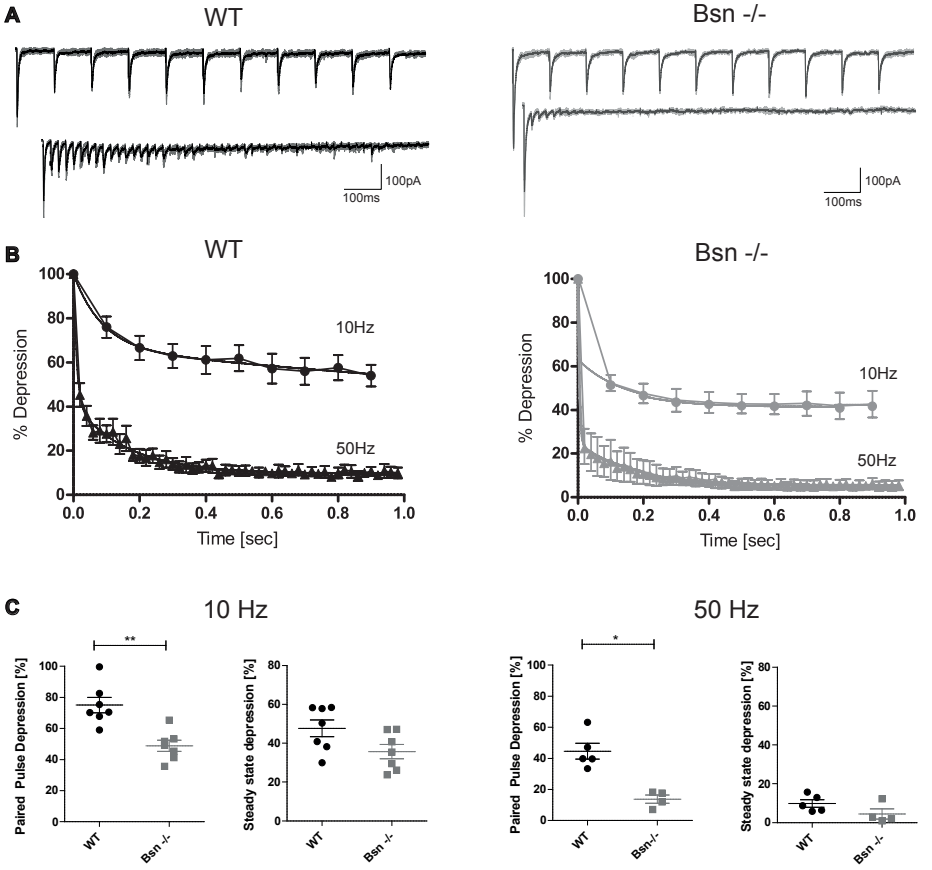

Figure 4. Short-term depression in WT and Bassoon deficient synapses. A Example traces depict the synaptic responses after stimulating WT and Bassoon deficient synapses at 10 and 50Hz. For each condtition and frequency five consecutive traces (in grey) and their corresponding average (in black) are plotted. **B** The average amplitude decay in WT and Bsn-/- synapses after stimulation at 10 and 50Hz is depicted and fitted by a biexponential decay curve. **C** The paired pulse ratio and steady state depression after 10 and 50Hz stimulation are shown for each genotype.

a increase of 66% in release probability in Bassoon deficient synapses, which is in line with the increase in paired-pulse ratio.

Recovery from Synaptic Depression in Bsn -/-

In a next step we asked whether Bassoon deficient synapses show alterations in the recovery from synaptic depression. We applied a 50 Hz train to completely deplete the presynaptic vesicle pool and tested for recovery with stimuli at increasing time intervals of 50ms. Exponential fits to the recovery reveal time constants of 738 ± 215 ms (n = 4) in Bsn-/- and of 486.6 ± 63.3 ms (n = 4) in WT synapses and steady state recoveries of 70.9 ± 5.9 % and 72.2 ± 5.0 %, respectively (Figure 6).

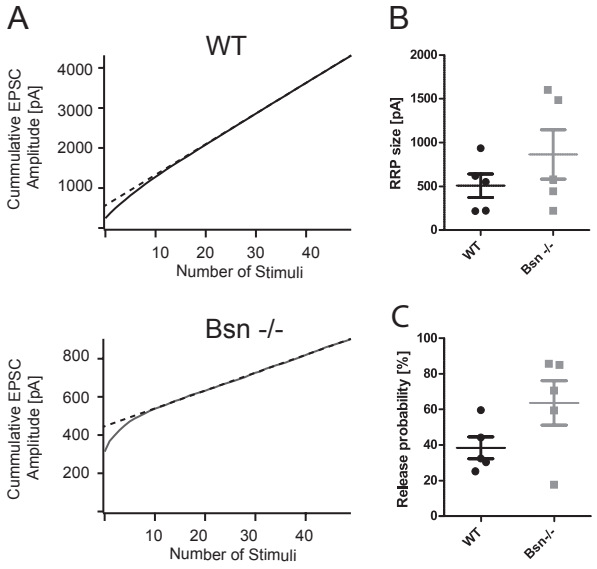

Figure 5. Pool properties of WT and Bassoon deficient synapses. A Plot of the cummulative EPSC amplitude in a WT and a Bassoon deficient synapse. Steady state EPSC amplitudes are linearly fitted and back-extrapolatated to their intersection with the ordinate for determining the ready-releasable pool (RRP) size. **B** The RRP size was determined for WT and Bsn-/- synapses as described in (**A**). **C** The realease probability was determined by dividing the RRP size by the EPSC amplitude of the first response in the 50Hz train - for both WT and Bsn-/- synapses.

DISCUSSION

We use the cortical layer 5 synapse in the PoM as a model to study the properties of synaptic transmission in absence of Bassoon. Our data shows, that Bassoon protein levels are reduced to ~50% after cre-mediated knockdown of Bassoon in cortical layer 5 terminals. To establish a single synapse stimulation paradigm, we co-labeld cortical driver synapses with Synaptophysin-EGFP and used laser-scanning confocal microscopy to place an electrical stimulation pipette that activates individual terminals. The loss of Bassoon induces a phenotype of increased basic transmission as well as faster synaptic depression during 10 and 50Hz stimulation, which aligns with an increase in synaptic release probability.

Even though the highly homologous structure of Piccolo and Bassoon suggests redundant protein functions, co-expression is found in some but not all synapses. For instance, both Piccolo and Bassoon co-localize in hippocampal synapses of primary cultures (Dieck et al., 1998; Fenster et al., 2000), but Bassoon expression patterns have been found highly variable at the Calyx of Held (Dondzillo *et al.*, 2010) and the Endbulb of Held terminals (Schulz Mendoza *et al.*, 2014), where only 60% and 66-84% of Piccolo

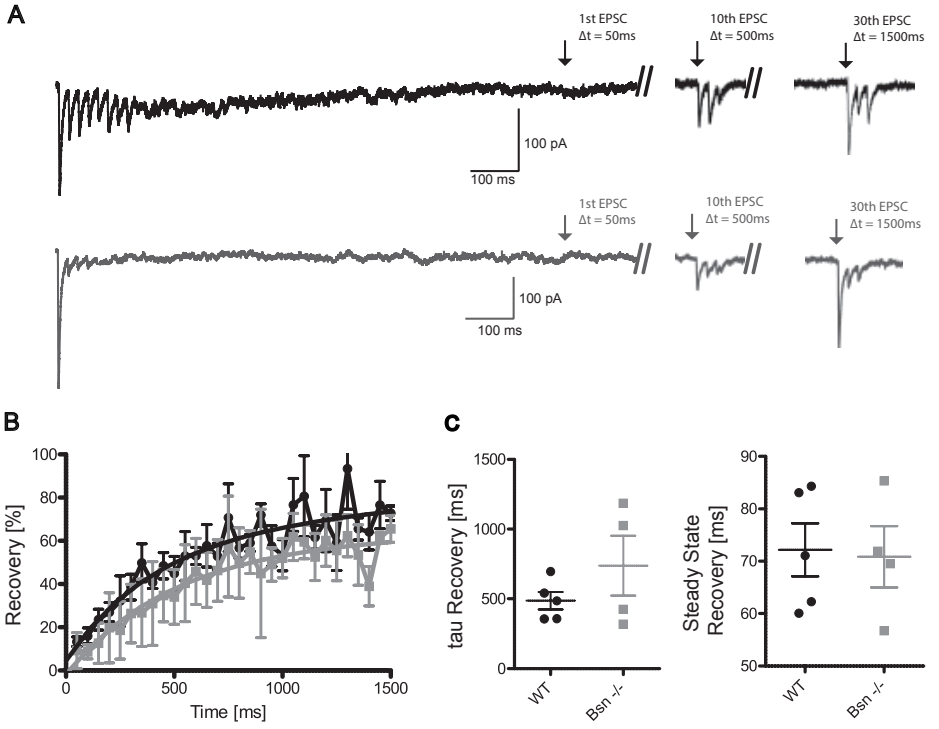

Figure 6. Synaptic recovery in WT and Bassoon deficient synapses. A After an initial depletion of the presynaptic vesicle pool with a stimulus train of 50Hz, the synaptic recovery was evaluated at increasing time intervals of 50ms. **B** The average recovered EPSC amplitudes are plotted for both WT and Bassoon deficient synapses and fitted with an exponential decay curve (WT: n = 5, Bsn-/-: n = 4). **C** The steady state and time constant of the recovery from synaptic depression are shown for both WT and Bassoon deficient synapses.

and Bassoon spots overlap, respectively. These results suggest differential targeting of Piccolo and Bassoon within a single synapse, which could account for variability in Bassoon immunoreactivity in WT and Cre negative synapses. Nevertheless, the evaluation of synaptic release in Piccolo and Bassoon double deficient synapses is of particular interest, as protein levels of either Piccolo or Bassoon might be upregulated in synapses lacking one of the two proteins (Altrock et al., 2003; Schulz Mendoza et al., 2014).

When investigating the basic synaptic transmission of PoM driver synapses, the amplitude in Bsn -/- synapses was increased but no differences in EPSC kinetics were found. However, interpretation of EPSC amplitudes in the PoM giant synapse is difficult, as EPSC amplitudes are highly variable in rat (Groh et al., 2008) and mouse (Seol & Kuner, 2015). Unaltered basic synaptic transmission in Bassoon deficient synapses was found

in MF-GC (Hallermann et al., 2010) and Endbulb of Held synapses (Schulz Mendoza et al., 2014).

Furthermore, synaptic release during sustained synaptic transmission was investigated in PoM giant synapses. The high release probability and short-term depression in response to train stimulation, makes PoM driver synapses an ideal model to study synaptic transmission (Groh *et al.*, 2008; Seol & Kuner, 2015). We find that Bassoon deficient synapses depress faster. These results are in line with results found previously in the Endbulb of Held synapse (Schulz Mendoza *et al.*, 2014) and the mossy fiber to granule cell synapse (Hallermann *et al.*, 2010), but in contrast to short-term plasticity phenotypes found in hippocampal synapses (Altrock *et al.*, 2003). Apart from the increase in paired-pulse ratio, we find an increase of release probability in Bassoon deficient synapses, which was also found in Bassoon deficient Endbulb of Held synapses (Schulz Mendoza *et al.*, 2014), but not in mossy fiber to granule cell or hippocampal synapses (Altrock *et al.*, 2003; Hallermann *et al.*, 2010). Importantly, the influence of post-synaptic components, such as AMPA – receptor desensitization, on synaptic depression and recovery was not evaluated and therefore postsynaptic effects on short-term plasticity cannot be excluded. In contrast to previouse studies, we find that the steady-state depression as well as the RRP size and the speed of synaptic recovery appear unchanged in Bassoon deficient PoM giant synapses. However, even though we can find trends towards an increase in RRP size and slower recovery in absence of Bassoon from the active zone, the low statistical power of our data set limits us in drawing final conclusions.

In summary, our results and the results found in previous studies support a model in which Bassoon accelerates the translocation of SV to release sites during sustained highfrequency transmission and in synapses which rely on efficient vesicle reloading (Hallermann *et al.*, 2010; Schulz Mendoza *et al.*, 2014).

METHODS

Animal model system

In this study we worked with a constitual Piccolo KO and a Cre-dependent Bassoon knock down (KD) model. In this mouse line exon 14 of Piccolo, encoding the C_2A-domain, is targeted (referred to as $Pclo^{\Delta Ex14}$), but the neomycin resistence cassette is still expressed (Mukherjee et al., 2010, B6.129-$Pclo^{tm1.Sud}$, The Jackson Laboratory). On top of the constitutive Piccolo KO, both allels of Bassoon exon 2 are flanked with loxP sites, which allows conditional KD by expression of cre recombinase (referred to as $Bsn^{lox/lox}$). Deletion of exon 2 induces a frameshift mutation in exon 3 to 10. Mutant mice heterozygous

for $Pclo^{\Delta Ex14}$ and homozygous for $Bsn^{lox/lox}$ were crossed and offspring was genotyped for Piccolo and Bassoon after obtaining a tail biopsy. The following primers were used for Bassoon: GCAGATTCTAGTCGGTGATCTAGC and GTTGCCTAATGTATGCAGAGTCC. Genotyping resulted in a 220 basepair (bp) fragment for wild-type and a 337 bp fragment for floxed Bassoon allels. Genotyping for Bassoon was discontinued after successful proof of floxed Bassoon allels, as mice were obtained as homozygous $Bsn^{lox/lox}$. The following primers were used for wild-type Piccolo: GCTCTGGTACAGAGGTAAAGCTTGC and TTGTGTCACGTAGTCAGACTG. The Piccolo KO was detected in a separate PCR reaction with the following primers: CCTTGAGGTCAATGTGATCAGC and CCAAGTTCTAATTCCATCAGAAGC. In this study, the Piccolo -/- mutants were not available. Instead, we worked with Piccolo +/+ WT littermates to establish the conditional Bassoon KD in cortico-thalamic driver synapses (refered to as Bsn -/-).

Plasmid cloning and Adenoassociated virus particles

Recombinant adeno-associated virus (AAV) particles of the chimeric 1/ 2 serotype were produced to express the fusion proteins Synaptophysin-EGFP (Schwenger & Kuner, 2010; Seol & Kuner, 2015) and iCre-2A-mOrange2 (Tang *et al.*, 2009; Seol & Kuner, 2015). The fusion peptides were inserted into pAM vector containing the CAG promoter, the woodchuck post-transcriptional regulatory element (WPRE) and the bovine growth hormone poly-A cassette. A combination of both viruses was used with a ratio of 1:1.

Stereotaxic injections

Stereotaxic injections were performed as previously described (Wimmer *et al.*, 2004). In short, 14-day-old mice were anaesthetized with a 1.5% mixture of isoflurane/oxygen and a unilateral craniotomy was made with a dental drill (Osada EXL-40). For cortical injections, a volume of ~ 1.5 µl virus was evenly distributed between 4 – 5 injection sites at the following x, y coordinates relative to bregma and midline (in mm): 0, 2.9; -0.25, 2 .9; -0.5, 2.9; -0.75, 2.9; -1, 2.9. In z-position, each of the described injections was made at -0.9 mm distance from the dura. The mice received preventive pain treatment by a subcutanous injection of Carprofen (0.5 mg/ml, 10 µl/g bodyweight) prior to surgery. Animals recovered within minutes after removing anaesthesia and were transfered back to their mothers.

Immunohistochemistry and confocal microscopy

For detecting Bassoon protein levels Synaptophysin-EGFP and iCre-2A-mOrange were co-injected in $Bsn^{lox/lox}$ animals. Bassoon was detected using a Bassoon mouse monoclonal antibody (Enzo, catalog number: O88778, 1:1000). Appropriate secondary antibodies coupled to Alexa 546 and Alexa 647 (Invitrogen, 1:1000) were used. PFA – fixed brain slices were permeabilized for 2 hours in 5 % Normal-goat-serum (NGS) and 1 %

Triton-X-100 diluted in PBS at room temperature. Primary antibodies were diluted in PBS containing 1 % NGS and 0.2 % Triton-X-100 and incubated over night at 4°C. After 3 washing steps with 2 % NGS in PBS for 15 minutes, secondary antibodies were diluted in PBS containing 1 % NGS and 0.2 % Triton-X-100 and incubated for 4 hours at room temperature. Three washing steps with 1 % NGS in PBS and three washing steps with PBS, 10 minutes each followed. Slices were mounted in Slow Fade Gold (Invitrogen).

For confocal imaging a Leica TCS SP5 confocal microscope with a 63x objective (HCX-PL APO, numerical apperture = 1.3) and glycerol-based immersion medium (refraction index adjusted to Slow Fade Gold) was used. Sequential scans were applied so that 488 nm excitation wavelength was scanned simultaneously with 633 nm wavelength, subsequently a scan with 561 nm followed. Z - stacks of 512 x 512 pixels were aquired at 400 Hz scanning frequency. The pinhole was adjusted to 1 airy unit and voxel sizes were adjusted to 0.81 µm in x,y and to 0.198 µm in z, resulting in a voxel volume of 0.0013 μm^3. Laser intensities and voltages in photomulitiplier tubes were kept constant within experiments.

Quantification of Immunohistological data

The protein expression level of Bassoon within the volume of Pom giant terminals was quantified. To extract the 3D volume of the presynaptic giant terminal, a manually defined threshold was applied on the synaptophysin–EGFP fluorescence and a connected component analysis was performed. For the quantification of Basson and Piccolo protein content in presynaptic terminals, average intensities of immunoreactivity within extracted terminals were calculated. Connected components containing 1000 and less voxels, which resembles a terminal volume of 1.3 μm^3, were excluded from further analysis, as their volume is too small to represent a synapse. After visual inspection, a volume threshold of 10 μm^3 was determined to identify giant synapses. Average Bassoon and mOrange2 intensities in each giant synapse were calculated. The giant terminals were declared mOrange2 positive or negative after visual inspection.

Preparation of acute slices

Acute brain slices were prepared 14-24 days after injection of Synaptophysin-EGFP and iCre-mOrange encoding AAV particles to the barrelcortex. After anaesthesia with isoflurane, mice were decapitated and thalamocortical slices of the right hemisphere containing somatosensory cortex and thalamus were prepared as reported previously . A vibratome (VT1200s, Leica) was used to cut 200 – 250 µm thick slices in ice cold slicing solution. The slicing solution contained (in mM) 85 NaCl, 2.5 KCl, 25 $NaHCO_3$, 1.25 NaH_2PO_4, 75 Sucrose, 3 $MgCl_2$ and 0.1 $CaCl_2$. Glucose was added to adjust osmolarity to 320-330 mOsmol/kg. Directly after slicing the slices were transfered to 37°C warm

artificial cerebrospinal fluid (ACSF) containing (in mM) 125 NaCl, 2.5 KCl, 25 $NaHCO_3$, 1.25 NaH_2PO_4, 1 $MgCl_2$ and 2 $CaCl_2$ and a osmolarity adjusted to 320-330 mOsmol/kg with Glucose. Slicing solution and ACSF was maintained at a pH of 7.3 by bubbling with 95 % O_2 and 5 % CO_2. The slices were incubated for 30-40 minutes at 37°C and afterwards kept at room temperature.

Electrophysiology

Whole cell recordings in voltage clamp modus were acquired using a EPC 10 plus amplifier controlled by Patch master software (HEKA, Lambrecht (Pfalz)). Data were acquired with a sampling rate of 40 kHz and filtered with a 10 kHz Besselfilter and subsequently with a 2.5 kHz filter. All recordings were performed at room temperature. Patch pipettes with an open tip resistence of 4 – 6 MΩ were pulled from 1.5 mm borosilicate cuvettes using a P97 horizontal puller (Sutter instruments). The patch pipette solution contained (in mM): 130 potassium gluconate, 20 KCl, 5 Na_2 phosphocreatine, 5 EGTA, 4 Mg-ATP and 0.5 Na-GTP. The pH of the intracellular patch solution was adjusted to 7.3 with KOH and osmolarity was adjusted to 310-315 mOsmol/kg. Recordings were not corrected for the liquid junction potential. Alexa Fluor 594 Hydrazide (Invitrogen, catalog number: A-10442) was present in all pipette filling solutions (30 µM). Currents were recorded with a holding potential of - 70 mV. Series resistence was usually 10-20 MΩ and compensated to 70-90 %.

Juxtasynaptic stimulation of single presynaptic terminals

Neurons and giant synapses were visualized using interference-scanning-gradient-contrast and confocal microscopy on a TCS – SP5 (Leica) equiped with a 20 x objective (HCX APO, numerical apperture = 1.3). Due to the fast scanning frequencies it was possible to acquire fluorecences of presynaptic synaptophysin-EGFP and mOrange as well as postsynaptic Alexa Fluor 594 simultaneously and to overlay them to IR-interference images (Figure 2). Therefore, it was possible to choose neurons embedded in mOrange2 and Synaptophysin-EGFP positive synapses for whole-cell recordings. Co-labelling with mOrange2 indicated nuclear Cre expression and thus Bassoon deficiency. The dendrites of thalamic relay neurons were visualized by Alexa 594 allowing the identification of POm giant synapses directly contacting the dendritic arbor. All recorded neurons showed hyperpolarization induced burst responses mediated by T-type Ca^{2+} channels and input resistances of 50 – 80 MΩ. Bipolar stimulation pipettes with an open tip diameter of 0.7 – 1.8 µm were pulled from theta glass and filled with ACSF containing 50 µM Alexa Fluor 594 Hydrazide (Invitrogen). For juxtasynaptic stimulation, the stimulation pipette was positioned within 1 µm close to the giant terminal and biphasic pulses were applied using a bipolar isolator (ISO- STIM 01DPI, npi). As established before, stimulation intensities (50 – 90 mV) and duration (30 – 400µs) were increased until an all-or-none

response was evoked (Groh *et al.*, 2008; Seol & Kuner, 2015). Moving the stimulation pipette only 1µm from the synaptic tip resulted in a loss of the postsynaptic current. Responses scaling with stimulation intensity or suggestive for di-synaptic transmission were discarded.

Data analysis

For analysis, IGOR Pro (Wavemetrics) software with custom written scripts and Matlab (MathWorks) were used. We applied double-exponential fits to determine the steady state depression after 50Hz depletion and used back-extrapolation of the cumulative EPSC amplitude to determine the RRP pool size (Schneggenburger *et al.*, 1999). We excluded outliers from the dataset. The release probability was then determined by dividing the RRP pool size by the EPSC amplitude generated by a single stimulation. Data was tested for normal distribution with the Kolmogorov-Smirnov Test. When data was normally distributed a two-tailed t-test was used. When data was not normally distributed the Mann-Whitney-Test was used for statistical analysis. For analysis of Bassoon turnover a one-way ANOVA was used with subsequent Bonferroni correction for mulitple comparisons. Data is presented as mean ± SEM.

ACKNOWLEDGEMENTS

We thank Michaela Kaiser, Claudia Kocksch and Richard Hertel for excellent techniqual support.

COMPETING INTERESTS

The authors state no conflict of interests.

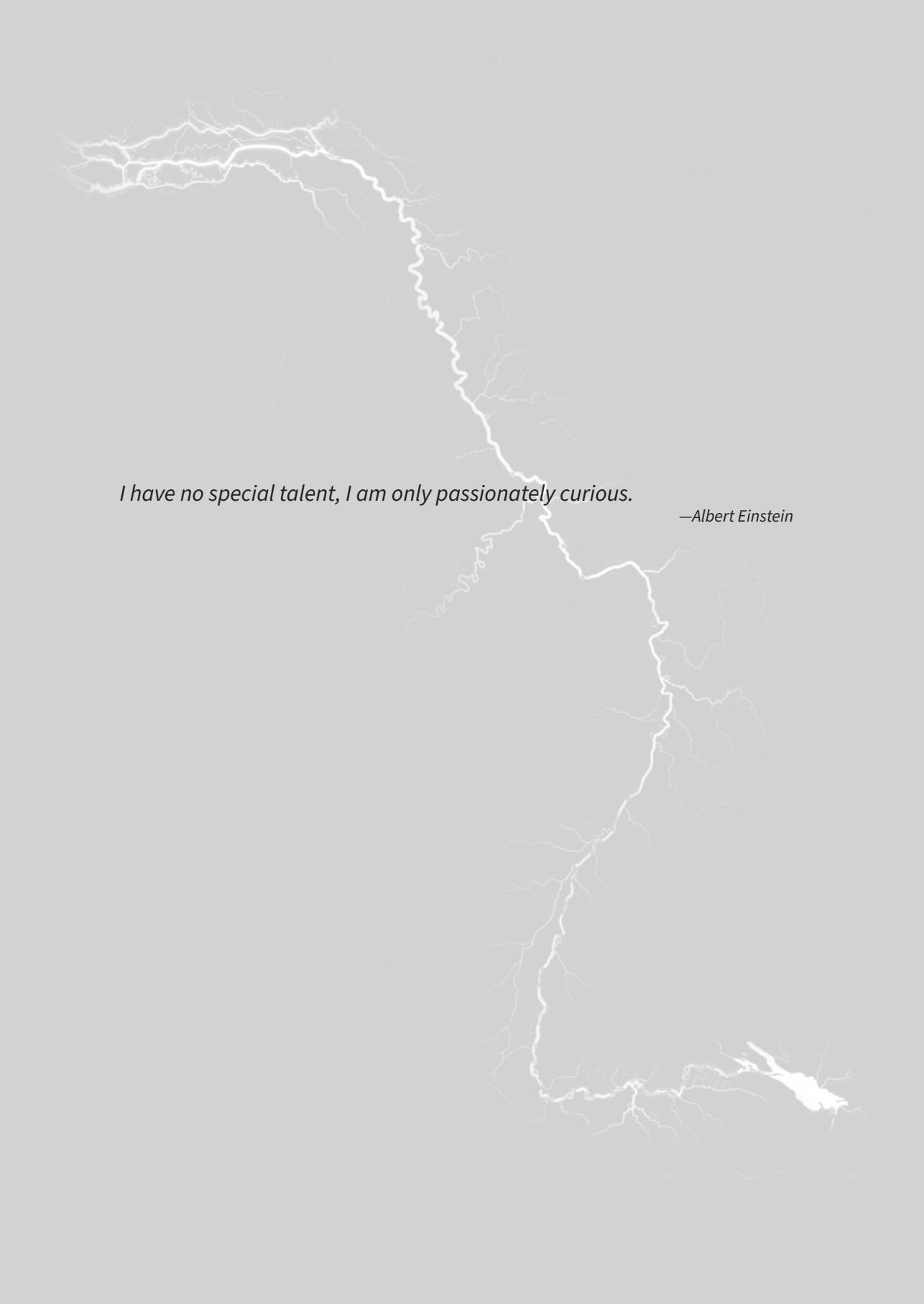

I have no special talent, I am only passionately curious.

—Albert Einstein

Chapter 3

Convergence of Primary Sensory Cortex and Cerebellar Nuclei Pathways in the Whisker System

Carmen B. Schäfer
Freek E. Hoebeek

ABSTRACT

To safely maneuver through the environment the brain needs to compare active sensory information with ongoing motor programs. This process occurs at various levels in the brain: at the lower level, i.e. in the spinal cord, reflexes are generated for the most primitive motor responses; at the intermediate level, i.e., in the brainstem, various nuclei co-process sensory- and motor-related inputs; and, at the higher level cerebellum and thalamo-cortical networks individually compute suitable commands for fine-tuned motor output. For sensorimotor processes the integrative capacities of the cerebral cortex and the cerebellum have been the topic of detailed analysis. Here, we use higher order sensorimotor integration in the whisker system as a model to evaluate the convergence pattern of primary sensory cortex projections and the cerebellar output nuclei throughout several brain nuclei. This prospective review focuses not only on the thalamus, but also incorporates extra-thalamic structures that could function as comparators of cerebellar output and sensory cortex output. Based on the literature on anatomical and physiological studies in the rodent brain and our qualitative data on the convergence of cerebellar sensory cortical projections we identify the superior colliculus as well as the zona incerta and the anterior pretectal nucleus as suitable candidates for cerebellocortical convergence. Including these putative comparators we discuss the potential routes for sensorimotor information flow between the cerebellum and cerebral sensory cortex with a focus on the modulation of thalamic activity by extra-thalamic structures.

KEYWORDS

Sensorimotor integration – cerebellar nuclei – barrel cortex – thalamus – extra-thalamic inhibition – circuit systems

LIST OF ABBREVIATIONS:

APT: anterior pretectal nucleus
BPN: basal pontine nucleus
CN: cerebellar nuclei
IntP: posterior interposed nucleus
IntA: anterior interposed nucleus
LatCN: lateral cerebellar nuclei
vM1: vibrissal primary motor cortex
NRTP: nucleus reticularis tegmentum pontis
POm: posteromedial thalamus
RN: red nucleus
vS1: vibrissal primary sensory cortex
SC: superior colliculus
SpV: spinal trigeminal nucleus
SpVi: spinal trigeminal nucleus pars interpolaris
VL: ventrolateral thalamus
VM: ventromedial thalamus
VPM: ventral posteromedial thalamus
dZI: dorsal zona incerta
vZI: ventral zona incerta

INTRODUCTION

One of the core tasks of the mammalian brain is to integrate sensory information with the current status of the body and the upcoming motor plans. Proper execution of this task is essential for optimizing motor commands and performance. Primary sensory information is relayed by the ascending spinal tracts to various integration centers in the brain, like the cerebellum and thalamus, which are also part of the motor domain (Alloway, 2008; Bosman *et al.*, 2011). Typically, impaired functioning of these integrative centers leads to impairment of both motor and sensory processing. Indeed, pathology in human cerebellum, thalamus or their projection areas have been linked to impaired sensorimotor integration (reviewed by Patel et al., 2014; Hwang et al., 2017).

The sensorimotor system of the brain is organized in a hierarchical manner in that lower order brain structures are situated at the in- and output stage of the motor system and mediate the impact of intermediate and higher level brain centers. For instance, neurons in the spinal cord not only enable sensory-evoked motor reflexes, but their activity also underlies cortically-controlled voluntary movements (Pearson & Gordon, 2013). At the intermediate level brainstem structures like the superior colliculus (SC) or the red nucleus (RN) provide a gateway for ascending sensory information and descending motor programs (Waldron & Gwyn, 1969; Killackey & Erzurumlu, 1981; Liang *et al.*, 2012). At the higher level, cerebral cortices like the sensory and motor cortices as well as thalamus and cerebellum participate in higher order information processing (De Zeeuw *et al.*, 2011; Huang *et al.*, 2013; Proville *et al.*, 2014; Chabrol *et al.*, 2015; Ishikawa *et al.*, 2015; Sreenivasan *et al.*, 2015; Suter & Shepherd, 2015; Mease *et al.*, 2016*a*, 2016*b*). The strategic positions and connections of the involved brain regions ensure a cross-level integration of sensorimotor integration that allows the refinement of complex tasks in challenging environmental conditions without loosing the efficacy of the most basic reflexes.

One of the essential principles in the control of movement is the guidance of motor programs by sensory inputs, which monitor the current state of the environment (Ramnani, 2006; Brooks *et al.*, 2015; Hooks, 2016). One of the best studied animal models for sensorimotor integration is the rodent whisker system. Decades of research on the vibrissal system identified several anatomical connections that support the conversion of sensory input to a well-planned motor output (reviewed by many papers, like Alloway, 2008; Bosman et al., 2011; Hooks, 2016b). In the whisker system, the main input of primary tactile information is relayed via the trigeminal nerve to the principal trigeminal nucleus (PrV) and onwards along the spinal trigeminal tract to the spinal trigeminal nucleus (SpV). Projections from the SpV innervate structures at all levels

of the sensorimotor systems, such as the inferior olive (Molinari *et al.*, 1996; Yatim *et al.*, 1996), pontine nuclei (Swenson *et al.*, 1984), superior colliculus (SC, Killackey and Erzurumlu, 1981), zona incerta (ZI, Simpson et al., 2008)) and anterior pretectal nucleus (APT, Yoshida et al., 1992), as well as thalamic nuclei (Chazeron et al., 2004; Guy et al., 2005; Chiaia et al., 1991a, 1991b; Williams et al., 1994; Veinante et al., 2000b) that relay these tactile inputs to the sensory barrel field cortex (vS1). Already in these subcortical nuclei sensory information will be integrated with representations of past, present and planned motor behavior. A simplified overview for the anatomical circuit can be found in Figure 1.

Higher order sensorimotor integration is a process mediated by local and long-range interconnections within cerebrum and cerebellum but also by communication between these two independently functioning systems (Popa *et al.*, 2013; Proville *et al.*, 2014). Studying the long-range connections between cerebral cortices of the whisker system revealed that, for instance vS1 has pronounced impact on the activity of primary vibrissal motor cortex (vM1) (Matyas *et al.*, 2010; Sreenivasan *et al.*, 2016) and vice versa (Petreanu *et al.*, 2009). In the cerebellum the integration of motor and sensory systems is also commonly found, both at the input (Huang *et al.*, 2013; Ishikawa *et al.*, 2015) and output stages (De Zeeuw *et al.*, 2011). The output of the cerebellum is relayed via the motor thalamus to vM1, where it additionally converges with inputs from sensory thalamus (Hooks *et al.*, 2013) and signals from vS1. Reciprocally, the cerebrum connects to the cerebellar cortex via a relay in the pontine nuclei, in which both cortical motor and sensory pathways remain strictly separated (Leergaard *et al.*, 2000, 2004).

The focus of our prospective review is the anatomical identification of brain structures that can compare cerebellar and cerebral sensory output. Our anatomical data, originating from a dual labelling approach of vS1 and lateral cerebellar nuclei (CN)/Interposed nuclei (Figure 2), show synaptic connections between the CN and various structures in the mid- and hindbrain that also receive synaptic input from vS1 (Figure 3). We discuss our findings in mouse brain by reviewing the available anatomical literature gathered in rodent brain, i.e., mostly rat. Based upon the outcome we propose a systems model that describes the feed-forward and feedback loops by which the output of CN and vS1 are integrated. Here, we want to outline potential anatomical hotspots for the convergence of both pathways with a focus on extra-thalamic structures relevant for cerebellocortical integration that could modulate sensorimotor integration within higher order thalamic nuclei.

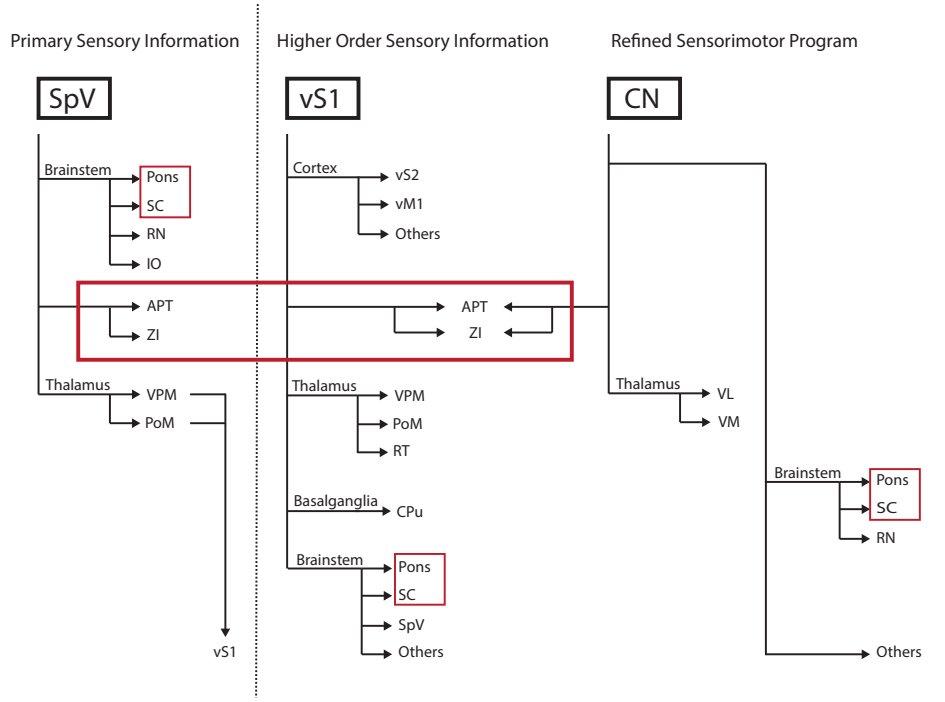

Figure 1. Simplified overview on the anatomical connectivity of primary sensory afferents, sensory cerebral output and cerebellar output. (Left) Primary sensory information reaches the thalamic, pre-thalamic and other brainstem areas via the ascending trigeminal fibers. (Middle) The output of primary sensory cortical (vS1) neurons descends to basal ganglia, thalamus, pre-thalamus and brainstem regions. (Right) Information on refined sensorimotor programs from the cerebellar nuclei (CN) traverses to thalamic, pre-thalamic and brainstem nuclei. The anterior pretectal nucleus (APT) and zona incerta (ZI) (in red) represent potential brain structures for the convergence of cerebellar output with sensory feedback systems. Abbreviations: spinal trigeminal nucleus (SpV), barrel cortex (vS1), cerebellar nuclei (CN), Pons: pontine nuclei consisting of basal pontine nuclei (BPN) and reticulotegmental nucleus of the pons (NRTP), inferior olive (IO), red nucleus (RN), superior colliculus (SC), anterior pretectal nucleus (APT), zona incerta (ZI), ventral posteromedial thalamic nucleus (VPM), posteromedial thalamic nucleus (POm), whisker responsive part of the secondary sensory cortex (vS2), whisker responsive part of primary motor cortex (vM1), reticular thalamic nucleus (RT), caudate putamen (CPu), ventrolateral thalamic nucleus (VL), ventromedial thalamic nucleus (VM).

SYNOPSIS ON SENSORIMOTOR INTEGRATION IN THE CEREBRUM AND CEREBELLUM

Cerebrum

Sensory information is integrated with past, present and planned motor performance at various levels of the central nervous system. Basic reflexes are controlled by the spinal cord and brain stem levels but cerebrum and cerebellum are dedicated to higher order sensorimotor integration. The cerebrum receives primary tactile information from vibrissal touch events via the trigeminal nuclei. Here, PrV forms projections to the ventral posteromedial nucleus (VPM) and posteromedial nucleus (POm) and also spinal

trigeminal nucleus pars interpolaris (SpVi) innervates both VPM and POm of the dorsal thalamic complex, albeit in unequal proportions (Chiaia *et al.*, 1991*a*, 1991*b*; Williams *et al.*, 1994; Veinante & Deschênes, 1999; Pierret *et al.*, 2000; Veinante *et al.*, 2000*a*). Generally, VPM forms the first-order 'relay' station of sensory information to the cortex, while the POm functions as a higher order thalamic nucleus (Reichova & Sherman, 2004). The primary targets of these thalamic nuclei are vM1 and vS1. Both VPM and POm project to vS1, where VPM innervates cortical layer 4 within the barrels while POm rather sends fibers to layer 5 and layer 1 of the septa localized between the barrels (Wimmer *et al.*, 2010). POm also projects to upper layers in vM1, which sets this higherorder thalamic nucleus at central stage in both the sensory as well as the motor system (Wimmer *et al.*, 2010; Hooks *et al.*, 2013). Interestingly, single axon reconstructions revealed that POm neurons innervate both vS1 and vM1 (Deschênes *et al.*, 1998; Ohno *et al.*, 2012). vS1 is of essential importance for the perception and processing of whisker inputs, as one of its core functions is to encode the location of whiskers over time (Crochet & Petersen, 2006; de Kock & Sakmann, 2009). Across cortical layers average spontaneous spiking rates of neurons in vS1 remain within 1-2 Hz, but upon active whisker movement layer 5A neurons have been reported to spike at 10 Hz (de Kock & Sakmann, 2009). From here, vS1 distributes this information via feedback projections to both VPM and POm in the thalamus, but also to extra-thalamic target areas such as vM1, ventral orbital cortex, caudate putamen, secondary sensory as well as perirhinal cortex, APT, ZI, SC, basal pontine nuclei (BPN) and SpV (see also Figure 1) (Aronoff *et al.*, 2010*a*; Smith *et al.*, 2015).

Cerebellum

The cerebellum supports the proper execution of motor plans by, for instance, encoding accurate timing of movements related to sensory inputs (Marr, 1969; Albus, 1971). Its highly organized cortical circuitry forms the core of an ideal sensorimotor learning machine necessary to generate these fine-tuned movements (Raymond *et al.*, 1996; De Zeeuw *et al.*, 2011). The cerebellar cortex receives primary tactile information via climbing fibers originating in the inferior olive and mossy fibers from BPN and SpV (Swenson *et al.*, 1984; Yatim *et al.*, 1996). In addition, sensory and motor-related information from cortical layers are relayed via BPN mossy fibers that synapse on granule cell dendrites in the cerebellar cortex (Huang *et al.*, 2013; Proville *et al.*, 2014). These inputs encode excitatory signals to the Purkinje cells and may coincide with climbing fiber-mediated excitation originating from the inferior olive. The resulting Purkinje cell spiking patterns are important determinants of the activity of neurons in the medial, interposed and lateral CN (Gauck & Jaeger, 2000; Alviña *et al.*, 2008; Hoebeek *et al.*, 2010; Bengtsson *et al.*, 2011; Person & Raman, 2011; Dykstra *et al.*, 2016). Apart from excitatory (mossy fiber and climbing fiber collaterals) and inhibitory afferents (Purkinje cell inhibition) it is likely that local GABAergic, glycinergic and glutamatergic axons and their collaterals

(Uusisaari *et al.*, 2007; Uusisaari & Knöpfel, 2011) also determine CN spiking patterns (De Zeeuw *et al.*, 2011). The resulting cerebellar output is dictated by the notably high intrinsic spiking activity (~ 50 Hz; (Raman & Bean, 1999)), which is in contrast to low spontaneous spike rates in vS1 neurons (e.g., de Kock & Sakmann 2009). Therefore, the whisker-evoked spiking patterns of cerebellar output neurons are different from cerebral cortex, in that both Purkinje cells and CN neurons reveal relatively high-firing rates and tend to encode the whisker movements with bouts of increased and/or decreased spiking (Bosman *et al.*, 2010; Chen *et al.*, 2016). CN spiking patterns will be integrated into ongoing sensorimotor processing by driving or modulating neuronal activity in downstream targets such as the thalamus, BPN, SC, APT and ZI (e.g. Bentivoglio and Kuypers, 1982; Teune et al., 2000).

POTENTIAL SITES OF CEREBELLO-CEREBRAL CONVERGENCE

Upon sensory stimulation both the cerebellum and the cerebrum receive tactile information from the SpV. Although it is widely acknowledged that these two information streams converge again, it is currently unknown how the brain manages to integrate refined cerebellar sensorimotor signals with higher order cortical sensory feedback. Previous anatomical and physiological studies identify the thalamic POm as a point of potential convergence (Teune *et al.*, 2000; Sosnik *et al.*, 2001; Groh *et al.*, 2008, 2013; Bosman *et al.*, 2011; Mease *et al.*, 2014, 2016*b*). However, also nuclei outside of the dorsal thalamic complex receive projections from both vS1 and CN. Some of these extra-thalamic sites provide monosynaptic input to POm and thereby, in principle, have the potential to modulate thalamic activity and thus sensorimotor integration. Below we will first discuss the evidence for potential overlap between vS1 and CN projections in dorsal thalamic nuclei followed by the extra-thalamic regions of interest.

Intra-thalamic convergence of vS1 and CN projections?

Cortico-thalamic projections from the barrel field of vS1 originate from layers 5/6 and innervate thalamo-cortical neurons in POm and VPM, which also receive primary tactile inputs (Deschênes *et al.*, 1998; Veinante *et al.*, 2000*b*; Groh *et al.*, 2013). Thereby the output of the primary sensory cortex provides a cortico-thalamo-cortical feedback loop that actively modulates ongoing higher order cortical processing. It is generally known that layer 6 of vS1 projects to both POm and VPM, whereas layer 5B exclusively projects to POm (Hoogland *et al.*, 1991; Bourassa *et al.*, 1995; Veinante *et al.*, 2000*b*). Due to this thalamic organization the VPM is classified as a firstorder thalamic nucleus responsible for the relay of primary sensory information, whereas the POm functions as a higher order thalamic nucleus essential for sensorimotor integration (Reichova & Sherman, 2004).

These two core thalamic nuclei relay and process sensory information necessary to encode object localization crucial for spatial but also perceptual processing of tactile cues (Ahissar *et al.*, 2000; Sosnik *et al.*, 2001). In addition to the excitatory thalamo-cortical and cortico-thalamic connections, both the ascending and descending projections are known to synapse on inhibitory neurons in the reticular thalamic nucleus. The descending projections from vS1 thereby provide inhibition on neurons localized in both VPM and POm (Bourassa *et al.*, 1995). The functional significance of these inhibitory loops via the reticular thalamic nucleus fall outside the scope of the current manuscript, but have recently been reviewed comprehensively (Halassa & Acsády, 2016).

Although controlling the timing of movements and reflexes is considered one of the core functions of cerebellar output (De Zeeuw *et al.*, 2011), it remains unclear how the cortico-thalamo-cortical integration of vibrissal sensation is modulated by CN activity patterns. CN neurons project to the thalamus but they mainly target nuclei involved in motor processing such as ventrolateral (VL) and ventromedial (VM) nucleus, thereby suggesting a cerebellar contribution to thalamo-cortical networks involved in sensorimotor integration (Asanuma *et al.*, 1983; Angaut *et al.*, 1985; Sawyer *et al.*, 1994; Aumann & Horne, 1999; Aumann *et al.*, 2000; Teune *et al.*, 2000; Aumann, 2002; Popa *et al.*, 2013; Proville *et al.*, 2014). Interestingly, single neuron tracing studies provide evidence of VL

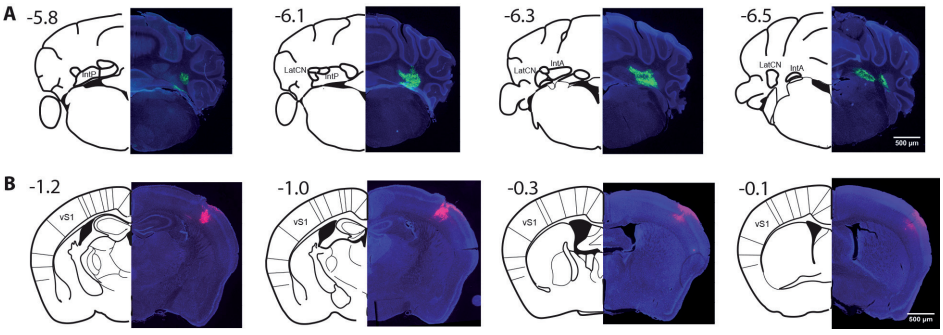

Figure 2. Labeling of cortical and cerebellar pathways. (A) For investigating the convergence pattern of projections from sensory barrel cortex (vS1) and cerebellar nuclei (CN), anterograde tracer was injected to both target brain areas. Adeno-associated viruses (AAV) can be used to transfect neurons and to express tracing molecules located in the cell membrane or within synaptic terminals. We used AAV to express a fluorescently tagged version of Synaptophysin under a CAG promotor, which is a synaptic vesicle glycomolecule ubiquitously expressed in all neurons of the brain that participate in synaptic transmission. For labeling cerebellar projection pathways, we used stereotaxic injection to deliver a volume of 200 nL of Synaptophysin-GFP expressing AAV to both hemispheres. We injected the cerebellum 2 mm lateral from the midline and 2 mm deep from the dura (rostro-caudal coordinates relative to bregma indicated in figure panels). With this injection strategy we transfected neurons in lateral CN (LatCN), posterior and anterior interposed nucleus (IntP, IntA), while projections from fastigial nucleus remain unlabeled. Numbers indicate the distance from bregma on the anterior-posterior axis outlined in the coronal sections of the Paxinos atlas (Paxinos & Franklin, 2001). (B) vS1 was labeled by using AAV expressing Synaptophysin-mOrange in the full anterior-posterior elongation. The virus was bilaterally delivered to each of the following three x-y coordinates from bregma and midline (in mm): (1) +/- 3, 0; (2) +/-3, -0.5; (3) +/-3, -1 at a depth of -0.9 mm from the dura. All 6 animals were sacrificed 3-4 weeks after viral injections.

and VM thalamo-cortical relay neurons that not only innervate cortical motor areas but also vS1 (Kuramoto *et al.*, 2009, 2013). The functional significance of these projections deserves in depth investigations, since such connections could underlie a cerebellar contribution to vS1 activity.

In addition, a projection from lateral CN to the most anterior portion of POm was reported earlier in rat (Teune *et al.*, 2000). To investigate the convergence pattern of sensory and cerebellar pathways, we assessed whether CN and vS1 form synaptic terminals in the same target regions (see Figure 2 for details). After co-injection of lateral CN/ Interposed nuclei and vS1 with virally-encoded synaptic markers in 6 mice we found that potential convergence of CN and vS1 axon terminals was limited in POm just as in any other nucleus of the dorsal thalamic complex (Figure 3A), but relatively prominent in several extra-thalamic nuclei (see below). However, our data do show that CN and vS1 both project to the most anterior portion of the POm (Figure 3B). Although we are aware that our experiments using anterograde viral tracing methods do not allow any conclusion regarding the complete absence of cerebello-cerebral convergence of CN and vS1 afferents, we would like to highlight that in contrast to dorsal thalamic nuclei we did consistently find considerable overlap of CN and vS1 projections in other brain areas (Figure 3). Therefore, we assume that cerebellar modulation of sensory information processing is at least partially mediated by extra-thalamic structures.

Cerebello-cortical integration outside of the dorsal thalamic complex

Even though sensory and motor information has to pass through the thalamus to reach cerebral higher order cortices, several sites of putative cerebello-cerebral convergence are found throughout the mid- and hindbrain that may act at the intermediate level of sensorimotor integration. One of these candidate sites for cerebello-cerebral convergence is the pons in the brainstem, which encompasses BPN and the reticulotegmental nucleus of the pons (NRTP). BPN receive dense projections from both sensory and motor cortices (Leergaard *et al.*, 2000, 2004; Hoffer *et al.*, 2005; Alloway, 2008; Aronoff *et al.*, 2010*a*), which remain strictly separated at this level (Leergaard *et al.*, 2004; Proville *et al.*, 2014), as well as inputs from CN (Angaut & Cicirata, 1988; Teune *et al.*, 2000). BPN efferents innervate the cerebellar cortex by means of numerous mossy fiber projections (Suzuki *et al.*, 2012). Our preliminary data indicate that the axonal termination fields of vS1 and CN axons in BPN do not overlap (data not shown). Whereas the NRTP is densely innervated by cerebellar fibers, we can only find a convergence with projections from vS1 in the ventral portion of the NRTP and in the dorsal peduncular area, which is localized directly in between medial lemniscus and longitudinal fascicle of the pons (data not shown). Given that, to our knowledge, these nuclei do not provide projections to

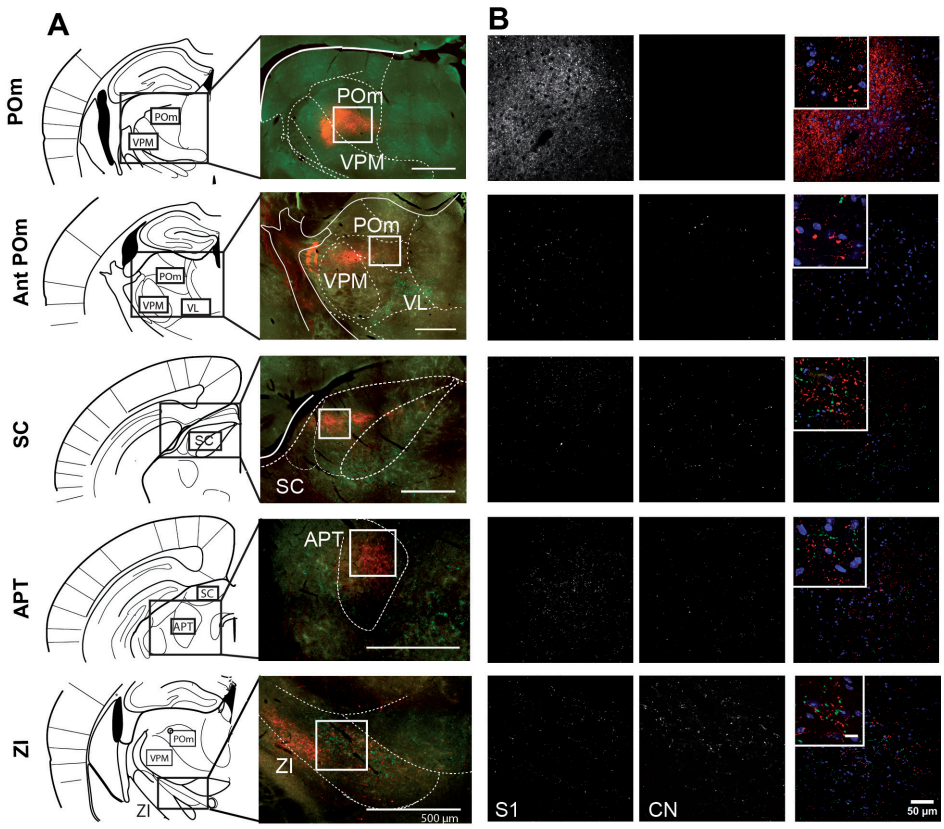

Figure 3. Thalamic and Extra-thalamic convergence of CN and S1 axon terminals. **A** The anatomical borders of posterior medial nucleus (POm), superior colliculus (SC), anterior pretectal nucleus (APT) and zona incerta (ZI), which form brain structures potentially receiving inputs from cerebellar nuclei (CN) and vibrissal primary sensory cortex (vS1), are outlined in coronal sections of the Paxinos brain atlas (Paxinos & Franklin, 2001). Synaptic terminals originating in vS1 are labeled by expression of Synaptophysin-mOrange and projections from CN were labeled by using Synaptophysin-GFP (see legend Figure 2 for more details). In the wide-field fluorescent image prominent projections from vS1 are shown in red and projections from CN are shown in green. Anatomical locations of the convergent fields can be determined from the overlay with the borders of the atlas. The scale bar is 500µm. **B** Higher magnification wide-field images of outlined boxes in A. S1 synapses are labeled in red and cerebellar synapses are labeled in green, while background fluorescence appears in yellow. The scale bar is 50µm.

thalamo-cortical networks, we argue that their contribution to higher order sensorimotor processing is limited.

The red nucleus is another brainstem nucleus involved in the control of movement and motor coordination via the rubrospinal tract. Both its parvo- and magnocellular parts receive a dense innervation from lateral CN and/or interposed nucleus (Teune *et al.*, 2000). We could not detect obvious innervations from vS1 (data not shown). Although several papers suggest a direct connection between vS1 and CN, we have not been able to find direct experimental evidence in the rodent literature (Aronoff *et al.*, 2010*b*; Bos-

man *et al.*, 2010) – in contrast to the abundant vM1-RN projections (see for instance, (Gwyn & Flumerfelt, 1974; Alloway *et al.*, 2010)). Nevertheless, future studies using adequate retrograde techniques (see, for instance, Tervo et al. 2016) should be performed to elucidate whether also at the level of the red nucleus cerebello-cerebral coherence enables sensorimotor integration in the whisker system.

The SC forms another midbrain site for convergence of sensory and cerebellar efferents. Its main task is to direct behavioral responses, such as saccadic eye movements or head movements, towards specific points of interest within the environment. The superficial layer of the SC receives input mainly from retina and visual cortical areas, whereas intermediate and deeper layers process sensorimotor and motor information, respectively. In addition, primary sensory efferents from SpV innervate SC (Killackey & Erzurumlu, 1981) and overlap with feedback projections from vS1 (Cohen *et al.*, 2008). From the cerebellar side, a topographically organized axonal projection has been shown to drive action potential firing in the lateral portions of the intermediate and deeper layers of the SC (Westby *et al.*, 1993; Teune *et al.*, 2000). Our data show that vS1 and CN axons co-terminate in the lateral portions of the intermediate and deeper SC layers (Figure 3C). Although the functional relevance of synaptic innervation of SC dendritic fields by CN and vS1 axons remains to be further investigated, the available data already seem to indicate a potential cerebellar role sensorimotor processing in the SC.

Alike this somatosensory region of the SC also the nearby pretectal complex contains a 'non-visual' sub-region: the APT, which locates between SC and the thalamus, is devoid of retinal axon terminals and has therefore been predominantly associated with sensorimotor functions as well as nociception (Scalia & Arango, 1979; Rees & Roberts, 1993; Murray *et al.*, 2010). The APT is typically divided by connectivity into a rostral pole and a caudal pole, the latter of which consists of the dorsal *pars compacta* and the ventral *pars reticulata*. Whereas the *pars compacta* receives input mainly from non-retinal visual systems (Cadusseau & Roger, 1991), the rostral pole and *pars reticulata* receive spinal input from the dorsal column nuclei (Yezierski, 1982), the trigeminal nuclei (Yoshida *et al.*, 1992) and vS1 (Foster *et al.*, 1989; Aronoff *et al.*, 2010*a*). Cerebellar axons have been shown to project densely throughout various portions of the APT (Sugimoto *et al.*, 1982; Asanuma *et al.*, 1983; Berkley, 1983; Teune *et al.*, 2000). Our current results show that both vS1 and CN axons synapse densely in the ventral portion of the APT (Figure 3) and thereby identify APT as another potential site of cerebello-cerebral convergence outside of the dorsal thalamic complex.

The ZI is located ventrally to the thalamus and elongates along the anterior-posterior axis. It has long been called the area of uncertainty, as it connects to various brain areas

such as the cerebral cortex, diencephalon, basal ganglia, brainstem and the spinal cord, indicating that the ZI is involved in many different brain functions. As reviewed by (Mitrofanis, 2005), the ZI can be divided into 4 main regions (rostral, caudal, dorsal and ventral) by connectivity and function. Whisker-sensitive trigeminal neurons project mostly to vZI (Roger & Cadusseau, 1985; Nicolelis *et al.*, 1992; Veinante *et al.*, 2000*a*). For sensorimotor integration the dorsal and ventral ZI (dZI; vZI) have been studied mostly, as both sensory and motor cortices project densely to these incertal regions (Roger & Cadusseau, 1985; Mitrofanis & Mikuletic, 1999; Veinante *et al.*, 2000*b*; Bartho *et al.*, 2007; Urbain & Deschênes, 2007; Aronoff *et al.*, 2010*a*). Also CN axons synapse densely in various ZI regions (Roger & Cadusseau, 1985; Aumann *et al.*, 1994; Aumann & Horne, 1996*a*, 1996*b*; Teune *et al.*, 2000). In line with these axonal cerebellar and cerebral tracing studies our results indicate that CN and vS1 axon terminals converge in both dZI and vZI (Figure 3). Patterns of overlap within both ZI areas might be underestimated as they depend on the precise location of injection within CN and vS1 areas.

We would like to emphasize that ZI, APT and SC not only innervate POm and interconnected cortices (Nicolelis *et al.*, 1995), but also project to other subcortical motor regions, like various parts of the basal ganglia ((Heise & Mitrofanis, 2006), red nucleus (Terenzi *et al.*, 1995) and ventral spinal cord (Waldron and Gwyn, 1969). Thus, such connections could in principle distribute the results from extra-thalamic cerebello-cerebral integration along various levels of the sensorimotor system. To retain the focus of the current review on the extra-thalamic sites for cerebello-cerebral integration we will discuss the connections of APT and ZI with a particular focus on their efferent projections to the higher order thalamic nuclei of the whisker system, i.e., POm. In addition we will address the emerging role of SC-output in modulating APT and ZI activity and discuss the potential impact of CN output on each of these regions. We will conclude with a prospective circuit diagram that represents our vision of how extra-thalamic cerebello-cerebral convergence contributes to sensorimotor integration within the whisker system.

Modulation of POm activity by extra-thalamic sources that receive CN and vS1 input

Interestingly, both ZI and APT have been suggested as extra-thalamic inhibitory nuclei that modulate thalamic spiking in an inhibitory pathway that functions in parallel to inhibition from reticular thalamic nucleus (Halassa & Acsády, 2016). Of note is that ZI and APT have precise thalamic projection territories while none of them receives thalamic feedback projections. In the sensory system both ZI and APT densely innervate POm but not the primary sensory relay nuclei such as VPM. This connectivity underlines the contribution of ZI and APT to higher order sensory integration (Barthó *et al.*, 2002; Bokor *et al.*, 2005). Anatomical and electrophysiological studies show that APT and ZI

indeed exert a strong and temporally precise inhibitory control on POm activity (Barthó *et al.*, 2002; Bokor *et al.*, 2005; Bartho *et al.*, 2007; Wanaverbecq *et al.*, 2008). This inhibition is mediated by axonal boutons that each have multiple release sites and are fully covered in a glial sheet, which together ensure the reliability of synaptic transmission. Due to their location on proximal dendrites close to the soma they can provide powerful control on somatic membrane fluctuations and thus control thalamic spiking (Barthó *et al.*, 2002; Bokor *et al.*, 2005).

Both ZI and APT are strongly interconnected with several hubs in the sensorimotor system. First of all, SpV innervates POm (Chiaia *et al.*, 1991*a*, 1991*b*), ZI (Simpson *et al.*, 2008) as well as APT (Yoshida *et al.*, 1992), thereby providing an ascending efference copy of primary tactile inputs to all three nuclei (Veinante *et al.*, 2000*a*). Second, output neurons from L5 of vS1 also innervate both ZI and APT, in addition to their descending projections to POm (Veinante *et al.*, 2000*b*; Trageser & Keller, 2004; Aronoff *et al.*, 2010*a*). Third, also vM1 sends projections to both ZI and APT (Miyashita *et al.*, 1994) and both ZI and APT are reciprocally connected (May *et al.*, 1997; Giber *et al.*, 2008). The fact that vM1 and vS1 are reciprocally interconnected (Matyas et al., 2010; Petereanu et al., 2010) and recipient of POm input (Deschenes et al., 1998; Ohno et al., 2012) underlines the complexity of the neuronal network at the higher level of sensorimotor integration.

The anatomical connectivity of the vS1–ZI–POm loop suggests that ZI can provide inhibitory control of POm spike timing and thus dynamically balance thalamic output to the cortex during behavioral tasks. It has been shown that ZI neurons are capable of integrating widespread cortical activity patterns, suggestive for a role in synchronizing thalamo-cortical signals by a feed-forward inhibitory pathway (Trageser & Keller, 2004; Bartho *et al.*, 2007). In line with this, ZI's high intrinsic spiking activity of about 30 Hz has been proposed to block sensory transmission in POm during rest (Lavalle *et al.*, 2005). During active whisking the same neuronal network could provide a cortical top-down disinhibitory gating mechanism for the relay of sensory information (see below) (Trageser & Keller, 2004; Urbain & Deschênes, 2007; Halassa & Acsády, 2016). A similar role for APT neurons is suggested by studies in which APT lesions resulted in increased spontaneous spiking rates in POm (Murray *et al.*, 2010). Therefore, the strong and temporally precise inhibition from both APT and ZI might function as a state-dependent gating mechanism for the thalamo-cortical transfer of sensory information.

Interestingly, also the whisker responsive parts of intermediate and deeper layers of the SC form excitatory synapses on vZI neurons (Roger & Cadusseau, 1985; Comoli *et al.*, 2003; Watson *et al.*, 2015; Kita *et al.*, 2016). The potency of this SC-ZI-POm projection is exemplified by the fact that SC-mediated excitation on vZI neurons is sufficient to inhibit

spontaneous activity in POm, which suggests the ZI to gate communication between SC and POm (May *et al.*, 1997; Watson *et al.*, 2015). Taking into mind that cerebellar efferents in SC drive action potential firing (Westby *et al.*, 1993), we propose that if the target neurons in the SC project to CN-target neurons in ZI, the resulting SC output may function as a feed-forward signal which integrates cerebellar information.

TOWARDS A CIRCUIT MODEL FOR EXTRA-THALAMIC CEREBELLO-CEREBRAL INTEGRATION

The execution of movements requires advanced sensorimotor integration by comparing a predictive motor command with a sensory feedback signal. The resulting sensory prediction error is incorporated in the execution commands. For voluntary movements execution commands originate in vM1. However, successful fine-tuning of movements also requires a cerebellar contribution. Even though cerebellar output already embodies an integrated sensorimotor signal, a comparison with current primary sensory inputs and higher order sensory signals from the cortex could facilitate the integration of cerebellar output with ongoing motor programs. The comparison of cerebellar output with sensory feedback resembles a checkpoint that follows sensorimotor processing within the cerebellar cortex. In this view, cerebellar output embodies a refined feed-forward model of a movement that is compared to the primary sensory information and to the result of higher order sensory processing. Although the details of how such comparators will function remain to be elucidated, we propose that this triangular signal integration is at least partially mediated by pre-thalamic centers of the sensorimotor system.

Sensorimotor systems can be grouped into feedback and feed-forward circuits (Figure 4): sensory feedback is used to continuously control ongoing responses by calculating an error signal between the execution of a motor plan and the current state of the environment; sensory feed-forward circuits provide predictive information about the state of the body after completion of the planned movement. Generally, in a feedback loop a comparator calculates the difference between a primary sensory signal and a reference signal. The comparator‘s output adjusts the motor plan until the calculated error signal is leveled out, i.e., the sensory feedback matches the reference and thus the desired movement will be generated (Ramnani, 2006). In contrast, a feed-forward circuit calculates the desired output signal that serves as a reference for the feedback loop. Incoming sensory signals about the current state of the body or potential disturbances in the environment are integrated to the current motor plan by a feed-forward comparator, which aims in adjusting motor plans in advance until the final execution goal is reached.

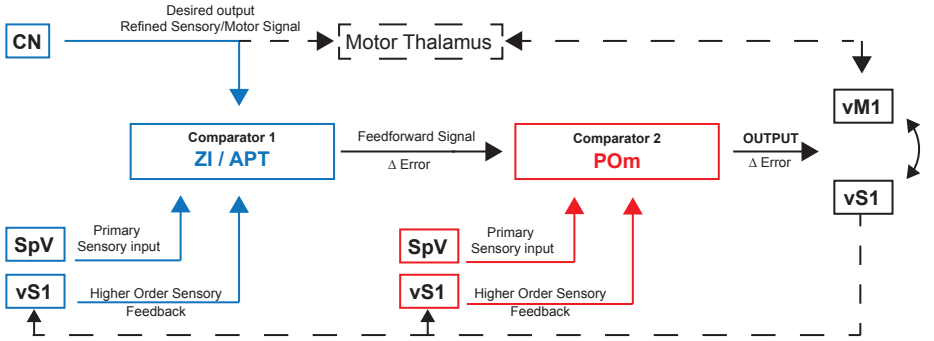

Figure 4. A circuit model for extra-thalamic cerebello-cerebral integration. In this circuit model we suggest cerebellar output to encode a refined sensorimotor feed-forward signal that, in the form of cerebellar nuclei (CN) axons, gets integrated with primary sensory input (predominantly originating from trigeminal nuclei; SpV) and the higher order feedback from primary sensory cortex (vS1). We suggest APT and ZI to function as pre-thalamic comparative structures that act as inhibitory feed-forward controllers on POm activity. The POm, in turn, is placed in the middle of the sensorimotor system receiving dense excitatory SpV and vS1 axon terminals, as well as inhibitory ZI and APT projections (see main text for references) and innervating both sensory and motor cortices. In this circuit model, the POm might also act as a central checkpoint for the comparison of ongoing fine-tuning of sensorimotor programs and the current state of the environment. Note that we indicated the CN-input to ZI/APT with a question mark, since no conclusive data has been published about the type of neurotransmitter released from CN terminals in these target nuclei, to the best of our knowledge. Other synaptic contacts are indicated with + for excitatory synapses and – for inhibitory synapses. Abbreviations: spinal trigeminal nucleus (SpV), barrel cortex (vS1), cerebellar nuclei (CN), anterior pretectal nucleus (APT), zona incerta (ZI), posterior medial thalamic nucleus (POm), whisker responsive part of primary motor cortex (vM1)

An example for successful feed-forward and feedback sensory integration was recently established for the vestibular system, which is an anatomically simple sensorimotor system essential for gait and posture control (Brooks *et al.*, 2015). In this system cerebellar output neurons serve a comparative function between feed-forward sensorimotor signals from the cerebellar cortex and sensory feedback from primary sensory sources. This signal integration was shown to actively mediate behavior during motor learning as well as passively control unexpected situations. Thereby, the vestibular system can mediate complex motor programs such as walking but can also take control in case of unexpected disturbances in the environment, such as an accident (Brooks *et al.*, 2015).

Both the literature and our preliminary findings indicate the ZI and APT could mediate cerebellar integration with sensory processing outside of the cerebellar cortex (Figure 4). In addition to their central location between inputs from CN, sensory and motor cortex the inhibitory effect of ZI and APT inputs on POm (Trageser & Keller, 2004; Bokor *et al.*, 2005; Lavalle *et al.*, 2005) could enable them to compare cerebellar output with primary tactile inputs and ongoing higher order sensory feedback. How this cortico-cerebellar integration comes about remains purely speculative, as a direct functional characterization of cerebellar synapses onto ZI and APT neurons is missing. Nevertheless, it was shown that motor cortical afferents can provide inhibitory drive onto vZI

neurons, which is mediated via interconnections with dZI neurons (Urbain & Deschênes, 2007). We speculate that ZI and/or APT due to their connectivity are suitable effectors of the cerebellar impact on whisker-related POm spiking.

The POm functions as a higher order thalamic sensorimotor integration center that is interconnected not only with S1 but also M1 (Viaene *et al.*, 2011; Hooks *et al.*, 2013; Gambino *et al.*, 2014). Tracing studies show that co-innervation of both cortices can even originate from single POm neurons (Deschênes *et al.*, 1998; Ohno *et al.*, 2012). These properties position the POm and thus indirectly also ZI and APT in a central location to gate the relay of tactile information to upper layers of both S1 and M1 (Figure 4). This theory sets the POm as a thalamic nucleus which compares the excitatory strength of primary sensory inputs from SpV and sensory feedback from L5 of S1 with inhibitory signals from pre-thalamic sensorimotor integratory centers, like ZI and APT, that also pre-process cerebellar output (Hoogland *et al.*, 1991; Bourassa *et al.*, 1995; Veinante *et al.*, 2000*a*; Lavalle *et al.*, 2005; Urbain & Deschênes, 2007; Giber *et al.*, 2015). The anatomical location of the POm in between inputs from i) primary sensory sources, ii) feedback projections from sensorimotor cortices and iii) integrating pre-thalamic sources of inhibition might enable this thalamic nuclei to function as a central checkpoint between ongoing sensorimotor integration and the current state of the environment.

ACKNOWLEDGEMENT

We thank Tom J. H. Ruigrok, Zhenyu Gao, Simona V. Gornati, Sander Lindeman, Valentina Riguccino, Sverrir V. Sigurdsson and Bas van Hoogstraten for fruitful discussions and critical comments on the manuscript and Elize D. Haasdijk for helping with immunohistochemistry. In addition we want to thank Prof. Dr. Thomas Kuner (University of Heidelberg, Germany) for providing the AAV-Synaptophysin constructs used for anatomical tracing.

FUNDING

C.B.S. and F.E.H. are generously supported by the Dutch organization for life sciences (NWO-ALW; VIDI grant #016.121.346).

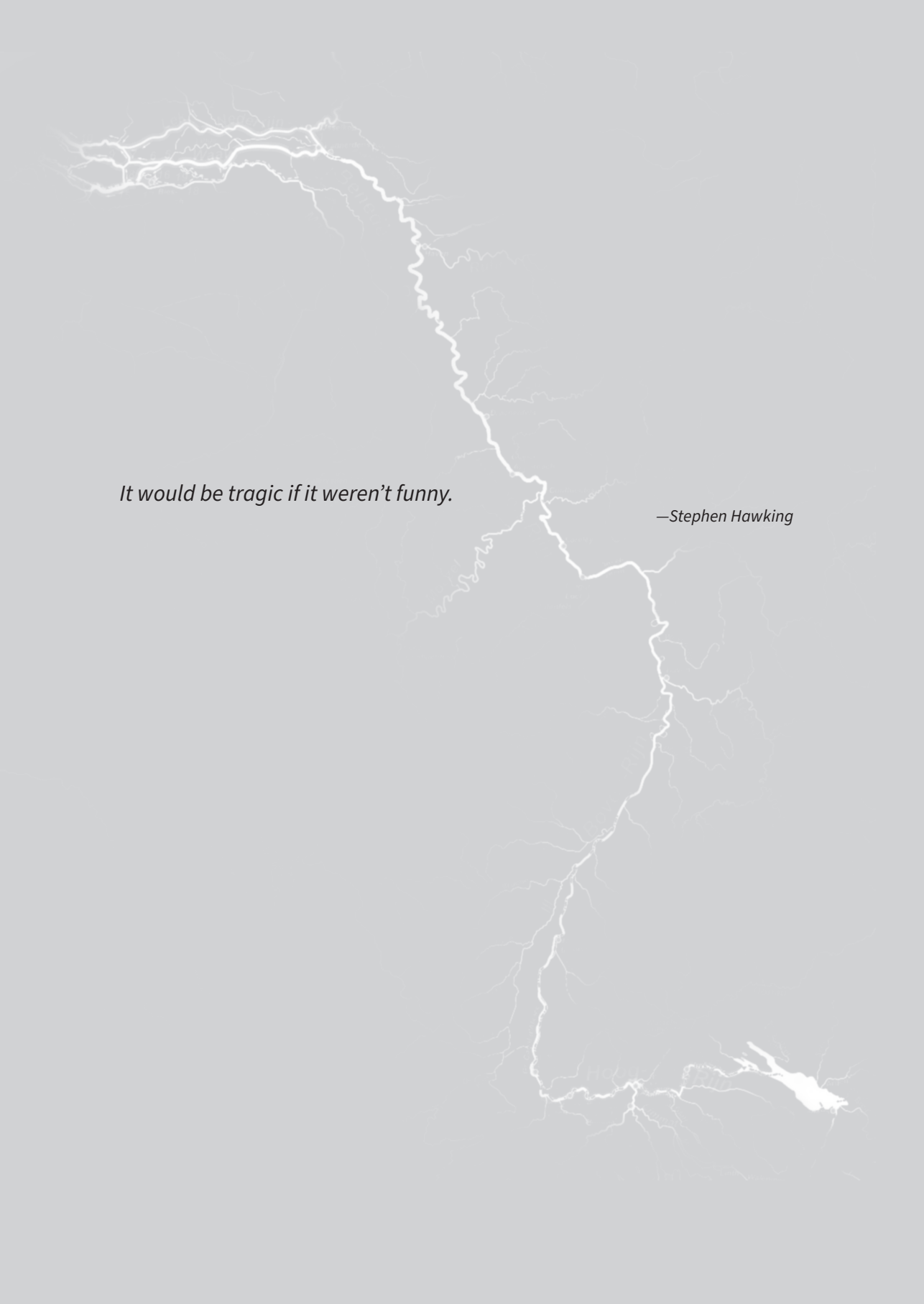

It would be tragic if it weren't funny.

—Stephen Hawking

Chapter 4

Differentiating cerebellar impact on thalamic nuclei

Simona V. Gornati*
Carmen B. Schäfer*
Oscar H.J. Eelkman Rooda
Alex Nigg
Chris I. De Zeeuw
Freek E. Hoebeek

*These authors contributed equally.

ABSTRACT

The cerebellum plays a role in coordination of movements and possibly also non-motor functions. Cerebellar nuclei (CN) axons connect to various parts of the thalamo-cortical network, but detailed information on the characteristics of cerebello-thalamic connections is lacking. Here, we assessed the cerebellar input to the ventrolateral (VL), ventromedial (VM) and centrolateral (CL) thalamus. Confocal and electron microscopy showed an increased density and size of CN axon terminals in VL compared to VM or CL. Electrophysiological recordings *in vitro* revealed that optogenetic CN stimulation resulted in enhanced charge transfer and action potential firing in VL neurons compared to VM or CL neurons, despite that the paired-pulse ratio was not significantly different. Together these findings indicate that the impact of CN input onto neurons of different thalamic nuclei varies substantially, which highlights the possibility that cerebellar output differentially controls various parts of the thalamo-cortical network.

INTRODUCTION

Cerebellar best-known functions are involved in coordinating motor activities. It contributes for example to learning new motor skills and prediction of the sensory consequences of action (Brooks et al., 2015; De Zeeuw and Ten Brinke, 2015; Manto et al., 2012). However anatomical, physiological and neuroimaging studies provide compelling evidence of the cerebellar involvement in various non-motor functions, like cognitive processes, language and emotion, which became established in both animal models and patients (Bodranghien et al., 2016; Peter et al., 2016; Stoodley et al., 2017; Tsai et al., 2012; Wang et al., 2014). For instance, it was recently shown that manipulating the cerebellar output affects sensorimotor integration by somatosensory and motor cortices and thereby could direct voluntary movements (Popa et al., 2013; Proville et al., 2014). The anatomical connections that underlie such wide impact of cerebellar activity on thalamo-cortical information processing do not only include cerebellar axons that innervate the premotor centers in the brainstem, like the red nucleus, but also a variety of nuclei within the thalamic complex, each of which has reciprocal connections with the cerebral cortex (Angaut et al., 1985; Aumann et al., 1994; Bentivoglio and Kuypers, 1982; Cohen et al., 1958; Daniel et al., 1987; Haroian et al., 1981; Herkenham, 1979; Teune et al., 2000).

The glutamatergic projection neurons located in the cerebellar nuclei (CN) connect to primary thalamic relay nuclei, like the ventrolateral (VL) nucleus, thalamic motor-associated nuclei such as the ventromedian (VM) nucleus and additionally to intralaminar nuclei such as centromedian, parafascicular and centrolateral (CL) nuclei (Aumann and Horne, 1996b; Teune et al., 2000). Historically the thalamic relay neurons have been divided in two fundamentally different sets: parvalbumin-positive ‘core’ neurons, which form topographically organized projections to middle layers of patches of cerebral cortex; and calbindin-positive ‘matrix’ neurons, which send more diffuse projections to the cortices and layers (Jones, 1998; Jones and Hendry, 1989). Provided that CN axons project to thalamic nuclei with high densities of core neurons, like VL and with high densities of matrix neurons, like VM and CL, this connectivity of cerebellar-recipient thalamic nuclei suggests that the cerebellar impact differentially affects cortical information processing. Moreover, single axon reconstructions of cerebellar-recipient zones within VL, VM and CL reveal that their axons also spread throughout other regions (Deschenes et al., 1996b; Kuramoto et al., 2009; Kuramoto et al., 2015) further highlighting that the cerebellar input can affect a wide range of thalamo-cortical networks and functions.

Apart from their connectivity to the cortex, the heterogeneity of cerebellar recipient thalamic nuclei also extends into the dendritic morphology. For instance, the cerebellar-

recipient zones of the VL and VM have been shown to contain neurons with 'bushy' dendrites (Clasca et al., 2012; Kuramoto et al., 2009; Kuramoto et al., 2015; Monconduit and Villanueva, 2005; Yamamoto et al., 1985) and thereby have a different appearance than CL neurons that show polarized dendritic branching (Deschenes et al., 1996b). This variability in the morphological aspects of thalamic neurons in the cerebellar-recipient nuclei corroborates the differential axonal projection patterns and suggests that the impact of cerebellar output on thalamic neurons varies for each target nucleus. Yet, the anatomical and electrophysiological data on the cerebello-thalamic projections lack an in-depth comparison of the cerebellar impact on the various thalamic targets.

So far, the electrophysiological studies that investigated the cerebello-thalamic projections focused on the VL nucleus. Intracellular recordings in this nucleus in anesthetized rats and cats revealed that electrical microstimulation of the CN neurons or the brachium conjunctivum triggered action potential firing (Bava et al., 1986; Rispal-Padel and Grangetto, 1977; Sawyer et al., 1994b; Uno et al., 1970), which matches the cerebellar-evoked responses in motor cortex (Rispal-Padel and Latreille, 1974; Steriade, 1995; Yoshida et al., 1966). Likewise, also single-pulse optogenetic stimulation in CN in the mouse brain has been proven to effectively control thalamo-cortical network activity (Kros et al., 2015; Proville et al., 2014). Morphological and ultrastructural analysis of the CN axon terminals in VL revealed that they typically synapse perisomatically on large diameter dendrites and form large terminals with various mitochondria and release sites (Aumann and Horne, 1996a, b; Aumann et al., 1994; Sawyer et al., 1994a). These findings function as a frame of reference, but a thorough understanding of the cerebellar impact on thalamo-cortical information processing is hampered by the lack of detailed *in vitro* cell physiological analysis and morphological characterization of the CN axonal projections throughout the various thalamic nuclei.

In order to elucidate how the cerebellar impact on thalamic neurons correlates to the specific nuclei, we studied the postsynaptic responses of thalamic relay neurons to selective stimulation of CN axons using *in vitro* whole cell recordings. We focused on neurons in the VL, VM and CL and correlated the electrophysiological data to the morphological details of the target neurons. Our results show that both pre- and post-synaptic aspects of the cerebello-thalamic transmission vary between these thalamic nuclei and thereby provide the first evidence for the functional diversification of the cerebellar impact on thalamo-cortical networks.

RESULTS

Thalamic nuclei receive various densities of CN axons and terminals

To assess the innervation of VL, VM and CL thalamic nuclei by cerebellar axons in the mouse brain, we transfected CN neurons located mostly, but not limited to the interposed CN with a virally encoded ChR2-YFP-expressing construct (Figure 1A). In several mice we found that the medial and lateral CN also contained ChR2-YFP-expressing neurons. In the thalamus we found the level of intensity of this membrane-bound fluorophore to be highest in the VL (55.9±8.0 a.u.) compared to VM (38.7±3.9 a.u.) and CL (25.8±2.3 a.u.) (p=0.529 for VL *vs* VM; p=0.002 for VL *vs* CL, p=0.136 for VM *vs* CL, K-W tests, Dunn's correction; Figure 1B and Table S1).

To dissociate between the active CN terminals and passing axons, we chose to stain for vesicular glutamate transporter 2 (vGluT2), which has previously been shown to label CN axon terminals (Kuramoto et al., 2009; Rovo et al., 2012), and solely quantify the double-labelled vGluT2-positive (vGluT2$^+$) ChR2-EYFP-expressing CN terminals. When we assessed these vGluT2$^+$-CN terminals using stacks of high–magnification images acquired with confocal microscopy and subsequently applied custom-written image analysis scripts, we found that the VL nucleus was most densely populated by vGluT2$^+$-CN terminals (total count 499 vGluT2$^+$-CN terminals; N=5 mice; Figure 1C-D) with a mean volume of 12.45±0.74 µm^3. As previously reported (Aumann et al., 1994), VM encompasses CN axons passing through, some of which send some branches in the most medial part of the nucleus (Figure 1E). The number of vGluT2$^+$-CN terminals in VM was lower compared to VL and their volume was significantly smaller (6.65±0.71 µm^3; n=172 terminals, p<0.0001, K-S test; Figure 1F,I and Table S1). The CL nucleus showed the lowest number of vGluT2$^+$-CN terminals and their volume was statistically different from VL but not from VM (5.85±0.9 µm^3; n=73 terminals; p=0.0002 for VL vs CL and p=0.966 for VM vs CL, K-S test; Figure 1G-I and Table S1). We observed a significantly higher density of vGluT2$^+$-CN terminals in VL compared to CL (p=0.024; K-W test), whereas the differences in density between VL-VM and VM-CL were not significantly different (p=0.334 and p=0.865, respectively; K-W tests; Figure 1J and Table S1). These data demonstrate that the cerebellar projection innervates preferentially VL and that these terminals are also bigger compared to VM and CL.

Basic transmission properties of cerebello-thalamic synapses differ across thalamic nuclei

It has been shown by sharp electrode recordings in anesthetized cats and rats that electrical stimulation of CN axons could elicit monosynaptic excitatory post-synaptic potentials (EPSPs) from which a fast spike could arise in VL relay cells (Sawyer et al., 1994b;

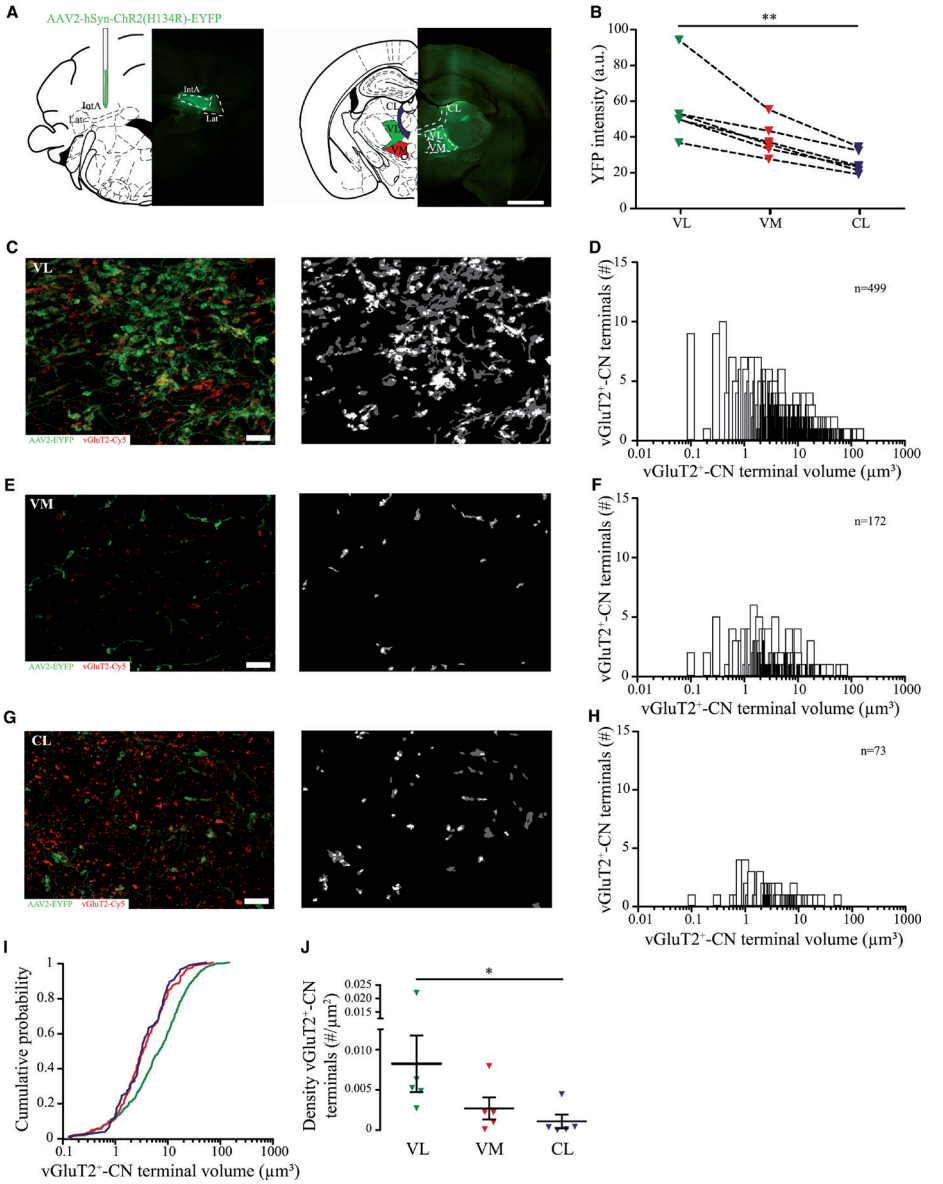

Figure 1. Variable innervation of VL, VM and CL nuclei by CN axons. ***A*** schematic representation of the experiment. *Left* AAV-injection in the interposed nucleus and (right) fluorescent (ChR2-EYFP) CN axons throughout the thalamic complex (3 weeks post-injection) of the same mouse. The nuclei of interest are highlighted in green (VL), red (VM) and blue (CL). This color code will be applied throughout all the figures. Scale bar indicates 1 mm. ***B*** percentage of YFP signal in the three nuclei of interest (N = 6 mice) normalized to fluorescence in VL. ***C***,***E***,***G*** *Left*: maximum intensity projection of *Z-stack* (14 µm thick) showing in green ChR2-EYFP stained CN axons, in red vGluT2 staining and *right* the result of the colocalization mask; gray indicates ChR2-EYFP-stained axons and white vGluT2$^+$ and EYFP ***D,F,H*** histograms showing vGluT2$^+$-CN terminal volume and number for VL, VM and CL (N=5 mice). ***I*** cumulative plot of the terminal volume (green: VL; red: VM; blue: CL). (VL vs CL p<0.001: VL vs VM p<0.001 and VM vs CL p=0.966; N=5 mice, K-S test). ***J*** average density of vGluT2$^+$-CN terminals (VL vs CL p=0.024). Data are presented as mean ± S.E.M; * p<0.05, *** p<0.001. K-W test was used. For full statistical report see Table S1.

Uno et al., 1970). To our knowledge, no data have been published about the postsynaptic currents underlying these changes in VL potentials, or about the postsynaptic responses of thalamic VM or CL cells. To gather these data we performed whole cell patch-clamp recordings of VL, VM and CL neurons in acutely prepared thalamic slices of mice that received bilateral CN injections with ChR2-EYFP-encoding AAV-vectors, which transfected neurons located mostly, but not exclusively, in the interposed nuclei (see material and methods section). We selected the recorded neurons based on their position in the slice, i.e. surrounded by ChR2-EYFP encoding CN axons, their monosynaptic responses to 470 nm optical stimulation (see below) and their anatomical location. Overall, we found that the resting membrane potential of VL (-71.6±0.9 mV), VM (-72.2±2.0 mV) and CL (-70.0±1.4 mV) neurons was not significantly different (p=0.736, one-way ANOVA), but that the input resistance of CL neurons was significantly higher than in VL neurons (p=1 for VL *vs* VM, p=0.012 for VL *vs* CL and p=0.175 for VM *vs* CL; n=49; K-W test). In all three thalamic nuclei single light pulses (1 ms, 470 nm, applied through the objective) elicited an EPSC (Figure 2A). These events were reliably blocked by bath-application of the voltage-gated Na^+-channel blocker tetrodotoxin (TTX) (n=5 cells; >99% decrease in charge transfer), which indicates that the postsynaptic events were triggered by action potential-driven release of glutamate from CN terminals (data not shown). The mean EPSC amplitude that we could maximally evoke was significantly higher in VL than in VM and CL (VL: -847.7±109.5 pA; VM: -165.0±40.2 pA; CL: -210.8±89.2 pA; p=0.001 for VL *vs* VM, p<0.001 for VL *vs* CL and p=1 for VM *vs* CL; K-W tests), which was also represented in the evoked charge (VL: -3820±595 pA*ms; VM: -862±235 pA*ms; CL: -1284±542 pA*ms; p=0.002 for VL *vs* VM; p=0.001 for VL *vs* CL, p=1 for VM *vs* CL; K-W tests; Figure 2B and Table S2). The variability in optically stimulated EPSC amplitude and charge was quantified by calculating the coefficient of variation (CV) (Figure 2C). We found significant differences in the CV of EPSC amplitudes (VL: 0.13±0.02; VM: 0.25±0.04; CL: 0.38±0.07; p=0.031 for VL *vs* VM, p=0.001 for VL *vs* CL; p=1 for VM *vs* CL, K-W tests, Dunn's correction; Figure 2D and Table S2) and of EPSC charge (VL: 0.13±0.02; VM: 0.28±0.04; CL: 0.47±0.12; p=0.03 for VL *vs* CL, p=0.025 for VL *vs* VM, p=1 for VM *vs* CL, K-W tests, Dunn's correction and Table S2). We found no significant correlation of the incubation time to the EPSC amplitude, nor to the CV of the EPSC amplitude (p=0.470, r_s=0.116 for EPSCs and p=0.269, r_s=0.161 for CV, Spearman correlation), which supports the notion that the difference in postsynaptic responses is actually due to a difference in the charge transfer between CN axons in VL, VM and CL neurons.

To establish the impact of neurotransmitter release from CN terminals on thalamic neurons' membrane potential we also recorded a subset of cells in current clamp (Figure 2E). When stimulated at maximum light intensity most VL neurons fired action potentials (9 cells out of 10) whereas most VM (3 out of 3) and CL neurons (4 out of 5;

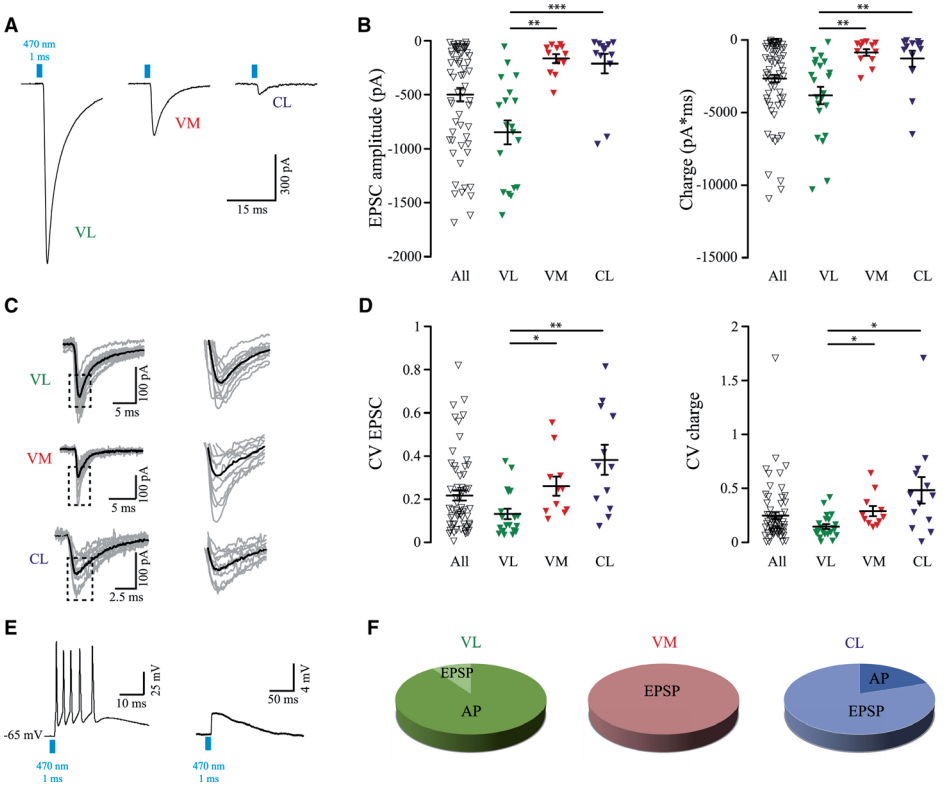

Figure 2. Charge transfer between CN axons and thalamic neurons differs for VL, VM and CL. ***A*** optical wide field stimulation of CN terminals (470 nm, 1 ms pulse length) evoked EPSCs of variable amplitude in VL, VM and CL. ***B*** quantification of EPSCs amplitude and charge for all recorded cells (n=63 for EPSC amplitude and n = 65 for charge) and for the nuclei of interest (EPSC: VL: n=19; VM: n=12; CL: n=13; charge: VL: n=22; VM: n=12; CL: n=13, respectively; 'All' category represents all cells recorded, of which some were not recovered by histology and therefore were not classified to a specific nucleus – note that all cells in VL, VM and CL are also represented in 'All'). ***C*** example traces of EPSCs amplitude in gray and average trace in black. Note the variability in EPSC amplitude of individual responses. ***D*** coefficient of variation (CV) for (left) EPSCs amplitude and (right) EPSC charge. ***E*** example traces of (left) action potential (AP) firing or (right) excitatory postsynaptic potential (EPSP) evoked by single pulse CN stimulation. ***F*** pie charts representing responses to CN stimulation recorded in current-clamp mode (VL: n=9 AP, n=1 EPSP; VM: n=3 EPSP; CL: n=1 AP, n=4 EPSP). Data are presented as mean ± S.E.M; * p<0.05, ** p<0.01, *** p<0.001. K-W was used. For full statistical report see Table S2.

Figure 2F) did not. The probability to elicit an action potential was not related to the resting membrane potential of the cell (p=0.628; r_s=-0.127, Spearman correlation). As we expected from the EPSC amplitudes, neurons in VL fired action potentials more readily than those in VM and CL.

Thalamic responses show paired-pulse depression and are predominantly sensitive to ionotropic glutamate receptor blockers

Thalamic afferents are often categorized as 'driver' or 'modulator' (Sherman, 2014; Sherman and Guillery, 1998). This classification is partially determined by the response

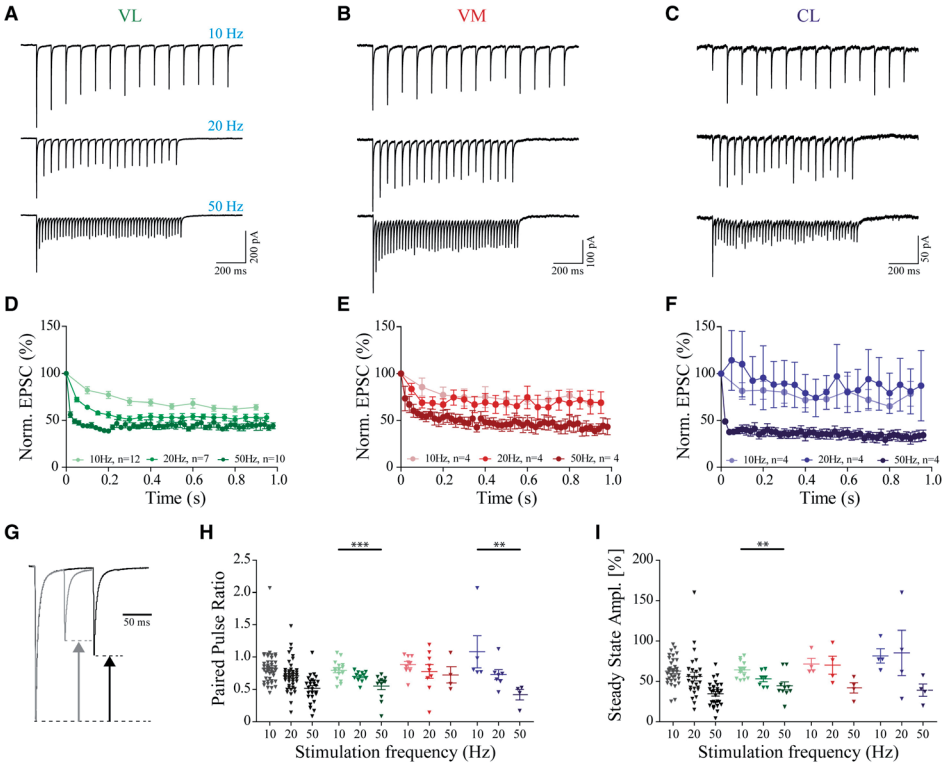

Figure 3. High-frequency stimulation results in paired-pulse depression of EPSC. ***A,B,C*** averaged responses of VL, VM and CL neurons (of 5 repeats) to 1 sec trains of 10 Hz, 20 Hz or 50 Hz stimuli. ***D,E,F*** average normalized EPSC amplitudes for 10, 20 and 50 Hz stimulus trains. ***G*** superimposed example responses (average of 5 repeats) to paired-pulse stimulation at 10 Hz (black) and 20 Hz (grey). ***H*** average paired pulse ratio at 10, 20 and 50 Hz for each recorded cell in each nucleus. ***I*** average normalized steady state response amplitude during the last 5 stimuli of the train for each cell in each nucleus. (For panels H VL: n=39; VM: n=22; CL: n=16 and I VL: n=29; VM: n=12; CL: n=12). ** p<0.01, *** p<0.001. K-W test was used. For full statistical report see Table S3.

to repetitive stimulation of presynaptic terminals: driver synapses are thought to show paired-pulse depression (PPD) whereas modulator synapses evoke paired-pulse facilitation (PPF) (Groh et al., 2008; Reichova and Sherman, 2004; Seol and Kuner, 2015). Although cerebellar input to motor thalamus has been listed as driver input (Sherman, 2014), short-term synaptic dynamics of thalamic responses following repetitive CN stimulation in VL, VM and CL still need to be evaluated. Here we performed voltage-clamp recordings while stimulating the CN terminals repetitively with trains of light pulses at 10, 20 and 50 Hz (Figure 3A-C). To evaluate the time course of the depression we normalized EPSC amplitudes to the first peak amplitude (Figure 3D-F).

In general, we found that the ratio between the amplitudes of the first two EPSCs showed a PPD at all frequencies tested (Figure 3G). At 50 Hz the second EPSC showed a ~twofold

reduction in amplitude compared to the initial one (VL: 0.52±0.06; VM: 0.72±0.12; CL: 0.41±0.08), whereas lower frequency stimulations showed a smaller effect on the paired-pulse depression. At 20 Hz the depression was around 30% of the first EPSC in all the nuclei (VL 0.70±0.02, VM 0.77±0.10, CL 0.73±0.07) whereas at 10 Hz only VL (0.80±0.03) and VM (0.88±0.04) neurons showed on average PPD but CL did not (1.08±0.25) (Figure 3H). When we compared the paired-pulse depression across all nuclei for each frequency, we found that the ratio between the first two responses did not show any significant difference between the nuclei (10 Hz: p=0.344; 20 Hz: p=0.168; 50 Hz: p=0.137, K-W tests, Dunn's correction; Figure 3H and Table S3).

Next, we analyzed the subsequent responses to the train stimulation to determine the average sustained release of presynaptic terminals during high frequency steady-state synaptic transmission (Figure 3A-C). For this analysis, the average phasic EPSC amplitude within the train was normalized to the average first EPSC amplitude for each frequency and each nucleus. Across all recorded cells, we find normalized steady state amplitudes of 64.4±3.1% (VL), 71.3±6.9% (VM) and 81.4±8.9% (CL) at 10 Hz: 53.1±3.6% (VL), 70.1±11.1% (VM) and 85.2±28.0% (CL) at 20 Hz and 44.4±5.0% (VL) 41.9±6.5% (VM) and 39.1±7.7% (CL) at 50 Hz (Figure 3I and Table S3). We found no significant differences between the values recorded per nucleus, but did find that in VL the steady-state depression was significantly higher at 50 Hz than at 10 Hz (p=0.005, K-W test, Figure 3I and Table S3). These data indicate that the general tendency for transmission at cerebello-thalamic synapses in VL, VM and CL is to show a depression of neurotransmitter release in response to repetitive stimulation.

Our results indicate that the synaptic transmission at cerebello-thalamic synapses in VL, VM and CL are glutamatergic, which matches previous *in vivo* findings on the excitatory responses of VL neurons evoked by microstimulation of the brachium conjunctivum or the neurons in CN (Bava et al., 1986; Rispal-Padel and Grangetto, 1977; Sawyer et al., 1994b; Uno et al., 1970). To elucidate whether these excitatory postsynaptic responses where mediated by ionotropic and/or metabotropic receptors we next tested the effects of their selective blockage on the responses to 50 Hz stimulus trains. Upon wash-in of AMPAR-antagonist NBQX the EPSC charge decreased from -74.6±2.4 nA*ms to -28.0±8.3 nA*ms and following the wash-in of NMDAR-antagonist APV the EPSC charge decreased even further to -13.5±4.3 nA*ms (p<0.001, Friedman test; Figure 4A,B and Table S4). Further application of blockers for the mGluRs most abundantly expressed in thalamic neurons (JNJ for mGluR1 and MPEP for mGluR5 (Liu et al., 1998; Reichova and Sherman, 2004)) did not affect the remaining current (-12.1±3.9 nA*ms; Friedman test, p=1; Figure 4B and Table S4), suggesting the absence of a substantial mGluR1- or mGluR5-mediated component in cerebellar transmission on thalamic neurons.

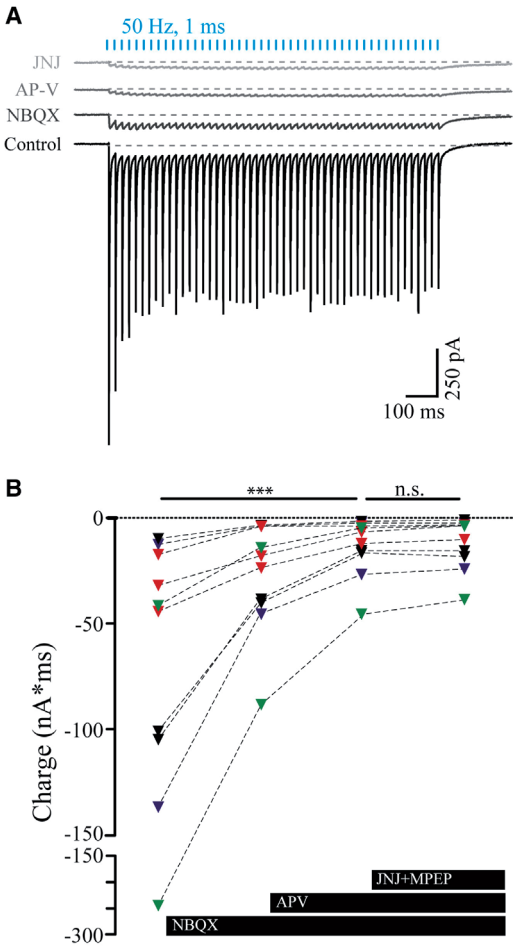

Figure 4. Thalamic responses to CN-stimulation are sensitive to ionotropic receptor blockers. ***A*** example traces of averaged EPSCs evoked by 1 sec train of 1 ms pulses at 50 Hz in control (aCSF) conditions and following application of NBQX, APV and JNJ to block AMPA, NMDA and mGluR1 and 5 receptors, respectively. ***B*** summary data showing the decrease of charge after drug application (VL in green, VM in red, CL in blue, undefined location in black; n=10 in total). *** p<0.001. For full statistical report see Table S4.

Postsynaptic determinants of variable CN-impact in thalamic cells

Next we evaluated whether the electrophysiological characteristics described above could be linked to the morphology of the thalamic neurons, bearing in mind that in rat thalamus the neuronal morphology in VL, VM and CL neurons varies (Clasca et al., 2012; Deschenes et al., 1996a; Deschenes et al., 1996b; Kuramoto et al., 2009; Kuramoto et al., 2015; Ohno et al., 2012; Rubio-Garrido et al., 2009). By reconstructing biocytin-filled neurons throughout the VL, VM and CL nuclei (Figure 5A) and analyzing their dendritic branching using a 3D-Sholl analysis (Figure 5B) we found that 23 VL neurons on average show a more elaborate branching pattern than the 14 CL neurons at 55 µm distance from

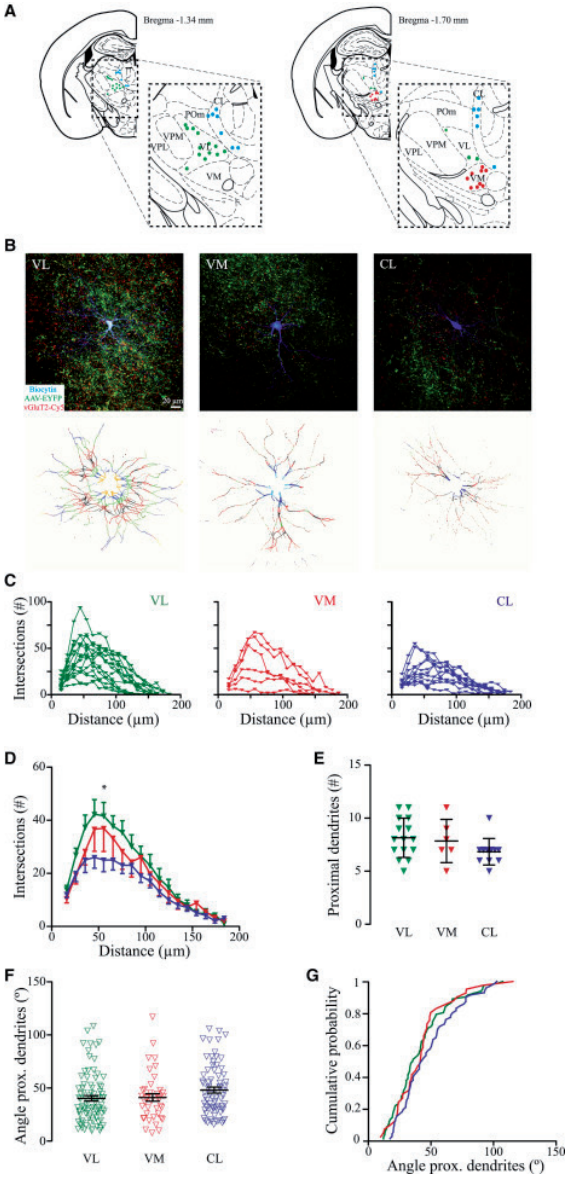

Figure 5. Morphological characterization of thalamic cells recorded in VL, VM and CL. ***A*** location of all recorded cells in VL, VM and CL projected on two coronal planes (Franklin and Paxinos, 2001). ***B*** *Top* maximum projections of the somato-dendritic morphology of biocytin-filled cells (blue), surrounding ChR2-EYFP labelled CN axons (green) and vGluT2-staining (red) for VL (left), VM (middle) and CL (right). *Bottom*: maximum projections of 10 µm-thick 3D-spheres surrounding an example neuron from VL, VM and CL (as indicated by the different colors along dendritic trees). ***C*** Sholl analysis shows dendritic arborisation by the number of intersections of the concentric spheres for VL (left), VM (middle) and CL (right) (VL: n=15; VM: n=6; CL: n=11). ***D*** average number of dendritic intersections is shown in 10 µm steps from the soma and each nucleus. ***E*** number of proximal dendrites as quantified at 15 µm distance from soma for VL, VM and CL (VL: n=15; VM: n=6; CL: n=11). ***F*** directionality of proximal dendrites (at 15 µm from soma center) is determined by the angle between individual dendrites. Note that the angle is proportional to the angular distance between two neighboring dendrites. ***G*** cumulative distribution of data represented in panel *F*. * $p<0.05$, ** $p<0.01$. For full statistical report see Table S5.

the soma (p<0.05, 2-way ANOVA; Mann Whitney comparison, Figure 5C,D and Table S5). The number of proximal dendrites (VL: 8.13±0.47; VM: 7.83±0.83; and CL: 6.83±0.34) was not significantly different between nuclei (p=0.115, K-W test; Figure 5E and Table S5). To better illustrate the dendritic architecture of cells in each of the three defined nuclei we also quantified the angular distance between dendrites at 15 µm from the soma. We found no significant difference in the angular distance (VL: 40.2±2.6°; VM: 41.1±3.5°; CL: 47.0±2.8°; p=0.14, K-W test; Figure 5F,G and Table S5). Although limited, these morphological distinctions between cerebellar-recipient neurons possibly corroborate the distinct electrophysiological characteristics, which together suggest a differential impact of cerebellar input to thalamic neurons.

Distribution and morphology of reconstructed CN terminals

Previous structural studies in rats suggested that in VL cerebellar terminals are larger than those in intralaminar nuclei (Aumann and Horne, 1996b). To further characterize the identity of cerebellar terminals for each recorded neuron, we stained the tissue slices containing the patched neurons for vGluT2 and assessed the morphology of the vGluT2$^+$-CN terminals using high magnification confocal microscopy (Figure 6A). The number of vGluT2$^+$-CN terminals on the recorded cells did not vary significantly between the nuclei (VL: 4.5±0.7; VM: 3.66±1.17; CL: 3.08±0.83; p=0.37, K-W test, Figure 6C, Table S6) neither their distance from soma (VL: 26.7±1.9 µm; VM: 33.8±5.7 µm; CL: 26.6±2.5 µm; p=0.58, K-W test, Figure 6D; Table S6). To enhance the x-y resolution and reduce the blurring caused by the point spread function, we deconvolved the images and selected the virus-labeled vGluT2$^+$-CN terminals to measure their volume (Figure 6B). We found that terminals onto recorded VL neurons had a larger volume (11.67±1.30 µm^3) than those onto recorded CL neurons (CL: 7.23±1.57 µm^3) (p=0.02, K-W test, Figure 6E-F and Table S6), whereas no significant differences were found comparing VM terminals (9.26±1.93 µm^3) to VL and CL (p=1.00 and p=0.35, respectively, K-W tests, Figure 6E-F and Table S6).

To further investigate CN axon terminal dimensions and characteristics of the post-synaptic structures we studied synaptic contacts at the ultrastructural level. To identify CN axon terminals in electron micrographs we collected VL, VM and CL tissue from mice which we injected with biotin dextran amine (BDA) in CN, which spread mostly, but not exclusively, in the interposed CN. Representative examples of the synaptic profiles formed by BDA- stained CN terminals and thalamic neurons are shown in Figure 7A. Measurements made from the profiles included terminal surface, number and size of mitochondria, dendritic diameter, PSD length and number of release sites per terminal (Figure 7B). Although we observed in the fluorescent images that the terminal size was significantly different between VL and CL, at the ultrastructural level the difference was not significant even though on average VL terminals appeared to be bigger

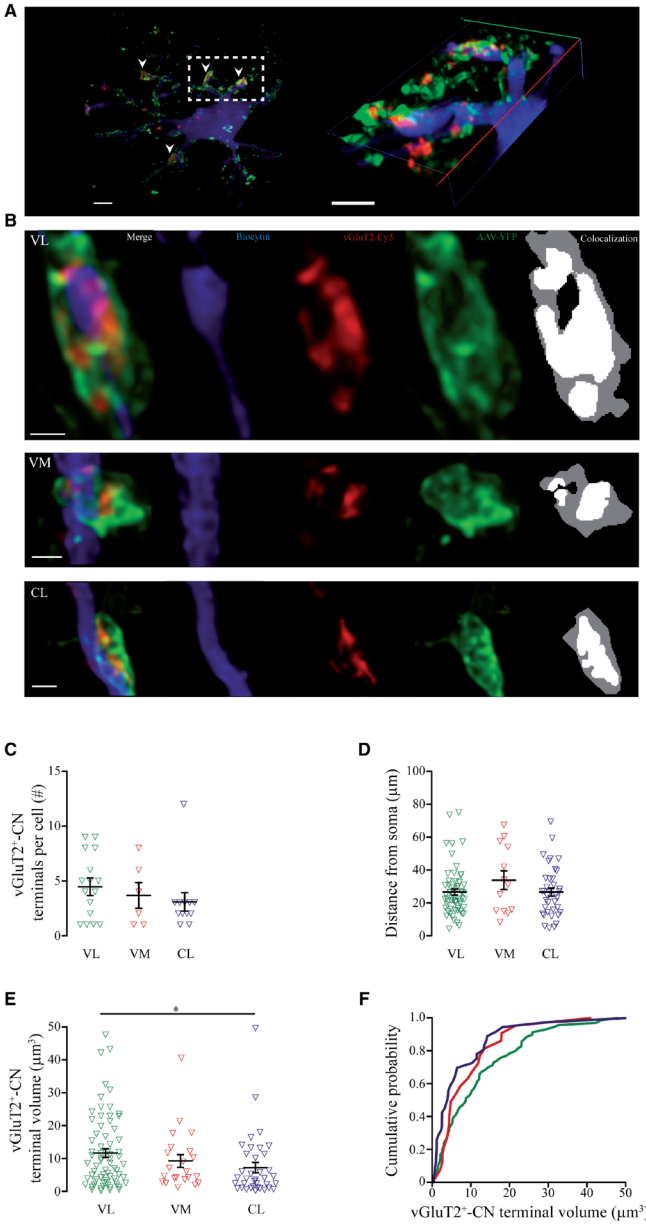

Figure 6. CN terminals of variable volume are similarly positioned along dendrites of recorded thalamic neurons. ***A*** maximum intensity projection of Z-stack image (22 µm thick) of biocytin filled neuron (blue: streptavidin-Cy3; green: ChR2-YFP terminals; Red: vGluT2-Cy5). Arrowheads indicate the vGluT2$^+$-CN terminals onto proximal thalamic dendrites. Scale bar 10 µm. *Right:* 3D reconstruction of inset in A. Scale bar 2.5 µm. ***B*** *Left four panels:* example of vGluT2$^+$-CN terminals in VL, VM and CL (blue: thalamic dendrite; red: vGluT2; green: CN terminal). *Right panel:* colocalization of ChR2-EYFP and vGluT2-staining to identify active terminals and calculate their volume based on ChR2-EYFP signal. Scale bar 1 µm. ***C*** summary data of the number of reconstructed vGluT2$^+$-CN terminals (VL: n=16; VM: n=6; CL: n=12). ***D*** summary data of distance of reconstructed terminals from soma (VL: n=60; VM: n=13; CL: n=37. ***E-F*** terminal volume (VL: n=71; VM n=22; CL n=37) and cumulative distribution. * p<0.05. For full statistical report see Table S6.

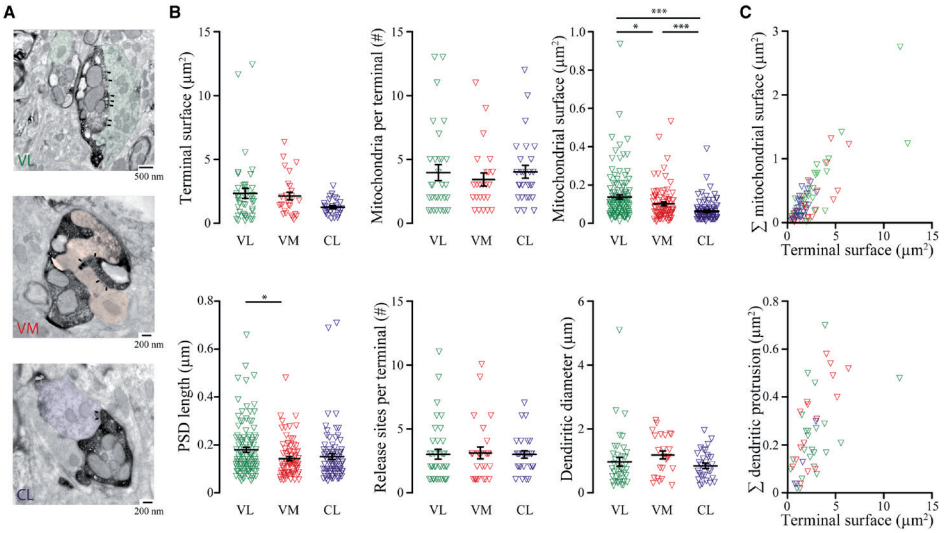

Figure 7. Ultrastructure of CN terminals in VL, VM and CL reveals pre- and post-synaptic specialization. ***A*** pseudo-colored ultramicrographs of CN terminal in VL (top), VM (middle) and CL (bottom). Note the complex structure of these terminals. Arrowheads indicate synapses. ***B*** quantification of terminal surface (top left; VL: n=48; VM: n=28; CL: n=27), number of mitochondria (top middle; VL: n=32; VM: n=27; CL: n=24), mitochondrial surface (top right; VL: n=124; VM: n=109; CL: n=82; VL vs VM p=0.034; VL vs CL p<0.001; VM vs CL p<0.001, K-W tests), length of post-synaptic density (PSD) (bottom left; VL: n=114; VM: n=81; CL: n=80; VL vs VM p=0.024; VL vs CL p=0.055; VM vs CL p=1; K-W test), release sites per terminal (bottom middle; VL: n=37; VM: n=27; CL: n=26; p=0.667, K-W test) and diameter of the contacted dendrite (bottom right; VL: n=40; VM: n=31; CL: n=25; p=0.080, K-W test). ***C*** *Top* correlation of the terminal surface with the sum of the surface occupied by mitochondria for each given terminal (VL: green; VM: red; CL: blue). *Bottom* Correlation of the terminal surface with the sum of the surface occupied by dendritic protrusions for each given terminal. Note that terminals without a mitochondria or dendritic protrusion are not represented in these correlation plots. * p<0.05, *** p<0.001. For full statistical report see Table S7.

(VL: n = 42 terminals; 2.35±0.38 µm^2; VM: n = 27 terminals; 2.07±0.31 µm^2; CL: n = 28 terminals; 1.23±0.11 µm^2 p=0.099, K-W test). We did observe a significant difference in the mitochondrial surface between VL and CL (VL: 0.13±0.01 µm^2; VM: 0.10±0.01 µm^2; CL: 0.06±0.01 µm^2; VL vs VM p=0.034; VL vs CL p<0.001; VM vs CL p< 0.001; K-W test; Figure 7B and Table S7), which correlated significantly with the total surface of the terminals (r_s=0.7156; p<0.0001, Spearman correlation; Figure 7C and Table S7). Another characteristic of cerebello-thalamic synapses we could observe in all three nuclei is that most terminals contained several release sites (VL: 2.97±0.38; VM: 3.08±0.47; CL: 2.96±0.29; p=0.667; K-W test) (Aumann et al., 1994). The axon terminals in VL and VM also showed a more complex interaction with the postsynaptic structures than in CL, in that we found dendritic protrusions inside the majority of the VL (24 out of 42 terminals) and VM (17 out of 27) terminals, whereas this was less common in CL (4 out of 28) terminals. No significant differences were found in the surface of the dendritic protrusions between the thalamic nuclei (VL: 0.23±0.16 µm^2; VM: 0.29±0.18 µm^2; CL: 0.13±0.12 µm^2; p=0.1723; K-W test). The surface area of the dendritic protrusions showed a significant correlation with

the terminals surface (r_s=0.6146; p<0.0001, Spearman correlation; Figure 7C and Table S7). At the post-synaptic side we found that although the dendritic diameter opposing CN terminals did not show any difference between the nuclei (VL: 0.97±0.13 µm; VM: 1.18±0.12 µm; CL: 0.84±0.08 µm; p=0.08; K-W test), we did find that the length of post-synaptic densities (PSD) was longer in VL (0.17±0.01 µm) compared to VM (0.14±0.01 µm) and CL (0.15±0.01 µm; VL vs VM: p=0.024; VL vs CL: p=0.055; VM vs CL: p=1; K-W test). Altogether, these ultrastructural findings support the notion that CN axons tend to synapse on proximal dendrites in all three studied nuclei, but that there may be a structural difference in the constellation of the pre- and post-synaptic sites which could correlate to the difference in transmission at CN-synapses throughout the thalamic complex.

DISCUSSION

Our data show that in mouse brain CN neurons innervate the VL thalamic nucleus more densely compared to VM and CL. Although the distribution matches that in other species (Angaut et al., 1985; Asanuma et al., 1983; Aumann and Horne, 1996b; Aumann et al., 1994; Bentivoglio and Kuypers, 1982; Cohen et al., 1958; Haroian et al., 1981; Teune et al., 2000) our study does provide one of the first quantitative comparisons of active CN axon terminals in VL, VM and CL, since we exclusively quantified the vGluT2$^+$-CN terminals that expressed ChR2-EYFP. Our density values of these CN terminals per nucleus (Figure 1) may very well be an underestimate of the total proportion of CN axons that innervate VL, VM and CL nuclei given that i) the injections of viral particles did not transfect the complete CN population projecting to these nuclei and ii) the use of vGluT2-antibodies most likely resulted in a limited penetrance into the slices, leaving those ChR2-expressing CN terminals located deeper into the slice unstained. These aspects possibly also confound the number and location of CN axon terminals on a single thalamic neuron (Figure 6) in that there may have been more CN terminals that contributed to the evoked charge transfer, but that due to their location, i.e., depth in the slice, some were identified as vGluT2-negative. Still, we would like to emphasize that the difference in the number of CN terminals between VL, VM and CL is likely to be independent from viral transfection rates or antibody penetrance since these data have been gathered from the same tissue samples.

A potential source for the variability of CN-evoked responses in thalamic neurons and the difference in CN-terminal morphology throughout the thalamic nuclei may be the location of the transfected CN neurons. According to previous anatomical studies that used classical neurotracers, glutamatergic projection neurons from the lateral, interposed and medial CN all innervate VL, VM and CL neurons with a clear preference for

the contralateral thalamic complex, but not excluding ipsilateral projections (Angaut et al., 1985; Haroian et al., 1981; Teune et al., 2000). Whereas we aimed for centering our bilateral viral injections in the interposed nuclei, we also found ChR2-EYFP transfected CN neurons in the lateral and/or medial CN in several mice. Although in principle it is possible that the variability in the recorded responses and terminal morphology is due to the transfection of glutamatergic CN neurons in various nuclei in both sides of the cerebellum, there are currently no data available supporting such notion. In fact, the few data available on the direct comparison between axon terminals from the various nuclei reveal that the dimensions and ultrastructural morphology in thalamic nuclei is comparable between axons originating from interposed and lateral CN (Aumann et al., 1994). These anatomical data are corroborated by the previous *in vivo* electrophysiological experiments using intracellular and extracellular recordings in anesthetized cats that revealed that electrical stimulation of both the interposed and lateral CN can evoke postsynaptic responses in single VL thalamic neurons (Bava et al., 1986; Rispal-Padel and Grangetto, 1977; Shinoda et al., 1985; Smith et al., 1978; Uno et al., 1970). A set of dedicated *in vitro* experiments using tissue with small injections in the single CN will provide further insight in the potential role of the various CN in the differentiation of the cerebellar impact on thalamic nuclei.

The electrophysiological characterization of thalamic responses to CN stimulation revealed that on average VL neurons showed larger EPSCs than those in VM or CL. As expected, these voltage-clamp results translated to a higher chance of action potential firing upon stimulation for VL than for VM and CL when recorded in current-clamp. Our data from VL and VM match earlier reports about faithful action potential firing by VL neurons upon CN or brachium conjunctivum stimulation (Bava et al., 1986; Rispal-Padel and Grangetto, 1977; Sawyer et al., 1994b; Steriade, 1995; Steriade et al., 1971; Uno et al., 1970) and provide the first detailed insights for synaptic transmission at CN-CL synapses (cf. (Bava et al., 1967; Chen et al., 2014)). Using 10, 20 and 50 Hz stimulus trains, we were able to sample the responses of thalamic neurons to physiologically relevant cerebellar input, since the firing rates reported for CN projections recorded *in vivo* range from ~30-100 Hz (as reviewed by (De Zeeuw et al., 2011)). We consistently found that the responses in VL, VM and CL neurons showed paired-pulse depression, which is suggested to play an important role in information processing by helping the system to adapt to ongoing levels of activity (Chung et al., 2002; Mease et al., 2014; Reichova and Sherman, 2004). In our current experiments the ChR2 off-kinetics limited us to stimulus frequencies well below the maximal CN firing rates, which may also have prevented us from recording a significant effect of mGluR-receptor blockage, in that the total mGluR-mediated currents in thalamic neurons evoked by a stimulus frequency of 50 Hz tends to be limited (see also (Viaene et al., 2013)). Therefore, we cannot rule out that the activation of either

pre- or postsynaptic modulatory mechanisms have affected the responses we recorded *in vitro*.

Referring to intracellular *in vivo* recordings, the cerebellar input on VL neurons has been classified as a driver input to neurons in the motor domain of the thalamus (Sawyer et al., 1994b; Sherman, 2014; Uno et al., 1970). However, several recent papers classify thalamic inputs in more than two categories: in addition to the 'driver' and 'modulator' inputs, a third category of 'driver-like' input has been defined (Bickford, 2015; Bickford et al., 2015). In the tecto-geniculate system the driver-like inputs have also been identified at the anatomical level by medium-sized terminals that contain round vesicles and innervate proximal dendrites, and at the electrophysiological level stable response amplitudes to trains of stimuli of up to 20 Hz (Kelly et al., 2003; Masterson et al., 2009). Our *in vitro* data showed that responses in VL neurons to stimulation of CN terminals meet a number of criteria used to define driver inputs (Sherman and Guillery, 1998): *i*) CN stimulation evokes a large post-synaptic current that *ii*) is solely mediated by ionotropic receptors and *iii*) depresses upon higher-frequency stimulation, *iv*) CN axons form large synaptic boutons that *v*) contact proximal thalamic dendrites. For CN terminals in VM and CL the categorization is less clear, since these only show some of the 'driver' characteristics. They lack mGluR-mediated transmission and proximal terminal location and their terminal volume is smaller. Moreover, the responses of VM and CL neurons to CN stimulation are significantly smaller, and CL neurons tend to show a stable paired-pulse ratio in response to 10 Hz stimulus trains. At the ultrastructural level, we also found a trend, although not significant, to a reduced terminal surface in CL compared to VL and a significantly smaller CL mitochondrial surface. Given that previous studies revealed that terminals with larger surface have a higher chance to release neurotransmitter compared to smaller terminals (Rollenhagen and Lubke, 2006; Zikopoulos and Barbas, 2007, 2012), our data may at least partially explain why the evoked response amplitude and charge in CL were smaller and more variable (Figure 2).

Further explanation for the difference in post-synaptic responses to CN stimulation between VL and the other nuclei may come from the difference in PSD length, which previously has been linked to neurotransmission efficacy (Geinisman, 1993). Our ultrastructural analysis of CN terminals further revealed that the characteristics described earlier for VL in the rat brain, i.e., large terminal surface, presence of multiple mitochondria, fragmented release sites and large diameter of opposing dendritic structure (Aumann and Horne, 1996a; Aumann et al., 1994; Sawyer et al., 1994a), are also found in mouse brain. The complexity of the cerebello-thalamic contacts in the VL and VM seemed more prominent, in that CN terminals in these nuclei were found to contain dendritic protrusions more often than in CL. This typical structure, found also in other large terminals in

thalamus, such as those formed by the piriform cortex in medial thalamus (Pelzer et al., 2017), enlarge the contact surface between axon terminals and the dendrite. However, in our current dataset we found no significant difference between the number of release sites for VL, VM or CL. Future experiments on the release properties of single CN terminals, alike those performed for 'giant' corticothalamic synapses in the sensory system (Groh et al., 2008; Seol and Kuner, 2015) should elucidate how the morphological characteristics can translate into the clear differentiation between postsynaptic responses in VL, VM and CL.

Our current findings provide new building blocks to construct the frame of reference for the impact of the cerebellar output on thalamic neurons. Given that mouse thalamus VL, VM and CL are free of interneurons, we argue that all our recordings are from thalamic relay neurons that synapse throughout the various regions of the cerebral cortex. By adapting the classification of relay neurons from rat thalamus (reviewed by (Clasca et al., 2012)), our VL recordings are from a mix of core (C)-type and matrix (M)-type neurons, VM recordings are from matrix (M)-type neurons and CL recordings from intralaminar (IL)-type neurons, which to some extent is supported by the reduced dendritic branching of CL neurons (Figure 6). If we assume that the axonal branching of C-, M- and IL-neurons in mouse brain indeed shows lamina-specific termination as described for rat (Deschenes et al., 1996b; Herkenham, 1979, 1980; Kuramoto et al., 2009; Kuramoto et al., 2015), our data indicate that the information conveyed by C- and M-type neurons in VL to manipulate activity of the middle and output layers of motor cortices (Kuramoto et al., 2009) that contribute to initiation of movement (Goldberg et al., 2013). In contrast, M-type VM neurons projections are more dense in layer 1 of widespread cortical areas, including the motor-associated, orbital, cingulate and visual areas in the rat (Kuramoto et al., 2015). Direct activation of cerebellar afferents to VM neurons indeed resulted in a widespread change of cortical activity to the gamma-band range (Steriade, 1995), which in these VM-projection regions have been linked to cognitive processes. Indeed, a recent study indicates that the cerebellar-recipient zone in mouse VM has a reciprocal connection with the prefrontal anterior lateral motor cortex that determines the ability to prepare a correct motor response to a sensory cue (Guo et al., 2017). For IL-type CL neurons it has been shown that their axons excite striatal, but also cortical neurons affecting motor, premotor, parietal, prelimbic and anterior cingulate processing, as well as regulating behavioral arousal levels (Berendse and Groenewegen, 1991; Chen et al., 2014; Gummadavelli et al., 2015).

Although it remains to be investigated how in *in vivo* conditions thalamic responses may differ between the different types of neurons, our study provides new insights into the diversity of the cerebellar impact on thalamo-cortical networks. Thalamo-cortical activ-

ity exhibits two distinct states, i.e., tonic and burst firing, which are related to different conditions such as waking, non-REM state, slow-wave sleep or even epileptogenic activity (McCormick and Bal, 1997). Thalamic afferents, like CN axons, are likely to modulate the activity of thalamo-cortical relay neurons from tonic to burst firing and vice versa. Indeed, single-pulse stimulation of CN neurons efficiently stops thalamo-cortical oscillations in epileptic mutant mice (Kros et al., 2015). The underlying mechanism may at least partially depend on the variable impact of CN axons on thalamic neurons, as we showed for VL, VM and CL. For instance, a brief pause in the firing of CN neurons, which can occur following synchronized activity in the cerebellar cortex (De Zeeuw et al., 2011) will most likely result in a recovery of synaptic PPD for all nuclei, but the first postsynaptic response in VL will be notably larger than in VM or CL. Such differential effects on thalamic action potential firing may potentially be modulated by cortical input, as well as glycinergic or cholinergic projections arising from brainstem (Giber et al., 2015; Miller et al., 1992) or GABAergic projections from substantia nigra (Buee et al., 1986), all of which may synergistically diversify the cerebellar impact on thalamo-cortical processes throughout the various (non-) motor domains.

EXPERIMENTAL PROCEDURES

Animals

All experiments were performed in accordance with the European Communities Council Directive. Protocols were reviewed and approved by the Dutch national experimental animal committees (DEC) and every precaution was taken to minimize stress, discomfort and the number of animals used. Data were collected from 21-56 day old C57BL/6NHsd mice of both sexes, which were purchased from Envigo laboratories (Horst, Netherlands).

Virus injections

We performed stereotaxic injections of adeno-associated virus carrying Channelrhodopsin2 AAV2-hSyn-ChR2(H134R)-EYFP into CN at 2 mm anterior-posterior and 1.5-2 mm medial-lateral to lambda. For localization of the injection sites 40 µm thick horizontal sections were obtained on a freezing microtome. The tissue was incubated with DAPI (300nM). Sections where rinsed and mounted on glass.

Electrophysiological recordings in slices and optogenetics

Electrophysiological recordings in coronal or horizontal slices were performed at 34 ± 1 ˚C aCSF 40 min after dissection. Internal solution was supplemented with biocytin for morphological reconstruction. Full-field optogenetic stimulation (1 ms, 470 nm peak excitation, 0.1 to 6.65 mW/mm^2) was generated using a Polygon4000 (Mightex, Toronto,

Canada) or a pE2 (CoolLED, Andover, UK). Pharmacology experiments were assessed adding AMPA- (10 µM NBQX), NMDA- (10 µM APV), mGluR1- (10 µM JNJ-16259685) and mGluR5- (50 µM MPEP) blockers to the aCSF.

Immunofluorescence and reconstruction

To visualize the recorded neurons and CN terminals, slices were stained for Streptavidin-Cy3 (Jackson Immunoresearch) and vGluT2 anti Guinea pig Cy5 (Millipore Bioscience Research Reagent). Using custom-written Fiji-scripts (ImageJ) we identified putative synaptic contacts that were isolated and morphologically studied using a LSM 700 microscope (Carl Zeiss). Stack's subsets of the connection were deconvolved using Huygens software (Scientific Volume Imaging) and the volume measured using a custom-written Fiji macro. To quantify the distance from soma for vGluT2-positive CN terminals we calculated the distance in 3 dimensions (using x-, y-, z-coordinates) between the center of the terminal and the center of the soma by Pythagorean Theorem. To determine the dendritic arborization of biocytin filled cells, we used the 3D Sholl analysis macro implemented in Fiji software (Ferreira et al., 2014).

Electron microscopy

Ultrastructural morphology was analyzed using electron microscope (CM 100, Philips). Staining for DAB and preparation of ultrathin section was performed as previously described (Hoebeek et al., 2008).

Data analysis and statistics

All numerical values are given as means and error bars are SEM. Parametric and non-parametric tests were chosen as appropriate and were reported in figure legends. Data analyses were performed using SPSS 22.0 software package.

Detailed experimental procedures and statistical analyses for each experiment can be found in Supplemental Experimental Procedures.

AUTHOR CONTRIBUTION

S.V.G. performed and analyzed the *in vitro* electrophysiological recordings, the confocal images acquisition and digital reconstructions. C.B.S. performed electrophysiological recordings and analysis and designed and performed Sholl analysis. O.H.J.E.R. performed channelrhodopsin and BDA injections for *in vitro* recordings and EM analysis. A.N. developed image analysis scripts and provided technical support for image acquisition. C.I.D.Z. and F.E.H. contributed financial and technical support. S.V.G. and F.E.H.

wrote the original draft. C.I.D.Z. and C.B.S. edited the manuscript. F.E.H. conceived and guided the project and performed ultrastructural analysis.

DECLARATIONS OF INTERESTS

The authors declare no competing financial interests.

ACKNOWLEDGEMENTS

We thank Daniel Dumas, Bas van Hoogstraten, Sverrir V Sigurdsson, Farnaz Nassirinia, Valentina Riguccini, Elena Tiddens, Saša Peter, Negah Rahmati, Avi Libster, Martijn Sierksma, Federica Brunero and the Hoebeek group for fruitful scientific discussions. We kindly thank Erika H. Goedknegt, Elize D. Haasdijk, Patrick Eikenboom and the OIC group for expert assistance in immunohistochemistry and/or imaging. S.V.G., C.B.S., O.H.J.E.R. and F.E.H. are generously supported by the Dutch organization for life sciences (NWO-ALW VIDI and Zon-MW TOP GO grants to F.E.H.) and C.I.D.Z. by ERC-Adv, ERC-PoC, NWO-ALW and Zon-MW grants.

SUPPLEMENTARY EXPERIMENTAL PROCEDURES

All experiments were performed in accordance with the European Communities Council Directive. Protocols were reviewed and approved by the Dutch national experimental animal committees (DEC) and every precaution was taken to minimize stress, discomfort and the number of animals used.

Animals

Data were collected from 21-56 day old C57BL/6NHsd mice of both sexes, which were purchased from Envigo laboratories (Horst, Netherlands).

Viral injections

Mice were anesthetized with isoflurane, (4% in 0.5 L/min O_2 for induction and 1.5% in 0.5 L/min O_2 for maintenance), carprofen (5 mg/kg), buprenorphine (50 µg/kg) and lidocaine (10%, local application). For optogenetic stimulation we stereotactically delivered adeno-associated virus (AAV) encoding Channelrhodopsin2 (ChR2) coupled with a EYFP fluorophore (AAV2-hSyn-ChR2(H134R)-EYFP) to the CN. Following bilateral craniotomies of ~0.5 mm above the interparietal bone (-2 mm anterior-posterior and 1.5-2 mm medial-lateral to lambda), 150-200 nl (at a rate of ~20 nl/min) of AAV was injected to the CN in both hemispheres. The viral vector was kindly provided by Prof. K. Deisseroth (Stanford University) through the UNC and UPENN vector cores.

Preparation of acute brain slices

Following 4-6 weeks of incubation isoflurane-anesthetized mice were decapitated, their brains were quickly removed and placed into ice-cold slicing medium containing (in mM): 93 NMDG, 93 HCl, 2.5 KCl, 1.2 $NaHPO_4$, 30 $NaHCO_3$, 25 Glucose, 20 HEPES, 5 Na-ascorbate, 3 Na-pyruvate, 2 Thiourea, 10 $MgSO_4$, 0.5 $CaCl_2$, 5 N-acetyl-L-Cysteine (osmolarity 310 ± 5; bubbled with 95% O_2 / 5% CO_2) (Ting et al., 2014). Next, 250-300 µm thick horizontal or coronal slices were cut using a Leica vibratome (VT1000S). For the recovery, brain slices were incubated for 5 min in slicing medium at 34 ± 1˚C and subsequently for ~40 min in aCSF (containing in mM: 124 NaCl, 2.5 KCl, 1.25 Na_2HPO_4, 2 $MgSO_4$, 2 $CaCl_2$, 26 $NaHCO_3$, and 20 D–glucose, osmolarity 310 ± 5; bubbled with 95% O_2 / 5% CO_2) at 34 ± 1˚C. After recovery brain slices were stored at room temperature (RT) before the experiments started. The accompanying hindbrain was post-fixed in 4% paraformaldehyde (PFA), for histological confirmation of the viral injection location (see below).

In vitro whole cell recordings

For all recordings, slices were bathed in 34 ± 1˚C ACSF (bubbled with 95% O_2 and 5% CO_2). Whole-cell patch-clamp recordings were performed using an EPC-9 or EPC-10

amplifier (HEKA Electronics, Lambrecht, Germany) for 20-60 min and digitized at 20 kHz. Resting membrane potential (V_{rest}) and input resistance (R_{in}) were recorded after whole-cell configuration was reached. Recordings were excluded if the series resistance (R_S) (assessed by -5 or -10 mV voltage steps following each test pulse) varied by >25% over the course of the experiment. Voltage and current clamp recordings were performed using borosilicate glass pipettes with a resistance of 3-5 MΩ when filled with K^+-based internal (in mM: 124 K-Gluconate, 9 KCl, 10 KOH, 4 NaCl, 10 HEPES, 28.5 Sucrose, 4 Na_2ATP, 0.4 Na_3GTP (pH 7.25-7.35; osmolarity ~290)). Recording pipettes were supplemented with 1 mg/ml biocytin to allow histological staining (see below). Current clamp recordings were corrected offline for the calculated liquid junction potential of -10.2 mV. All recordings were performed in the presence of picrotoxin (100 µM, Sigma-Aldrich) to block $GABA_A$-receptor-mediated IPSCs.

Full-field optogenetic stimulation (470 nm peak excitation) was generated using a Polygon4000 (Mightex, Toronto, Canada) or a pE2 (CoolLED, Andover, UK), that were controlled using TTL-pulses generated by the HEKA amplifier. Light intensities at 470 nm were recorded using a photometer (Newport 1830-C equipped with an 818-ST probe, Irvine, CA) at the level of the slice. Typically the light intensities sufficient to trigger the maximal response amplitude in thalamic cells ranged from 0.1 to 6.65 mW/mm^2. To trigger neurotransmitter release from transfected CN axons we delivered 1 ms light pulses at 0.1 Hz and an intensity resulting in the maximally evoked response, unless stated otherwise. To characterize the postsynaptic receptors we sequentially bath-applied AMPA- (10 µM NBQX), NMDA- (10 µM APV), mGluR1- (10 µM JNJ-16259685) and mGluR5- (50 µM MPEP) blockers. Each drug was added only after the EPSC amplitude stabilized. All drugs were purchased from Tocris (Bristol, UK). To ensure that we recorded action potential-driven neurotransmitter release most experiments were concluded by bath application of 10 µM tetrodotoxin (TTX), which blocked all post-synaptic responses in the recorded thalamic neurons. The responses evoked in thalamic neurons by optogenetic stimulation of CN axons were solely of monosynaptic origin, which matches the known absence of local interneurons and of local axon collaterals in the nuclei we studied (Jones, 2007).

Immunofluorescence

To visualize the recorded neurons and CN axons, slices were placed in 4% PFA (in 0.12 M PB) for at least 24 hrs (Marx et al., 2012). Subsequently, slices were transferred into 0.1 M PBS and rinsed with PBS 3 times for 10 min. Slices were incubated for 1 hr at RT in blocking solution (containing 10% normal horse serum (NHS) and 0.5% triton diluted in PBS), which was followed by over-night incubation with primary antibody for vesicular glutamate transporter type 2 (vGluT2) (anti Guinea Pig; Millipore Bioscience Research Reagent; 1:2000 diluted in PBS containing 2% NHS and 0.4% Triton). Slices were subse-

quently rinsed 3 times for 10 min and incubated for 2 hrs with Streptavidin-Cy3 (1:200, Jackson Immunoresearch) and anti Guinea Pig Cy5 (1:200, Jackson Immunoresearch) diluted in PBS containing 2% normal horse serum and 0.4% triton. Sections were rinsed in PBS, mounted with Vectashield (Vector laboratories) and imaged with a LSM 700 confocal microscope (Carl Zeiss Microscopy, LLC, USA).

For localization of the injection sites, the cerebellum was removed from forebrain and fixed with PFA 4% for 5 to 10 days on a shaker at 4°C. Serial 40 µm thick horizontal sections were obtained on a freezing microtome. The tissue was rinsed in PBS solution and then transferred in blocking solution for 1 hr at RT and subsequently incubated for 10 min with DAPI (300nM). Sections where rinsed with 0.01M PB and mounted on glass.

Fluorescence microscopy and reconstruction

Guided by calbindin D28-K staining (primary: Calbindin α-rabbit 1:7000, Swant Inc, #CB-38a; secondary: 405 nm rabbit-α-donkey 1:400, Jackson Immunoresearch #A421) and a reference atlas (Franklin and Paxinos, 2001) we outlined the thalamic nuclei of interest. For each nucleus the expression pattern of ChR2-YFP was quantified with RGB measure function of Fiji (ImageJ) in order to have the mean intensity among the region of interest (ROI).

Recorded neurons were labeled with biocytin. Epifluorescent tile images were obtained using a 20X/0.30 NA (air) objective and a LSM 700 microscope (Carl Zeiss). The position of labeled neurons was confirmed using a stereotactic atlas (Franklin and Paxinos, 2001). Terminals positive to VGluT2 staining were identified and morphologically studied using confocal images that were captured using the following excitation wavelengths: 488 nm (YFP), 555 nm (Cy3) and 639 nm (Cy5). Terminals were imaged using a 40X/1.30 NA (oil) objective by acquiring a stack of images with 0.5 digital zoom and a voxel size of 313 nm width x 313 nm length x 300 nm depth. Using custom-written Fiji-scripts (ImageJ) we identified putative synaptic contacts, i.e. YFP-positive varicosities that colocalized with vGluT2-staining that are within 1 µm distance from the recorded neurons. Once synaptic contacts were isolated high resolution image stacks were acquired using a 63X1.4 NA oil objective with 1X digital zoom, a pinhole of 1 Airy unit and significant oversampling for deconvolution (voxel dimension is: 46 nm width x 46 nm length x 130 nm depth calculated according to Nyquist factor; 8-bit per channel; image plane 2048 x 2048 pixels). Signal-to-noise ratio was improved by 2 times line averaging. Stack's subsets of the connection were deconvolved using Huygens software (Scientific Volume Imaging). Further analysis was performed using a custom-written Fiji macro. The color channels (YFP, Cy3 and Cy5) of the images were split to get separate stacks. The YFP and Cy3 channels were Gaussian blurred (sigma = 1) and selected by a manually set threshold. A binary open function

was done on both images (iterations = 4, count = 2) and objects were removed if their size was <400 pixels (YFP) or <120 pixels (Cy3). A small dilatation was done on the red image (iteration = 1, count = 1). With the image calculator an 'and-operation' was done using the binary red and green image. The values 255 (white) of the binary YFP image were set to 127. This image and the result of the AND-operation were combined by an OR-operation. The resulting image was measured with the 3D-object counter plugin for volumes and maximum intensities. Only objects containing pixels with an intensity of 255 (overlap) are taken in account for analysis. Estimation of synapse density (number of terminals/area μm^2) was obtained for each nucleus by dividing the number of terminals by the image area (DeKosky and Scheff, 1990). To quantify the distance from soma for vGluT2-positive CN terminals on reconstructed neurons we used a custom-written macro in Fiji software (ImageJ). Briefly, we calculated the distance in 3 dimensions (using x-, y-, z-coordinates) between the center of the terminal and the center of the soma by Pythagorean Theorem.

3D Sholl analysis

To determine the dentritic arborization of biocytin filled cells, we used the 3D Sholl analysis macro implemented in Fiji software (Ferreira et al., 2014). For preprocessing, image stacks over a z-volume of 18.5 - 87.5 µm were binarized. Stacks with excessive background signal were excluded from further analysis. Subsequently the dendritic arborization was measured in concentric shells of 10 µm distance starting with 15 µm distance from the center of the soma. At this first sphere we manually counted the number of primary dendrites and assessed their directionality by calculating the radial angle between the primary dendrites.

Electron microscopy

Four mice were injected with anterograde neuronal tract tracer biotinylated dextran–amine (10% BDA in 0.1 M PB, pH 7.4, molecular weight 10,000) by iontophoresis (pulses of 4 µA, 10 min) with a glass micropipette (tip opening, 8–10 µm) in the interpositus and lateral CN. After 5 days mice were anesthetized with an overdose of nembutal (i.p.) and transcardially perfused with 4% PFA and 1% glutaraldehyde in phosphate buffer. Brains were removed, kept overnight in 4% PFA, and cut into 60 µm thick coronal sections using a vibratome. Sections were subsequently washed in PBS, incubated for 20 min in 3% H_2O_2 (in PBS) to remove endogenous peroxidase activity of blood, washed again, placed for 1 hr in 10% NHS and finally incubated for 24 hrs in ABC-HRP (Vector). At the end of the immunostaining, the sections were stained with 0.5% 3,3-diaminobenzidine tetrahydrochloride (DAB) and 0.01% H_2O_2 for 15 min at RT. Ultimately, the sections were osmicated with 1% osmium in 8% glucose solution, dehydrated in propyleen oxide, and embedded in araldite (Durcupan, Fluka, Germany). Guided by staining levels in semithin

sections (0.5 µm thick), we made pyramids of the VL, VM and CL nuclei. Ultrathin sections (60 nm) were cut using an ultramicrotome (Leica, Germany), mounted on nickel grids, and counterstained with uranyl acetate and lead citrate. CN axon terminals were photographed at various magnifications (range 3900X-25500X) using an electron microscope (CM 100, Philips, Eindhoven, Netherlands) and analyzed off-line using standard measurement functions in Fiji (ImageJ). To limit the possibility that our electron micrographs contained various images of the same pre- and postsynaptic structures we separated our ultrathin sections by various semi-thin sections.

Data analysis and statistics

Current and potential traces were acquired using Pulse and Patchmaster software (HEKA) and stored for offline analysis. Single stimulus data was analyzed using Clampfit software (Molecular Devices), while trains of stimuli were analyzed with custom written routines in Igor Pro 6.1 (Wavemetrics, Lake Oswego, Oregon). To evaluate the variability of EPSC amplitude and charge transfer we calculated the coefficient of variation (CV): the ratio between standard deviation and mean. For trains of stimuli, the peak amplitude of each evoked postsynaptic current (EPSC) was detected relative to baseline. All EPSC amplitudes within the train were normalized to the first EPSC. The total charge during train stimulation was calculated by determining the area under the curve between the first and the last stimulus relative to baseline. For all recordings averages of at least 5 sweeps per cell were calculated. The steady state amplitude was calculated by averaging the amplitude of responses to the last 5 stimuli.

Using GraphPad PRISM and SPSS software packages we ran statistical comparisons between the thalamic nuclei (VL, VM and CL) by one-way ANOVA, Kruskal-Wallis (K-W) or Kolmogorov-Smirnov (K-S) tests as indicated in the main text. Statistical difference for pharmacology data was assessed using Friedman test. For Sholl analysis a two-way ANOVA was used with Mann Whitney multiple comparison test. We corrected missing values by the Last observation carried forward (LOCF) method. Correlation coefficients were calculated using Spearman. We defined $p<0.05$ as a significant difference. Throughout the main text we report a subset of the statistical data; all details are provided in the Supplemental data tables that accompany each figure. Summarized data are represented as mean ± standard error of the mean. Throughout the figures data from VL are indicated in green, VM in red and CL in blue, unless stated otherwise.

Table S1 – Statistical analysis of all data related to Figure 1

Panel	Test applied	P-value	Degrees of freedom	Population size	Definition of population	Correction
1B	Kruskal Wallis	*0.003* -VL-VM 0.529 -VM-CL 0.136 *-VL-CL 0.002*	2	18	6 mice	Dunn-Sidak
1I	Kolmogorov Smirnov	*VL-VM <0.001* VM-CL 0.966 *VL-CL <0.001*		671 terminals 245 terminals 572 terminals	5 mice	Bonferroni
1J	Kruskal Wallis	*0.028* VL-VM 0.334 VM-CL 0.865 *VL-CL 0.024*	2	15	5 mice	Dunn-Sidak

Table S2 – Statistical analysis of all data related to Figure 2

Panel	Test applied	P-value	Degrees of freedom	Population size	Definition of population	Correction
2B ***EPSC Amplitude***	Kruskal Wallis	*<0.001* *VL-VM 0.001* VM-CL 1 *VL-CL <0.001*	2	44 cells	40 mice	Dunn-Sidak
2B **EPSC Charge**	Kruskal Wallis	*<0.001* *VL-VM 0.002* VM-CL 1 *VL-CL 0.001*	2	47 cells	40 mice	Dunn-Sidak
2D **EPSC CV**	Kruskal Wallis	*0.001* *VL-VM 0.031* VM-CL 1 *VL-CL 0.001*	2	42 cells	40 mice	Dunn-Sidak
2D **Charge CV**	Kruskal Wallis	*0.001* *VL-VM 0.025* VM-CL 1 *VL-CL 0.03*	2	46 cells	40 mice	Dunn-Sidak

Table S3 – Statistical analysis of all data related to Figure 3

Panel 3H	Test applied	P-value	Degrees of freedom	Population size	Definition of population	Correction
VL	Kruskal Wallis	*0.002* 10-20 Hz 0.492 *10-50 Hz 0.001* 20-50 Hz 0.111	2	39 cells	29 mice	Dunn-Sidak
VM	Kruskal Wallis	0.496	2	22 cells	9 mice	
CL	Kruskal Wallis	*0.006* 10-20 Hz 0.234 *10-50 Hz 0.004* 20-50 Hz 0.230	2	16 cells	9 mice	Dunn-Sidak

Panel 3H	Test applied	P-value	Degrees of freedom	Population size	Definition of population	Correction
10 Hz	Kruskal Wallis	0.344	2	29 cells	18 mice	
20 Hz	Kruskal Wallis	0.168	2	27 cells	13 mice	
50 Hz	Kruskal Wallis	0.137	2	20 cells	16 mice	

Panel 3I	Test applied	P-value	Degrees of freedom	Population size	Definition of population	Correction
VL	Kruskal Wallis	*0.007* 10-20 Hz 0.464 *10-50 Hz 0.005* 20-50 Hz 0.529	2	29 cells	29 mice	Dunn-Sidak
VM	Kruskal Wallis	*0.037* 10-20 Hz 1 10-50 Hz 0.056 20-50 Hz 0.118	2	12 cells	9 mice	Dunn-Sidak
CL	Kruskal Wallis	0.077	2	12 cells	9 mice	

Panel 3I	Test applied	P-value	Degrees of freedom	Population size	Definition of population	Correction
10 Hz	Kruskal Wallis	0.167	2	20 cells	18 mice	
20 Hz	Kruskal Wallis	0.321	2	18 cells	13 mice	
50 Hz	Kruskal Wallis	0.867	2	15 cells	16 mice	

Table S4 – Statistical analysis of all data related to Figure 4

Panel 4B	Test applied	P-value	Degrees of freedom	Population size	Definition of population	Correction
Control *vs* NBQX	Friedman	0.500	3	10 cells	9 mice	*
NBQX *vs* NBQX+APV	Friedman	0.146	3	10 cells	9 mice	Dunn-Bonferroni
Control *vs* NBQX+APV	Friedman	*<0.001*	3	10 cells	9 mice	Dunn-Bonferroni
NBQX+APV *vs* NBQX-AP5-MPEP+JNJ	Friedman	1.000	3	10 cells	9 mice	Dunn-Bonferroni
NBQX *vs* NBQX+APV+ MPEP+JNJ	Friedman	*0.019*	3	10 cells	9 mice	Dunn-Bonferroni

* http://www-01.ibm.com/support/docview.wss?uid=swg21508972

Table S5 – Statistical analysis of all data related to Figure 5

Panel	Test applied	P-value	Degrees of freedom	Population size	Definition of population	Correction
5D *Intersection 55 µm*	2-way ANOVA	VL-VM 0.733 VM-CL 0.350 *VL-CL 0.018*		26 cells	26 mice	
5E	Kruskal Wallis	0.015	2	33 cells	26 mice	Dunn-Sidak
5F	Kruskal Wallis	0.141	2	164	26 mice	
5G	Kolmogorov-Smirnov	VL-VM 0.831 VM-CL 0.136 VL-CL 0.343		93 123 112	26 mice	Bonferroni

Table S6 – Statistical analysis of all data related to Figure 6

Panel	Test applied	P-value	Degrees of freedom	Population size	Definition of population	Correction
6B	Kruskal Wallis	0.373	2	34 cells	24 mice	Dunn-Sidak
6C	Kruskal Wallis	0.586	2	110 cells	24 mice	Dunn-Sidak
6E	Kruskal Wallis	*0.027* VL-VM 1.00 VM-CL 0.353 *VL-CL 0.023*	2	130 terminals	24 mice	Dunn-Sidak

6F	Kolmogorov Smirnov	VL-VM 0.834 VM-CL 0.080 *VL-CL 0.044*	93 terminals 59 terminals 108 terminals	24 mice	Bonferroni

Table S7 – Statistical analysis of all data related to Figure 7

Panel 7B	Test applied	P-value	Degrees of freedom	Population size	Definition of population	Correction
Terminal surface	Kruskal Wallis	0.099	2	97 terminals	4 mice	Dunn Sidak
Number of Mitochondria	Kruskal Wallis	0.468	2	83 terminals	4 mice	Dunn Sidak
Mitochondria Surface	Kruskal Wallis	*<0.001* *VL-VM 0.034* *VM-CL <0.001* *VL-CL <0.001*	2	315 mitochondria	4 mice	Dunn Sidak
PSD length	Kruskal Wallis	*0.012* *VL-VM 0.024* VM-CL 1.000 VL-CL 0.055	2	275 PSD	4 mice	Dunn Sidak
Number of Release sites	Kruskal Wallis	0.667	2	90 terminals	4 mice	Dunn Sidak
Dendritic diameter	Kruskal Wallis	0.080	2	97 dendrites	4 mice	Dunn Sidak
7C Protrusion surface vs terminal surface	Spearman	R=0.6146 *P*<0.001		44 protrusions	4 mice	
7C Protrusion surface vs terminal surface	Spearman	R=0.7156 *P*<0.001		82 mitochondria	4 mice	

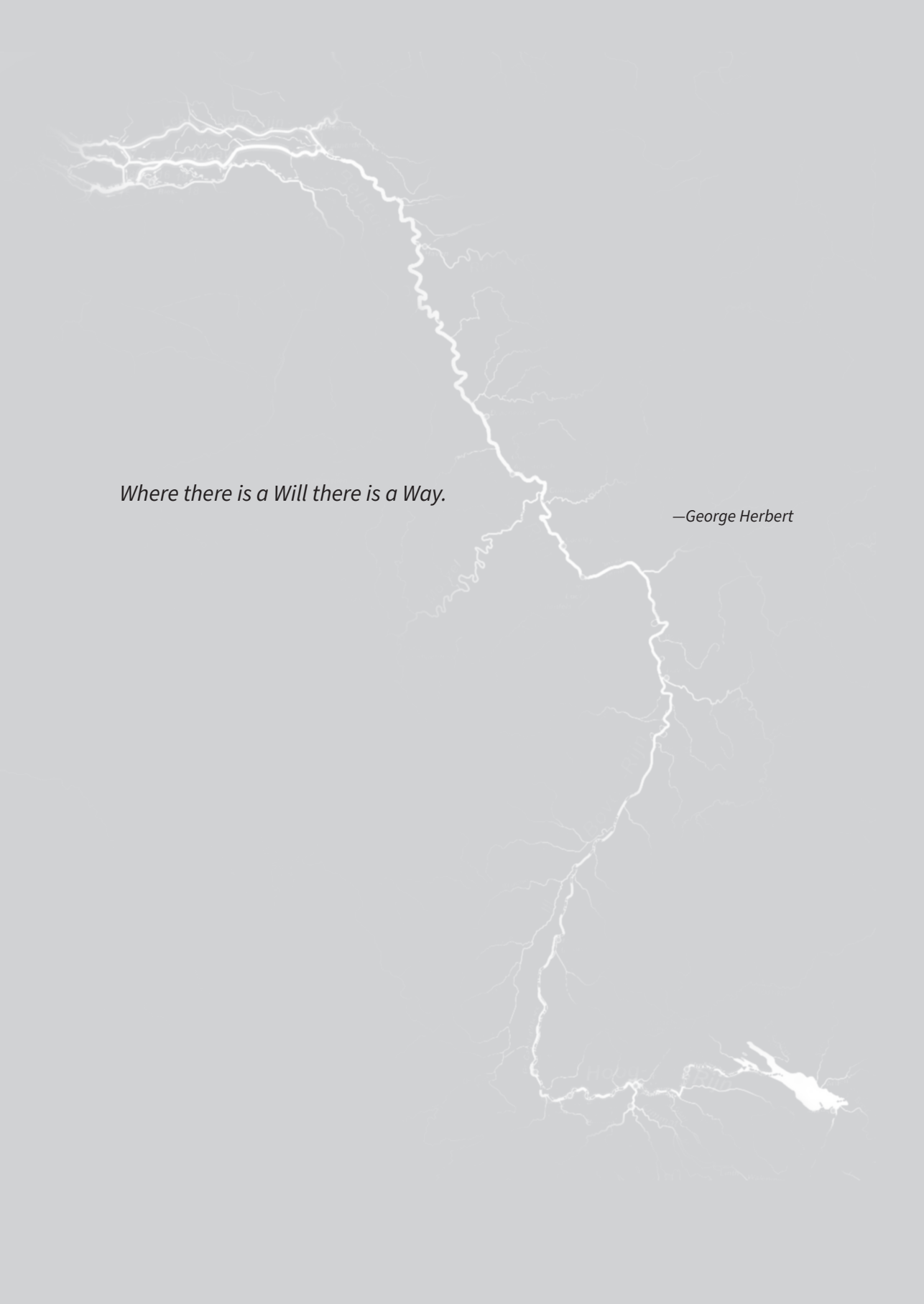

Where there is a Will there is a Way.

—George Herbert

Chapter 5

Temporal dynamics of the Cerebello-Cortical Convergence in Ventro-Lateral Motor Thalamus

Carmen B. Schäfer
Zhenyu Gao
Chris I. De Zeeuw
Freek E. Hoebeek

ABSTRACT

Orchestrating complex movements requires well-timed interaction of cerebellar, thalamic and cerebral structures, but the mechanisms underlying the integration of cerebro-cerebellar information in motor thalamus remain largely unknown. Here we investigated how excitatory inputs from cerebellar nuclei (CN) and primary motor cortex layer VI (M1-L6) neurons may regulate the activity of neurons in the mouse ventrolateral (VL) thalamus. Using dual-optical stimulation of the CN and M1-L6 axons and *in vitro* whole-cell recordings of the responses in VL neurons, we studied the individual responses as well as the effects of combined CN and M1-L6 stimulation. Whereas CN inputs evoked large-amplitude responses that were depressed upon repetitive stimulation, M1-L6 inputs elicited small-amplitude responses that were facilitated upon repetitive stimulation. Moreover, pauses in CN stimuli could directly impact VL spiking probability, an effect that was modulated by VL membrane potential. When CN and M1-L6 pathways were co-activated, motor cortical afferents increased the thalamic spike output in response to cerebellar stimulation, indicating that CN and M1 synergistically, yet differentially, control the membrane potential and spiking pattern of VL neurons.

INTRODUCTION

Successful movement requires an estimation of the sensory consequences of a motor plan and the integration of well-timed error signals into ongoing sensorimotor processing (Ramnani, 2006; Brooks *et al.*, 2015). This complex task requires the communication of multiple brain areas, such as the cerebellum, thalamus and motor cortex. The execution of acquired movements is mediated by cerebellar computation, in that genetic and functional lesions throughout various cortical and deeper cerebellar regions are known to disrupt execution of motor behavior (Gao *et al.*, 2018). Subsequently, the cerebellar output, embodied by projection neurons in the cerebellar nuclei (CN), is integrated in the ventrolateral nucleus (VL) of the thalamus with inhibitory input from reticular thalamus and cholinergic neuromodulatory input from mesencephalic nuclei and from there relayed to various layers of the motor cortex (Kha *et al.*, 2000; Teune *et al.*, 2000; Kuramoto *et al.*, 2009; Proville *et al.*, 2014; Svoboda & Li, 2017; Gornati *et al.*, 2018). In addition, VL neurons receive excitatory input from cortical layer 6 neurons of the primary motor cortex (M1 L6) (Yamawaki & Shepherd, 2015; Jeong *et al.*, 2016). The interaction of subcortical and cortical inputs has been shown to determine thalamic output in the proprioceptive and visual system (Groh *et al.*, 2008; Sherman & Guillery, 2011; Mease *et al.*, 2014; Bickford *et al.*, 2015). It is therefore of key importance to improve our understanding of cerebello-cortical integration at the level of the motor thalamus. Here we focused on how M1 L6 inputs modulate the responses in VL thalamus evoked by CN stimulation.

At rest, the baseline firing rates of CN range between 30 and 100 Hz (Hoebeek *et al.*, 2010; Sarnaik & Raman, 2018), while VL and cortical L6 neurons fire at low frequencies between 5 and 20 Hz (Lamarre *et al.*, 1971; Vitek *et al.*, 1994; Beloozerova *et al.*, 2003; Marlinski *et al.*, 2012; Olsen *et al.*, 2012; Proville *et al.*, 2014). Once movement execution starts, neurons in the interposed nuclei evolve into phasic patterns including high-frequency bursts of spiking (e.g., scratch movement in cats (Antziferova *et al.*, 1980), locomotion in cats (Armstrong & Edgley, 1984) and mice (Sarnaik & Raman, 2018). It has been shown that stimulation of the cerebellar cortical crus I lobule results in well-timed and rapid alterations in interposed CN activity patterns that precede an increase in spiking by VL thalamus neurons (Proville et al., 2014). These recent findings align with earlier published data about the thalamic and cortical responses evoked by cerebellar stimulation (Moruzzi, 1950; Sakata *et al.*, 1966; Bava *et al.*, 1967, 1986; Uno *et al.*, 1970; Sasaki *et al.*, 1972; Rispal-Padel *et al.*, 1973, 1987; Rispal-Padel & Latreille, 1974; Shinoda, 1985; Jörntell & Ekerot, 1999). However, it remains an open question how CN-VL synaptic transmission, which is subject to paired-pulse depression (Uno *et al.*, 1970; Sawyer *et al.*, 1994; Gornati *et al.*, 2018), and M1-L6-VL transmission interact in individual neurons

and corroborate the VL spiking patterns that are characterized by burst-pause and tonic spiking. In more detail, it is unclear how the pauses in the CN spiking, which are thought to decode the timing of specific sensory events (as reviewed by (De Zeeuw *et al.*, 2011), can affect VL spiking activity and how cortico-thalamic modulation of VL membrane potential affects these supposed responses.

In the current study we investigated the interplay between CN and M1-L6 inputs in VL neurons in an *in vitro* preparation, which allows us to pharmacologically and optogenetically manipulate the activities of these inputs. We recorded VL membrane potentials in whole cell patch clamp mode in combination with dual-optical stimulation techniques to selectively stimulate CN and M1-L6 axons. Our results show that pauses in CN spiking are a determinant of VL output and that M1-L6 inputs modulate the cerebellar induced spiking in VL neurons, together constructing a low-pass filter that can be fine-tuned in a timing-dependent manner.

RESULTS

To confirm that in our preparation CN and M1-L6 inputs converge on VL neurons that in turn project to the primary motor cortex, we injected adeno-associated virus (AAV) expressing constructs that fluorescently label presynaptic terminals: synaptophysin-mOrange into CN and a mix of AAV expressing synaptophysin-GFP and Cholera toxin-B (CTB, retrograde tracer) into M1. We found that synapses originating from CN and M1-L6 neurons indeed converged within close proximity on CTB labelled VL neurons, which innervate M1 (**Figure 1**, n = 3).

To identify the cell-physiological mechanisms that enable VL neurons to integrate CN with M1-L6 inputs we performed whole cell patch-clamp recordings in acutely prepared coronal slices in *Ntsr1-Cre* mice injected with AAV allowing the selective optical stimulation of CN axons (ChR2-EYFP) and/or M1-L6 axons (flex-ChrimsonR-TdTomato). We first evaluated the effect of optical CN stimulation on VL neurons in acute slices of Ntsr1-Cre mice in which CN neurons express ChR2-EYFP. For the 82 thalamic cells included in

the study the series resistance was 11.5±2.6 MΩ and the membrane resistance was 186.2±90.3 MΩ. Upon stimulation of ChR2-expressing CN fibers with a single 1 ms light pulse at 470 nm (**Figure 2A**), we recorded an EPSC of 1107±849 pA carrying a charge of 4745±3217 pA*ms with a CV of 0.08±0.04 (**Figure 2A-D**, n=35). The evoked current was independent of the incubation time, i.e. the time between the day of injection and the day of recording (linear regression: r^2=0.0045; n=28). Next, we stimulated the cerebellar

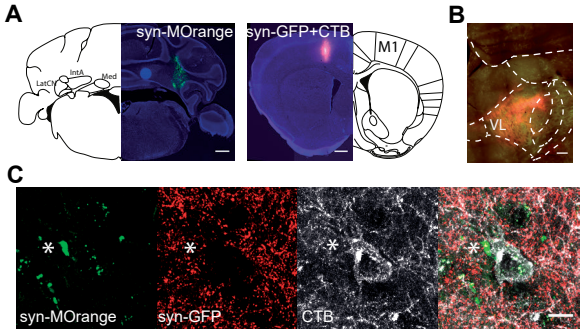

Figure 1. Morphological evaluation of the cerebello-thalamo-cortical connectivity. (**A**) Injection spots which represent synaptophysin-mOrange expression in cerebellar nuclei and co-labelling of synaptophysin-GFP and cholera toxin subunit B (CTB) in primary motor cortex (M1) (scale bar: 500 µm). Synaptophysin-mOrange is represented in green and synaptophysin-GFP in red. (**B**) The input from CN and M1 converges within the VL nucleus and overlaps with CTB labelling (scale bar: 500 µm). (**C**) Representative high-magnification image of a cerebellar synapse (asterix) and M1 synapses that converge on a CTB-labeled VL neuron (white), which in turn projects back into the same area of M1 (n = 3, scale bar: 10 µm). Abbreviations:, lateral cerebellar nuclei (LatCN), anterior interposed nucleus (IntA), medial cerebellar nucleus (Med), primary motor cortex (M1), ventrolateral thalamic nucleus (VL).

inputs with frequencies of 20, 35 and 50 Hz, which resulted in a decrease of EPSC amplitudes with paired pulse ratios of 67.3±10.9% (n=27), 59.3±16.8% (n=24) and 49.4±19.1% (n=35), respectively (**Figure 2F-H**, Friedman-test, 20 Hz vs. 50 Hz and 35 Hz vs 50 Hz *P*-values<0.001, **Table 1**) and steady state responses of 47.8±19.0% (n = 27), 37.4±14.4% (n=24) and 25.6±13.0% (n=35) (**Figure 2F-G, I**, Friedman-test, 20 Hz vs. 50 Hz and 35 Hz vs. 50 Hz; *P*-values<0.001, **Table 1**). To evaluate how the post-synaptic responses would recover from the depressed amplitude, we tested the impact of a pause length between the end of the stimulus train and the first subsequent CN stimulus. We tested pause lengths between 50 and 2000 ms. The recovery of the cerebellar EPSC amplitude evoked by 50 Hz stimulus train was best fit by a single exponential fit (**Figure 2J-K**, R-square: 0.38, Plateau: 81.9%, Tau: 524.4 ms, **Table 1**). We also tested whether the recovery from a pause of 100 ms was dependent on the stimulus train frequency. The CN-evoked response after 100 ms pauses were not significantly different between the recordings in which 20, 35 or 50 Hz stimulus trains were used (**Figure 2L,** 20 Hz: 49.2±13.5%, n=25; 35 Hz: 47.4±12.7%, n=21; 50 Hz: 47.7±12.6%, n=28; Friedman-test, *P*=0.324, **Table 1**).

In current clamp, VL neurons showed a resting membrane potential of -73.4±3.8 mV (n = 82, **Figure 2M, Table 1**). Upon optical CN stimulation 13 VL neurons responded with an initial burst of 2.24±2.16 action potentials, 9 VL neurons fired a single action potential or less and 4 did not fire an action potential in this setting (**Figure 2N-O**). Following the initial response the spiking probability reached a steady state value of 0.20±0.38 spikes per stimulus during the last 500 ms of the 20 Hz stimulus train and 0.15±0.32

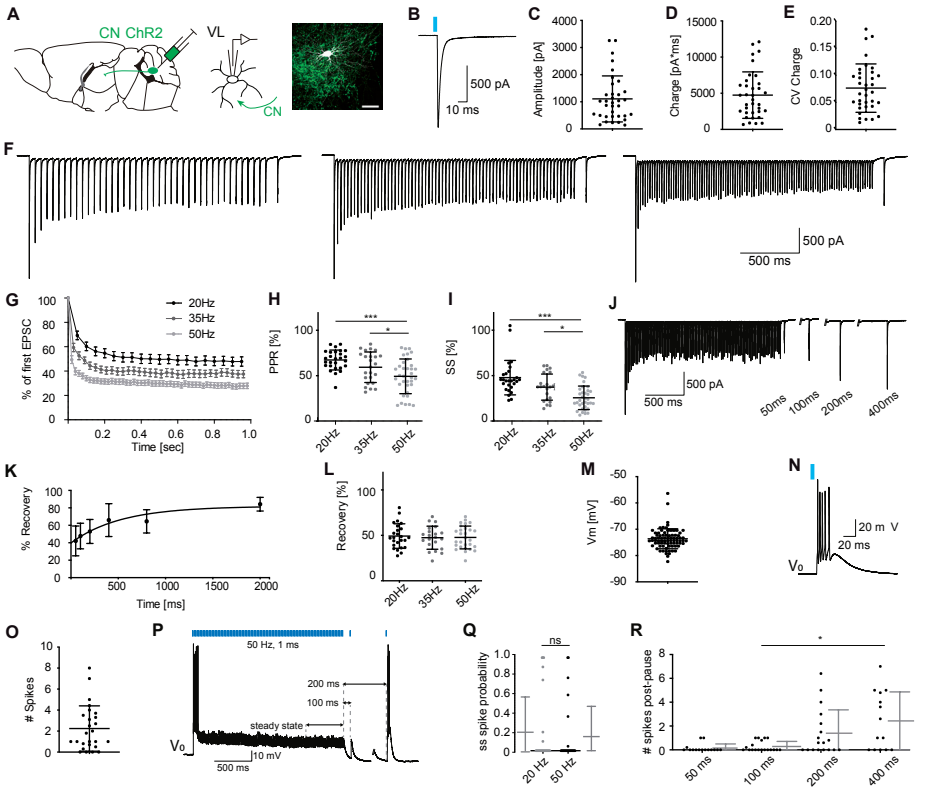

Figure 2. The effect of cerebellar stimulation on VL neurons. (**A**) Schematic representation of CN-VL connectivity and experimental design in a parasagittal schematic. Immunofluorescent illustration of a patch-clamped neuron embedded in ChR2-expressing CN fibers taken from a coronal section (green, scale bar: 50 µm). (**B**) Example trace illustrating the optogenetically evoked response (1 ms, 470 nm) in a VL neuron. (**C-E**) The amplitude (**C**), charge (**D**) and coefficient of variation of the charge (**E**, CV) for CN-evoked EPSCs. (**F**) Example traces depicting CN-evoked responses to 20, 35 and 50 Hz stimulus trains of 2 s followed subsequently by a single 100 ms pause and a single CN stimulus. (**G**) Normalized steady state (ss) depression evoked by 20, 35 and 50 Hz stimulus train of 1 s. (**H,I**) The paired pulse ratio (**H**, PPR) and ss current (**I**) evoked by train stimulation with 470 nm at 20, 35 and 50 Hz. The example trace (**J**) depicts the time-dependent recovery of the compound cerebellar event, which is quantified in (**K**). (**L**) The recovery of the CN-evoked response in VL neurons after 100 ms pause was independent of frequency. (**M**) The resting membrane potential (V_m) of VL neurons is quantified. The thalamic burst response after cerebellar stimulation and at resting potential (V_0) is shown in the example trace in (**N**) and quantified in (**O**). (**P**) Example trace of VL responses to 50 Hz stimulation followed by 100 or 200 ms pauses at V_0. (**Q**) Spike probability during the steady state (ss), i.e. the last 500 ms of the stimulus train, at 20 Hz and 50 Hz. (**R**) Number of spikes evoked by single pulse CN stimulus after the extended pause following the stimulus train. All error bars represent standard deviation (SD) except for panel (G), in which error bars represent standard error of the mean (SEM) for illustrative purposes. 'ns' indicates not significant and * P<0.05, ** P<0.01, *** P<0.005.

spikes per stimulus during the last 500 ms of the 50 Hz stimulus trains (**Figure 2P,Q**; P=0.0625, Wilcoxon-signed rank (WCR) test, n=25, **Table 1**). We investigated whether the spiking probability of VL neurons can be affected by implementing a pause after the CN stimulus train. We recorded the responses to a single CN stimulus after a pause of 50, 100, 200 or 400 ms and found that increasing the pause length increased the number of

action potentials (**Figure 2R**; 0.15±0.35, 0.28±0.42, 1.39±1.96 and 2.43±2.43 respectively; Friedman-test, 100 ms vs 400 ms: *P*=0.019, n=19 and n=14, respectively; **Table 1**). These data show that the spiking probability of VL neurons can be modulated by both the frequency during the CN stimulus train as well as by the duration of the pause between the end of train and the subsequent CN stimulus.

To decipher how fluctuations in membrane potential affect responses of VL neurons to CN stimulus trains, we injected depolarizing currents while stimulating ChR2 expressing CN fibers at 50 Hz (**Figure 3A**). With increasingly depolarized membrane potentials, the number of action potentials fired upon the first CN-stimulus decreased, but the spike probability following CN stimulation during the steady state increased (**Figure 3B-C**; number of action potentials upon 1st stimulus: 3.00±2.03 at -85 mV and 1.20±0.82 at -60 mV; steady state: 0.11±0.27 at -85 mV and 0.37±0.39 at -60 mV, Cochran-Armitrage test: *P*<0.0001 and 0.03267; n=22 and 20, respectively; **Table 2**). In a next step, we focus on thalamic cells in which cerebellar stimulation induces subthreshold spiking patterns and evaluate how 100 ms and 200 ms pauses as well as shifts in membrane potential affect the thalamic spike output. We found that pauses of 200 ms increase the thalamic spike output at resting and hyperpolarized potentials while depolarized potentials equalized that effect. In more detail at potentials of -70mV a pause of 200 ms significantly increased thalamic spiking when compared to responses during steady state (number of action potentials: 0.35±0.49 at steady state; 0.62±0.42 after 100 ms pause; 2.08±1.52 after 200 ms pause, 200 ms vs. steady state: p=0.0201, n=9, Friedman-test; **Figure 3D**, **Table 2**). We found a similar effects at -75 mV, in that a pause of 200 ms results in significantly increased number of spikes compared to responses during steady state and after 100 ms

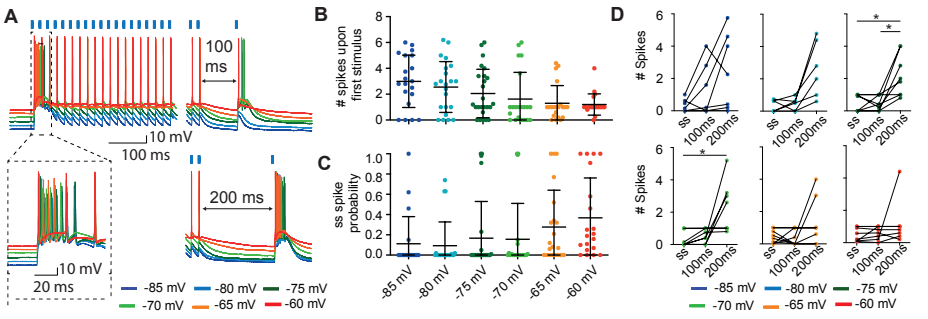

Figure 3. Fluctuations in membrane potential affect VL spike output after cerebellar stimulation. (**A**) Example showing VL responses to 50 Hz CN stimulus trains (1 ms 470 nm, in absence of ChrimsonR-expression) and a subsequent 100 or 200 ms pause followed by a single CN stimulus. The increasing membrane potential (indicated by different colors) reduces the number of action potentials fired upon the first CN-stimulus (**B**) and enhances the spike probability in the steady state (ss) (**C**). (**D**) Across membrane potentials, the average number of spikes increased after a pause of 100 and 200 ms compared to ss-values. All error bars represent SD. * *P*<0.05

pauses (number of action potentials: 0.49±0.52 at steady state, 0.50±0.0.44 after 100ms pause and 2.18±1.30 after 200 ms pause; steady state vs. 200 ms: *P*=0.0121, 100 ms vs. 200 ms: *P*=0.0179, n=8; Friedman-test, **Figure 3D**, **Table 2**). Both at more hyperpolarized (-80 mV and depolarized potentials (-65 mV and -60 mV) the effects of a pause in the 50 Hz CN stimulation train were not significant (all p-values > 0.456; Friedman-test, **Figure 3D**, **Table 2**).

In a next step, we tested the responses of VL neurons to optical stimulation of layer 6 pyramidal cells in the primary motor cortex (M1-L6). Hereto we infected M1-L6 neurons in *Ntsr1-Cre* mice with flex-ChrimsonR and to further investigate the short-term synaptic response patterns of M1-L6 and CN inputs, we applied train stimuli (**Figure 4A**). After one second of 10 or 20 Hz stimulation at 585 nm the M1-L6 EPSCs increased from 26.4±19.7 pA to 75.4±73.6 pA at 10 Hz and from 31.9±31.7 pA to 99.8±114.9 pA at 20 Hz (**Figure 4B-E**; WCR-test, *P*<0.0001 for 10 Hz (n=30) and 20 Hz (n=39); **Table 3**), corresponding to 258.8±118.8% and 242.8±138.4% of initial amplitudes, respectively. In a next step we evaluated the effect of M1-L6 on the depolarization of the thalamic membrane potential (**Figure 4F**). On average, optical stimulation of M1-L6 fibers with 585 nm pulses of 15 ms at 10 Hz resulted in a steady state depolarization of 3.3±1.6 mV (**Figure 4G-I**; range 0.5-5.5 mV), which shifted the average membrane potential from -72.8± 1.8mV to -69.1±3.1 mV (**Figure 4I**; WCR-test, *P*=0.0039, n=9; **Table 3**). Stimulation at 20 Hz induced

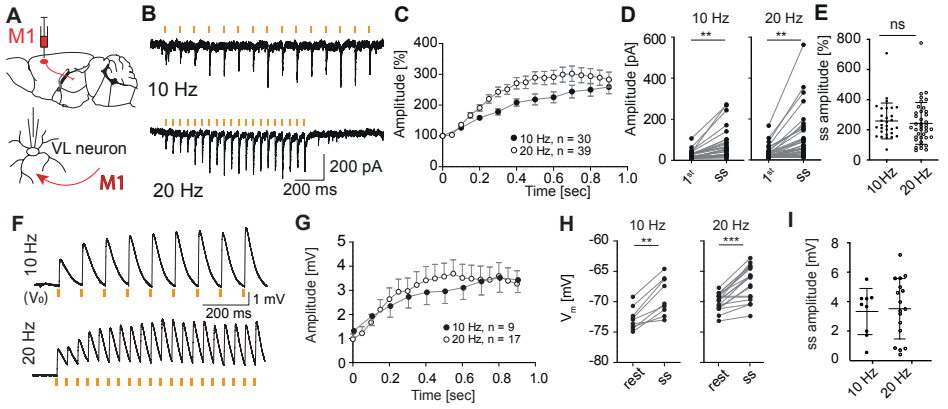

Figure 4. M1-L6 neurons modulate VL membrane potential. (**A**) Schematic representation of the optical stimulation approach by expressing ChrimsonR-tdTomato (Chrimson) in M1-L6 in *Ntsr1-Cre* transgenic mice. (**B-E**) Optical stimulation with 15 ms, 585 nm light pulses selectively activated M1-L6 fibers and result in an increased EPSC amplitude during the steady state (ss) of the stimulus trains of 10 and 20 Hz when compared to the first stimulus (1st). (**E**) The ss facilitation of M1-L6 inputs to VL neurons is not different between 10 and 20 Hz stimulus trains. As for B-E for current clamp recordings. (**F**) Example traces and (**G-H**) average membrane depolarizations evoked by 10 and 20 Hz M1-L6 stimulus trains (15 ms, 585 nm). V_0 indicates -73 mV for these example traces. ** indicates *P*<0.01 and *** indicates *P*<0.001. Error bars in (C) and (G) represent SEM for illustrative purposes and error bars in (E) and (I) represent SD.

a depolarization of 3.5±2.1 mV (**Figure 4G-I**; ranging from 0.4 mV to 7.2 mV), resulting in a membrane potential shift from -72.5±1.8 mV to -68.4±3.5 mV (WCR-test, *P*=0.0005, n=17; **Table 3**). To confirm the facilitating response pattern of layer 6 inputs from M1, we expressed AAV-DIO-ChR2 in *Ntsr1-Cre* mice. With this construct optical stimulation at 20 Hz also induced a facilitating post-synaptic responses in VL neurons, albeit with a stronger depolarizing effect (average steady state EPSP amplitude 10.9±5.3 mV; ranging from 6.4 mV to 16.7 mV; shift in membrane potential from -69.3±1.9 mV to -57.7±3.9 mV, n=3), confirming the modulatory role of L6 input on VL neurons.

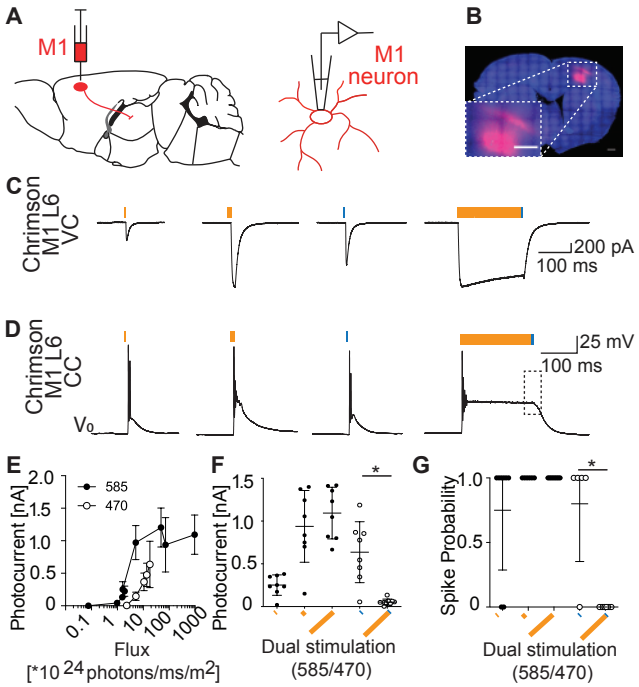

Figure 5. Photosensitivity of ChrimsonR expressing M1 L6 neurons. (**A**) Schematic illustration of ChrimsonR expression and patch-clamp recording from ChrimsonR expressing M1-L6 neurons. (**B**) Layer 6 specific expression of ChrimsonR-tdTomato in motor cortex of *Ntsr1-Cre* mice. (inset: high-magnification image of injection spot; scale bar 200 µm). (**C,D**) Representative recordings of the photo-response from ChrimsonR-tdTomato expressing M1-L6 neurons after stimulation with 1, 15 and 200 ms light at 585 nm and 1 ms at 470 nm, when recorded in voltage-clamp (VC) (**C**) and at resting potential (V_0) in current-clamp (CC) (**D**). To independently excite cerebellar synapses in thalamic slices (see Fig. 6 and 7), the M1-L6 neuron was desensitized to light at 470 nm by applying a 200 ms stimulation at 585nm, following which a 1 ms stimulus at 470 nm failed to evoke an action potential in M1-L6 neurons (square in right panel of **D**). V_0 indicates -71 mV for these example traces. (**E,F**) Pulses of 1, 15 and 200 ms at 585 and 1 ms at 470 nm with corresponding photonfluxes (**E**) resulted in photocurrents that maximized in response to 15 ms of 585 nm (**F**). The photocurrent in response to 1 ms stimulation at 470 nm is significantly decreased after 200 ms pre-stimulation at 585 nm (**F**). (**G**) These photocurrents induced AP firing after stimulation at 585 nm and 470 nm, but the dual-optotical stimulation paradigm prevents AP firing in M1-L6 neurons upon co-stimulation by 585 nm and 470 nm. * indicates *P*<0.05. Error bars represent SD.

Furthermore, we aimed to prove that in our preparation both CN and M1-L6 inputs converge onto single VL cells. Therefore we recorded VL responses following dual optical stimulation of AAV-ChR2-expressing CN fibers at 470 nm and AAV-flex-ChrimsonR-expressing M1-L6 fibers at 585 nm in *Ntsr1-Cre* mice (Klapoetke *et al.*, 2014; Hooks *et al.*, 2015). In this experimental setup, ChR2-expressing CN axons are solely excited by 470 nm light pulses, but ChrimsonR-expressing M1-L6 axons are sensitive to stimulation at 470 nm and 585 nm. To avoid potential cross-talk we used prolonged stimulation at 585 nm to desensitize ChrimsonR expressing motor cortical fibers to stimulation at 470 nm (Hooks *et al.*, 2015). To ensure exclusive stimulation of M1-L6 or CN fibers, we first evaluated photocurrents of ChrimsonR expressing M1-L6 neurons (**Figure 5A-D**). For our optical stimulation approach we used pulses of 1 ms at 470 nm and 1, 15 and 200 ms at 585 nm that corresponded to photonfluxes of $18.08*10^{24}$ photons/ms/m^2 for 1 ms at 470 nm and $4.8*10^{24}$ to 960*1024 photons/ms/m^2 for 1 to 200 ms at 585 nm, respectively (**Figure 5E**). We found that the photocurrents evoked by stimulation at 585 nm maximized at 15 ms (1 ms 585 nm: 251.5±119.0 pA, 15 ms 585 nm: 938.8±419.5 pA, 200 ms 585 nm: 1094.0±302.0 pA; n=8 for all groups; **Figure 5E,F**; **Table 4**). In these recordings, we found that 1 ms stimulation at 470 nm evoked 636.5±356.2 pA of current. We were able to confirm the efficacy of the desensitization protocol, in that after 200 ms pre-stimulation at 585 nm, the additional current evoked by 1 ms stimulation at 470 nm is significantly decreased to 52.5±35.0 pA (**Figure 5F**, Kruskal-Wallis test, $P<0.05$, n=8; **Table 4**). These maximal photocurrents induced action potential firing in ChrimsonR positive M1-L6 neurons (spiking probability at 1 ms 585 nm: 0.75±0.46, n=8; 15 ms 585 nm: 1.0±0.0, n=6; 200 ms 585 nm: 1.0±0.0, n=8; 1 ms 470 nm: 0.80±0.45, n=5), except when a 200 ms 585 nm pulse preceded the 1 ms 470 nm (0.0±0.0, n=8, Kruskall-Wallis test, $P<0.05$; **Table 4**). In addition, we desensitized the ChrimsonR-expressing M1-L6 neurons to 470 nm light by applying a pre-stimulation pulse for 200 ms at 585 nm, which saturates motor cortical photocurrents and prevents spike induction upon the subsequent 470 nm light pulse (**Figure 5F,G;** Hooks et al., 2015; Klapoetke et al., 2014). This dual-optical stimulation paradigm prevents action potential firing in M1-L6 neurons upon co-stimulation with light at 585 nm and 470 nm. As a final control, we assessed the kinetics of the ChrimsonR photocurrent to determine the maximal stimulation frequency we can apply to thalamic slices (**Figure 2**). Therefore, we measured the channel closing rate ('tau off') of ChrimsonR after 15 ms illumination at 585 nm, which at maximal stimulation intensity was 13.1±1.2 ms, indicating that 20 Hz photostimulation is feasible.

To ensure that the wavelengths of our optical stimulation allow the selective stimulation of ChR2-expressing CN axons by 470 nm but not by 585 nm, we set out to record photocurrent and spike probabilities in ChR2-expressing CN neurons evoked by these wavelengths (**Figure 6A-H**). Stimulation

pulses of 15 ms at 585 nm, 200 ms at 585 nm, 1 ms at 470 nm and the dual-optical stimulation paradigm (200 ms 585 nm followed by 1 ms 470 nm) induced a maximal photocurrent of 24.9±23.2 pA, 42.8±29.8 pA, 683.9±361.5 pA and 712.0±364.3 pA, respectively (n=7 for all groups; **Figure 6I; Table 5**). The decay ('tau off') of the ChR2 photocurrent was 8.5±2.5 ms for 1 ms at 470 nm and 8.6±2.5 ms for 1 ms light at 470 nm preceded by 200 ms at 585 nm (n=7 for all groups; **Figure 6J**; **Table 5**). As expected, the optical stimulation at 585 nm did not induce action potential firing (15 ms and 200 ms: 0±0 %),

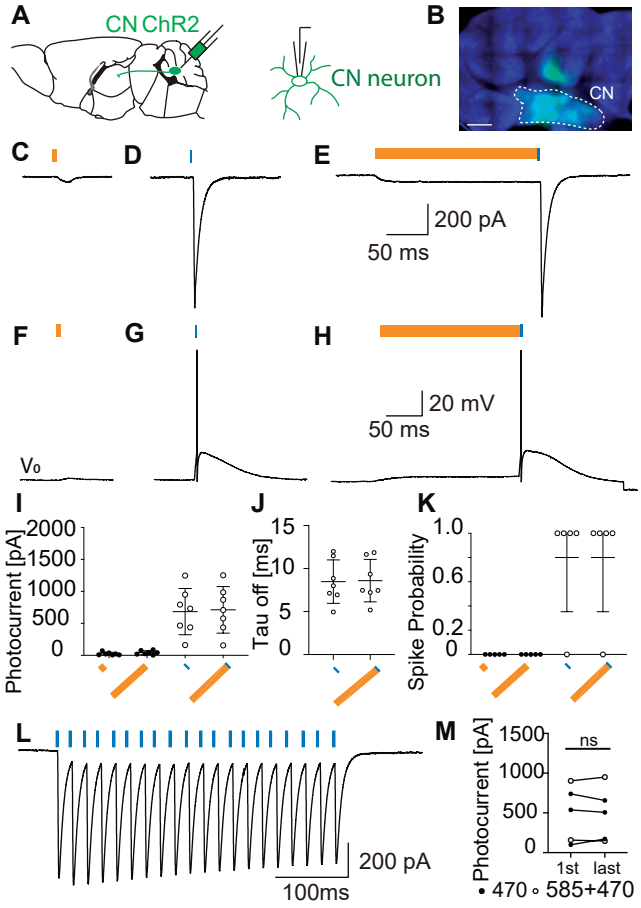

Figure 6. Photosensitivity of ChR2-expressing CN neurons. (**A**) Schematic illustration of injection strategy and patch-clamp recording from ChR2-expressing CN neurons. (**B**) ChR2 expression in CN (scale bars 500 µm) (**C-H**) Representative recordings of the photo-response from ChR2 expressing CN neurons after stimulation with 15 ms light at 585 nm (**C**), 1 ms light at 470 nm (**D**) and 200 ms light at 585 nm followed by 1 ms at 470 nm (**E**) when recorded in voltage-clamp (VC) (**C-E**) and at resting potential (V_0 = -70 mV) in current-clamp (**F-H**). Quantification of the photocurrent (**I**), the decay (tau off) of the photocurrent (**J**) as well as the induced spike probabilities (**K**). Representative recording of the photocurrent during stimulation with 50 Hz at 470 nm (**L**). The optical stimulation at 50 Hz reliably elicits inward currents, in that the peak current after first (1st) and last (last) stimulus in the train is stable (**M**). 'ns' indicates not significant. Error bars represent SD.

while stimulation with 1 ms at 470 nm as well as the dual stimulation paradigm (200 ms 585 nm and 1 ms 470 nm) induced spiking in 80±45% of the neurons (n=5 for all groups; **Figure 6K**; **Table 5**). To investigate whether the closing kinetics of ChR2 and their dark-state behavior at the intended stimulus duration of 1 ms allows reliable stimulation with 50 Hz, we compared the relative change in photocurrent during a 50 Hz stimulus train of 1 ms light pulses at 470 nm with and without co-stimulation at 585 nm (**Figure 6L-M**). We recorded no significant difference between the photocurrents at the beginning and end of the stimulus train (1st stimulus: 487.4±352.4 pA; last stimulus: 486.2±339.1 pA; **Figure 6M**; WCR-test, *P*>0.99, n=5; **Table 5**). These data show that stimulation at 585 nm does not induce spiking in CN neurons, while stimulation with short pulses of 1 ms at 470 nm induce strong photocurrents that do not depress at 50 Hz and reliably trigger action potentials.

We next applied our dual optical stimulation paradigm to independently activate ChrimsonR-expressing M1-L6 fibers and ChR2-expressing CN fibers in thalamic slices and evaluated the individual postsynaptic responses (**Figure 7A-E**). For M1-L6 stimulation we used a 20 Hz stimulus train of 15 ms pulses at 585 nm and found that the EPSC

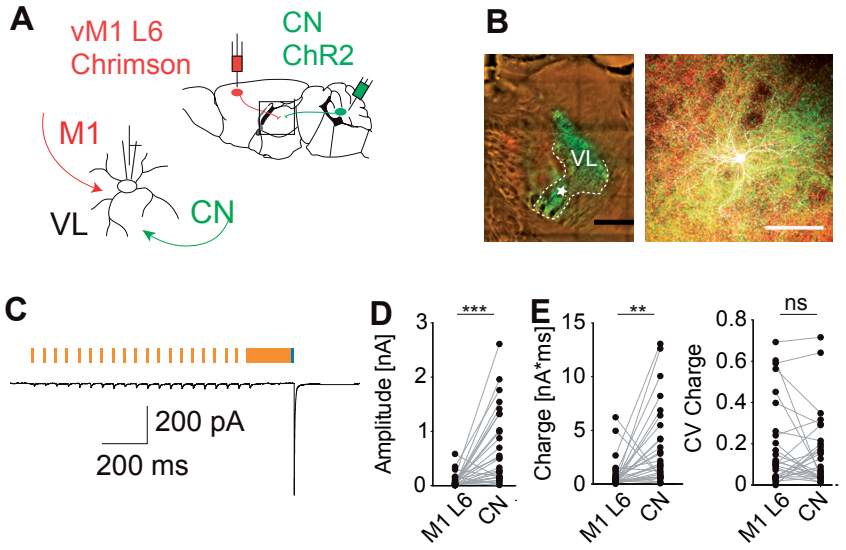

Figure 7. Physiological convergence of CN and M1 L6 in motor thalamus. (**A**) Schematic representation of the dual-optogenetic stimulation approach by expressing ChrimsonR-tdTomato (Chrimson) in M1-L6 and ChannelRhodopsin-EYFP (ChR2) in CN in *Ntsr1-Cre* transgenic mice. (**B**) Fluorescent images of Chrimson-positive M1-L6 fibers (red), ChR2-positive CN fibers (green) and a biocytin-filled VL neuron (white, scale bars: 100 µm). (**C**) Representative VL recording during 20 Hz M1-L6 stimulation (15 ms 585 nm, orange) and a single CN stimulus (200 ms 585 nm and 1 ms 470 nm, blue). The amplitude (**D**), charge and the coefficient of variation (CV) of the charge evoked by M1-L6 and CN stimuli (**E**). 'ns' indicates not significant, ** *P*<0.01 and *** *P*<0.001.

amplitudes increased from 18.6±21.3 pA to a steady state value of 89.7±130.0 pA. The subsequent single pulse stimulation of 1 ms at 470 nm of CN fibers (following a 200 ms pulse of 585 nm) evoked an EPSC of 688.4±691.8 pA, which contrasts with M1-L6 responses (WCR-test CN vs. M1-L6 facilitated, *P*<0.0001, n=28; **Figure 7C-E; Table 6**). As we activate the full population of CN and M1-L6 inputs synchronously, we analyzed the charge and and its CV to determine for variability of the multi-synaptic inputs. The total charge transferred was 888±1457 pA*ms for M1-L6 after the last 1 ms stimulus at 585 nm in the 1 second lasting train at 20 Hz and 3308±3746 pA*ms for the subsequent single pulse of 470 nm that selectively activated CN terminals (**Figure 7E**; WCR-test CN vs. M1-L6 facilitated, *P*<0.0012, n=28; **Table 6**). Despite this significant difference in total charge transferred, the variability was not different (CV M1-L6 charge: 0.19±0.21; CV CN charge: 0.16±0.18; **Figure 7E**; WCR-test, *P*=0.6406, n=28; **Table 6**).

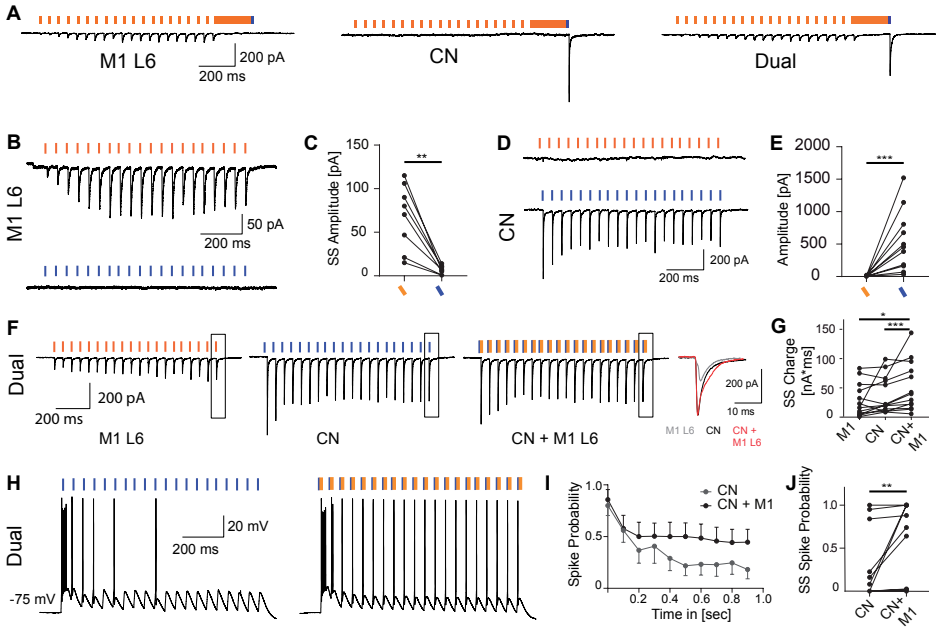

Figure 8 Motor cortical afferents modulate cerebellar induced spike transfer in the VL motor thalamus. (**A**) Example traces illustrating the connectivity pattern of VL cells that are innervated by M1 L6, CN or by both M1 L6 and CN (**B**) Example trace of a VL cell that is exclusively innervated by ChrimsonR-expressing M1-L6 fibers which are excited by 585 nm light, but not by 460 nm light (**C**). (**D**) Example trace of a VL cell that is exclusively innervated by ChR2-expressing CN fibers, which are excited by 460 nm light, but not by 585 nm light (**E**). (**F**) In VL cells that which are innervated by both ChrimsonR-expressing M1-L6 fibers and ChR2-expressing CN fibers, 585 nm light pulses evoked EPSCs with increasing amplitude and 460 nm light pulses evoked EPSCs with decreasing amplitude. The inset illustrates the accumulation of both currents in the charge of the compound responses. The total charge during the last 500 ms of the stimulus train is quantified in (**G**). (**H**) Example traces illustrating that co-stimulation of motor cortical afferents can shift the cerebellar induced spike output of VL cells. The spike probability is quantified in the average spike probability per stimulus (**I**) as well as in the average steady state (ss) spike probability per cell and stimulus condition in (**J**). Error bars in (I) represent SEM for illustrative purposes

In order to investigate the convergence of postsynaptic responses evoked CN and M1-L6 inputs in more detail, we adapted our optical stimulation paradigm to allow co-stimulation of CN and M1-L6 inputs. Therefore we use the initial dual optical stimulation paradigm do identify thalamic cells that are exclusively innervated by motor cortical or cerebellar fibers as well as thalamic cells that receive both inputs (**Figure 8A**). In a next step we want to further limit the responsiveness of Chrimson-expressing motor cortical fibers to blue stimulation by limiting the light pulses to wavelengths upto 460 nm and minimizing the corresponding light intensity. Next, we use excitation with 20 Hz stimulus trains with 1 ms pulses of light at 460 nm as well as 15 ms pulses at 585 nm to show that motor cortical fibers are exclusively activated after stimulation at 585 nm. During the last 500 ms of the stimulus train, 20 Hz stimuli at 585 nm evoked significantly more current than at 460 nm, with the latter evoking practically no current (**Figure 8B,C;** 20 Hz 585 nm: 68.0±37.3 pA, 20 Hz 460 nm: 6.8±4.7 pA, n=8, WCR-test, *P*=0.0078, **Table 7**). The same amplitude difference was found for CN stimulation, in that at 460 nm 1 ms pulses evoked a significantly bigger response than 15 ms pulses at 585 nm, with the latter stimulus evoking practically no response (**Figure 8D,E;** 20 Hz 585 nm: 6.6±5.7 pA, 20 Hz 460 nm: 539.1±468.4 pA, n=11, WCR-test, *P*=0.0010, **Table 7**). We identified VL neurons of which both CN and M1-L6 inputs responded to optical stimulation, i.e. neurons that showed a facilitating response to 585 nm train stimulation and a depressing response to 460 nm train stimulation. In these dually connected neurons we set out to pair the 460 nm and 585 nm stimuli (**Figure 8F**). We find that the postsynaptic currents induced by co-stimulating motor cortical and cerebellar afferents result in a summation of the motor cortical and the cerebellar inputs at the soma. To quantify the summation of both compound responses, we quantify the accumulation of the total charge during the steady state of the stimulation (**Figure 8G;** M1 L6: 28.6±27.9 nA*ms, CN: 37.9±31.5 nA*ms, CN plus M1-L6: 52.3±42.1 nA*ms, n=13, Friedman-test, *P*=0.0004, **Table 7**). When motor cortical fibers were co-activated with cerebellar stimulation, the steady state spike probability after pulses with 20 Hz was increased to 0.45±0.47 spikes when compared to 0.23±0.39 spikes (**Figure 8I-J**, n=14, WCR-test, P=0.0078, **Table 7**) after activating cerebellar fibers exclusively. These data indicate that indeed the co-activation of M1-L6 modulates the spiking probability of VL neurons in response to CN stimulus trains.

DISCUSSION

Here we show that cortical projections from M1-L6 evoke facilitating postsynaptic responses in VL neurons that modulate the membrane potential at the subthreshold level, whereas the cerebellar inputs from CN elicit responses sufficient to induce thalamic spiking. Our *in vitro* data reveal that attenuated responses to cerebellar stimulation in

VL thalamic neurons are restored after a brief pause in the stimulus train. The modulation of the membrane potential of VL neurons by M1-L6 in effect also controls the VL spiking, in that their probability to fire following repetitive CN stimulation was higher at depolarized levels. Accordingly, an increase in membrane potential depolarization dampened the differences between initial and steady state responses of VL neurons when CN input was paused for 100 to 200 ms. This synergistic modulation of both inputs enables the motor thalamus to operate as a low-pass filter, in which a response to the high-frequency cerebellar input can be adapted based on motor cortical feedback.

In the thalamus the transfer of subcortical inputs to the motor cortex is dictated by the state of the thalamic membrane potential (Jahnsen & Llinas, 1984*a*; Mccormick & Bal, 1997; Mease *et al.*, 2014). Our findings show that repetitive stimulation of M1-L6 fibers induces short-term facilitation of postsynaptic responses in VL, which allows these modulatory inputs to depolarize the thalamic membrane potential, albeit below the threshold for action potential initiation. A previous report on synaptic connectivity between M1-L6 and VL reported the responses to single pulse stimulation to be remarkably weak or absent compared to the impact of M1-L6 neurons on other thalamic nuclei (Yamawaki & Shepherd, 2015). Still, the repetitive stimulation paradigm in the current study revealed facilitating response patterns irrespective of whether the ChR2 or ChrimsonR construct was expressed.

The output of layer 6 neurons of the motor cortex probably affect the membrane potential of thalamic VL neurons by activating their t-type calcium channels. Their activation in turn allows the thalamic cells to fire the characteristic low threshold calcium spike (LTS) and the burst of action potentials (Jahnsen and Llinas, 1984a, 1984b) that we typically found in response to CN stimulation (**Figure 3F**). The degree of t-type channel de-inactivation is time- and voltage-dependent and determines the number of spikes transferred within a burst (Jahnsen & Llinas, 1984*a*) and thereby the timing of thalamic spiking (Wolfart *et al.*, 2005; Mease *et al.*, 2014, 2017). In our data we found that the membrane potential level, which we modulated using somatic current injections or by selective activation of M1-L6 axons, indeed modulated the number of action potentials that a single CN stimulus evoked in VL neurons, which is in accordance with the previous findings from the visual thalamo-cortical system (McCormick and Von Krosigk, 1992).

In addition to the responses to single CN stimuli, we also investigated the responses of VL neurons to high-frequency CN stimulus trains. In various *in vitro* and *in vivo* experimental settings it has been shown that CN neurons can fire continuously up to 100 Hz or higher (Antziferova et al. 1980; Armstrong and Edgley 1984; Raman et al. 2000; Hoebeek et al. 2010; Ohmae et al. 2013; Ten Brinke et al., 2017). Our dual-optogenetic

patch-clamp approach limited us to realistically model CN input, because it only permitted us to synchronously activate the full population of cerebellar fibers at a maximum of 50 Hz (Klapoetke *et al.*, 2014). Despite these limitations, we were able to investigate how the CN-evoked responses in VL neurons altered after brief pauses in the stimulus train. We found that the responses rapidly recovered from the paired-pulse depression and increased the number of action potentials evoked by CN stimuli. These data suggest that spike coding of thalamic neurons that project to motor cortex depends on the recovery of synaptic depression and de-inactivation of t-type calcium channels during a pause in high-frequency CN spiking. Our findings in the motor system are in line with previous reports on the impact of conjunctive activation of subcortical and cortical driver inputs in sensory and visual thalamus (Hoogland *et al.*, 1991; Groh *et al.*, 2008, 2013; Bickford *et al.*, 2015).

The low-pass filter function within VL suggests that the paired-pulse depression characteristic of the cerebello-thalamic synapses transforms high-frequency cerebellar spiking patterns into a low-frequency thalamic spiking pattern that, upon pauses in cerebellar spiking, which release the synapses from paired-pulse depression, shows a peak in spiking probability. In addition, our costimulation experiments, in which we combined M1-L6 with CN optical stimulation, revealed that synaptic transmission from M1-L6 pyramidal cells onto VL neurons modulates the impact of the synaptic transmission from CN neurons and can increase the spiking probability evoked by individual CN stimuli during a stimulus train, reverting the effect of CN-VL paired-pulse depression (**Figure 8J**). Thereby our results indicate that the gain of the low-pass filter can be modulated by M1-L6 input. Future studies need to address the modulation of VL output by CN and M1-L6 inputs during movement execution and behavior. One aspect that will be of relevance, is to investigate the potential role of feedforward inhibition: in the *in-vivo* situation M1-L6 neurons mono-synaptically innervate excitatory neurons in VL as well as inhibitory neurons in the reticular thalamic nucleus (RTN), which in turn provide feed-forward inhibition to thalamo-cortical relay neurons (Yamawaki & Shepherd, 2015; Halassa & Acsády, 2016). The depressing short-term release dynamics of RTN synapses in the thalamus shift the balance between excitation and inhibition induced by M1-L6 towards depolarized membrane potentials (Mease *et al.*, 2014; Crandall *et al.*, 2015). In our current study we blocked inhibitory inputs from RTN to exclusively study the interaction of cerebellum and the feedback from motor cortex. Our data show that the depolarizing shift in membrane potential after M1-L6 activation increases the spiking probability evoked by cerebellar stimulation, i.e. M1-L6 input modulates the gain of cerebello-thalamic transmission. Recent evidence indicates that the synchronicity of M1-L6 inputs to thalamic neurons is important to determine the gain of spike transfer from VL to motor cortex (Wolfart *et al.*, 2005; Mease *et al.*, 2014). The combination of

cerebellar spike timing, response amplitude in VL neurons as well as their membrane potential can modulate the spike transfer to motor cortex along a continuum, as it has previously been shown for the sensory thalamo-cortical processing (Whitmire et al. 2016).

MATERIAL AND METHODS

Ethical Approval

All experiments were performed in accordance with the European Communities Council Directive. All animal protocols were approved by the Dutch national experimental animal committee (DEC). For all experiments $Tg^{(Ntsr1\text{-}cre)GN220Gsat}$ (*Ntsr1-Cre*) transgenic mice were used, which in combination with Cre-dependent AAV constructs allows expression in L6 neurons (Gong *et al.*, 2007) as well as glutamatergic, thalamus-projecting CN neurons (Houck & Person, 2015; Dumas *et al.*, 2019). The colony was originally purchased from the MMRRC repository and maintained by backcrossing with $C57Bl/6^{OlaHsd}$ mice. The genotype was tested by PCR reaction using toe-tissue gathered at postnatal (P) 7-10. For physiology experiments *Ntsr1-Cre* mice were injected with AAV-particles (see below) at P21 and for anatomical experiments at P60-P120. All animals had *ad libitum* access to food and water and the absolute number of animals used for this study was 66. In the end of the experiment, the mice were anaesthetized with isoflurane and decapitated.

Surgical Procedures and Viral Vectors

For surgery mice were anaesthetized with isoflurane (5% in 0.5 L/min O_2 during the induction and 1.5% in 0.5 L/min O_2 for maintainance). During the surgery the body temperature was maintained at 37°C and the depth of the anaesthesia was controled by monitoring the breathing frequency of the mouse. Following the systemic application of buprenorphine (i.p. injection; 50 µg/kg bodyweight) local application of lidocain (10%) on the dorsal skin of the head, a skin incision of ~2 cm was made to expose dorsal skull bones and sagittal suture. Craniotomies of 0.5-2 mm were established above the planned injection sites. For injections to M1, 200 nl of adeno-associated virus (AAV) was injected to each of the following stereotaxic coordinates relative to bregma and midline (x, y; in mm): (1) 1.5, 1; (2) 1.5, 1.25; (3) 1.5, 1.5 at -0.9 depth from the dura. For injections to the CN, 200 nL of AAV was injected 2 mm posterior to lambda, 2 mm lateral to the midline at a depth of -2 mm from the dura and on the contralateral side to M1 injections. For optical stimulation experiments, AAV2.9-hSyn-FLEX-ChrimsonR-tdTomato (provided by Prof. Bryan Roth through the UNC vector core) and AAV2.9-Ef1a-FLEX-ChR2(H134R)-EYFP were injected to M1 and AAV2.9-hsyn-ChR2(H134R)-EYFP was injected to CN (provided by Prof. K. Deisseroth through the UNC vector core). Infected neurons express

Channelrhodopsin2 (ChR2) or ChrimsonR molecules in their cell membrane, which form cation-permeable ion-channels that are activated by 470 nm light or 470-585 nm light, respectively (Klapoetke *et al.*, 2014). ChR2 molecules also contain enhanced yellow-fluorescent protein (EYFP) and ChrimsonR molecules the red-fluorescent marker tdTomato. For all optical stimulation experiments, we injected the motor cortex that is ipsilateral to the recorded VL thalamus and the contralateral CN. Mice that showed ChR2 expression in vestibular nuclei neurons were excluded from analysis. For anterograde tracing of CN and M1-L6 axons and identification of their terminals we injected 200 nl of AAV constructs (chimeric serotype 1 and 2) carrying CAG_Synaptophysin_eGFP or CAG_Synaptophysin_mOrange (kindly provided by Prof. T. Kuner, Heidelberg University), respectively. For retrograde tracing of VL axons projecting to M1 we injected 1% Cholera toxin subunit B (CTB).

Preparation of Acute Slices

Following 3-6 weeks of incubation time after the viral injection isoflurane-anesthetized mice were decapitated, their brains were quickly removed and placed into ice-cold slicing medium containing (in mM): 93 NMDG, 93 HCl, 2.5 KCl, 1.2 $NaHPO_4$, 30 $NaHCO_3$, 25 Glucose, 20 HEPES, 5 Na-ascorbate, 3 Na-pyruvate, 2 Thiourea, 10 $MgSO_4$, 0.5 $CaCl_2$, 5 N-acetyl-L-Cysteine (osmolarity 310±5; bubbled with 95% O_2 / 5% CO_2). Next, 250 µm thick coronal slices including the motor cortex (Figure 3), cerebellum (Figure 6) or thalamus (all other Figures) were cut using a vibratome (VT1000S; Leica Biosystems, Nussloch, Germany). For the recovery, brain slices were incubated for 5 min in slicing medium at 34±1˚C and subsequently for ~40 min in artifical cerebrospinal fluid (ACSF; containing in mM: 124 NaCl, 2.5 KCl, 1.25 Na_2HPO_4, 2 $MgSO_4$, 2 $CaCl_2$, 26 $NaHCO_3$, and 20 D–glucose, osmolarity 310±5; bubbled with 95% O_2 / 5% CO_2) at 34±1˚C. After recovery brain slices were stored at room temperature for >30 min before the experiments started to extend the longivity of the recordings. For confirmation of the injection spots, motor cortices and hindbrain were conserved in 4% paraformaldehyde (PFA).

Electrophysiology and Photostimulation

For all recordings, slices were bathed in 34±1˚C ACSF (bubbled with 95% O_2 / 5% CO_2) and supplemented with 100 µM picrotoxin to block for GABAergic inputs, e.g., evoked by neuronal activity in the adjacent reticular nucleus, which was present in the thalamic slices. Whole-cell patch-clamp recordings were performed using an EPC-10 amplifier (HEKA Electronics, Lambrecht, Germany) for 20-60 min and digitized at 50 kHz. We recorded upto 3 cells per slice. Recordings were excluded if series or input resistances (RS and RI, respectively) varied by >25% over the course of the experiment or if RS exceeded a maximum of 25 MΩ. Voltage and current clamp recordings were performed using borosilicate glass pipettes with a resistance of 3-6 MΩ when filled with K^+-based internal

(in mM: 124 K-Gluconate, 9 KCl, 10 KOH, 4 NaCl, 10 HEPES, 28.5 Sucrose, 4 Na_2ATP, 0.4 Na_3GTP (pH 7.25-7.35; osmolarity 295 ± 5)). All recording pipettes were supplemented with 1 mg/mL Biocytin (Sigma-Aldrich, St. Louis, USA) to allow histological staining (see below). When necessary internal solution was supplemented with QX-314 (10 mM, Sigma-Aldrich, St. Louis, USA), a blocker of voltage-gated Na^+-channels, to prevent escape spikes in response to photocurrents in M1 and CN neurons. Current clamp recordings were corrected offline for the calculated liquid junction potential of -10.3 mV.

Dual-optical stimulation was induced using a pE-2 (CoolLED, Andover, UK) with LED wavelengths at 470 nm and 585 nm in combination with a dichroic mirror at 580 nm (filterset 15 without excitation filter, Carl Zeiss, Jena, Germany) and a 40X objective (Carl Zeiss). Light intensities were recorded by collecting photons across an area of 1 cm^2 (PM400 Optical Power Meter, Thorlabs, Newton, USA) and the power was back calculated to the area of the focal spot to determine stimulation intensities. The photon flux was calculated by converting the irradiance via the following formula:

$$N = E * \left(\frac{\lambda * 10^{-9}}{h * c}\right)$$

in which N is the number of photons, E is the irradiation in [W/m^2], λ is the wavelength in [nm], h is the Max-Planck constant and c is the speed of light. Full-field dual-optical stimulation with 585 nm was applied for 15 ms with an intensity of 1.66 mW/mm^2 and a photonflux of ~$4.8*10^{24}$ photons/ms/m^2, while stimulations at 470 nm were applied for 1ms with intensities ranging from 0.99–7.65 mW/mm^2 (maximally ~$18.08*10^{24}$ photons/ms/m^2). The photostimulation resulted in maximally inducible response amplitudes from CN and M1-L6 fibers. For the further refinement of this optical stimulation approach we restricted blue light to wavelengths above 460 nm (ET445/30x, Chroma Technology, Vermont, USA) and maximal intensities of 1.3 mW/mm^2. To ensure that we recorded action potential driven neurotransmitter release a portion of the CN and M1-L6 stimulation experiments were concluded by bath application of 10 µM tetrodotoxin (TTX, Tocris, Bristol, UK), an antagonist of voltage-gated sodium channels, which completely blocked the post-synaptic responses (data not shown).

Histology

For the histological reconstruction of the patched neurons, the brain slices were placed in 4% paraformaldehyde (PFA; in 0.1 M PB and pH 7.3) for 3-5 days. After rinsing the slices with 0.1 PB, they were placed in 10 mM Na-citrate at 80°C for 3 h and afterwards blocked for 2 h at RT (10% normal horse serum (NHS) and 0.5% Triton-X100 in PBS).

Biocytin-filled neurons were visualized by overnight incubation with Streptavidin-Cy5 conjugated antibody (1:400, Jackson Immunoresearch).

Image Acquisition and Analysis

Widefield images and confocal images were acquired on a LSM 700 microscope (Carl Zeiss) by using a 20X/0.30 NA and 63X/1.4NA objective, respectively. For the morphological reconstruction of the Synaptophysin-mOrange and Synaptophysin-GFP labeld synapses we used excitation wavelengts at 555 and 488 nm, respectively. For the morphological reconstruction of ChR2-expressing fibers, ChrimsonR-expressing fibers and biocytine-filled, Cy5-labelled cells we used excitation wavelength 488 nm, 555 nm and 639 nm, respectively.

Quantification and Statistical Analysis

All recording paradigms (i.e. sweeps) were repeated 3-10 times and averaged for further analyses. Data analysis was performed using Clampfit software (HEKA Electronics) or custom written routines in IGOR Pro 6.21 (Wavemetrics, Lake Oswego, Oregon, USA). For trains of stimuli, the peak amplitude of each evoked postsynaptic current/potential (EPSC/EPSP) was detected relative to baseline. To normalize the EPSC amplitudes within the train, the amplitude of each EPSC was divided by the amplitude of the first EPSC. During train stimulation the current and voltage responses reached a plateau phase, which we defined as the 'steady state' response period. For calculating the average current amplitude as well as the average postsynaptic membrane depolarization, we calculated the responses during the last 100 ms of the train. To determine the average spike probability during the steady state of the train, we averaged the responses across the last 500 ms of the stimulus train. In figures 2 and 4 we used a 2 sec-long stimulus train, while we used a 1 sec-long train in all other figures. To limit the impact of cerebellar response variability on the spike output, we excluded recordings in which the charge transferred from CN terminals was highly variable. We calculated the variability of the charge by the coefficient of variation (CV; the ratio of the standard deviation to the mean). VL recordings in which the CV of the CN-evoked charge exceeded 0.2 were excluded from the analysis (n=2). All data were tested for normal distribution with the Kolmogorov-Smirnov test. For statistical comparisons Mann-Whitney-test, Wilcoxon matched-pairs signed rank test or Friedman-test with correction for missing values by pairwise exclusion were applied. For trend analysis the Cochran Armitrage test was applied. For statistical analyses GraphPad PRISM, SPSS and R software packages were used. In all datasets the N represents the number of neurons recoded from. All datasets were corrected for multiple comparisons.

Data and Software availability

Data and software codes will be made available upon consent of the lead author (f.e.hoebeek@umcutrecht.nl).

AUTHOR CONTRIBUTION

C.B.S. performed all experimental work and analysis. C.B.S. and F.E.H. designed the experiments. F.E.H. and Z.G. provided technical support. F.E.H., Z.G. and C.I.D.Z. provided financial support. C.B.S. and F.E.H. wrote the original draft, Z.G. and C.I.D.Z. edited the manuscript. F.E.H. conceived and guided the project.

CONFICT OF INTEREST

The authors declare no conflicts of interest.

FUNDING

C.B.S. and F.E.H. are supported by the Dutch organization for life sciences (NWO-ALW; VIDI grant #016.121.346) and Medical Sciences (TOP-GO #91210067). Z.G. is supported by the Dutch organization for life sciences (NWO-ALM; VENI grant #863.14.001 and NWO-CAS grant #012.200.14) and the Erasmus MC fellowship. C.I.D.Z. thanks the Dutch Organization for Medical Sciences (Zon-MW; TOP-GO #91210067), Life Sciences (ALW; #854.10.004), ERC-adv (#294775), ERC-POC (#768914) and LISTEN (#6) of the EU, as well as Medical NeuroDelta (#7) for support. In addition the authors are funded by the Dutch Organization for Medical Sciences (ZonMw), Life Sciences (ALW-ENW-Klein), the European Research Council (Advanced and Proof of Concept grants), the EU LISTEN Innovative Training Network programme, the Medical NeuroDelta programme, LSH-NWO (Crossover, INTENSE), Albinism Vriendenfonds NIN, van Raamsdonk fonds, and the Trustfonds of Erasmus University, Rotterdam. None of the funding bodies had any input to the study design or outcome.

ACKNOWLEDGEMENT

We kindly thank Simona V. Gornati, Oscar H.J. Eelkman Rooda, Valentina Riguccini and Bas van Hoogstraten for fruitful scientific discussions and we thank Prof. Dr. Thomas

Kuner for providing Synaptophysin virus constructs. We thank Erika H. Goedknegt, Elize D. Haasdijk, Mandy Rutteman, and Patrick Eikenboom for helping with immunohistochemical experiments.

.

SUPPLEMENTARY TABLES

Table 1 Statistical analysis for all data in Figure 2

Panel	Unit	Mean ± SD	Normal distribution	Pairing	Test applied	P-value	N
2c	Amplitude [pA]	1107.0 ± 849.0	No	NA	NA	NA	35
2d	Charge [pa*ms]	4745.0 ± 3217.0	Yes	NA	NA	NA	35
2e	CV	0.076 ± 0.045	Yes	NA	NA	NA	35
2h	Paired pulse ratio (PPR) [%]	20Hz: 67.3 ± 10.9 35Hz: 59.3 ± 16.8 50Hz: 49.4 ± 19.1	Yes Yes Yes	No No No	Friedman test, Bonferroni correction for multiple comparisons	20Hz vs 35Hz =0.789 20Hz vs 50Hz <0.001 35Hz vs 50Hz <0.001	27 24 35
2l	Steady state (SS) [%]	20Hz: 47.8 ± 19.0 35Hz: 37.8 ± 14.4 50Hz: 25.6 ± 13.0	No Yes Yes	No No No	Friedman test, Bonferroni correction for multiple comparisons	20Hz vs 35Hz =0.262 20Hz vs 50Hz <0.001 35Hz vs 50Hz <0.001	27 24 35
2k	Recovery [%]	50ms: 42.1 ± 17.1 100ms: 47.7 ± 14.7 200ms: 52.9 ± 13.8 400ms: 65.9 ± 18.8 800ms: 64.5 ± 13.4 2000ms: 84.2 ± 7.9	Yes Yes Yes Yes Yes Yes	No No No No No No	Single Exponential fit	Y0: 39.7 Plateau: 81.9 Tau: 524.4 R^2: 0.38	12 11 12 12 6 5
2l	Recovery [%]	20Hz: 49.2 ± 13.5 35Hz: 47.4 ± 12.7 50Hz: 47.7 ± 12.6	Yes Yes Yes	No No No	Friedman test, Bonferroni correction for multiple comparisons	0.324	25 21 28
2m	Resting Potential [mV]	-73.6 ± 3.80	No	NA	NA	NA	82
2o	# spikes	2.24 ± 2.16	No	NA	NA	NA	26
2q	Steady State spike probability	20Hz: 0.20 ± 0.38 50Hz: 0.15 ± 0.32	No No	Yes Yes	Wilcoxon signed rank test	0.0625	25 25

2r	# spikes post-pause (at resting potential)	50ms: 0.15 ± 0.35 100ms: 0.28 ±0.42 200ms: 1.39 ± 1.96 400ms: 2.43 ± 2.43	No No No Yes	Yes Yes Yes Yes	Friedman test, Bonferroni correction for multiple comparisons	50ms vs. 100ms =1.0 100ms vs. 200ms =1.0 50ms vs. 200ms =1.0 50ms vs. 400ms =0.171 200ms vs. 400ms =0.602 100ms vs. 400ms =0.019	15 19 18 14

Table 2 Statistical analysis for all data in Figure 3

Panel	Unit	Mean ± SD	Normal distribution	Pairing	Test applied	P-value	N
3b	# spikes	-85mV: 3.00 ± 2.03	Yes	No	Cochran Armitrage Trend Test	=0.0001	20
		-80mV: 2.55 ± 1.97	Yes	No			22
		-75mV: 2.01 ± 1.87	No	No			25
		-70mV: 1.64 ± 2.07	No	No			21
		-65mV: 1.29 ± 1.37	No	No			21
		-60mV: 1.20 ± 0.82	No	No			20
3c	Steady state spike probability	-85mV: 0.11 ± 0.27	No	No	Cochran Armitrage Trend Test	=0.03267	20
		-80mV: 0.09 ± 0.23	No	No			22
		-75mV: 0.17 ± 0.36	No	No			25
		-70mV: 0.16 ± 0.35	No	No			21
		-65mV: 0.28 ± 0.36	No	No			21
		-60mV: 0.37 ± 0.39	No	No			20

3d	# spikes	-85mV ss: 0.32 ± 0.39	No	Yes	Friedman Test	-85mV: =0.0505,	7
		-85mV 100ms: 1.23 ± 1.63	No	Yes		ss vs. 100ms:	7
		-85mV 200ms: 2.48 ± 2.35	No	Yes		>0.9999, ss vs.	7
		-80mV ss: 0.33 ± 0.37	No	Yes		200ms: =0.0693,	6
		-80mV 100ms: 0.45 ± 0.39	No	Yes		100ms vs 200ms:	6
		-80mV 200ms: 2.60 ± 1.73	No	Yes		=0.5443;	6
		-75mV ss: 0.49 ± 0.52	No	Yes		-85mV: =0.0327,	8
		-75mV 100ms: 0.50 ± 0.44	No	Yes		ss vs. 100ms:	8
		-75mV 200ms: 2.18 ± 1.30	No	Yes		>0.9999, ss vs.	8
		-70mV ss: 0.35 ± 0.49	No	Yes		200ms: =0.0911,	9
		-70mV 100ms: 0.62 ± 0.43	No	Yes		100ms vs 200ms:	9
		-70mV 200ms: 2.09 ± 1.52	No	Yes		=0.0911;	9
		-65mV ss: 0.53 ± 0.43	No	Yes		-75mV: =0.0009,	9
		-65mV 100ms: 0.49 ± 0.50	No	Yes		ss vs. 100ms:	9
		-65mV 200ms: 1.30 ± 1.34	No	Yes		>0.9999, ss vs.	9
		-60mV ss: 0.55 ± 0.43	No	Yes		200ms: =0.0121,	9
		-60mV 100ms: 0.67 ± 0.39	No	Yes		100ms vs 200ms:	9
		-60mV 200ms: 1.16 ± 1.25	No	Yes		=0.0121;	9
						-70mV: =0.0017,	
						ss vs. 100ms:	
						>07158, ss vs.	
						200ms: =0.0201,	
						100ms vs 200ms:	
						=0.3765;	
						-65mV: =0.4599,	
						ss vs. 100ms:	
						>0.9999, ss vs.	
						200ms: >0.9999,	
						100ms vs 200ms:	
						>0.9999;	
						-60mV: =0.5303,	
						ss vs. 100ms:	
						>0.9999, ss vs.	
						200ms: >0.9999,	
						100ms vs 200ms:	
						>0.9999	

Table 3 Statistical analysis for all data in Figure 4

Panel	Unit	Mean ± SD	Normal distribution	Pairing	Test applied	P-value	N
4d	Amplitude [pA]	10Hz 1st: 26.4 ± 19.7 10Hz Steady state: 75.4 ± 73.6	No No	Yes	Wilcoxon signed rank test	<0.0001	30
		20Hz 1st: 31.9 ± 31.7 20Hz Steady state: 99.8 ± 114.9	No No	Yes	Wilcoxon signed rank test	<0.0001	39
4e	Amplitude [%]	10Hz: 258.8 ± 118.8 20Hz: 242.8 ± 138.4	No No	No	Mann Whitney test	0.3934	30 39
4h	Vm [mV]	10Hz rest: -72.8 ± 1.8 10Hz Steady state: -69.1 ± 3.1	Yes Yes	Yes	Wilcoxon signed rank test	0.0039	9
		20Hz rest: -72.5 ± 1.8 20Hz Steady state: -68.4 ± 3.5	Yes Yes	Yes	Wilcoxon signed rank test	0.0005	17
4i	Amplitude [mV]	10Hz: 3.3 ± 1.6 20Hz: 3.5 ± 2.1	Yes Yes	No	Mann Whitney test	0.7464	9 17

Table 4 Statistical analysis of all data in Figure 5

Panel	Unit	Mean ± SD	Normal distribution	Test applied	P-value	N
5f	Photo-current [nA]	1ms 585nm: 251.5 ± 119.0	Yes	Friedman test, Bonferroni correction for multiple comparisons	1ms 585nm vs. 15ms 585nm: =0.339	8
		15ms 585nm: 938.8 ± 419.5	Yes		1ms 585nm vs. 200ms 585nm: =0.133	8
		200ms 585nm: 1094 ± 302	Yes		1ms 585nm vs. 1ms 470nm: =1.0	8
		1ms 470nm: 636.5 ± 356.2	Yes		1ms 585nm vs. 585nm + 470nm: =0.477	8
		585nm+470nm: 52.5 ± 35.0	No		15ms 585nm vs. 200ms 585nm: =1.0	10
					15ms 585nm vs. 1ms 470nm: =1.0	
					15ms 585nm vs. 585nm + 470nm: < 0.001	
					200ms 585nm vs. 1ms 470nm: =1.0	
					200ms 585nm vs. 585nm + 470nm < 0.001	
					1ms 470nm vs. 585nm + 470nm: =0.003	

5g	Spike probability	1ms 585nm: 0.75 ± 0.46 15ms 585nm: 1.0 ± 0.0 200ms 585nm: 1.0 ± 0.0 1ms 470nm: 0.80 ± 0.45 585nm+470nm: 0.0 ± 0.0	Yes NA NA NA NA	Friedman test, Bonferroni correction for multiple comparisons	1ms 585nm vs. 15ms 585nm: =1.0 1ms 585nm vs. 200ms 585nm: =1.0 1ms 585nm vs. 1ms 470nm: =1.0 1ms 585nm vs. 585nm + 470nm: =0.328 15ms 585nm vs. 200ms 585nm: =1.0 15ms 585nm vs. 1ms 470nm: =1.0 15ms 585nm vs. 585nm + 470nm: =0.09 200ms 585nm vs. 1ms 470nm: =1.0 200ms 585nm vs. 585nm + 470nm: =0.057 1ms 470nm vs. 585nm + 470nm: =0.012	8 6 8 5 8

Table 5 Statistical analysis of all data in Figure 6

Panel	Unit	Mean ± SD	Normal distri-bution	Test applied	P-value	N
6i	Photo-current [nA]	15ms 585nm: 24.9 ± 23.2 200ms 585nm: 42.8 ± 29.8 1ms 470nm: 683.9 ± 361.5 585nm+470nm: 712.0 ± 364.3	Yes Yes Yes Yes	Friedman test, Dunns correction for multiple comparisons	15ms 585nm vs. 200ms 585nm: =1.0 15ms 585nm vs. 1ms 470nm: =0.011 15ms 585nm vs. 585nm + 470nm: =0.006 200ms 585nm vs. 1ms 470nm: =0.078 200ms 585nm vs. 585nm + 470nm = 0.043 1ms 470nm vs. 585nm + 470nm: =1	7 7 7 7
6j	'tau off' [ms]	1ms 470nm: 8.5 ± 2.5 585nm+470nm: 8.6 ± 2.5	Yes Yes	Unpaired t-test	0.932	7 7

6k	Spike probability	15ms 585nm: 0 ± 0 200ms 585nm: 0 ± 0 1ms 470nm: 0.8 ± 0.45 585nm+470nm: 0.8 ± 0.45	No No No No	Friedman test, Bonferroni correction for multiple comparisons	15ms 585nm vs. 200ms 585nm: =1.0 15ms 585nm vs. 1ms 470nm: =0.3 15ms 585nm vs. 585nm + 470nm: =0.3 200ms 585nm vs. 1ms 470nm: =0.3 200ms 585nm vs. 585nm + 470nm: =0.3 1ms 470nm vs. 585nm + 470nm: =1	5 5 5 5
6m	Photo-current [pA]	first: 487.4 ± 352.4 last: 486.2 ± 339.1	Yes Yes	Paired t-test	0.965	5

Table 6 Statistical analysis for all data in Figure 7

Panel	Unit	Mean ± SD	Normal distri-bution	Pairing	Test applied	P-value	N
7d	Amplitude [pA]	CN: 688.4 ± 691.8 M1 L6: 89.7 ± 130.0	No No	Yes	Wilcoxon signed rank test	<0.0001	28
7e	Charge [pA*ms]	CN: 3308.0 ± 3746.0 M1 L6: 888.5 ± 1457.0	No No	Yes	Wilcoxon signed rank test	0.0012	28
7e	CV	CN: 0.16 ± 0.18 M1 L6: 0.19 ± 0.21	No No	Yes	Wilcoxon signed rank test	0.6406	28

Table 7 Statistical analysis for all data in Figure 8

Panel	Unit	Mean ± SD	Normal distri-bution	Pairing	Test applied	P-value	N
8c	Amplitude [pA]	585nm: 68.0 ± 37.3 460nm: 6.8 ± 4.7	No No	Yes	Wilcoxon signed rank test	0.0078	8
8e	Amplitude [pA]	460nm: 539.1 ± 468.4 585nm: 6.6 ± 5.7	No No	Yes	Wilcoxon signed rank test	0.0010	11
8g	SS Charge [nA*ms]	M1 L6: 28.6 ± 27.9 CN: 37.9 ± 31.5 CN&M1-L6: 52.3 ± 42.1	Yes No Yes		Friedman test	M1 vs CN: 0.5094 M1 vs CN+M1: 0.0324 CN vs CN+M1: 0.0003	13 13 13
8j	Spike probability	CN: 0.23 ± 0.39 CN&M1-L6: 0.45 ± 0.47	No No	Yes	Wilcoxon signed rank test	0.0078	14 14

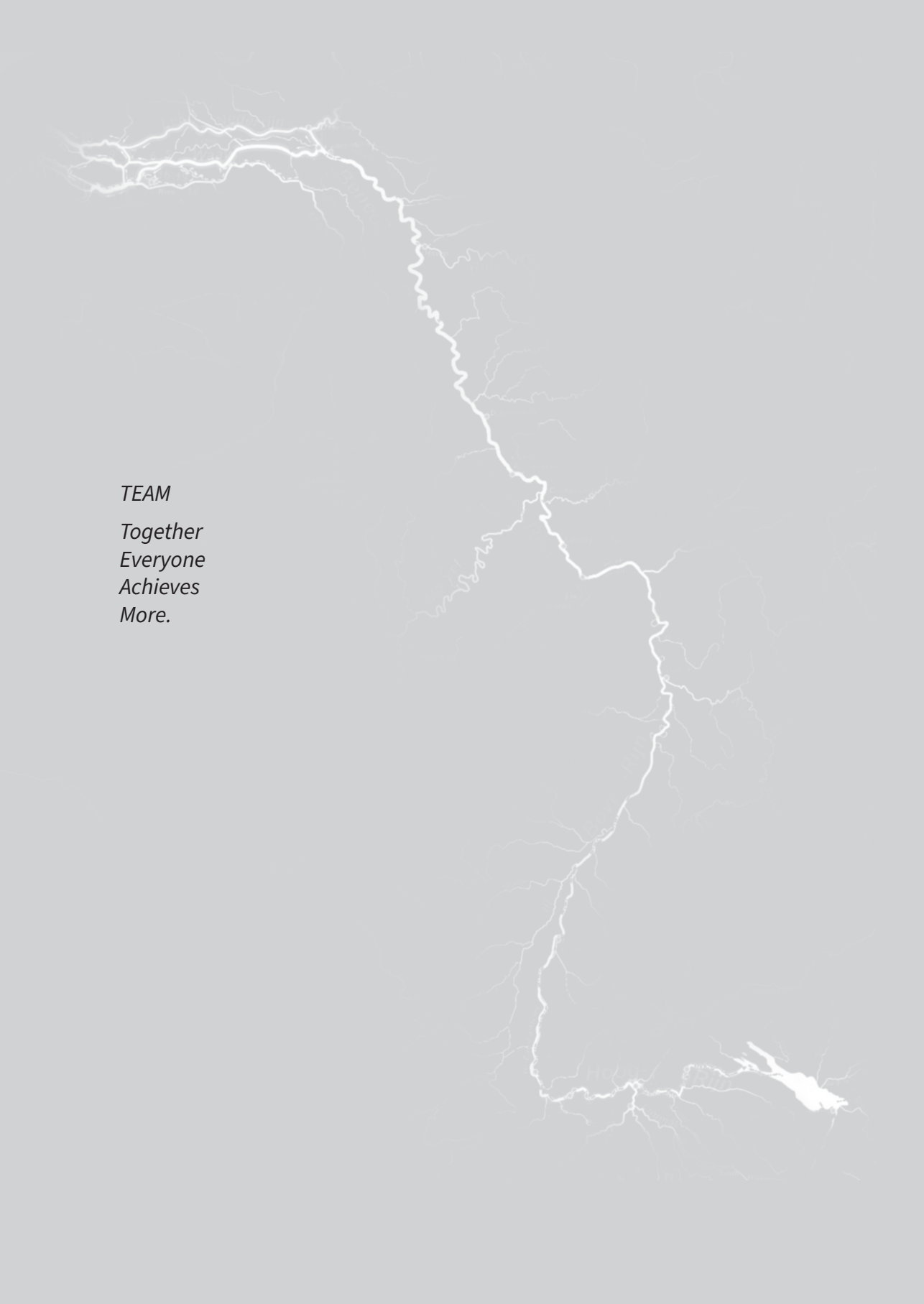

TEAM

Together
Everyone
Achieves
More.

Chapter 6

RHEB/mTOR-hyperactivity causing cortical malformations drives seizures through increased axonal connectivity

Martina Proietti Onori
Linda M.C. Koene*
Carmen B. Schäfer*
Mark Nellist
Marcel de Brito van Velze
Zhenyu Gao
Ype Elgersma*
Geeske M. van Woerden*

*These authors contributed equally

ABSTRACT

Hyperactivation of the mTOR pathway, can cause malformation of cortical development (MCD) with associated epilepsy and intellectual disability through a yet unknown mechanism. Here we made use of the recently identified dominant-active mutation in *Ras Homolog Enriched in Brain 1* (*RHEB*), RHEBp.P37L, to gain insight in the mechanism underlying the epilepsy caused by the hyperactive mTOR pathway. Focal expression of RHEBp.P37L in mouse somatosensory cortex results in an MCD-like phenotype, with increased mammalian target of rapamycin (mTOR) signaling, ectopic localization of neurons and reliable generalized seizures. We show now that the mTOR-dependent seizures in this model are caused by enhanced axonal connectivity, causing hyperexcitability of distally connected neurons. Indeed, blocking axonal vesicle release from the RHEBp.P37L neurons alone, completely stopped the seizures and normalized the hyperexcitability of the distally connected neurons. These results provide new evidence of the extent of anatomical and physiological abnormalities caused by mTOR hyperactivity, beyond local malformations, that can lead to generalized epilepsy.

INTRODUCTION

Malformations of cortical development (MCD) are a heterogenous group of micro- and macroscopic cortical abnormalities, such as focal cortical dysplasia (FCD), megalencephaly, lissencephaly and periventricular nodular heterotopia (Barkovich et al., 2012). MCD arise from disturbances in cortical development during early embryogenesis and are often linked to epilepsy and intellectual disability (ID) (Juric-Sekhar and Hevner, 2019; Leventer et al., 2008; Represa, 2019). It is estimated that up to 40% of intractable or difficult to control childhood seizures are due to MCD, and *vice versa*, at least 75% of the patients with MCD will develop seizures (Leventer et al., 1999).

The mammalian (or mechanistic) target of rapamycin (mTOR) is a kinase that mediates many cellular processes, including neuronal progenitors proliferation and cell growth (Laplante and Sabatini, 2012; Saxton and Sabatini, 2017). mTOR forms 2 distinct protein complexes, characterized by different binding partners, mTORC1 and mTORC2 (Bhaskar and Hay, 2007). mTORC1 is regulated by the tuberous sclerosis complex (TSC) and the Ras Homolog Enriched in Brain 1 (RHEB) (Parmar and Tamanoi, 2010). RHEB, a member of the RAS family of small GTPases, is the direct activator of mTORC1 (Bai et al., 2007). The conversion of active GTP-bound RHEB to the inactive GDP-bound form is mediated by the TSC complex, which acts as a RHEB GTPase activating protein (GAP) (Li et al., 2004). In response to nutrients and growth factors the TSC complex is inhibited, allowing activation of mTORC1 by RHEB-GTP (Manning and Cantley, 2003; Sabatini, 2017). Studies in *Rheb* knock-out mice showed that RHEB activity is the rate limiting step for mTOR activation in the brain, and that neuronal functioning in particular is sensitive to increased RHEB-mTOR signaling (Goorden et al., 2015).

Hyperactivation of the mTOR pathway by mutations in genes encoding components of the mTOR pathway (*e.g. AKT3*, *PIK3CA*, *DEPDC5*, *PTEN*, *TSC1, TSC2, RHEB* and *MTOR* itself) has been associated with different types of MCD, such as megalencephaly and FCD, as well as with epilepsy (Crino, 2011; Juric-Sekhar and Hevner, 2019; Moffat et al., 2015). The underlying genetic variability explains the heterogeneity of MCD and illustrates the challenges involved in understanding the mechanisms underlying MCD-associated epilepsy.

The discovery of genetic mutations that cause FCD or other types of MCD, allowed the generation of animal models to study the development of MCD and associated epilepsy (Chevassus-au-Louis et al., 1999; Wong and Roper, 2016). In particular, *in utero* electroporation (IUE), that allows for the spatial and temporal control of transgene expression during embryonic development, has been used to generate mouse models with focal

malformations and epilepsy (Hanai et al., 2017; Hsieh et al., 2016; Park et al., 2018; Ribierre et al., 2018).

One recent FCD mouse model was generated by using IUE to overexpress the constitutively active RHEBp.S16H mutant (Yan et al., 2006). This results in mTOR hyperactivity, FCD and spontaneous seizures (Hsieh et al., 2016). Recently we identified two *de novo* mutations in *RHEB* (c.110C>T (p.P37L) and c.202T>C (p.S68P)) in patients with ID, epilepsy and megalencephaly (Reijnders et al., 2017), providing for the first time a clinically relevant link between RHEB and MCD. IUE of a construct encoding the RHEBp.P37L mutant caused severe focal cortical lesions, resembling periventricular nodular heterotopia, and diffuse neuronal misplacement in the cortex. Furthermore, the mice reliably developed spontaneous seizures starting at three weeks of age (Reijnders et al., 2017). The anatomical and phenotypical features of this novel mouse model, fully recapitulating the most prominent characteristics of MCD (focal lesions and epilepsy), make this a powerful tool and clinically relevant novel model to study the mechanisms underlying mTOR and MCD-related epilepsy.

Making use of the patient-related RHEBp.P37L mutation, we provide evidence that persistent activation of the mTOR pathway results in anatomical and functional changes in axonal connectivity, and that this is causing increased excitability of distally connected neurons and the development of generalized seizures.

RESULTS

The RHEBp.P37L protein is resistant to TSC complex inhibition and causes aberrant cortical development *in vivo*

The RHEBp.P37L mutation was identified in patients with ID, megalencephaly and epilepsy, and it was proposed to act as a gain of function mutation (Reijnders et al., 2017), but why was not yet shown. It could potentially be that the mutation renders the RHEB protein resistant to the GAP-function of the TSC complex. To assess whether the TSC complex can convert RHEBp.P37L from its active GTP- to its inactive GDP-bound state, we compared the effects of transient *in vitro* overexpression of the RHEBp.P37L mutant with wild-type RHEB (RHEB WT) and the RHEBp.S16H mutant, a well-known gain of function mutant of RHEB recently used to generate an FCD mouse model (Hsieh et al., 2016; Yan et al., 2006). In the absence of TSC, overexpression of RHEB WT as well as both RHEB mutants caused increased mTORC1 activity, as measured by T389-phosphorylation of co-expressed S6K, a direct substrate of the mTORC1 kinase (**Figure 1A**, see **Supplementary Table 1** for statistics overview). In the presence of the TSC complex,

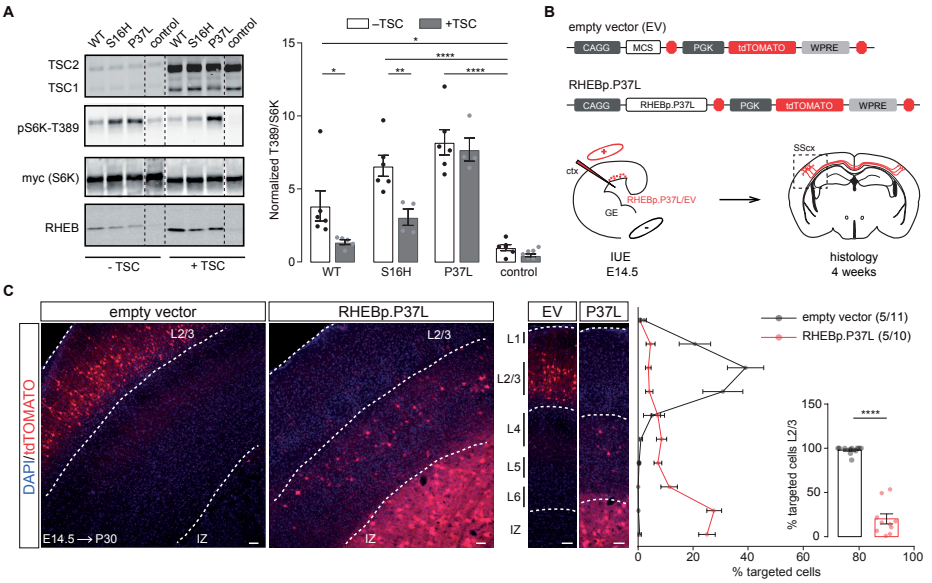

Figure 1A-C. The RHEBp.P37L protein is resistant to TSC complex inhibition and causes aberrant cortical development *in vivo*. (A) Wild-type RHEB (WT), p.S16H or p.P37L constructs were transiently co-expressed with an S6K reporter construct and the TSC complex in HEK 293T cells to assess the effect on mTORC1 activity. Quantification of the ratio of T389-phosphorylated S6K to total S6K was calculated relative to control condition, in absence or presence of the TSC complex (control indicates empty vector pcDNA3); dashed lines indicate where an irrelevant lane in the original scan was excluded from the picture; bar graph represents mean ± SEM and single data points represent the number of independent biological samples per condition; for statistics see **Supplementary Table 1**. **(B)** Schematic representation of the main constructs used throughout the experiments and overview of the experimental design. MCS indicate the multiple cloning site with specific restriction sites (AscI and PacI in this case) to insert the gene of interest. Each construct was delivered by *in utero* electroporation (IUE) at E14.5 to target the progenitor cells of layer 2/3 pyramidal neurons in the somatosensory cortex (SScx); ctx=cortex; GE=ganglion eminence. **(C)** Representative confocal images of the targeted SScx counterstained with DAPI showing the transfected cells (tdTomato+) in red (see also **Figure S1A**) and quantification of tdTomato+ cells across the different layers of the SScx with percentage of cells reaching layer 2/3 (L2/3) in the inset (bins 1-5 from the top). Dotted lines indicate the border of the intermediate zone (IZ, bottom) and delineate L2/3. Numbers in the legend indicate number of targeted mice (N=5) and total number of pictures analyzed (n=11, n=10); results are represented as mean ± SEM and single data points in the bar graph indicate the number of pictures analyzed; inset analysis: Mann-Whitney U = 0, p<0.0001, two-tailed Mann-Whitney test.

mTORC1 activity was reduced in the RHEB WT and RHEBp.S16H expressing cells, but not in the RHEBp.P37L expressing cells (**Figure 1A**). Here, presence or absence of TSC resulted in similar levels of S6K phosphorylation, confirming that the patient-derived RHEBp.P37L acts as a gain of function mutation which is resistant to inhibitory action of the TSC complex (**Figure 1A**).

Using IUE, we have previously shown that overexpression of the RHEBp.P37L mutant, but not RHEB WT, results in the formation of a heterotopic nodule as well as spontaneous epilepsy in 100% of the targeted mice (Reijnders et al., 2017), providing us with a valuable model to study the mechanisms behind mTORC1-dependent and MCD-related

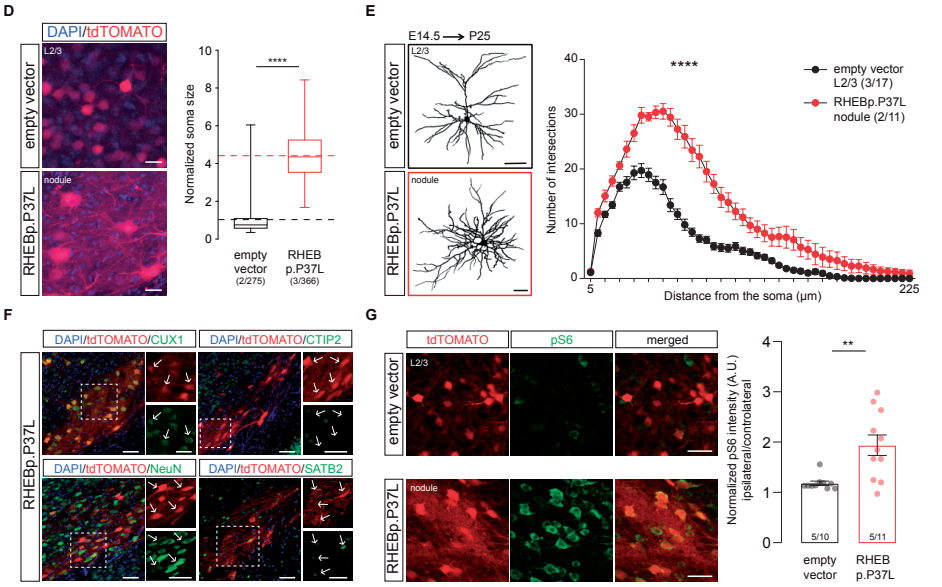

Figure 1D-G. The RHEBp.P37L protein is resistant to TSC complex inhibition and causes aberrant cortical development *in vivo*. (D) Soma size quantification of L2/3 empty vector expressing cells and RHEBp.P37L expressing cells in the nodule; box plots represent minimum and maximum values with median, dashed lines represent the mean values for empty vector (black) and for RHEBp.P37L (red); numbers indicate number of targeted mice (N=2, N=3) and number of cells analyzed (n=275, n=366); Mann-Whitney U = 1940, p<0.0001, two-tailed Mann-Whitney test. **(E)** Reconstruction and Sholl analysis of dendritic morphology of biocytin filled cells in L2/3 of the SScx (for empty vector control) and RHEBp.P37L cells in the nodule; numbers in the legend indicate number of targeted mice (N=3, N=2) and number of cells analyzed (n=17, n=11); data are presented as mean ± SEM; interaction group condition/distance from the soma: F(44, 1144) = 15.69, mixed-effects analysis; p<0.0001. **(F)** Representative images of the nodule stained with CUX1 (L2/3 marker), CTIP2 (L5 marker), SATB2 (cortical projection neurons marker) or NeuN (mature neurons marker); arrows in the zoomed pictures point at examples of targeted cells; for an overview see **Figure S1B**). **(G)** Representative images of the targeted L2/3 (SScx) of empty vector control and nodule showing increased pS6-240 levels for the ipsilateral targeted cortex in RHEBp.P37L targeted mice; for an overview see **Figure S1C**; bar graph represents mean ± SEM and single data points indicate the values of each normalized ipsilateral/contralateral pS6 intensity; numbers in the bars indicate number of targeted mice (N=5) and number of pictures analyzed (n=10, n=11); Mann-Whitney U = 13, p = 0.002, two-tailed Mann-Whitney test). Histological analysis for **(D) (F)** and **(G)** was performed on 5 weeks old mice. * p<0.05, ** p<0.01, **** p<0.0001; scale bars: 20 µm (D), 50 µm (C, E-G).

epilepsy. To confirm previous results, we used IUE to introduce the RHEBp.P37L vector or an empty vector control at E14.5 in progenitor cells that give rise to layer 2/3 (L2/3) pyramidal neurons of the somatosensory cortex (SScx) (**Figure 1B**). As shown previously, overexpression of RHEBp.P37L resulted in a clear migration deficit, with only 20% of the targeted cells reaching the outer layers of the cortex (L2/3) compared to 97% in the empty vector condition (**Figure 1C**, inset). The non-migrated transfected neurons remained in the white matter to form a heterotopic nodule lining the ventricle in the adult brain (**Figure 1C** and **Figure S1A**).

Further characterization of the RHEBp.P37L-dependent MCD, revealed that while the general cortical layer architecture remained intact (**Figure S1A)**, ectopic RHEBp.P37L overexpressing cells showed cytological abnormalities, with dysmorphic appearance and enlarged soma size (**Figure 1D** and **Figure S1A**). Sholl analysis of biocytin filled cells in the heterotopic nodule of RHEBp.P37L expressing neurons revealed that the cells in the nodule presented a more complex arborization compared to empty vector control cells in L2/3 (**Figure 1E**). Transfected ectopic neurons preserved the molecular identity of mature L2/3 pyramidal cells, being positive for the neuronal marker NeuN and the outer layer molecular marker CUX1 and negative for the deeper layer marker CTIP2 (**Figure 1F** and **Figure S1B**). Additionally, 80% of the targeted neurons were SATB2 positive, showing that, despite being mislocalized, they maintained the excitatory callosal projection identity (**Figure 1F** and **Figure S1B**). Importantly, RHEBp.P37L-transfected cells were negative for interneuron-specific markers such as GABA and PV (**Figure S1C**). Finally, mice overexpressing RHEBp.P37L showed an overall increase in ribosomal protein S6 phosphorylation, a commonly used readout for mTORC1 activity, in the transfected (ipsilateral) SScx compared to the empty vector condition (**Figure 1G** and **Figure S1D**).

Overexpression of RHEBp.P37L *in vivo* causes mTORC1-dependent spontaneous generalized tonic-clonic seizures and abnormal neuronal network activity

In order to study the mechanism behind mTOR-dependent MCD-related epilepsy, we next assessed the reliability of seizure development using our RHEBp.P37L mutant model. To assess the reliability of spontaneous seizure development, the RHEBp.P37L mice were continuously monitored from weaning (P21) using wireless electroencephalography (EEG) placing electrodes bilaterally on the SScx until at least 2 months of age (**Figure 2A**). Spontaneous seizures started to appear in all RHEBp.P37L transfected mice (N=12), at 3 weeks of age, with an average onset of 33 days, while none of the control mice (N=6) developed any epileptic events, confirming previous data (Reijnders et al., 2017) (**Figure 2B** and **Figure S2A**). These seizures were highly stereotypical, characterized by the loss of upright posture followed by a tonic-clonic phase with convulsions and twitching behavior. EEG analysis showed that the seizures were characterized by an increase in frequency and amplitude of brain activity (**Figure 2C**, box 3 ictal activity) compared to baseline interictal activity (**Figure 2C**, box 2) and baseline activity of control mice (**Figure 2C**, box 1). The calculated average duration of an epileptic event was 40 seconds (mean ± SEM: 42.6 ± 1.33), followed by a post-ictal depression phase of variable length (**Figure 2C**, box 4 post-ictal activity). The average number of seizures per day, measured across multiple EEG sessions over at last 2 consecutive days for each session, was 4 (mean ± SEM: 3.8 ± 0.76), with variability between mice as well as over time (**Figure S2B**). Additionally, no correlation was found between the average number of

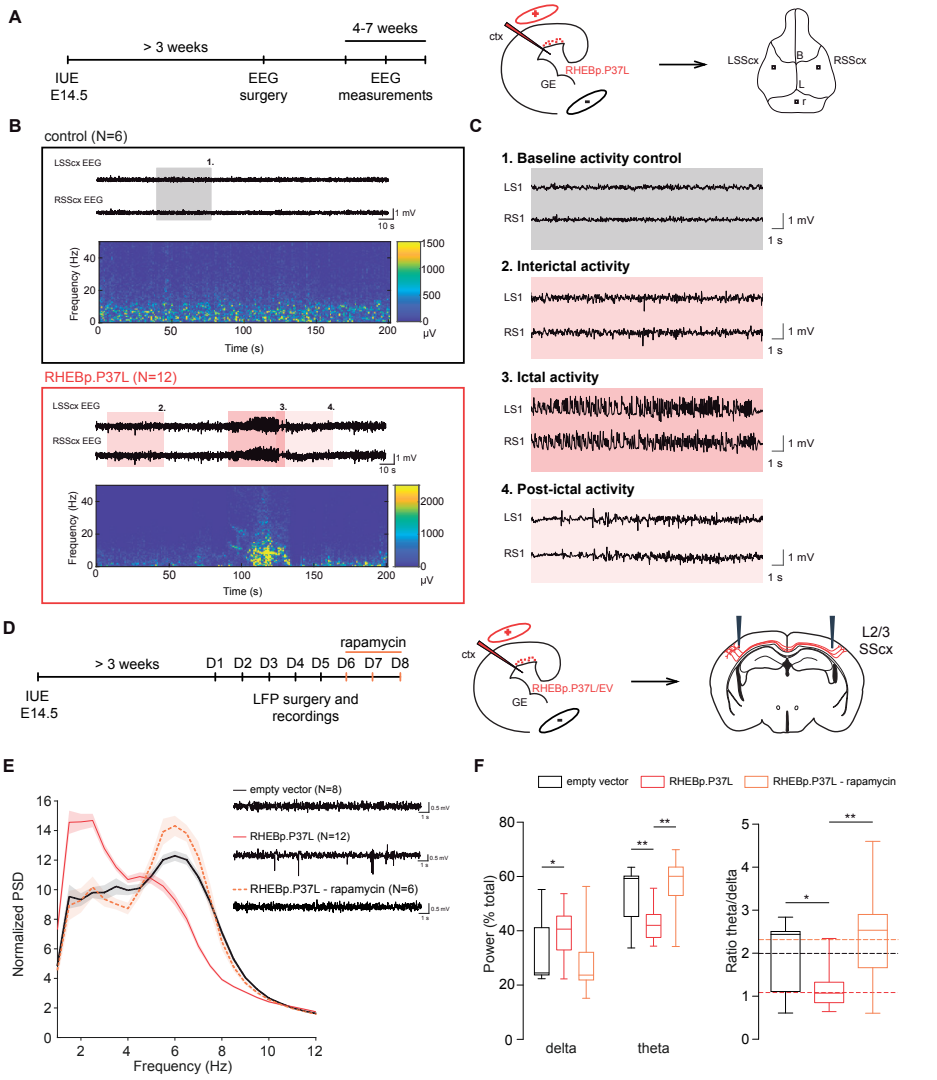

Figure 2. Overexpression of RHEBp.P37L *in vivo* causes mTORC1-dependent spontaneous generalized tonic-clonic seizures and abnormal neuronal network activity

(A) Timeline and experimental design indicating the cortical area targeted with the IUE and position of the electrodes placed during the EEG surgery (LSScx = left SScx; RSScx = right SScx; B = bregma; L= lambda; r = reference electrode). **(B)** Example EEG traces and spectrogram of 5 weeks old control mouse (N=6, non-targeted mice from the same litters as the RHEBp.P37L mice) and RHEBp.P37L mouse (N=12); see also **Figure S2A-C**; colored boxes are zoomed in panel **(C)**. **(C)** Highlighted EEG traces showing: box 1. the baseline activity of a control mouse; box 2. the interictal activity, box 3. the ictal (seizure) activity and box 4. the post-ictal phase of a RHEBp.P37L targeted mouse. **(D)** Timeline and experimental design indicating the cortical area targeted with the IUE, the position of the electrodes for the local field potential (LFP) recordings and the IP rapamycin injections. **(E)** Example LFP traces for each group condition and normalized power spectrum density (PSD) averaged bilaterally over the overall consecutive days of recording (for the PSD until 50 Hz see **Figure S2D**); N indicates number of mice analyzed for each group; data are represented as mean (thick line) ± SEM (shading area). **(F)** Calculation of the *delta* (2-4 Hz) and *theta* (4-8 Hz) frequency bands over the total power of the PSD presented in **(E)**, and relative ratio *theta*/*delta* (see also **Figure S2E**); box plots represent minimum and maximum values with median, dashed lines represent the mean values for each group; for statistics see **Supplementary Table 2**; * $p<0.05$, ** $p<0.01$, *** $p<0.001$.

seizures over all the recording days and the average number of targeted cells per mouse, confirming previous literature (Nguyen et al., 2019) (**Figure S2C**).

Electrographic frequency dynamics of the interictal phases, and especially *theta* oscillations, have been proven to be good predictors for epilepsy outcome, compared to epileptiform spikes or high-frequency oscillations (HFOs), in several rodent models of epilepsy (Chauvière et al., 2009; Milikovsky et al., 2017). Therefore, using local field potential (LFP) recordings, with the recording electrodes placed bilaterally in the SScx at the depth of L2/3, we assessed the frequency dynamics of cortical brain activity in the interictal periods of RHEBp.P37L expressing mice, starting from 4 weeks of age (**Figure 2D**). The normalized averaged power spectrum of the RHEBp.P37L group did not reveal a significant difference between the ipsilateral and contralateral (non-targeted) SScx (targeting: $F(1, 22)=1.43$, $p=0.25$, non-significant, Two-way repeated measure ANOVA; data not shown), therefore measurements from both sides were pooled. Whereas the total power across 5 days of recording did not differ between the RHEBp.P37L (N=12) and the control group (N=8) (Mann-Whitney $U = 157$, $p = 0.35$, non-significant, two-tailed Mann-Whitney test, data not shown), a significant difference in the *delta* (2-4 Hz), *theta* (4-8 Hz) and *gamma* (30-50 Hz) frequency bands of the normalized power spectrum was seen in the RHEBp.P37L group compared to the control group (**Figure 2E-F** and **Figure S2D**; statistics in **Supplementary Table 2**). The difference in the *theta* and *gamma* frequency bands, but not in the *delta*, could be reverted to the control condition by injecting the RHEB mice with 10 mg/kg rapamycin intraperitoneally for 3 consecutive days (**Figure 2E-F** and **Figure S2D-E**; statistics in **Supplementary Table 2**), proving that in our model the seizures are caused by hyperactivity of the mTOR pathway. Additionally, this result indicates that *theta* oscillations, which negatively correlate with *gamma* frequencies (Milikovsky et al., 2017), are a good predictor for epileptogenesis in hyperactive mTOR-dependent models.

The heterotopic nodule is neither necessary nor sufficient to induce spontaneous seizures

Cortical malformations occur during early embryonic development and are generally associated with the development of epileptic activity (Represa, 2019). Therefore, a transient treatment with mTOR inhibitors during brain development might prevent the formation of a cortical malformation and could consequently reduce the chances of developing epilepsy. To assess if early transient down-regulation of the mTORC1 pathway upon overexpression of RHEBp.P37L could prevent the development of heterotopic nodules, we injected pregnant female mice with 1 mg/kg of rapamycin for 2 consecutive days starting 1 day after IUE of the RHEBp.P37L vector (**Figure 3A**). Prenatal down-regulation of the mTORC1 pathway significantly improved the migration of the

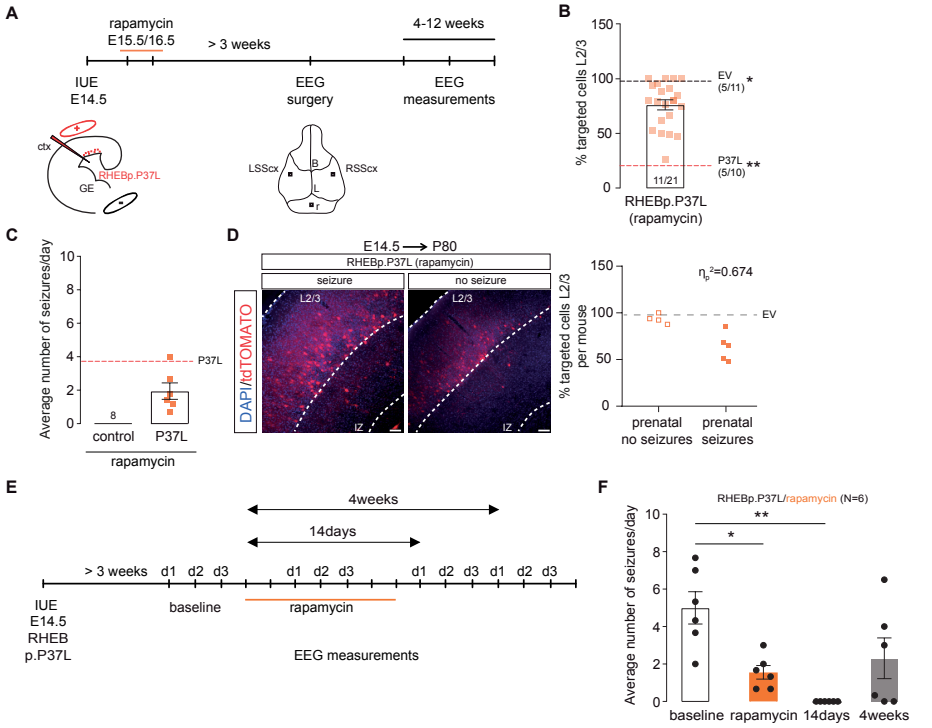

Figure 3. Rapamycin administration prevents the formation of a heterotopic nodule and stops the occurrence of seizures

(A) Schematic representation of the timeline of the IUE, SC rapamycin injections, EEG surgery and measurements. **(B)** Quantification of the percentage of tdTomato+ cells that managed to migrate out to L2/3 in mice prenatally exposed to rapamycin; data are presented as mean ± SEM, single data points represent the values of each picture analyzed and dashed lines indicate the mean value of cells reaching L2/3 in empty vector control mice (black line) and in RHEBp.P37L mice (red line); numbers in the graph indicate number of mice (N=11, N=5) and number of pictures analyzed (n=21, n=11, n=10); (% targeted cells in L2/3: $H(2) = 25.97$, $p < 0.0001$, Kruskal-Wallis test; EV *vs* RHEBp.P37L-prenatal rapamycin, $p = 0.05$; RHEBp.P37L *vs* RHEBp.P37L-prenatal rapamycin, $p = 0.002$, RHEBp.P37L *vs* EV, $p < 0.0001$, Dunn's multiple comparisons test; * $p<0.05$, ** $p<0.01$. **(C)** Average number of seizures per day of each targeted mouse prenatally treated with rapamycin and showing spontaneous seizures measured with EEG between 4 and 12 weeks of age (N = 6); control mice are non-targeted mice from the same litters as the RHEBp.P37L mice prenatally exposed to rapamycin (N = 8); data are presented as mean ± SEM, the dashed line indicates the average number of seizures of RHEBp.P37L mice not treated with rapamycin (Mann-Whitney $U = 17.5$, $p = 0.09$, two-tailed Mann-Whitney test) **(D)** Representative images of RHEBp.P37L mice prenatally exposed to rapamycin that showed or did not show seizures; the quantification graphs shows the degree of association between the migration phenotype shown in panel B and here presented as % of targeted cells in L2/3(dependent scale variable) for each mouse and the absence or presence of seizures (independent nominal variable) in RHEBp.P37L mice (N=4 and N=5, respectively, with the exclusion of the mice that showed heterotopia); the dashed line represents the mean value of the empty vector control group already shown in B, as comparison; η_p=0.821, η_p^2=0.674, Eta measure of association, with values of η_p close to one indicating strong association. **(E)** Schematic representation of the timeline of the IUE, systemic rapamycin injections and EEG measurements performed for 3 consecutive days over different sessions over time. **(F)** Average number of seizures per day of each mouse treated with rapamycin (N = 6) measured before treatment (baseline), during and after rapamycin injections; data are presented as mean ± SEM (Rapamycin effect over time: $F(2.04, 10.19)=9.1$, $p=0.005$, RM one-way ANOVA; baseline *vs* rapamycin: $p=0.03$; baseline *vs* 14days: $p=0.005$; baseline *vs* 4weeks: $p=0.17$; Dunnett's multiple comparisons test. * $p<0.05$, ** $p<0.01$. Scale bars: 100 µm.

targeted neurons, with 75% of the targeted cells successfully migrating out (**Figure 3B**). In addition, prenatal rapamycin treatment successfully prevented the formation of a heterotopic nodule in 9 out of 11 mice. However, 7 out of the 11 targeted mice (58%) still showed spontaneous seizures, including 5 mice that did not develop a discernable heterotopic nodule, with an average number of seizures per day similar to RHEBp.P37L mice not treated with rapamycin (**Figure 3C**). Average onset of seizures was also comparable to the non-treated RHEBp.P37L mice (mean ± SEM: 32.6 days ± 2.3; Chi square (1) = 0.16, $p = 0.69$, Log-rank test, data not shown). Hence, the presence of a heterotopic nodule is not required for RHEBp.P37L mediated seizures, and reducing the formation of these nodules does not always prevent epileptogenesis. When splitting the data of the cortical migration patterns shown in **Figure 3B** for mice with and mice without seizures, a clear correlation was observed between the migration pattern of RHEBp.P37L expressing cells and the presence or absence of seizures: RHEBp.P37L-prenatal treated mice with seizures showed a more severe migration deficit of RHEBp.P37L expressing cells compared to prenatal treated RHEBp.P37L expressing mice that were seizure free (**Figure 3D**). In fact, the percentage of cells that reached L2/3 of the SScx of RHEBp.P37L-prenatal treated mice with seizures (63%), was significantly lower than RHEBp.P37L-prenatal treated mice without seizures (93%) or control mice (98%) (% targeted cells in L2/3: H(2) = 22.08, $p < 0.0001$, Kruskal-Wallis test; empty vector *vs* RHEBp.P37L-no seizures, $p > 0.99$; empty vector *vs* RHEBp.P37L-seizures, $p < 0.0001$; RHEBp.P37L-no seizures *vs* RHEBp.P37L-seizures, $p = 0.002$; Dunn's multiple comparisons test, data not shown). These results indicate that ectopic cells do facilitate the process of epileptogenesis.

Hyperactivation of mTORC1 is sufficient to cause seizures, independent of the presence of cortical malformations (Abs et al., 2013), even when the mTORC1 activity is increased in a limited set of neurons (Hsieh et al., 2016). Moreover, the cortical malformation by itself, in the absence of continued mTORC1 signaling, does not cause epilepsy, as was also shown by brain-wide inhibition of mTORC1signaling (Hsieh et al., 2016). To confirm that brain-wide suppression of mTORC1 activity could reduce seizures also in our mouse model, we treated a group of mice showing seizures (N=6; 5-6 weeks old) systemically for 7 days with the allosteric mTORC1 inhibitor rapamycin (10 mg/kg) (**Figure 3E**), which reduced and temporarily abolished the occurrence of seizures within one week from the last day of rapamycin administration (**Figure 3F**). However, seizures reoccurred starting 3 weeks after the last injection of rapamycin in 4 out of 6 mice, indicating that sustained inhibition of mTORC1 is required to fully suppress the seizures and that the presence of a heterotopic nodule alone is not sufficient to promote the seizures (**Figure 3F**).

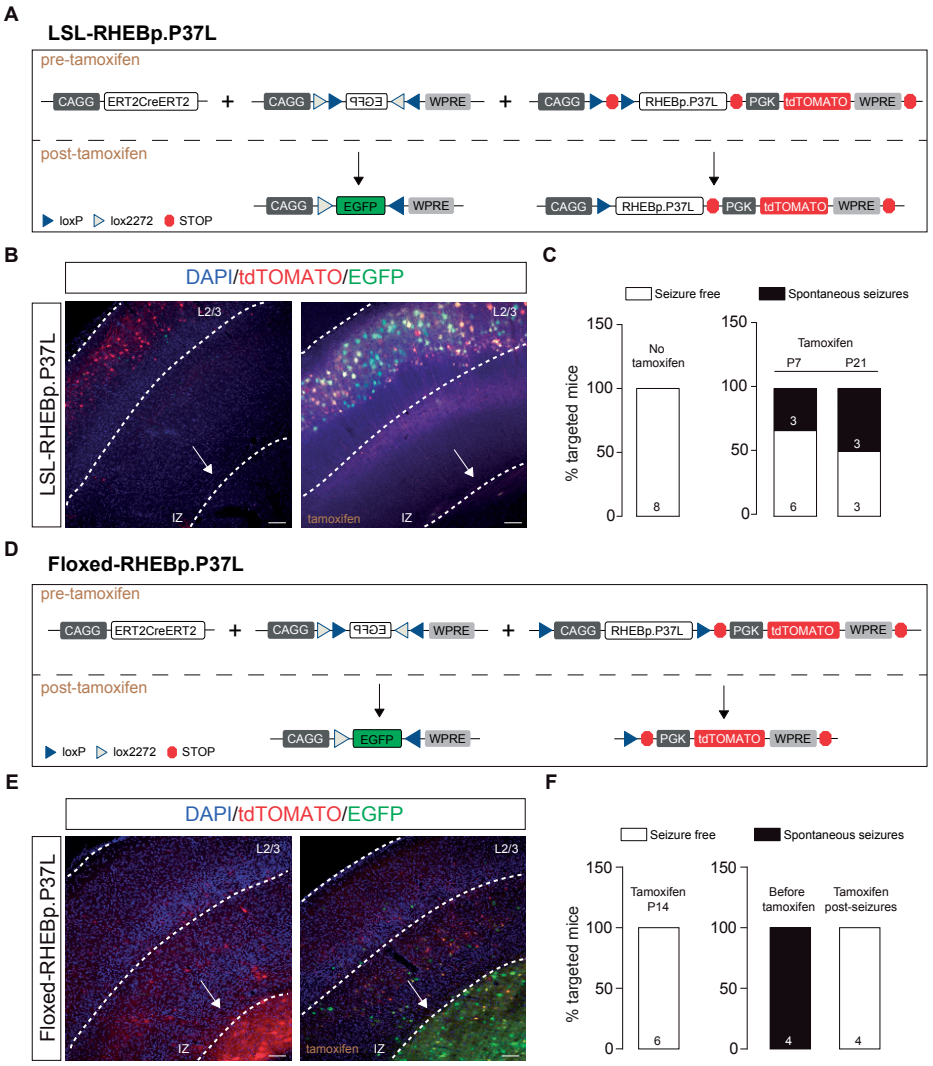

Figure 4. The heterotopic nodule is neither necessary nor sufficient to induce spontaneous seizures
(A and D) Schematic representation of the DNA plasmids used in the experiment. The Lox-Stop-Lox (LSL) or the floxed construct was expressed in combination with the CAGG-ERT2CreERT2 and a CAGG-DIO-EGFP constructs. The EGFP in the CAGG-DIO-EGFP construct is expressed only upon tamoxifen injection, providing a measure of efficient cre-dependent recombination (see representative images in **B** and **E**). **(B)** Representative images showing efficient cre recombination upon tamoxifen administration in adult mice injected *in utero* with the LSL construct; note the absence of heterotopic nodule (indicated by the white arrow)**(C)** Bar graphs indicating the percentage of targeted mice showing seizures after injection at either P7 or P21 for 4 consecutive times with tamoxifen and measured with EEG until 12 weeks of age; numbers in the bar plots indicate the number of mice. **(E)** Representative images showing efficient cre recombination upon tamoxifen administration in adult mice injected *in utero* with the floxed construct; note the presence of heterotopic nodule (indicated by the white arrow) **(C)** Bar graphs indicating the percentage of targeted mice showing seizures after injection at either P14 or upon seizure development for 4 consecutive times with tamoxifen and measured with EEG until 12 weeks of age; numbers in the bar plots indicate the number of mice. Scale bars: 100 µm.

To further confirm the necessity of increased mTOR activity in a subset of cells, irrespective of the presence of a cortical malformation, for the development of epilepsy, we used IUE to focally introduce in the SScx a Lox-Stop-Lox (LSL)-RHEBp.P37L vector (**Figure 4A**) or floxed-RHEBp.P37L vector (**Figure 4D**) together with a vector expressing the ERT2Cre-ERT2 fusion protein. This allowed us to switch the RHEBp.P37L gene respectively on or off during different stages of cortical development. IUE of the LSL-RHEBp.P37L construct in the absence of tamoxifen administration, did not result in a migration deficit, or seizures, indicating that the LSL cassette successfully prevented RHEBp.P37L expression (**Figure 4B**). However, once expression of RHEBp.P37L was induced by administration of tamoxifen either at P7 or P21, a subset of the mutant mice (38% of the P7 group and 50% of the P21 group) developed spontaneous seizures (**Figure 4C**), albeit with a delayed onset compared to mice that express RHEBp.P37L throughout development (**Figure S3**). Expression of the floxed-RHEBp.P37L vector in absence of tamoxifen, resulted in the development of a heterotopic nodule as well as seizures, as expected (**Figure 4E**). Inducing RHEBp.P37L deletion at P14 (**Figure 4F**), prevented the development of seizures, despite the presence of a heterotopic nodule (**Figure 4E**). Furthermore, inducing deletion of RHEBp.P37L after epileptogenesis, completely abolished the seizures within 10 days from gene deletion (N=4, last EEG measurements performed between day 85 and 90) (**Figure 4F**). Taken together, these results confirm that RHEBp.P37L expression in a limited number of cells drives seizure development and that cortical malformations are neither necessary nor sufficient for the development of spontaneous seizures, as shown by the pharmacological data.

RHEBp.P37L expression induces aberrant axonal development both *in vitro* and *in vivo* and functional increased contralateral L2/3 and L5 connections

The mTOR pathway plays an important role in axonal outgrowth, with functional effects on neuronal network formation (Choi et al., 2008; Gong et al., 2015; Nie et al., 2010). Because increasing mTOR signaling in a limited number of neurons in the brain is enough to cause seizures, independently from cell misplacement, we hypothesized that this could be due to aberrant neuronal connectivity caused by RHEBp.P37L overexpression. Therefore, we investigated the effect of RHEBp.P37L on axonal length and branching both *in vitro* and *in vivo*. Overexpression of RHEBp.P37L in primary hippocampal neurons *in vitro* caused a significant increase in axonal length and axonal branching, compared to the empty vector control (**Figure 5A**). *In vivo*, axons from callosal projection neurons originating from the superficial layers of the SScx project to the homotopic contralateral hemisphere, where they mostly innervate L2/3 and L5 pyramidal neurons (Fenlon et al., 2017; Petreanu et al., 2007). They also send collaterals to L2/3 and, more strongly, L5 pyramidal neurons within the same column ipsilaterally, participating in

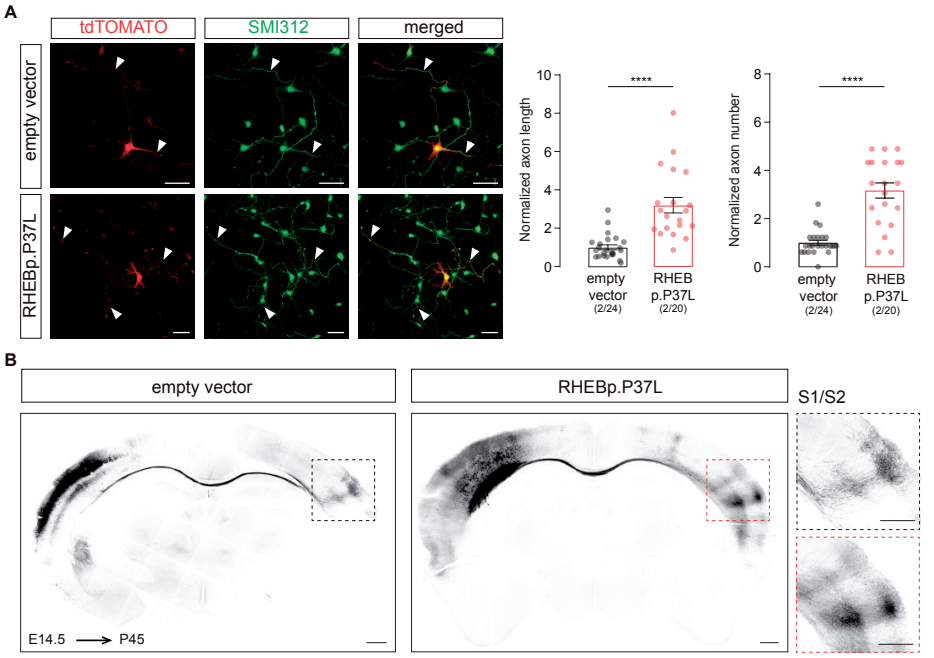

Figure 5A-B. RHEBp.P37L overexpression induces an increase in axon length and branching both *in vitro* and *in vivo*
(A) Representative images of primary hippocampal cultures transfected at day *in vitro* 1 (DIV1) with either empty vector control or RHEBp.P37L constructs (tdTomato, in red) stained at DIV4 with a pan axonal marker SMI312 (in green); arrowheads indicate the axons; bar graphs represent mean ± SEM and single data points indicate the number of cells analyzed; numbers indicate number of neuronal cultures (N=2) and total number of cells analyzed (n=24, n=20); axonal length: Mann-Whitney U = 32, $p<0.0001$, Mann-Whitney test; axonal branches: Mann-Whitney U = 53, $p<0.0001$, Mann-Whitney test. **(B)** Overview coronal sections in grey scale stained with anti-RFP antibody of an empty vector and a RHEBp.P37L mouse brain *in utero* electroporated on the left S1 and magnification of the axon terminals on the contralateral S1; scale bars: 500 µm.
** $p<0.01$, **** $p<0.0001$; scale bars: 50 µm **(A)**, 500 µm **(B)**, 100 µm **(C)**.

local circuitry (Fame et al., 2011; Petreanu et al., 2007). Therefore, it is conceivable that *in vivo* overexpression of RHEBp.P37L affects callosal projections to the non-targeted contralateral SScx hemisphere. Analysis of the contralateral callosal axonal growth in matched coronal sections with comparable targeting revealed that upon RHEBp.P37L overexpression, axonal terminals in the contralateral hemisphere, show a broader distribution compared to controls, reaching the primary (S1) and secondary (S2) SScx (**Figure 5B**). Furthermore, a significant difference was found in the distribution of the axonal terminals across the different layers in the contralateral hemisphere. While in the control condition most of the terminals in the contralateral SScx were located in L2/3, with a lower abundance in L5 (Fenlon et al., 2017), in the RHEBp.P37L mice we found that most of the terminals were located in the deeper layers of the SScx, suggesting an improper cortical connectivity (**Figure 5C**). Furthermore, zooming in on the axonal projections on the contralateral cortex of RHEBp.P37L mice revealed the presence of

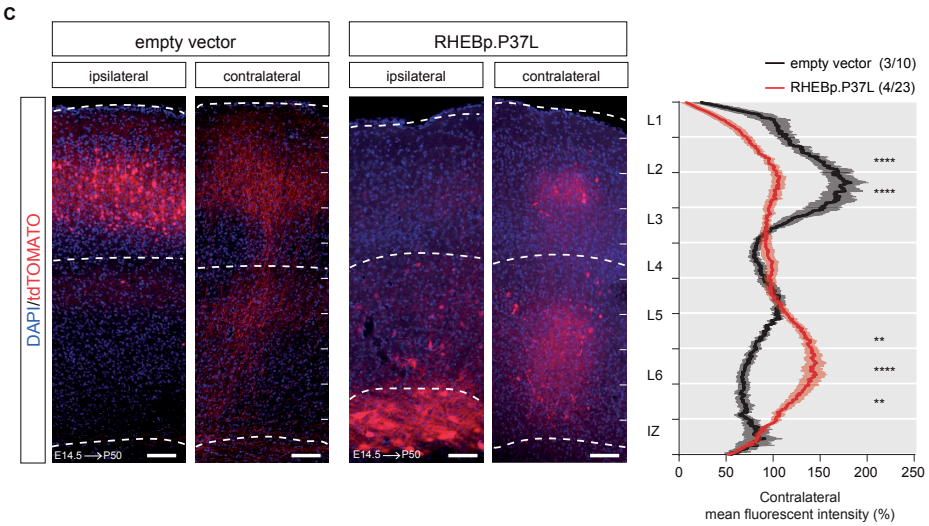

Figure 5C. RHEBp.P37L overexpression induces an increase in axon length and branching both *in vitro* and *in vivo*
(C) Representative images of ipsilateral and contralateral S1 area of an empty vector and a RHEBp.P37L mouse coronal section (P50) with quantification of the axonal projections across the different layers in the contralateral cortex measured as normalized fluorescent intensity of the tdTomato signal; numbers in the legend indicate number of targeted mice (N=3, N=4) and number of contralateral pictures (n=10, n=23) analyzed; data are presented as mean (thick line) ± SEM (shading area); interaction group condition/cortical layers: $F(9, 279)=13.96$, $p<0.0001$, mixed-effects analysis; control *vs* RHEBp.P37L L2/3 (bin2-3 from the top): $p<0.0001$; control *vs* RHEBp.P37L L5-L6: bin7, $p=0.0074$, bin8, $p<0.0001$, bin 9, $p=0.002$; Bonferroni multiple comparisons test.
** $p<0.01$, **** $p<0.0001$; scale bars: 50 µm **(A)**, 500 µm **(B)**, 100 µm **(C)**.

enlarged *boutons* and terminals positive for Synapsin-1 and VGLUT1, markers for synaptic vesicles and glutamatergic neurons, respectively (**Figure S4A**). EM analysis of these boutons confirmed that the boutons are on average twice the size of control boutons and filled with neurotransmitter vesicles, which potentially could result in increased connectivity compared to control (**Figure S4B**).

To investigate if the contralateral axonal projections with these synaptic terminals showing altered morphology are functional and indeed showed increased connectivity, we made use of optogenetics. We used IUE to introduce channelrhodopsin-2 (pCAGGS-ChR2-Venus) (Petreanu et al., 2007) together with either the empty vector control or the RHEBp.P37L construct in targeted neurons and recorded the postsynaptic responses (EPSCs) to widefield optogenetic stimulation by patch-clamping L2/3 and L5 pyramidal neurons in the (non-targeted) contralateral S1 where axonal terminals could be observed (**Figure 6A** and **Figure S5A**). Analyzing the amplitude of EPSCs following optogenetic stimulation in L5 and L2/3 of the contralateral S1, we observed an overall increase in response in the RHEBp.P37L condition compared to the empty vector control condition (see **Supplementary Table 3** for statistics) (**Figure 6B**). When analyzing the

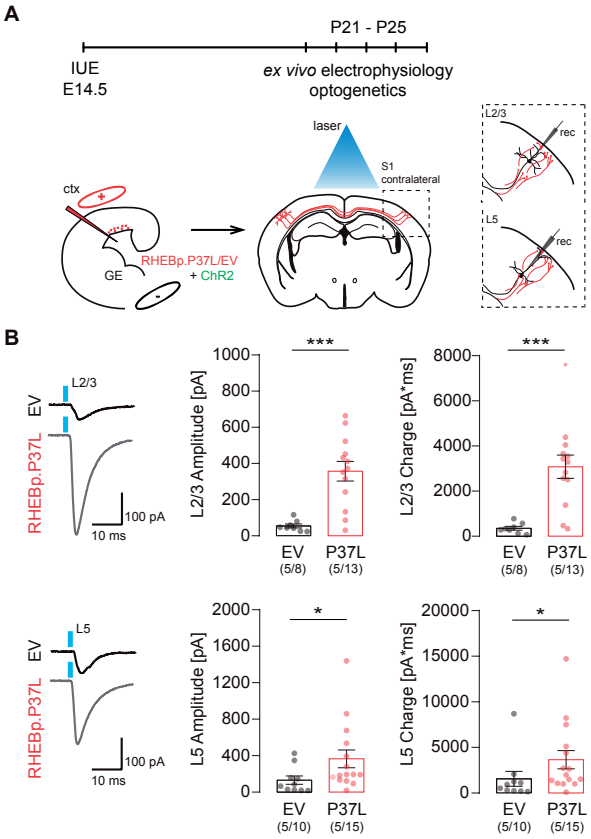

Figure 6. Overexpressing RHEBp.P37L increases synaptic connectivity on the contralateral hemisphere.
(A) Schematic representation of the timeline and experimental conditions of the IUE and *ex vivo* whole-cell patch clamp recordings in contralateral L2/3 and L5 upon wide-field optogenetic stimulation. **(B)** Example traces and analysis of the compound postsynaptic responses after photostimulation (blue light), showing the postsynaptic response amplitudes and total charge in contralateral L2/3 and L5 in empty vector (EV) and RHEBp.P37L expressing slices; numbers in the graph indicate number of targeted mice (N=5) and number of cells (n=8, n=13, n=10, n=15) analyzed; data are presented as mean ± SEM and single data points indicate the values of each cell; for statistics see **Supplementary Table 3**; * p<0.05, *** p<0.001.

total charge of the compound postsynaptic response we observed similar response patterns (**Supplementary Table 3** for statistics) (**Figure 6B**). Bath application of tetrodotoxin (TTX) in the RHEBp.P37L group decreased the post-synaptic responses evoked by photo-stimulating ChR2 expressing fibers to noise level, which is indicative of action potential driven neurotransmitter release (**Figure S5B**). The basic properties (resting membrane potential [Vm] and membrane resistance [Rm]) of L2/3 and L5 contralateral cells in empty vector control and RHEBp.P37L conditions were not different (**Supplementary Table 3** for statistics). These data suggest increased synaptic connectivity to the contralateral S1 upon overexpression of RHEBp.P37L.

Loss of axonal projections or blocking vesicle release of RHEBp.P37L expressing neurons is sufficient to stop seizures

Having shown that the RHEBp.P37L expressing neurons show stronger axonal innervation and synaptic connectivity to neurons in the contralateral hemisphere, we investigated whether these altered neuronal projections drive the seizures. To assess this, we made use of the Tetanus toxin light chain, known to specifically cleave the SNARE-complex protein Synaptobrevin/VAMP2 (Syb2) (Schiavo et al., 1992). VAMP2 is part of the SNARE complex that allows synaptic vesicles fusion and the release of neurotransmitters (Gaisano et al., 1994) and recently it has been shown to mediate the vesicular release of Brain Derived Neurotrophic Factor (BDNF) from axon and dendrites, thereby regulating proper cortical connectivity (Shimojo et al., 2015). Intrinsic neuronal activity during early brain development is crucial for axonal growth and branching, and blocking synaptic transmission using Tetanus toxin interferes with proper cortical axonal formation, resulting in the reduction and disappearance of axonal projections (Wang et al., 2007). Indeed, when RHEBp.P37L was co-transfected with a Tetanus toxin construct (TeTxLC)

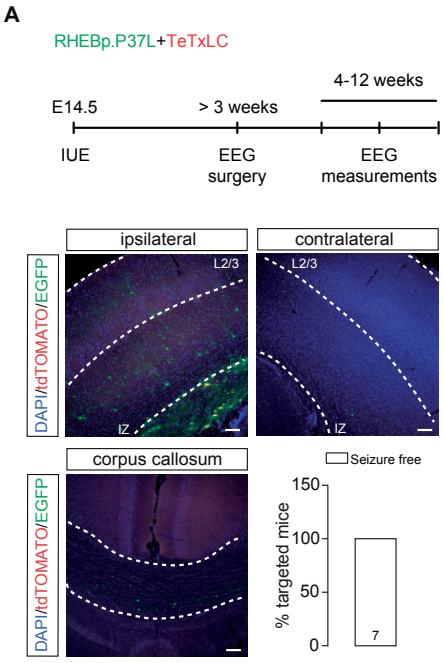

Figure 7A. Loss of axonal projections or blocking vesicle release of RHEBp.P37L expressing neurons is sufficient to stop seizures. (A) Schematic representation of the timeline of the IUE, EEG surgery and measurements upon expression of a RHEBp.P37L (construct expressing EGFP, in green) and a Tetanus toxin construct (TeTxLC, construct expressing tdTomato, in red). Example figures of ipsilateral targeted S1, corpus callosum and contralateral S1 of an *in utero* electroporated adult mouse at 12 weeks of age.) Note the absence of axonal projections on the contralateral side. The bar graph shows percentage of seizure-free targeted mice measured with EEG until 12 weeks of age. Numbers in the bar graph indicate number of mice.

that is active during embryonic development, we observed a complete block of callosal axonal growth in the contralateral SScx (**Figure 7A**). Furthermore, the mice targeted with the RHEBp.P37L and TeTxLC constructs did not develop any seizures, suggesting

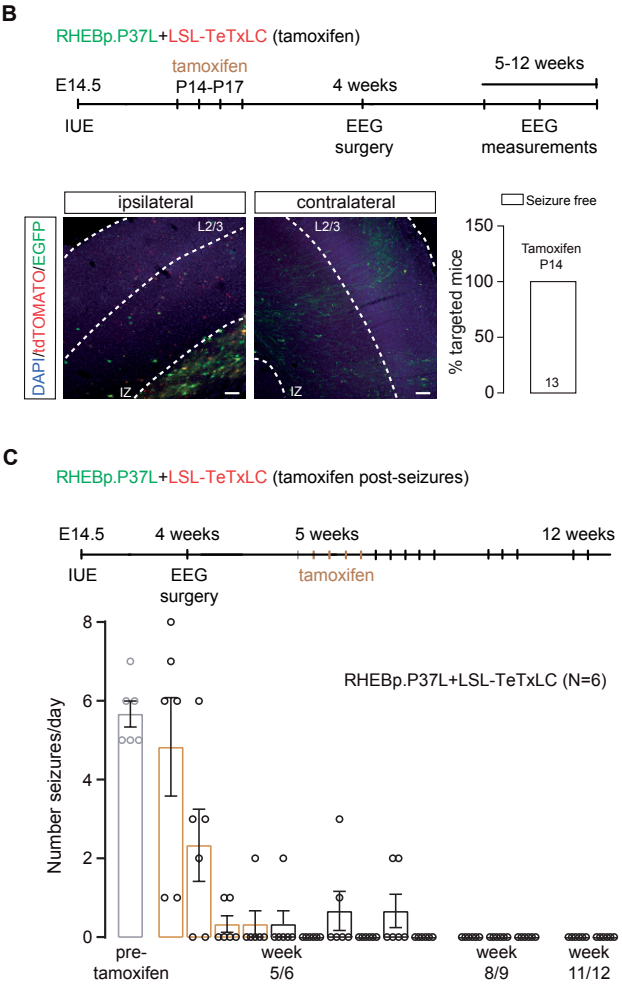

Figure 7B-C. Loss of axonal projections or blocking vesicle release of RHEBp.P37L expressing neurons is sufficient to stop seizures. (B) Schematic representation of the timeline of the IUE, tamoxifen administration, EEG surgery and measurements upon expression of a RHEBp.P37L (construct expressing EGFP, in green) and a LSL-Tetanus toxin construct (LSL-TeTxLC, in red). Example figures of ipsilateral targeted area (left) and contralateral cortex of an *in utero* electroporated adult mouse (12 weeks) injected with tamoxifen starting at P14 for 4 times. The bar graph shows percentage of targeted mice developing seizures upon early tamoxifen injection (P14) and measured with EEG until 12 weeks of age. Numbers in the bar graphs indicate number of mice. **(C)** Schematic representation of the timeline of the IUE, EEG surgery and measurements and tamoxifen administration upon expression of a RHEBp.P37L (construct expressing EGFP, in green) and a LSL-Tetanus toxin construct (LSL-TeTxLC, in red). Tamoxifen was administered for 4 consecutive days after seizures were first measured for full 24 hours and mice were continuously monitored with EEG for 10 consecutive days. Mice were measured again at week 8/9 and finally at week 11/12 before sacrifice. data are presented as mean ± SEM (Tamoxifen effect over time: $F(2.8, 14.20)=17.9$, $p<0.0001$, RM one-way ANOVA). Scale bars: 100 µm.

that the abnormal axonal connectivity might mediate the expression of seizures in our mouse model (**Figure 7A**).

The complete loss of callosal axonal branching upon embryonic activation of TeTxLC, prevented us from testing whether increased synaptic transmission drives seizure development. Therefore, to enable activation of the Tetanus toxin upon Tamoxifen injection at post-developmental stages, we generated an inducible LSL-TeTxLC construct and co-transfected this construct with RHEBp.P37L and the CAGG-ERT2CreERT2 vector (see **Figure 4A**). This allowed us to assess whether, once (abnormal) axonal projections are established, blocking vesicular release either prevents the development of seizures, or stops seizures once they have developed. Activation of the Tetanus toxin during postnatal development, but before seizure onset (P14), completely prevented the development of seizures while allowing the axons to grow and branch to the contralateral side (**Figure 7B**). Administering tamoxifen in 5 weeks old mice, when the cortical connectivity is complete and after the mice showed seizures revealed that epilepsy is not an irreversible process (**Figure 7C**). Already after 2 days of tamoxifen administration, 3 out of 6 mice stopped showing any seizures and 2 weeks after the last tamoxifen injection all mice appeared to be seizure free (**Figure 7C**). These results indicate that inhibiting synaptic transmission by blocking vesicular release from the targeted cells is enough to stop the occurrence of seizures in our mouse model.

Neurons in the contralateral homotopic cortical area in RHEBp.P37L expressing mice show increased excitability

To obtain more insight into the cellular mechanisms that underlie epilepsy in our model, we used whole-cell patch clamp to measure intrinsic physiological properties of the RHEBp.P37L expressing neurons, of (ipsilateral) neurons directly surrounding the targeted cells, and of the contralateral neurons in homotopic cortical areas (**Figure 8A**). Whole cell patch clamp recordings were performed by recording from pyramidal neurons in S1 of 3 weeks old mice. For the RHEBp.P37L expressing neurons (tdTomato positive), we recorded from neurons that managed to migrate out to L2/3 of S1 to be able to compare their physiological properties with 'empty vector' control cells in L2/3 that expressed the tdTomato gene without expressing the RHEBp.P37L protein (**Figure 8A**). RHEBp.P37L expressing neurons showed an increase in the capacitance (*Cm*) compared to empty vector control cells (**Figure 8B** and see **Supplementary Table 4** for statistics), which is consistent with the increase in soma size (median of control empty vector cells L2/3: 1.005, n cells=22; median RHEBp.P37L cells L2/3: 1.377, n cells=24; Mann-Whitney U = 105, p=0.0003, Two-tailed Mann-Whitney test, data not shown). Additionally, the membrane resistance (*Rm*) was decreased, whereas the resting membrane potential (*Vm*) was unchanged compared to empty vector control cells (**Figure 8B** and

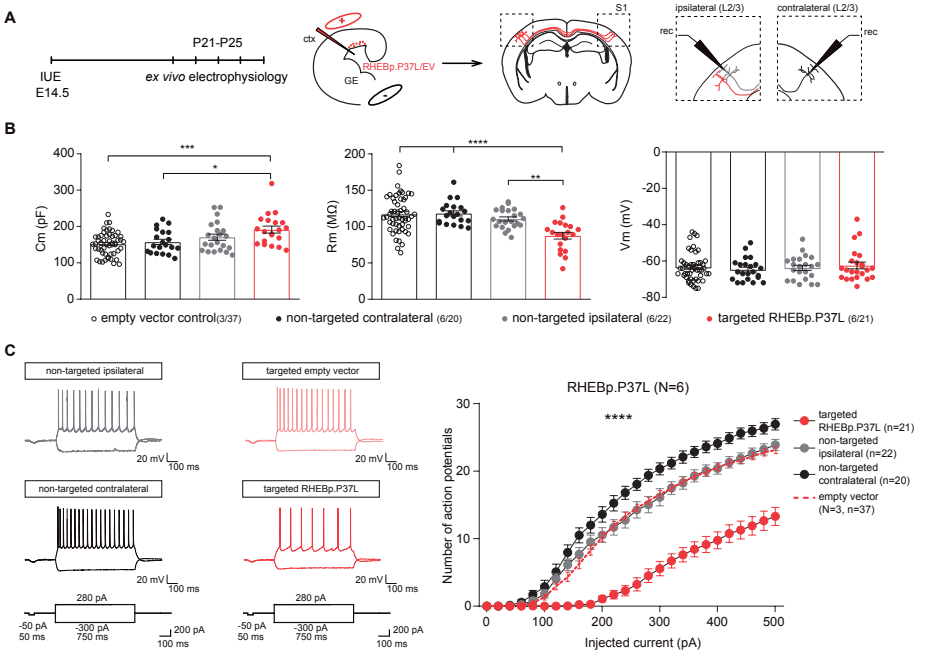

Figure 8A-C. Neurons in the contralateral homotopic cortical area in RHEBp.P37L mice show increased excitability that can be reversed by blocking vesicles release. (A) Schematic representation of the timeline and experimental conditions of the IUE and *ex vivo* whole-cell patch clamp recordings showing the targeted cells patched in the targeted S1, L2/3 and non-targeted L2/3 cells in the ipsilateral and contralateral sides. **(B)** Analysis of the passive membrane properties (capacitance [Cm], membrane resistance [Rm] and resting membrane potential [Vm]) of pyramidal cells in L2/3 (targeted and non-targeted) of control empty vector mice and targeted and non-targeted pyramidal cells in L2/3 of RHEBp.P37L mice; numbers in the legend indicate number of targeted mice (N=3, N=6) and number of cells (n=37, n=20, n=22, n=21) analyzed; data are presented as mean ± SEM and single data points indicate the values of each cell; for statistics see **Supplementary Table 4**). **(C)** Example traces and number of action potentials in response to increasing depolarizing currents; number of mice and cells is as indicated in **(B)**; data are presented as mean ± SEM and the red dashed line represents the pooled mean value ± SEM of targeted and non-targeted cells in empty vector control mice (N=3) shown separately in **Figure S5**, for comparison; for statistics see **Supplementary Table 4**).

see **Supplementary Table 4** for statistics). Depolarizing the neurons with increasing current injections, showed that the excitability of cells expressing the empty vector were not different from non-targeted neurons in the same mice or compared to non-targeted mice (**Figure S6A**). In contrast, RHEBp.P37L expressing neurons were hypoexcitable compared to control neurons measured in mice expressing the empty vector as well as to non-targeted neurons ipsilateral and contralateral (**Figure 8C** and see **Supplementary Table 4** for statistics), without a change in the threshold *Vm* to fire action potentials ($F(3, 94) = 0.59$, $p=0.62$, non-significant, One-way ANOVA). This result is again in agreement with the observed increased soma size and concomitant increased cell capacitance and decreased membrane resistance. RHEBp.P37L expressing neurons located in the nodule behave similarly to the RHEBp.P37L positive neurons that managed to migrate out to

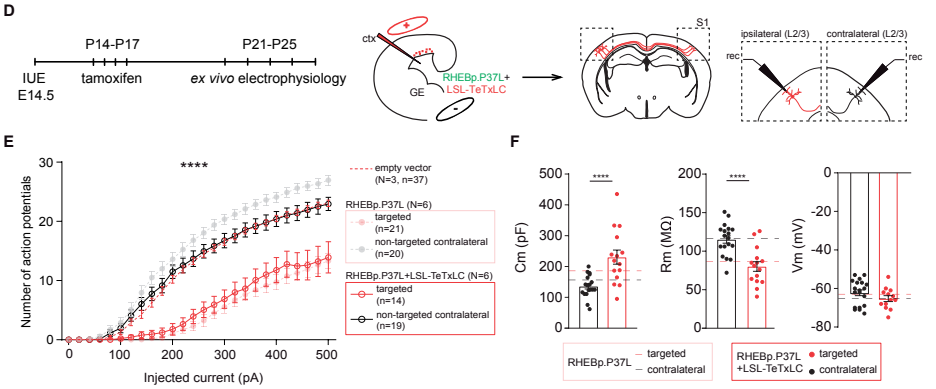

Figure 8D-F. Neurons in the contralateral homotopic cortical area in RHEBp.P37L mice show increased excitability that can be reversed by blocking vesicles release. (D) Schematic representation of the timeline and experimental conditions IUE, tamoxifen injections and *ex vivo* whole-cell patch clamp recordings in L2/3 of ipsilateral and contralateral S1 cortex. **(E)** Number of action potentials in response to increasing depolarizing currents of cells expressing both RHEBp.P37L and LSL-TeTxLC in L2/3 ipsilateral S1 and non-targeted cells in L2/3 contralateral S1; data are presented as mean ± SEM and dashed lines represent the mean values ± SEM of the pooled control cells from empty vector mice shown in **Figure S5** and of the RHEBp.P37L mice from **Figure 8C**, for comparison; N=number of mice, n=number of cells analyzed; for statistics see **Supplementary Table 5**. **(F)** Analysis of passive membrane properties (Cm, Rm and Vm) of pyramidal cells in L2/3 of mice targeted with RHEBp.P37L and LSL- TeTxLC in ipsilateral S1 and non-targeted cells on the contralateral side; data are presented as mean ± SEM and the dashed lines indicate the mean values of capacitance, membrane resistance and resting membrane potential of RHEBp.P37L targeted cells in L2/3 and contralateral cells shown in **Figure 8B**, for comparison; for statistics see **Supplementary Table 5**. * p<0.05, ** p<0.01, *** p<0.001, **** p<0.0001.

L2/3. Indeed, they exhibit a similar level of hypoexcitability (**Figure S6B**) and besides a small increase in membrane capacitance (*Cm*), similar passive properties as the L2/3 RHEBp.P37L positive neurons (**Figure S6C**). This suggests once more that the location of these cells is not the primary determinant of the physiological behavior of RHEBp.P37L expressing neurons. Notably, while ipsilateral non-transfected neurons surrounding the RHEBp.P37L expressing neurons in mice did not show changes in excitability compared to empty vector control, non-transfected neurons in L2/3 on the *contralateral* hemisphere showed a significant increase in excitability (**Figure 8C** and see **Supplementary Table 4** for statistics), suggesting that the ectopic cells affect long-range connected neurons.

To experimentally address if the aberrant connectivity could cause the increase in excitability in neurons on the contralateral cortex, we again made use of the inducible LSL-TeTxLC construct and co-transfected this construct with RHEBp.P37L and the CAGG-ERT2CreERT2 vector to enable activation of the Tetanus toxin upon Tamoxifen injection at post-developmental stages (See **Figure 7B**). Whole-cell patch clamp recordings revealed that activating the Tetanus toxin early during development (P14) (**Figure 8D**), completely reversed the hyperexcitability phenotype of the contralateral non-targeted cells observed in the RHEBp.P37L mice (**Figure 8E**) while the targeted cells

co-transfected with the RHEBp.P37L and the Tetanus toxin maintained the hypoexcitable phenotype and the basic properties observed in the RHEBp.P37L group (**Figure 8E-F** and see **Supplementary Table 5** for statistics). Taken together, these data indicate that the abnormal axonal connectivity caused by RHEBp.P37L overexpression is the primary driver of the hyperexcitability phenotype of contralateral L2/3 pyramidal neurons, which in turn could be the main driver of epilepsy.

DISCUSSION

In this study, we investigated the mechanisms behind the spontaneous tonic-clonic seizures in a mouse model for mTOR-related MCD, generated by spatially and temporally restricted overexpression of an mTOR-pathway related ID mutation in *RHEB* (Reijnders et al., 2017). We showed that the RHEBp.P37L mutant is resistant to inhibition by the TSC complex and that restricted overexpression causes mTORC1 hyperactivity and the development of heterotopia with typical cellular features of human MCD such as enlarged dysplastic neurons with altered morphology and mTORC1 activation. Furthermore, the presence of cortical malformations is accompanied by the development of spontaneous tonic-clonic seizures and alterations of the cortical brain dynamics that are rescued by administration of rapamycin, an mTOR inhibitor. Using a pharmacological and genetic approaches we showed that the mTOR-dependent epilepsy likely arises from altered axonal connectivity, through which long-range connected (supposedly healthy) neurons are affected. Indeed, blocking either mTOR activity or vesicle release from the relatively few neurons in which mTOR is hyperactive, is enough to stop or prevent seizures.

Similar to previously generated IUE mouse models of MCD, our model developed clear heterotopia, strikingly resembling focal human cortical malformations, associated with mTORC1 hyperactivity and reliable spontaneous seizures (Hanai et al., 2017; Hsieh et al., 2016; Lim et al., 2015; Park et al., 2018; Ribierre et al., 2018). The malformation in our mouse model is characterized by white matter heterotopia and neuronal misplacement across the different cortical layers, but maintains the molecular fingerprint belonging to L2/3 neurons. However, it is difficult to categorize it as a specific type of MCD because it expresses characteristics of both FCD type I and type IIa (with no Balloon cells observed) (Barkovich et al., 2012). Nonetheless, the targeted cells have features common to several types of mTOR dependent MCD, including enlarged and dysplastic cells with mTORC1 hyperactivation (Crino, 2011).

Previously it has been shown that brain wide activation of the mTOR pathway is sufficient to induce seizures in the absence of any cortical malformations (Abs et al., 2013).

However, these models do not address the role of mTOR signaling in MCD related pathophysiology. To address that, an elegant IUE mouse model was generated which expressed the constitutive active RHEBp.S16H protein. These mice showed a migration deficit resembling FCD and spontaneous epilepsy (Hsieh et al., 2016). Using this mouse model, it was also shown that the presence of a cortical malformation is not necessary to induce seizures (Hsieh et al., 2016). Notably, these mice did not show epilepsy when the SScx was targeted, and hence the investigators suggested that the SScx might be a non-epileptogenic area. This is in contrast with our mouse model using the human ID-related RHEBp.P37L mutant and with several studies that manipulate other components of the mTOR pathway, where targeting the SScx reliably induces seizures (Baek et al. 2015, D'Gama et al 2017; Lim et al., 2015; Hu et al., 2018, Ribierre et al., 2018).

Our mouse model offers a good tool to test novel AEDs *in vivo*. However, considering the variability in the number of seizures exhibited, it will be beneficial to focus on different parameters when assessing the potential therapeutic efficiency of AEDs. For this purpose, the *theta* frequency oscillation, which we found to be affected and normalized upon rapamycin treatment, represents a good biomarker for assessing the potential therapeutic value of treatments in our mouse model (Chauvière et al., 2009; Milikovsky et al., 2017).

Everolimus and rapamycin (Sirolimus) have been shown in randomized controlled trials to be beneficial for treating TSC associated epilepsy (Overwater et al., 2019; Overwater et al., 2016), but not for treating the cognitive deficits (Krueger et al., 2017; Iris E. Overwater et al., 2019). In this study we investigated the potential of a short prenatal rapamycin treatment in improving both malformation defects and epilepsy, but preventing the possible side effects (developmental delays and poor gain weight) (Tsai et al., 2013). We showed that a 2-day rapamycin treatment during a critical time point of prenatal development can cause a substantial improvement of the cortical malformation defects and prevent the development of seizures in almost 50% of the cases. Future studies will have to assess if a combination of prenatal and postnatal treatment with rapamycin in mice can be sufficient to significantly reduce the epileptic events, as shown for brain malformations, without causing major side effects (Tsai et al., 2013; Way et al., 2012).

Surgery is often an alternative to AEDs for treating MCD-related epilepsy. Human electrophysiological findings show that seizures can often have multiple starting points, besides the brain lesion itself (Chassoux et al., 2008; Major et al., 2009). Therefore, from a clinical point of view, it is important to determine whether seizures originate from cells surrounding the cortical malformation. Even though EEG and LFP do not have the spatial resolution to assess the primary epileptogenic zone in our model, we showed

that persistent mTORC1 hyperactivation in the targeted cells is the primary cause of epilepsy. In fact, genetically removing the RHEBp.P37L mutant, either before or after seizure development, was sufficient to prevent or stop the epilepsy.

Surprisingly, when exploring the causes of epileptogenesis, we observed that the neurons expressing the RHEBp.P37L both in layer 2/3 and in the heterotopic nodule are hypoexcitable, which is consistent with the increase in soma size but does not provide an obvious physiological explanation for the seizures observed in our mouse model. This is in sharp contrast with human studies that show that cytomegalic neurons from resected brain tissue of MCD patients are hyperexcitable and might therefore play a central role in the generation of epileptic discharges (Cepeda et al., 2005; 2013). However, we observed a clear increase of intrinsic excitability and in postsynaptic responses upon optogenetic stimulation of RHEBp.P37L cells in contralateral homotopic S1 cells. This suggests that RHEBp.P37L expressing cells induce cellular changes in anatomically connected neurons, which might underlie, or at least exacerbate, the epilepsy phenotype. This would further support the hypothesis suggested in literature that the interaction between abnormal and normal cells in the brain results in an epileptic focus and might explain also the insurgence of epilepsy in more mild cases of MCD (Abdijadid et al., 2015; Cepeda et al., 2006; Blumcke et al., 2009; Mathern et al., 2007). Notably, the alterations we observed in our model extend well beyond the cells surrounding the cortical malformation, as we found physiological changes were present contralateral to the targeted side. Considering the abnormal axonal connectivity seen in our mouse model, this raises the possibility that other anatomically connected cortical and subcortical areas not analyzed in this study might also be affected, thereby providing an explanation for how a small percentage of targeted hypoexcitable cells, independent of their location, can lead to generalized epilepsy. Therefore, we propose a model in which subtle microscopic alterations and aberrant connectivity, either through an increase in synaptic connections or an increase in the strength of synaptic contacts caused by mTOR hyperactivity, are sufficient to drive epileptogenesis.

By increasing axonal connectivity, RHEBp.P37L expressing neurons could potentially alter synaptically connected neurons through neurotransmitter release. But they can also affect neighboring (including synaptically non-connected) cells through the release of extracellular vesicles such as exosomes (Budnik et al., 2016). The vesicles might mediate pathogenicity as was previously shown *in vitro* (Patel et al., 2015). Our results show that although most electrophysiological parameters of the ipsilateral non-targeted cells are unaltered compared to control, there is a small trend for an increased membrane capacitance (Cm) in these cells (see **Figure 8B**). Whether this is caused by a non-cell autonomous effect, or a secondary effect due to presence of seizures, remains to be in-

vestigated. With the use of Tetanus toxin, we showed that the effects on the contralateral side are directly driven by the abnormal enhanced axonal connectivity, since blocking vesicle release specifically from the RHEBp.P37L expressing neurons, completely rescued the epilepsy and normalized the intrinsic firing properties of the non-targeted contralateral neurons. Tetanus toxin is primarily used to block synaptic transmission due to its effect on neurotransmitter release, acting on the SNARE complex protein VAMP2 (Schiavo et al., 1992). Given the observed increased axonal connectivity and the finding that distally connected cells were physiologically affected, this strongly suggests that neurotransmitter mediated communication is primarily causing the epilepsy phenotype. This notion is further supported by the optogenetics experiments that showed increase postsynaptic responses upon stimulating the RHEBp.P37L expressing neurons. While it has been proposed that specific tetanus insensitive VAMP proteins (such as VAMP7) are involved in the release of exosomes into the extracellular space (Fader et al., 2009), we cannot exclude the additional contribution of other types of vesicles to the observed phenotype. Recently it was shown that Tetanus toxin sensitive SNAREs also drive the release of BDNF (Shimojo et al., 2015). Some studies suggest that BDNF might contribute to epileptogenesis (Binder et al., 2001), suggesting that abnormal BDNF signaling could further increase the epileptic phenotype seen in our mouse model. Understanding the contribution of these different signaling pathways is important for the development of targeted therapeutic strategies to treat MCD associated epilepsy.

In summary, making use of a hyperactive RHEB mutant that was previously identified in patients with ID, megalencephaly and epilepsy, as a model for human mTOR-related MCD associated epilepsy, we show that a few neurons with increased mTOR activity can be the driving force behind MCD-related epilepsy through aberrant connectivity, resulting in increased excitability of distant non-targeted neurons which can be reversed by blocking vesicular release.

MATERIALS AND METHODS

Mice

Unless subjected to a surgical procedure, all experimental mice were kept group-housed in IVC cages (Sealsafe 1145T, Tecniplast) with bedding material (Lignocel BK 8/15 from Rettenmayer) on a 12/12 hr light/dark cycle at 21°C (±1°C), humidity at 40-70% and with food pellets (801727CRM(P) from Special Dietary Service) and water available *ad libitum*. For the neuronal cultures, FvB/NHsD females were crossed with FvB/NHsD males (both ordered at 8-10 weeks old from Envigo). For the IUE, females FvB/NHsD (Envigo) were crossed with males C57Bl6/J (ordered at 8-10 weeks old from Charles River). Both females

and males from the *in utero* electroporation litters were included in the experiments and no prescreening for successful electroporation was performed before recruitment in the studies. Young (starting from P7) and adult mice were used and the specific age for each experiment is indicated either in the results section or in the figures' legends. Activation of the ERT2CreERT2 fusion protein (Matsuda and Cepko, 2007) was achieved by intraperitoneal administration of tamoxifen for 4 consecutive days (0.1 mg/g of bodyweight) dissolved in sunflower oil (20 mg/ml) at the ages specified in the results section and in the figures. For inhibition of the mTOR pathway, rapamycin (Sigma-Aldrich) was dissolved in dimethylsulfoxide (10 mg/ml) and injected intraperitoneally in adult mice (> 4 weeks) for postnatal experiments (10 mg/kg) or subcutaneously in pregnant females (E15.5/E16.5) for prenatal experiments (1 mg/kg).

All animal experiments were conducted in accordance with the European Commission Council Directive 2010/63/EU (CCD approval AVD1010020172684).

HEK293T cell cultures and transfection

HEK293T cells were grown in Dulbecco's modified Eagle medium (DMEM; Lonza, Verviers, Belgium) supplemented with 10% fetal bovine serum, 50 U/ml penicillin and 50 µg/ml streptomycin in a 5% CO_2 humidified incubator at 37°. Before transfection, 1 x 10^5 HEK293T cells were seeded per well of 6-well culture dishes and transfected 24 hours later with expression constructs encoding the *RHEB* variants (0.2 µg), the S6K reporter (0.2 µg), *TSC1* (0.2 µg) and *TSC2* (0.2 µg) using Lipofectamine 2000 (Invitrogen, Carlsbad, CA, USA). To ensure that a total of 0.8 µg plasmid DNA was added per well, empty pcDNA3 vector was included where necessary. The day after transfection, the growth medium was replaced with DMEM without glucose and incubated for a further 4 hours prior to harvesting and western blot analysis.

Western blotting

After transfection, HEK293T cells were transferred on ice, washed with PBS (4 °C) and lysed in 70 µl 50 mM Tris-HCl pH 7.6, 100 mM NaCl, 50 mM NaF, 1% Triton X100 in the presence of protease and phosphatase inhibitors (Complete, Roche Molecular Biochemicals, Woerden, The Netherlands). Cell lysates were subjected to immunoblotting using the following primary antibodies: anti-RHEB mouse monoclonal (Groenewoud et al., 2013), anti-TSC1 and TSC2 rabbit polyclonal (Van Slegtenhorst et al., 1998), T389-phosphorylated S6K (1A5, #9206, Cell Signaling Technology), and rabbit anti-myc (#2272, Cell Signaling Technology), all 1:1000. Primary antibody binding was assessed by incubation with goat anti-rabbit (680 nm) and anti-mouse (800 nm) conjugates (1:15000, Li-Cor Biosciences, Lincoln, USA) followed by detection on an Odyssey near-infrared scanner (Li-Cor Biosciences).

Neuronal primary hippocampal cultures and transfection

Primary hippocampal neuronal cultures were prepared from FvB/NHsD wild type mice according to the procedure described in (Banker and Goslin, 1988). Neurons were transfected at 1 day *in vitro* (DIV1) with the following DNA constructs: control empty vector (1.8 µg per coverslip) and RHEB p.P37L (2.5 µg per coverslip). Plasmids were transfected using Lipofectamine 2000 according to the manufacturer's instructions (Invitrogen).

Plasmids

cDNA encoding the *RHEB* (NM_005614.3) c.110C>T (p.P37L) mutation was synthesized by GeneCust. The c.46-47CA>TG (p.S16H) variant was generated by site-directed mutagenesis (Invitrogen) using the following primers: Fw 5' – gcgatcctgggctaccggCAtgtggggaaatcctcatt – 3' and Rev 5' – aatgaggatttccccacaTGccggtagcccaggatcgc – 3'. All *RHEB* gene variants were cloned in our dual promoter expression vector using AscI and PacI restriction sites (Reijnders et al., 2017) and the empty vector used as control refers to the dual promoter expression vector without a gene inserted and expressing either tdTOMATO or EGFP (specified in the figures or in the figures' legends). Expression constructs for TSC1, TSC2 and a myc-tagged S6K reporter were as described previously (Dufner Almeida et al., 2019). The following DNA plasmids were obtained from Addgene: pGEMTEZ-TeTxLC (Addgene plasmid #32640; http://n2t.net/addgene:32640; RRID:Addgene_32640) (Yu et al., 2004); RV-CAG-DIO-EGFP (Addgene plasmid #87662; http://n2t.net/addgene:87662; RRID:Addgene_87662) (Ciceri et al., 2013); pCAG-ERT2CreERT2 (Addgene plasmid #13777; http://n2t.net/addgene:13777; RRID:Addgene_13777) (Matsuda and Cepko, 2007); pCAGGS-ChR2-Venus (Addgene plasmid #15753; http://n2t.net/addgene:15753; RRID:Addgene_15753) (Petreanu et al., 2007). The TeTxLC was isolated by PCR using the following primers: Fw 5' – taagcaggcgcgccaccatgccgatcaccatcaacaa – 3' and Rev 5' – gccatggcggccgcgggaattcgat – 3' and inserted in our dual promoter expression vector using AscI and NotI restriction sites. To generate the loxP-STOP-loxP (LSL) constructs (loxP-STOP-loxP-*RHEB* p.P37L and loxP-STOP-loxP-TeTxLC) the LSL sequence was obtained from the Ai6 CAG-Floxed ZsGreen in Rosa 26 targeting vector (Addgene plasmid #22798; http://n2t.net/addgene:22798; RRID:Addgene_22798) using multiple cloning sites and inserted just after the CAGG promoter and before the beginning of the gene in our dual promoter expression vector containing either *RHEB*p.P37L or TeTxLC. The floxed *RHEB* p.P37L construct was generated by introducing two loxP site sequences before the CAGG promoter and at the end of the *RHEB*p.P37L gene, with the same orientation to ensure proper deletion. To achieve this, the following couples of oligonucleotides were used for annealing: Fw 5'- cgcgtATAACTTCGTATAGCATACATTATACGAAGTTATg - 3', Rev: 5'- ctagcATAACTTCGTATAATGTATGCTATACGAAGTTATa - 3'; Fw: 5'- taaATAACTTCGTATAGCATACATTATACGAAGTTATg - 3', Rev: 5'- tcgacATAACTTCGTATAATGTATGCTATACGAAGTTATttaat - 3'.

In utero electroporation

IUE was performed as described previously (Saito and Nakatsuji, 2001). Pregnant FvB/NHsD mice at E14.5 of gestation were used to target the progenitor cells giving rise to pyramidal cells of the layer 2/3. Each *RHEB* DNA construct (including the LSL and floxed conditions) was diluted to a final concentration of 0.5 µg/µl in fast green (0.05%), while other plasmids were diluted to a concentration of 1.5-2 µg/µl. The DNA solution was injected into the lateral ventricle of the embryos while still *in utero*, using a glass pipette controlled by a Picospritzer ® III device. When multiple constructs were injected, a mixture of plasmids was prepared to achieve a final concentration of 1.5-2 µg/µl, keeping the *RHEB* concentration constant throughout all the experiments. To ensure proper electroporation of the injected constructs (1-2 µl) into the progenitor cells, five electrical square pulses of 45V with a duration of 50 ms per pulse and 150 ms inter-pulse interval were delivered using tweezer-type electrodes connected to a pulse generator (ECM 830, BTX Harvard Apparatus). The positive pole was placed to target the developing somatosensory cortex. Animals of both sexes were used to monitor seizure development, for *ex vivo* electrophysiology experiments, or for histological processing with no exclusion criteria determined by a postnatal screening of the targeting area.

Immunostainings

For immunocytochemistry analysis, neuronal cultures were fixed 3 days post-transfection with 4% paraformaldehyde (PFA)/4% sucrose, washed in PBS and incubated overnight at 4°C with primary antibodies in GDB buffer (0.2% BSA, 0.8 M NaCl, 0.5% Triton X-100, 30mM phosphate buffer, pH7.4). Mouse pan anti-SMI312 (1:200, BioLegend, #837904) was used to stain for the axon and, after several washings in PBS, donkey anti-mouse-Alexa488 conjugated was used as secondary antibody diluted in GDB buffer for 1 hour at room temperature (1:200, Jackson ImmunoResearch). Slides were mounted using mowiol-DABCO mounting medium.

For the staining of brain tissue sections, mice were deeply anesthetized with an overdose of Nembutal and transcardially perfused with 4% PFA in PB. Brains were extracted and post-fixed for 1 hour in 4% PFA. They were then embedded in gelatin and cryoprotected in 30% sucrose in 0.1 M Phosphate Buffer (PB) overnight, frozen on dry ice, and sectioned using a freezing microtome (40 µm thick). Immunofluorescence was performed on free-floating sections that were first washed multiple times in PBS and blocked in 10% normal horse serum (NHS) and 0.5% Triton X-100 in PBS for 1 hour at room temperature. Primary antibodies diluted in PBS containing 2% NHS and 0.5% Triton X-100 were added at room temperature overnight. The day after, sections were washed three times with PBS and secondary antibodies were added diluted in PBS containing 2% NHS and 0.5% Triton X-100. After washing in PBS and 0.05 M PB, sections were counterstained

with 4′,6-diamidino-2-phenylindole solution (DAPI, 1:10000, Invitrogen) before being washed in PB 0.05 M and mounted on slides using chromium (3) potassium sulfate dodecahydrate (Sigma-Aldrich) and left to dry. Finally, sections were mounted on glass with mowiol (Sigma-Aldrich).

Biocytin labelling was achieved by fixating the patched slices overnight in 4% PFA in PB at 4°. Slices were then washed multiple times in PBS and incubated with Alexa488-Streptavidin (1:200; #016-540-084, Jackson ImmunoResearch) or AlexaCy5-Streptavidin (1:200; #016-170-084, Jackson ImmunoResearch) overnight at 4°. The next day, after washing in PBS and 0.05 M PB, sections were counterstained with DAPI (1:10000, Invitrogen) and mounted on glass with mowiol (Sigma-Aldrich).

When performing Nissl stainings, few selected free floating sections corresponding to the Somatosensory cortex were mounted on glass using chromium (3) potassium sulfate dodecahydrate (Sigma-Aldrich) and left to dry overnight. Slides were stained in 0.1 % Cresyl Violet for 4-10 minutes, then rinsed briefly in tap water to remove excess stain, dehydrated in increasing percentages of alcohol, cleared with xylene and covered using Permount (Fisher Scientific).

The primary antibodies used in this study to stain for the specific targets indicated for each experiment in the figures' legends were: anti-rabbit pS6 (Ser 240/244), 1:1000; Cell signaling, catalog #5634; anti-rabbit RFP, 1:2000; Rockland, catalog 600-401-379; anti-rabbit RHEB, 1:1000, Proteintech Group Inc., catalog 15924-1-AP; anti-rabbit CUX1, 1:1000; Proteintech Group Inc., catalog 11733-1-AP; anti-rat CTIP2, 1:200; Abcam, catalog ab18465; anti-rabbit NeuN, 1:2000; Millipore catalog ABN78 (RRID: AB_10807945); anti-mouse SATB2, 1:1000; Santa cruz, catalog sc-81376; anti-rabbit synapsin 1, 1:1000; Merck Millipore, catalog #AB1543P; anti-guinea pig VGLUT1, 1:1000; Merck Millipore, catalog #AB5905; anti-rabbit GABA, 1:500; Sigma-Aldrich, catalog #A2052 and anti-rabbit PV, 1:1000; Swant, catalog #PV 27; Secondary antibodies used were: donkey anti rabbit 488, catalog #711-545-152; donkey anti rabbit 647, catalog #711-605-152; donkey anti rabbit Cy3, catalog #711-165-152; donkey anti mouse 488, catalog #715-545-150; donkey anti mouse 647, catalog #715-605-150; donkey anti rat Cy5, catalog #712-175-150; donkey anti guinea pig 647, catalog #706-605-148; all from Jackson ImmunoResearch, 1:200.

Immuno-electron microscopy

Mice *in utero* electroporated with either empty vector or RHEBp.P37L were anesthetized at P21 with an overdose of nembutal (i.p.) and transcardially perfused with 10 ml saline and subsequently 50 ml 4% PFA and 0.5% glutaraldehyde in cacodylate buffer. The brain was removed and post-fixed overnight in 4% PFA. 80-µm thick coronal sections

were cut on a vibratome (Technical Products International, St. Louis, USA) and sections corresponding to the somatosensory cortex where further processed for DAB staining. dtTomato positive terminals were visualized by incubating the sections with the avidin-biotinperoxidase complex method (ABC) for 24-48 hrs (Vector Laboratories, USA) and subsequently developed with DAB (0.05%, Life Technologies) as the chromogen. The vibratome sections were rinsed and post-fixed in 1% osmium tetroxide, stained with 1% uranyl acetate, dehydrated and embedded in araldite (Durcupan ACM; Fluka, Buchs, Switzerland). Ultrathin (50-70 nm) sections were cut on an ultramicrotome (Leica, Wetzlar, Germany), mounted on formvar-coated copper grids and contrasted with 2% uranyl acetate and 1% lead citrate (Fluka). The grids were subsequently rinsed twice with TBST and incubated for 1 h at room temperature in goat anti-rabbit IgG labeled with 10 nm gold particles (Aurion) diluted 1:25 in TBST. Somatosensory cortex sections containing tdTomato positive terminals were photographed using an electron microscope (Philips, Eindhoven, Netherlands) and the size of the terminals was analyzed using FIJI software.

LFP and EEG recordings

Starting from 3 weeks of age surgeries were performed according to the procedures described in (Koene et al., 2019; Kool et al., 2019). After at least three days of recovery from the EEG surgical procedure, mice were connected to a wireless EEG recorder (NewBehavior, Zurich, Switzerland) for 24 hours per day for at least two consecutive days (one session of recordings). EEG recordings were manually assessed by two different researchers blind for the genotypes to check for occurrence of seizures, defined as a pattern of repetitive spike discharges followed by a progressive evolution in spike amplitude with a distinct post-ictal depression phase, based on the criteria described in (Kane et al., 2017). If no seizures were detected during the first week *post*-surgery, mice were recorded for another session of 48-56 hr for a maximum of four sessions over four weeks *post*-surgery. During the days in which no EEG recordings were performed, mice were monitored daily to assess for the presence of behavioural seizures and discomfort.

For the LFP recordings, two days after the surgical procedure, mice were head-fixed to a brass bar suspended over a cylindrical treadmill to allow anaesthesia-free recording sessions and placed in a light-isolated Faraday cage as described in (Kool et al., 2019). Mice were allowed to habituate to the set-up before proceeding to the recording. LFP measurements were acquired every day in sessions of 20-30' for five or eight consecutive days, using the Open Ephys platform with a sampling rate of 3 kS/s and a band pass filter between 0.1 and 200 Hz. For the power spectrum analysis, the average power density spectrum of all the days of recording was obtained using MATLAB software (MathWorks; RRID:SCR_001622). The mean relative power was calculated over four frequency bands

relative to the total power: delta (2–4 Hz), theta (4–8 Hz), beta (13–30 Hz), and gamma (30–50 Hz).

At the end of each experiment, mice were sacrificed for immunohistological analysis to assess electrodes' positioning, amount of targeting and efficiency of cre-dependent recombination when tamoxifen was administered.

Ex vivo slice electrophysiology for excitability

P21-P25 mice of both sexes *in utero* electroporated with the plasmids specified in the figures and in the legends for each experiment were anaesthetized with isoflurane before decapitation. The brain was quickly removed and submerged in ice cold cutting solution containing (in mM): 110 Choline Chloride, 2.5 KCl, 1.2 NaH_2PO_4, 26 $NaHCO_3$, 25 D-glucose, 0.5 $CaCl_2$, 10 $MgSO_4$. Acute 300 µm coronal slices were made of the somatosensory cortex using a vibratome (HM650V, Microm) while being saturated with 95% O_2/5% CO_2. The slices were immediately transferred to a submerged slice holding chamber and incubated at ±34°C for 5 min before being transferred to a second slice holding chamber also kept at ±34°C. The second holding chamber contained the same artificial cerebrospinal fluid (ACSF) as was used during all recordings and contained (in mM): 125 NaCl, 3 KCl, 1.25 NaH_2PO_4, 26 $NaHCO_3$, 10 glucose, 2 $CaCl_2$, 1 $MgSO_4$. During the slicing procedure and experimental recordings, slices were saturated with 95% O_2/5% CO_2. Slices recovered for an hour at room temperature before starting the experiment. After the experiment, slices were fixed in 4% PFA overnight and then transferred to PBS until further processing. Whole-cell patch clamp recordings were obtained from the soma of visually identified L2/L3 pyramidal neurons from the S1 cortex with an upright microscope using IR-DIC optics (BX51WI, Olympus, Tokyo, Japan). Targeted cells in the ipsilateral side were identified by the presence of either tdTomato or GFP, depending on the experiment, elicited by an Olympus U-RFL-T burner. All recordings were done under physiological temperatures of 30± 1 °C. Patch clamp pipettes were pulled from standard wall filament borosilicate glass to obtain electrodes with a tip resistance between 2-4 MΩ. All recordings were performed using a Multiclamp 700B (Molecular Devices, Sunnyvale, CA, USA) and digitized by a Digidata 1440A (Molecular Devices, Sunnyvale, CA, USA). For the current clamp recordings, pipets were filled with a K-gluconate internal solution containing (in mM): 125 K-gluconate, 10 NaCl, 10 HEPES, 0.2 EGTA, 4.5 MgATP, 0.3 NaGTP and 10 Na-phosphocreatine. For analysis of cell morphology, biocytin (5%) was added to the intracellular solution. The final solution was adjusted to a pH of 7.2–7.4 using KOH and had an osmolarity of 280 ± 3. After getting a seal of at least 1 GΩ, whole cell configuration was obtained by applying brief negative pressure together with a short electric pulse. Prior to breaking in, cell capacitance was compensated. Series resistance was monitored but not corrected. Recordings with an unstable series resistance and higher

than 20 MΩ were rejected. Membrane potentials were not corrected for liquid junction potential. Resting membrane potential was measured immediately after break in.

Each sweep started with a small and short hyperpolarizing step (-50 pA, 50 ms) to monitor access resistance. Action potentials were triggered by square step current injections into the patched neurons while holding them at -70 mV. Steps were 750 ms long and started at -300 pA with increments of 20 pA. The number of action potentials and action potential properties were analyzed using Clampfit 10.7.0.3 (Molecular Devices, LLC, USA). For each cell, the first action potential at rheobase was analyzed. The threshold was calculated by plotting the first derivative of the trace. The threshold was defined when the first derivative was lower than 10 mV/ms. Series resistance was calculated offline for each cell by plotting the difference in voltages between baseline and the hyperpolarizing steps. A linear line was plotted to visualize passive current only. The tau was calculated by fitting a standard exponential on the end of the hyperpolarizing steps. From tau and series resistance, capacitance was calculated.

Ex vivo slice electrophysiology for optogenetics

P21-P25 mice of both sexes *in utero* electroporated either with the RHEBp.P37L and pCAGGS-ChR2-Venus plasmids or the empty vector and pCAGGS-ChR2-Venus plasmids (Petreanu et al., 2007), were anaesthetized with isoflurane before decapitation. The brain was quickly removed and submerged in ice cold cutting solution containing (in mM): 93 NMDG, 93 HCl, 2.5 KCl, 1.2 $NaHPO_4$, 30 $NaHCO_3$, 25 glucose, 20 HEPES, 5 Na-ascorbate, 3 Na-pyruvate, 2 Thiourea, 10 MgSO4, 0.5 CaCl2, 5 N-acetyl-L-Cysteine (osmolarity 310 ± 5; bubbled with 95% O_2 / 5% CO_2) (Ting et al., 2014). Next, 250 µm thick coronal slices were cut using a Leica vibratome (VT1000S). For the recovery, brain slices were incubated for 5 min in slicing medium at 34 ± 1˚C and subsequently for ~40 min in ACSF (containing in mM: 124 NaCl, 2.5 KCl, 1.25 Na_2HPO_4, 2 $MgSO_4$, 2 $CaCl_2$, 26 $NaHCO_3$, and 20 D–glucose, osmolarity 310 ± 5mOsm; bubbled with 95% O_2 / 5% CO_2) at 34 ± 1˚C. After recovery brain slices were stored at room temperature. For all recordings, slices were bathed in 34 ± 1˚C ACSF (bubbled with 95% O_2 / 5% CO_2). Whole-cell patch-clamp recordings were recorded with an EPC-10 amplifier (HEKA Electronics, Lambrecht, Germany) and sampled at 20 kHz. Resting membrane potential and input resistance were recorded after whole-cell configuration was reached. Recordings were excluded if the series resistance or input resistance (RS) varied by >25% over the course of the experiment. Voltage and current clamp recordings were performed using borosilicate glass pipettes with a resistance of 3-5 MΩ that was filled with K-gluconate-based internal solution (in mM: 124 K-gluconate, 9 KCl, 10 KOH, 4 NaCl, 10 HEPES, 28.5 sucrose, 4 Na_2ATP, 0.4 Na_3GTP (pH 7.25-7.35; osmolarity 290 ± 5mOsm)). Recording pipettes were supplemented with 1 mg/ml biocytin to check the location of the patched cells with histological staining. Cur-

rent clamp recordings were corrected offline for the calculated liquid junction potential of -10.2 mV.

Full-field optogenetic stimulation (470 nm peak excitation) was generated by the use of a TTL-pulse controlled pE2 light emitting diode (CoolLED, Andover, UK). Light intensities at 470 nm were recorded using a photometer (Newport 1830-C equipped with an 818-ST probe, Irvine, CA) at the level of the slice. To trigger neurotransmitter release from targeted axons we delivered a 1 ms light pulse with an intensity of 99.8 mW/mm^2 at a frequency of 0.1 Hz. To ensure that we recorded action potential-driven neurotransmitter release most experiments were concluded by bath application of 10 µM tetrodotoxin (TTX), which blocked all post-synaptic responses in the recorded pyramidal neurons.

Imaging and analysis

Images of Nissl stained sections were acquired in brightfield with a Nanozoomer scanner (Hamamatsu, Bridgewater, NJ) at a 40X resolution using the NDP.view2 software. All immunofluorescent images were acquired using a LSM700 confocal microscope (Zeiss). For the analysis of the axons *in vitro*, at least ten distinct confocal images from two different neuronal batches were taken from each coverslip for each experiment (20X objective, 0.5 zoom, 1024x1024 pixels; neurons were identified by the red immunostaining signal). The simple neurite tracer plugin from the FIJI ImageJ software was used for the analysis of the axonal length and branches. Overview images of the coronal sections were acquired by tile scan with a 10X objective. Zoom in images of the targeted area (ipsilateral) and contralateral S1 were taken using a 10X objective. For the migration analysis, confocal images (10X objective, 0.5 zoom, 1024x1024 pixels) were taken from 2 – 3 non-consecutive sections from at least 2/3 electroporated animals per condition. Images were rotated to correctly position the cortical layers, and the number of cells in different layers were counted using the 'analyze particles' plugin of FIJI. The results were exported to a spreadsheet for further analysis. Cortical areas from the pia to the ventricle were divided into 10 bins of equal size and the percentage of tdTomato-positive cells per bin was calculated. The counting of the number of targeted cells per mouse was performed by selecting three non-consecutive (250-300 um apart) targeted sections, with one section being the most targeted and the other two immediately frontal and caudal from this. The total number of tdTomato+ cells per section was quantified and an average number of those three sections per mouse was calculated to obtain a representative value corresponding to the amount of targeting per mouse. The soma size analysis was performed on z-stacks images acquired using a 20X objective, 1 zoom, 1024x1024 pixels, of the targeted cells in both empty vector control and *RHEB*p.P37L coronal sections. A ROI around each targeted cell in maximum intensity projection pictures was defined using the FIJI software and the area of the soma was measured using

the 'Measure' option in ImageJ. The analysis of the size of EM boutons was performed using the FIJI software. For the analysis of pS6 intensity levels, confocal images (10X objective, 0.5 zoom, 1024x1024 pixels) of the ipsilateral and contralateral S1 cortex were acquired with the same master gain from both control and RHEB groups previously stained together against pS6 (240/244). The overall intensity level of the staining for each picture was measured using the 'RGB measure' plugin of FIJI and the values of each ipsilateral side were normalized against the corresponding contralateral side and plotted as averaged values. The analysis of the fluorescent intensity of the axonal branches over the contralateral cortical layers, was obtained from 3-4 matched coronal sections from at least 3 different animals per group with comparable amount of targeting. The axonal arborization was measured selecting the S1/S2 border, drawing a straight segmented line with adjusted width and length and resized in 1000 bins, and using the 'plot profile' option of the analyze section of FIJI to measure the fluorescent intensity of the tdTomato signal over the different layers. The values obtained for each section were exported to a spreadsheet were they were normalized against the mean background fluorescent intensity calculated on a non-targeted, cortical area of fixed size and plotted as averaged values over 10 bins of equal size. For the analysis of the morphology of biocytin filled pyramidal cells and ectopic cells in the nodule labelled with streptavidin-488 or streptavidin-Cy5, z-stacks images were taken using a 20X objective, 0.5 zoom, 1024x1024 pixels, to include the dendritic tree. Maximum intensity projection pictures were analyzed using the SynD software for the MATLAB platform to automatically detect the dendritic morphology and perform Sholl analysis (Schmitz et al., 2011).

Statistics

Normality of the distribution for the different experiments was determined using either the Wilk–Shapiro test or the Kolmogorov-Smirnov test. Statistical analysis was performed using a one-way ANOVA (or corresponding non-parametric Kruskal-Wallis test), two-way repeated-measures ANOVA or mixed-effects analysis, Student's t test (or corresponding non-parametric Mann-Whitney test) and correlation/association analysis. The specific test used for each experiment and relative significance are specified in the figures' legends, in the supplementary tables or in the results section (when data are not shown in a figure). For all statistical analyses α was set at 0.05. Values are represented as average ± SEM or as median, minimum and maximum values (specified in the figures' legends). No samples or mice were excluded from the final analysis. Group sizes, biological replicates, number of cells, samples or brain sections are indicated in the figures and their corresponding legends. All statistical tests were performed either using GraphPad Prism 8.0 (RRID: SCR_002798) or SPSS Statistics v25.0 (RRID:SCR_002865).

ACKNOWLEDGEMENTS

The authors would like to thank Elize Haasdijk, Charlotte de Konink, Hang Le Ha, Anne Polman and Chi Yeung for their technical contribution and Minetta Elgersma-Hooisma for managing the mouse colony. We also would like to thank Enzo Nio for advice regarding the code used to analyze the data and Steven Kushner and Dick Jaarsma for fruitful discussions. This work was supported by the Dutch TSC foundation (STSN) (G.M.v.W) and the Dutch Epilepsy foundation (Epilepsie fonds) (Y.E.).

COMPETING INTERESTS

The authors declare no competing interests.

AUTHOR CONTRIBUTIONS

Conceptualization, M.P.O., Y.E. and G.M.v.W.; Methodology, M.P.O. , Y.E. and G.M.v.W.; Investigation, M.P.O., L.M.C.K., C.B.S., M.N.; Formal Analysis: M.P.O., L.M.C.K., C.B.S., M.N.; Software, M.d.B.v.V.; Writing – Original Draft: M.P.O. and G.M.v.W.; Writing – Review & Editing: M.P.O., L.M.C.K., C.B.S., M.N., M.d.B.v.V., Z.G., Y.E., G.M.v.W.; Visualization: M.P.O.; Supervision: G.M.v.W.; Funding Acquisition: Y.E. and G.M.v.W.

SUPPLEMENTARY TABLES

Supplementary Table 1. Statistical analysis related to Figure 1A

Test applied: Two-way ANOVA

Source of variation	F (DFn, DFd)	P value	P value summary
TSC -/+	F (1, 35) = 13.38	0.0008	***
Group condition	F (3, 35) = 42.39	<0.0001	****
Interaction	F (3, 35) = 2.377	0.0866	ns

Post hoc: Sidak's multiple comparisons test

	Comparison	Adjusted P value	P value summary
TSC – *vs* TSC+	RHEB wt	0.0486	*
	RHEBp.S16H	0.0049	**
	RHEBp.P37L	0.9791	ns
	Empty vector control	0.9621	ns

Post hoc: Tukey's multiple comparisons test

	Comparison	Adjusted P value	P value summary
TSC –	RHEB wt vs RHEBp.S16H	0.0205	*
	RHEB wt vs RHEBp.P37L	0.0001	***
	RHEB wt vs Empty vector control	0.0151	*
	RHEBp.S16H vs RHEBp.P37L	0.2859	ns
	RHEBp.S16H vs Empty vector control	<0.0001	****
	RHEBp.P37L vs Empty vector control	<0.0001	****
TSC+	RHEB wt vs RHEBp.S16H	0.3696	ns
	RHEB wt vs RHEBp.P37L	<0.0001	****
	RHEB wt vs Empty vector control	0.7682	ns
	RHEBp.S16H vs RHEBp.P37L	0.0009	***
	RHEBp.S16H vs Empty vector control	0.0603	ns
	RHEBp.P37L vs Empty vector control	<0.0001	****

ns: non-significant, * $p<0.05$, ** $p<0.01$, *** $p<0.001$, **** $p<0.0001$

Supplementary Table 2. Statistical analysis related to Figures 2E-F and Figure S2D-E

Test applied LFP: Two-way RM ANOVA

Source of variation	F (DFn, DFd)	P value	P value summary
Band Frequency	F (1.100, 53.92) = 353.7	P<0.0001	****
Group condition	F (2, 49) = 1.011	P=0.3714	ns
Interaction Band frequencies/ group condition	F (6, 147) = 7.456	<0.0001	****
Tukey's multiple comparisons test	**Comparison**	**Adjusted P value**	**P value summary**
delta	empty vector control vs. RHEBp.P37L	0.0479	*
	empty vector control vs. RHEBp.P37L - rapamycin	0.9614	ns
	RHEBp.P37L vs. RHEBp.P37L - rapamycin	0.0856	ns
theta	empty vector control vs. RHEBp.P37L	0.0024	**
	empty vector control vs. RHEBp.P37L - rapamycin	0.8288	ns
	RHEBp.P37L vs. RHEBp.P37L - rapamycin	0.0053	**
beta	empty vector control vs. RHEBp.P37L	0.2043	ns
	empty vector control vs. RHEBp.P37L - rapamycin	0.0637	ns
	RHEBp.P37L vs. RHEBp.P37L - rapamycin	0.0071	**
gamma	empty vector control vs. RHEBp.P37L	0.0039	**
	empty vector control vs. RHEBp.P37L	0.8465	ns
	empty vector control vs. RHEBp.P37L - rapamycin	0.0016	**

Test applied ratio theta/delta: Kruskal-Wallis test

Kruskal-Wallis H	df	P value	P value summary
13.37	2	0.0012	**
Dunn's multiple comparisons test	**Comparison**	**Adjusted P value**	**P value summary**
ratio theta/delta	empty vector control vs. RHEBp.P37L	0.0169	*
	empty vector control vs. RHEBp.P37L - rapamycin	>0.9999	ns
	RHEBp.P37L vs. RHEBp.P37L - rapamycin	0.0036	**

ns: non-significant, * $p<0.05$, ** $p<0.01$, **** $p<0.0001$

Supplementary Table 3. Statistical analysis related to Figure 6

Test applied: Two-tailed Mann-Whitney test

Parameter/ Layer	Unit	Mean ± SEM	Mann-Whitney U P value	P value summary
Amplitude L2/3	pA	control: 54.54±10.77 RHEBp.P37L: 356.80±54.06	U = 7 p=0.0004	***
Amplitude L5	pA	control: 132.0±45.71 RHEBp.P37L: 365.70±97.59	U = 34 p=0.0226	*
Charge L2/3	pA*ms	control: 353.40±82.25 RHEBp.P37L: 3079.0±516.90	U = 6 p=0.0003	***
Charge L5	pA*ms	control: 1552.0±816.10 RHEBp.P37L: 3658.0±1007.0	U = 36 p=0.0308	*
Vm L2/3	mV	control: -77.83±1.50 RHEBp.P37L: -76.43±2.22	U = 51.50 p=0.9851	ns
Vm L5	mV	control: -73.0±0.55 RHEBp.P37L: -73.53±1.16	U = 70 p=0.7933	ns
R series L2/3	MΩ	control: 11.97±0.94 RHEBp.P37L: 11.88±0.71	U = 51 p=0.9576	ns
R series L5	MΩ	control: 14.91±1.11 RHEBp.P37L: 12.46±0.86	U = 47 p=0.1289	ns
Rm L2/3	MΩ	control: 105.50±10.92 RHEBp.P37L: 97.08±8.69	U = 45 p=0.6324	ns
Rm L5	MΩ	control: 131.50±22.75 RHEBp.P37L: 130.70±8.22	U = 57 p=0.3383	ns

ns: non-significant, * $p<0.05$, *** $p<0.001$

Supplementary Table 4. Statistical analysis related to Figure 8B-C

Test applied on basic properties: One-way ANOVA

Basic properties	F (DFn, DFd)	P value	P value summary
Cm	F (3, 111) = 6.525	P=0.0004	***
Rm	F (3, 111) = 10.47	P<0.0001	****
Vm	F (3, 111) = 0.3580	P=0.7834	ns

Post hoc: Tukey's multiple comparisons test

Comparison	Cm Adjusted P Value	Cm Summary	Rm Adjusted P Value	Rm Summary	Vm Adjusted P Value	Vm Summary
control vs. contralateral RHEBp.P37L	0.9218	ns	0.9970	ns	0.9028	ns
control vs. ipsilateral RHEBp. P37L	0.1568	ns	0.6241	ns	0.9974	ns

control vs. targeted RHEBp.P37L	0.0003	***	<0.0001	****	0.9585	ns
contralateral RHEBp.P37L vs. ipsilateral RHEBp.P37L	0.6314	ns	0.6506	ns	0.9751	ns
contralateral RHEBp.P37L vs. targeted RHEBp.P37L	0.0171	*	<0.0001	****	0.7394	ns
ipsilateral RHEBp.P37L vs. targeted RHEBp.P37L	0.2425	ns	0.0033	**	0.9337	ns

Test applied on excitability (RHEBp.P37L vs control): Mixed-effects model analysis

Source of variation	F (DFn, DFd)	P value	P value summary
Injected current	F (2,770, 265.6) = 1228	<0.0001	****
Group condition	F (3, 96) = 44.64	<0.0001	****
Interaction current/condition	F (75, 2397) = 29.02	<0.0001	****

Post hoc: Tukey's multiple comparisons test

Main effect: group condition	Mean difference	Adjusted P Value	P value summary
targeted RHEBp.P37L vs. ipsilateral RHEBp.P37L	7.349	<0.0001	****
targeted RHEBp.P37L vs. contralateral RHEBp.P37L	-0.2674	<0.0001	****
targeted RHEBp.P37L vs. control	-2.948	<0.0001	****
ipsilateral RHEBp.P37L vs. contralateral RHEBp.P37L	-7.616	<0.0001	****
ipsilateral RHEBp.P37L vs. control	-10.3	0.9447	ns
contralateral RHEBp.P37L vs. control	-2.681	<0.0001	****

ns: non-significant, * $p<0.05$, ** $p<0.01$, *** $p<0.001$, **** $p<0.0001$

Supplementary Table 5. Statistical analysis related to Figure 8E-F

Test applied on basic properties: One-way ANOVA

Basic properties	F (DFn, DFd)	P value	P value summary
Cm	F (3, 69) = 10.43	P<0.0001	****
Rm	F (3, 69) = 16.01	P<0.0001	****
Vm	F (3, 73) = 0.8526	P=0.4697	ns

Post hoc: Tukey's multiple comparisons test

Comparison	Cm Adjusted P Value	Cm Summary	Rm Adjusted P Value	Rm Summary	Vm Adjusted P Value	Vm Summary
targeted RHEBp.P37L vs. targeted RHEBp.P37L/LSL-TeTxLC	0.1347	ns	0.7179	ns	0.6715	ns
targeted RHEBp.P37L vs. contralateral RHEBp.P37L/LSL-TeTxLC	0.0087	**	0.0004	***	0.9996	ns

targeted RHEBp.P37L/LSL-TeTxLC vs. contralateral RHEBp.P37L/LSL-TeTxLC	<0.0001	****	<0.0001	****	0.7032	ns
targeted RHEBp.P37L/LSL-TeTxLC vs. contralateral RHEBp.P37L	0.0006	***	<0.0001	****	0.6425	ns
contralateral RHEBp.P37L/LSL-TeTxLC vs. contralateral RHEBp. P37L	0.5782	ns	0.9675	ns	0.9971	ns
targeted RHEBp.P37L vs. targeted RHEBp.P37L/LSL-TeTxLC	0.1347	ns	0.7179	ns	0.6734	ns

Test applied on excitability: Mixed-effects model analysis

Excitability RHEBp.P37L/ LSL-TeTxLC	F (DFn, DFd)	P value	P value summary
Injected current	F (2.357, 251.5) = 870.7	<0.0001	****
Group condition	F (4, 107) = 3714	<0.0001	****
Interaction current/condition	F (100, 2667) = 21.99	<0.0001	****

Post hoc: Tukey's multiple comparisons test

Comparison	Mean difference	Adjusted P Value	P value summary
control vs. targeted RHEBp.P37L/LSL-TeTxLC	6.556	<0.0001	****
control vs. contralateral RHEBp.P37L/LSL-TeTxLC	-0.3674	0.9490	ns
targeted RHEBp.P37L vs. targeted RHEBp.P37L/LSL-TeTxLC	-0.7935	0.4371	ns
targeted RHEBp.P37L vs. contralateral RHEBp.P37L/LSL-TeTxLC	-7.717	<0.0001	****
contralateral RHEBp.P37L vs. targeted RHEBp.P37L/LSL-TeTxLC	9.504	<0.0001	****
contralateral RHEBp.P37L vs. contralateral RHEBp.P37L/LSL-TeTxLC	2.581	0.0002	***

ns: non-significant, ** $p<0.01$, *** $p<0.001$, **** $p<0.0001$

SUPPLEMENTARY FIGURES

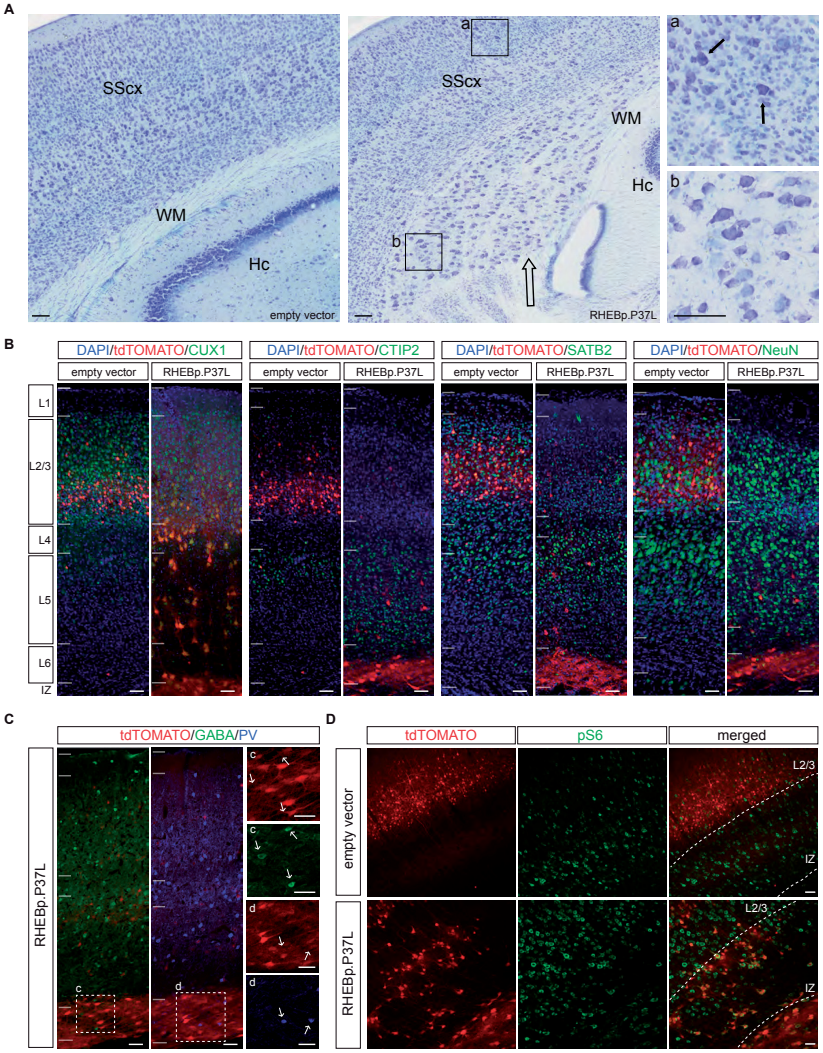

Figure S1. Cells overexpressing the RHEBp.P37L construct show enlarged soma size, maintain the molecular identity of pyramidal cells L2/3 and show mTOR hyperactivity. (A) Nissl staining of coronal brain sections from 5 weeks old mice shows the presence of a clear heterotopia (indicated by the empty arrow) in the white matter (WM) of RHEBp.P37L targeted somatosensory cortex (SScx) compared to the empty vector control situation. Boxes *a* and *b* represent magnifications of layer 2 (*a*) and the heterotopia (*b*) highlighting the targeted dysplastic and enlarged cells (indicated by the arrows); Hc: hippocampus; scale bars:100 µm. **(B)** Representative overview images of coronal sections (SScx) of empty vector control and RHEBp.P37L targeted mice (5 weeks old) probed with common cortical layers markers CUX1 (L2/3 marker), CTIP2 (L5 marker), SATB2 (cortical projection neuron marker) or NeuN (mature neuron marker). **(C)** Representative images of coronal sections (SScx) of RHEBp.P37L targeted mice (5 weeks old) probed with GABA and PV markers for interneurons; magnification pictures of the heterotopia in (*c*) and (*d*) show that GABA and PV positive cells (indicated by the white arrows) are not positive for tdTomato **(D)** overview of the targeted SScx of empty vector control and RHEBp.P37L targeted mice stained for pS6-240, a readout of mTOR activity; IZ: intermediate zone. Scale bars: 50 µm.

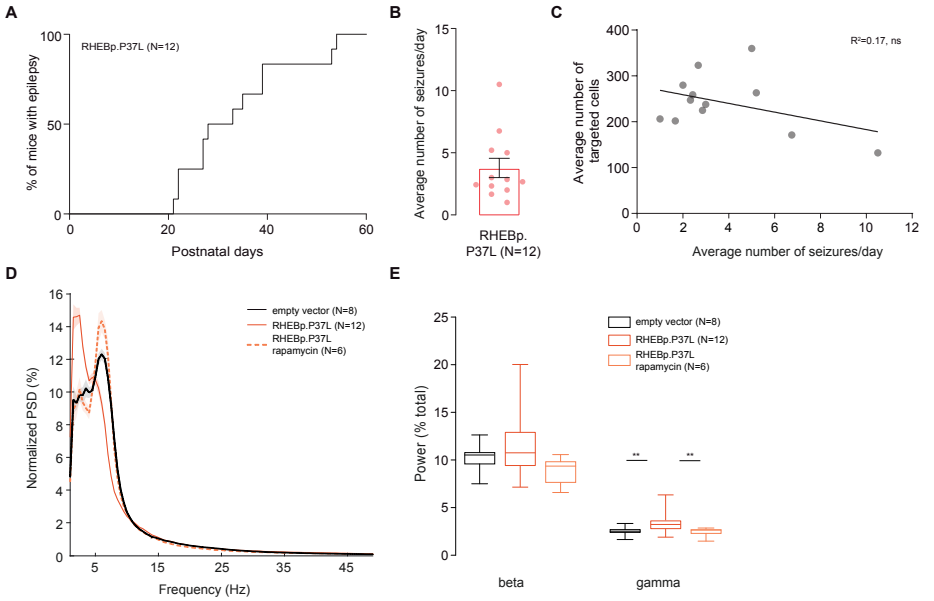

Figure S2. RHEBp.P37L mice show spontaneous seizures and alterations in the LFP gamma frequency band. (A) Onset of seizure activity for the RHEBp.P37L group (mean ± SEM: 33.33 days ± 3.26; N indicates number of mice). **(B)** Average number of seizures per day of mice showing seizure activity measured with EEG until 9-12 weeks of age; each data point represents the average per mouse measured at least over two separate sessions of recordings (3 days each) **(C)** Simple scatter correlation graph with best fit regression line (Y = -9.5*X + 278.1), showing no correlation between the average number of targeted cells (measured over 3 anatomically matched non-consecutive targeted slices per mouse) and the average number of seizures per animal shown in figure (B); r(10) = -0.41, $p = 0.19$, two-tailed Pearson's correlation; ns, non-significant. **(D)** Extended Normalized Power spectrum density (PSD) shown in Figure 3E to include the *beta* and *gamma* frequencies (till 50 Hz); data are presented as mean (thick lines) ± SEM (shadows); N in the legend indicates number of mice per group. **(E)** Quantification of the *beta* (13-30 Hz) and *gamma* (30-50 Hz) frequency bands over the total power; box plots represent minimum and maximum value with median; N in the legend indicates number of mice per group. See **Supplemental Table 2** for statistics; ** $p<0.01$.

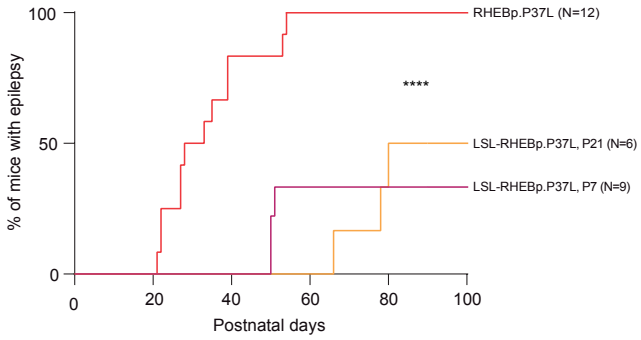

Figure S3. Delayed seizure development in LSL-RHEBp.P37L mice injected with tamoxifen.
Onset of seizure activity for the LSL-RHEBp.P37L groups after treatment with tamoxifen (4 injections) starting at either P7 (purple line, mean ± SEM: 50 days ± 0) or at P21 (yellow line, mean ± SEM: 74.6 days ± 4.37) compared to the RHEBp.P37L group (red line) (Chi square (2) = 25.33, $p < 0.0001$; Log-rank test; N indicates number of mice).

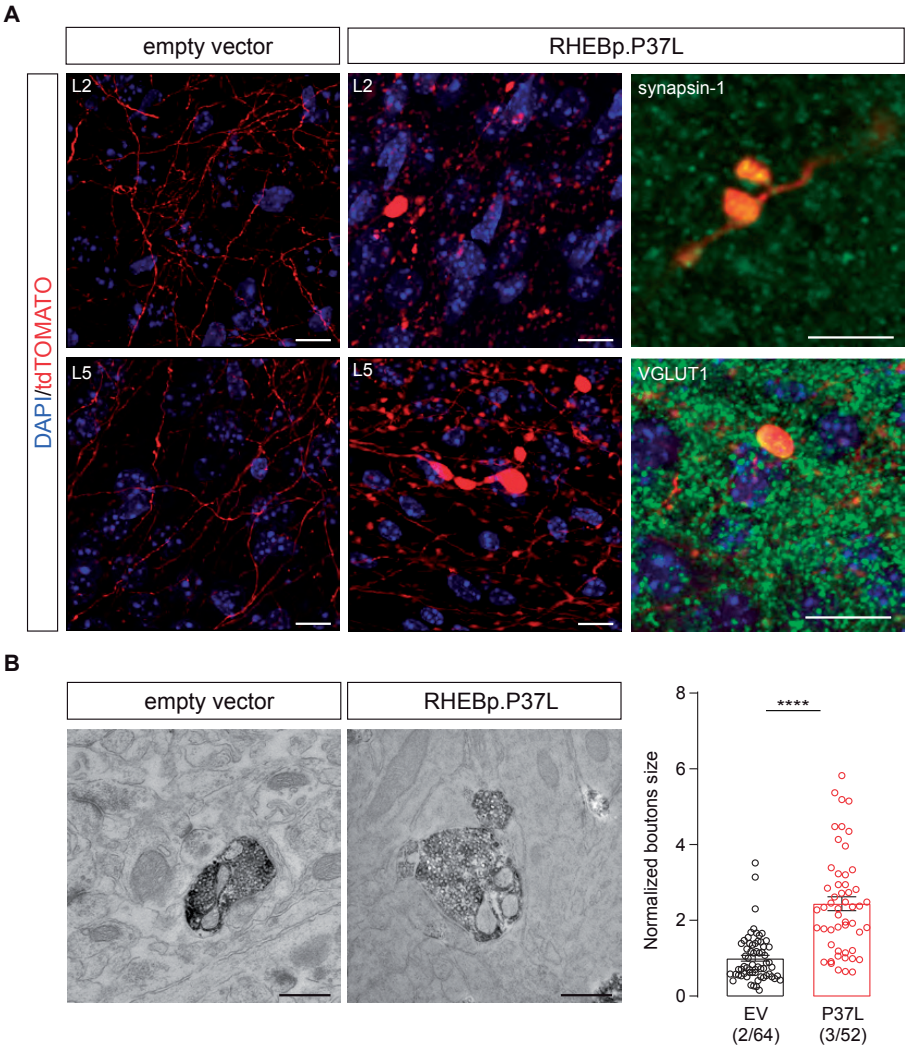

Figure S4. Synaptic *boutons* in RHEBp.P37L mice have an altered morphology and are bigger in size. (A) Representative zoomed in pictures of the contralateral S1 (L2/3 and L5) of both control empty vector mice and RHEBp.P37L mice (P50); note the presence of enlarged terminals and *boutons* in RHEBp.P37L expressing cells that are positive for Synapsin-1 (a marker for synaptic vesicles, in green) and VGLUT1 (a marker for glutamatergic neurons, in green). Scale bars: 10 µm (overview), 5 µm (*boutons*). **(B)** Representative EM pictures of contralateral S1 *boutons* of control empty vector mice and RHEBp.P37L mice (P21) and quantification of the size, showing increase in size in the RHEBp.P37L mice (Mann-Whitney U = 465, $p < 0.0001$, ****, two-tailed Mann-Whitney test); numbers in the graph indicate number of animals/number of boutons analyzed. Scale bars: 500 nm.

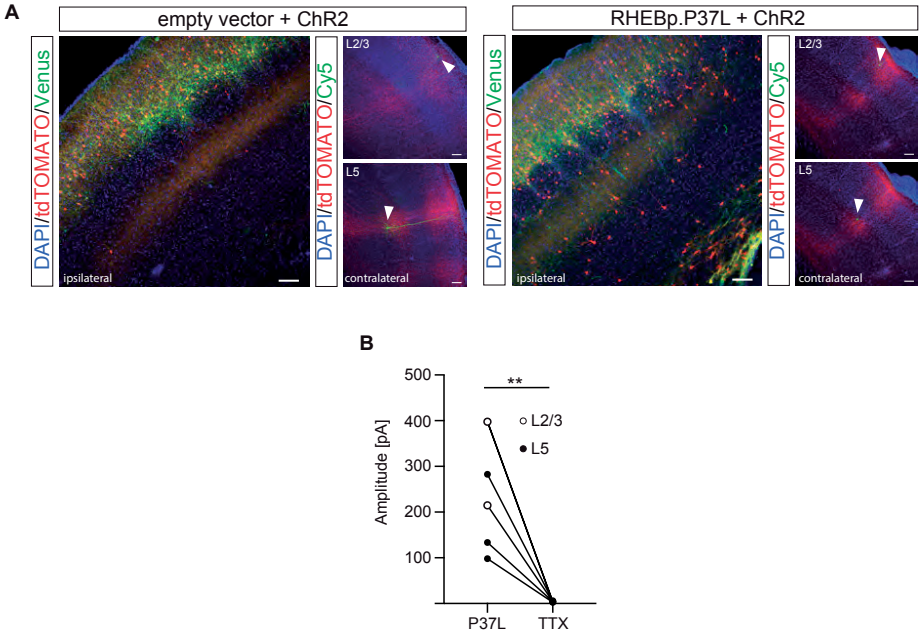

Figure S5. Action potentials driven neurotransmitter release in RHEBp.P37L/Channelrhodopsin-2 expressing fibers.

(A) Representative images showing expression of channelrhodopsin-2 (ChR2, in green) and either empty vector (left) or RHEBp.P37L (right) constructs in red (tdTomato+ cell) on the ipsilateral targeted S1; examples of contralateral patched cells in either L2/3 or L5 filled with byocitin and stained with streptavidin-Cy5 are shown for each condition and indicated with arrowheads (note that for the contralateral pictures ChR2-Venus is not shown and green represents byocitin-Cy5); scale bars: 100 µm. **(B)** Wash-in of tetrodotoxin (TTX) in RHEBp.P37L slices proves the action potential dependence of photostimulation evoked responses in L2/3 and L5; t(5)=4.8, p=0.005, two-tailed paired t-test; ** $p<0.01$.

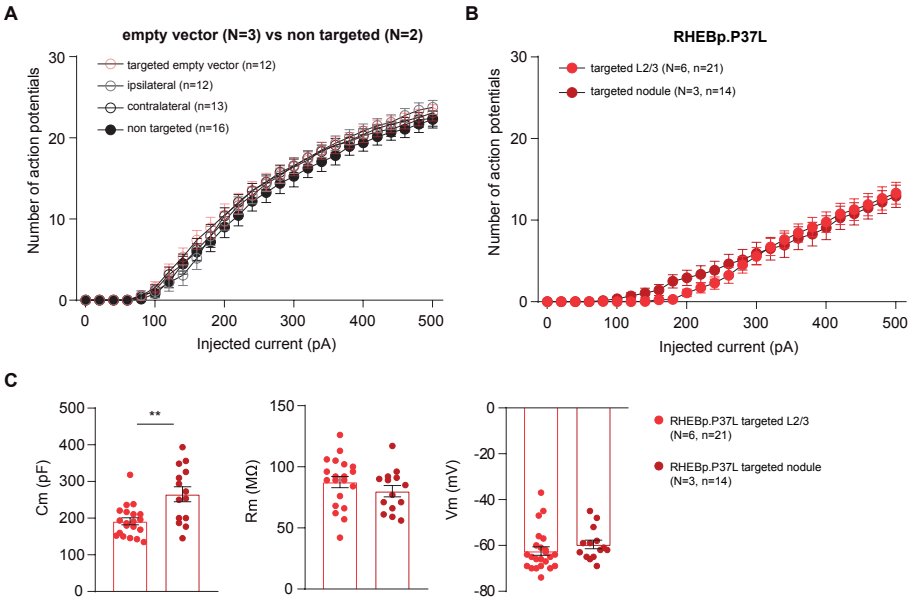

Figure S6. Excitability phenotype of control cells from empty vector control and non-targeted mice and physiological characterization of cells targeted with the RHEBp.P37L in the heterotopic nodule.
(A) Number of action potentials in response to increasing depolarizing currents shows that there is no difference in excitability in empty vector targeted mice or non-targeted mice; data are presented as mean ± SEM; interaction injected current/group condition: F (75, 1225) = 0.7275, non-significant; mixed-effects analysis; N = number of mice and n = number of cells analyzed. **(B)** Number of action potentials in response to increasing depolarizing currents shows that there is no difference in excitability in cells targeted with RHEBp.P37L based on their location (L2/3 and nodule); data are presented as mean ± SEM; interaction injected current/group condition: F (25, 824) = 0.95, non-significant; mixed-effects analysis; N = number of mice and n = number of cells analyzed. **(C)** Analysis of the passive membrane properties (capacitance [Cm], membrane resistance [Rm] and resting membrane potential [Vm]) of pyramidal cells in L2/3 and cells in targeted cells in the nodule of RHEBp.P37L mice; note the increase in capacitance of the targeted cells in the nodule, suggesting a bigger soma size compared to L2/3 cells; Cm: t(32) = 3.6; p = 0.001, two-tailed unpaired t test; Vm: t(35) = 1.02; p = 0.31, two-tailed unpaired t test; Rm: t(32) = 1.11; p = 0.28, two-tailed unpaired t test; numbers in the legend indicate number of targeted mice (N) and number of cells (n) analyzed; data are presented as mean ± SEM and single data points indicate the values of each cell.

Creativity is Intelligence Having Fun.

—Albert Einstein

Chapter 7

A Novel Subtype of Cerebro-Spinal Projection Neuron that Innervates Cerebellar Nuclei

Carmen B. Schäfer
Anan Li
Bas van Hoogstraten
Bibi Bouwen
Hana Hasanbegovic
Nico Flierman
Youri Adolfs
Jeroen Pasterkamp
Wilfried Fj van IJcken
Chris De Zeeuw
Freek E. Hoebeek
Zhenyu Gao

ABSTRACT

Cortico-spinal neurons in the motor cortex form a well described cell population with distinct anatomical connectivity patterns and genetic profiles. Here, we characterize a undescribed cerebellar projecting subpopulation of cortico-spinal neurons in the motor cortex. Initially, we use retrograde viral tracing to map the inputs to the deep cerebellar nuclei and discover cerebellar-projecting cells in layer V of prefrontal cortex, insular cortex and motor cortex. We focus on the motor cortical population and use rabies virus mediated tracing and fMOST-guided single axon reconstruction for the anatomical input-output mapping of cerebro-cerebellar projecting cells, respectively. Here, we find that their downstream innervation pattern compares to the general population of motor cortical cortico-spinal neurons while they receive their input from local cortical networks. In addition, we use RNA-sequencing to compare the genetic profile of cerebellar-projecting and brainstem-projecting cortico-spinal neurons and find that both cell populations form two distinct subpopulations. Our anatomical data provides first evidence for direct cerebro-cerebellar connectivity and suggests that this subtype of motor cortical projection neurons provides a direct and ipsilateral pathway for cerebro-cerebellar communication that contrast the well described disynaptic route via the pontine nuclei.

INTRODUCTION

Volitional movements are programmed to achieve particular goals, which require the integration of sensory inputs as well as outcome related error correction (Guo *et al.*, 2014; Herzfeld *et al.*, 2015; Galiñanes *et al.*, 2018). This is achieved by dedicated neuronal communication across inter-connected brain areas in cerebral cortices, cerebellum and brainstem (Svoboda & Li, 2017; Arber & Costa, 2018). As an example for the multi-regional dependence of movement execution, the goal-directed forelimb reaching movements is dependent on motor cortex, cerebellum and brain stem, each of which contribute to specific aspects of motor control (Esposito *et al.*, 2014; Galiñanes *et al.*, 2018; Becker & Person, 2019; Sauerbrei *et al.*, 2020; Ruder *et al.*, 2021).

The execution and learning of skilled movements requires an intact motor cortex as acute motor cortical inactivation (Guo *et al.*, 2015; Morandell & Huber, 2017; Galiñanes *et al.*, 2018) and motor cortical lesion (Ramanathan *et al.*, 2006) results in deficits in movement execution. Volitional movements are mediated by dynamically interacting neuronal subpopulations that intermingle in layer 2/3 and layer 5 of motor cortex (Harris & Shepherd, 2015; Economo *et al.*, 2018; Winnubst *et al.*, 2019). Correlating neuronal activity with behavioral performance during movement execution or during the learning and adaptation of skilled movements identifies neuronal subclasses with selective population dynamics. During movement execution, specific phases of motor performance such as motor planning, movement onset and sensory integration are accompanied by selective activity patterns and distinct neuronal response types (Li *et al.*, 2015; Elsayed *et al.*, 2016; Chen *et al.*, 2017; Guo *et al.*, 2017*b*; Lara *et al.*, 2018). Within motor cortical layer 5, the movement initiative command is assumed to be mediated by cortico-spinal neurons (CSN) as they form the final stage for cortical output and send direct projections into the brainstem and the spinal chord (Lemon, 2008). More specifically, spatially defined groups of CSNs are assumed to encode distinct aspects of movement associated motor skills, as region-specific manipulations indicate that CSNs from caudal or rostral forelimb motor cortical areas control reaching or grasping (Wang *et al.*, 2017). During the learning of skilled movements subsets of CSNs in layer V (L5) are selectively active while other subpopulations are selectively active during quiescence (Komiyama *et al.*, 2010; Peters *et al.*, 2014, 2017). This suggests that cortical activity is dynamic during learning and that movements early and late in learning are represented by different activity patterns. Therefore, monitoring the success and error of the outcome of movements is essential for the adaptation of movement and learning processes. It has been shown that outcomes of previous successes and failures is reported in post-movement activity in late and prolonged spike patterns that are independent of movement kinematics or reward signals (Levy et al., 2020).

Motor cortical CSNs innervate a wide collection of subcortical targets such as basal ganglia, thalamus as well as motor related centers in the midbrain and brainstem such as the superior colliculus, pontine nuclei and reticular formation (Lemon, 2008; Harris & Shepherd, 2015; Economo *et al.*, 2017; Winnubst *et al.*, 2019; Peng *et al.*, 2020). This wide-spread subcortical projection pattern allows the motor cortex to inform downstream targets about upcoming motor plans and to initiate executive motor commands (Wang *et al.*, 2017). Nevertheless, the exact relationship between the functional specification of individual CSN types and their downstream projection targets remain to be disentangled.

On the other side of the brain, the cerebellum has been postulated to contribute to the fine-tuning of motor commands by utilizing either forward or inverse models of sensory feedback errors (de Zeeuw *et al.*, 1988; Simpson *et al.*, 1996; Ruigrok & Voogd, 2000; Soetedjo *et al.*, 2008; Brooks *et al.*, 2015; Herzfeld *et al.*, 2015). The cerebellar output is dependent on primary sensory feedback from the periphery but also on updates on cortical activity. In particular for motor planning, the communication between the motor cortex and the cerebellum is essential to update motor output with internal error-estimates that allow the fine-tuning of movements (Proville *et al.*, 2014; Gao *et al.*, 2018; Wagner *et al.*, 2019). The cerebellar nuclei are the main recipient of the integrated and error-pruned information from the cerebellar cortex (Person & Raman, 2011; Ten Brinke *et al.*, 2017; Wang *et al.*, 2020). As the cerebellar output structure, cerebellar nuclei project to a large collection of downstream subcortical regions (Teune *et al.*, 2000), that could contribute to various motor and non-motor functions.

It is generally believed that motor cortex conveys its information to cerebellum via a disynaptic pathway. In more detail, L5 neurons project to the pontine nuclei, which give rise to mossy fiber projections that innervate the cerebellar cortex and nuclei predominantly contralateral to the motor cortex. The integrated signal from the cerebellar cortex is relayed to the cerebellar nuclei contralateral to the motor cortical projection neuron.

Here, we report a non-canonical direct cerebro-cerebellar pathway by which the L5 neurons of the motor cortex directly project to the cerebellar nuclei. Such a ‘short cut’ connection bypasses the crucial relay regions such as pontine nuclei and cerebellar cortex, and allows motor cortex to directly access the ipsilateral cerebellar nuclei. We use fluorescence micro-optical sectioning tomography - guided (fMOST-guided) single-axon reconstructions to show that this novel cerebro-cerebellar pathway allows fast communication between both brain areas and provides a unique ipsilateral route that contrasts the contra laterality of conventional disynaptic cerebro-cerebellar communication. Furthermore, we use RNA-sequencing to identify cerebellar-projecting CSNs

as a subpopulation of CSNs of which the genetic profile is distinct from a brainstem-projecting subpopulation. In line with these results, rhabies virus based circuit mapping shows that DCN-projecting CSNs receive their inputs from local networks while brainstem-projecting subpopulations receives a higher proportion of inputs from long-range cortical sources. We use downstream-target based anatomical tracing, genetic profiling and circuit mapping to identify cerebro-cerebellar projecting cells as a distinct subpopulation of CSNs.

RESULTS

To map the afferents of the Deep Cerebellar Nuclei (CN) we used adeno-associated virus (AAV) that is predominantly absorbed by axonal fibers and retrogradely transported (AAVretro, Tervo *et al.*, 2016). We injected AAVretro that encodes red-fluorescent protein (RFP) or green-fluorescent protein (GFP) in C57Bl/6 mice and thereby labelled CN-projecting cells. Apart from the more commonly studied brainstem nuclei, we found labelled neurons throughout the cerebral cortex (Figure 1A-D). We found that 46.6 +/- 6.6% of all cerebro-cerebellar projecting cells localized to motor cortex (MC), while 23.9

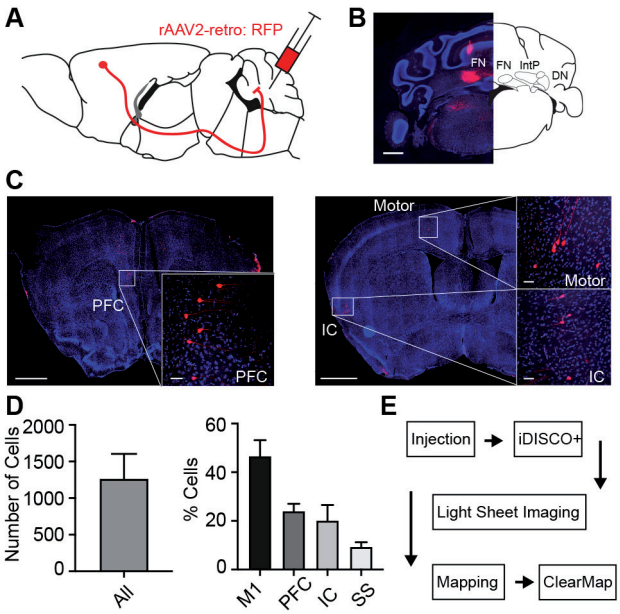

Figure 1A-E. Retrograde tracing reveals cerebro-cerebellar projecting cells. **A** Illustration of viral tracing strategy in which retro-RFP injection to the Cerebellar Nuclei (DCN) (**B**) reveals cerebro-cerebellar projecting cells in the prefrontal cortex (PFC), motor cortex (Motor) and insular cortex (IC) (**C**). (**D**) Quantification of cerebro-cerebellar projecting cells. (**E**) Pipeline for iDISCO clearing based cell atlas-registration and cell mapping in the cortex. Scale bars **A-F**: 1000µm and 100µ in inlay.

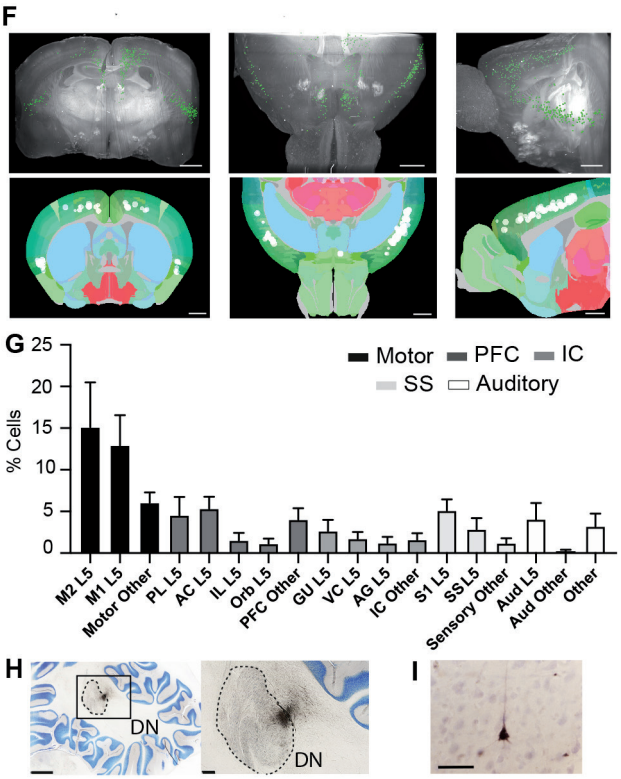

Figure 1F-I. Retrograde tracing reveals cerebro-cerebellar projecting cells. (**F**) Images showing cerebro-cerebellar projecting cells mapped into 3D brain atlas and quantified by ClearMap analysis algorithms (**G**). Clearmap based quantification of cerebro-cerebellar projecting cells. n = 3. (**H**) Injection spot of Choleratoxin B (CTB) in Dentate nucleus (DN) of a rhesus monkey. (**I**) CTB labelled pyramidal cell in motor cortex of a rhesus monkey. Scale bars **A-F**: 1000µm and 100µ in inlay. Scale bar in (**H**) is 2.5mm and 500µm in inlay. Scale bar in (**I**) is 25µm.

+/- 3.1% of the cells localize to prefrontal cortex (PFC), 20.1 +/- 6.4% to insular cortex (IC) and 9.3 +/- 1.9% to sensory cortex (SS, n = 10; Figure 1D). To study the subregional distribution and laminar specificity of cerebro-cerebellar projecting cells in more detail, we applied IDISCO based brain clearing in combination with automated atlas registration and ClearMap based cell mapping (Renier *et al.*, 2014, 2016) (Figure 1E-G). Hereto, we injected AAVretro encoding Cre into the DCN of Ai32 reporter mice to label cerebellar input areas. This alternative approach confirms the diverse cortical location of CN-projecting neurons (Figure 1F, n=3). We found that cerebro-cerebellar projecting cells localize to layer V (LV) of motor cortex (secondary motor cortex LV: 15.1 +/- 5.4%, primary motor cortex LV: 12.9 +/- 3.6%, other motor cortical areas: 6.1 +/- 1.2%), prefrontal cortex (prelimbic cortex LV: 4.5 +/- 2.2%, anterior cingulate cortex LV: 5.3 +/- 1.4%, infralimbinc cortex LV: 1.5 +/- 0.9%, orbitofrontal cortex L5: 1.1 +/- 0.6%, other Prefrontal areas: 4.0 +/- 1.3%), insular cortex (gustatory cortex LV: 2.6 +/- 1.3%, visceral cortex L5: 1.7 +/- 0.8%, agranular insular cortex L5: 1.2 +/- 0.7%, other Insular areas: 1.6 +/- 0.8%),

sensory cortex (primary sensory cortex L5: 5.1 +/- 1.3%, supplementary sensory cortex L5: 2.9 +/- 1.3%, other sensory areas: 1.2 +/- 0.6%) as well as auditory cortex (auditory cortex L5: 4.1 +/- 1.9%, other auditory areas: 0.2 +/- 0.2%) and other cortical areas 3.2 +/- 1.5% of cells (Figure 1F, n = 3). Furthermore, we were interested in understanding whether the individual subpopulations that localize to PFC, IC and MC have nuclei specific innervation preferences in the cerebellum. Therefore, we targeted small volume injected AAVretro encoding GFP and RFP or Choleratoxin B (CTB) in either the fastigial (FN), interposed (IntP) and lateral (DN) nuclei of the DCN.

We found that the distribution of labelled neurons throughout the motor, sensory, prefrontal, insular and auditory cortex was not significantly different between the CN, indicating similar innovation patterns from cerebral cortex to all three nuclei (Supplementary Figure 1A-D, p = 0.8619, n = 3, 2way-ANOVA). In addition to labeling cerebro-cerebellar projecting cells in the cortex of mice, we identified this cell population in higher developed mammals such as rhesus monkeys. Therefore, we injected a small volume of CTB to the DN of a rhesus monkey and detected a total amount of 60 cells in layer 5 of the motor cortex (Figure 1H, I; n = 1).

As the highest proportion of cerebro-cerebellar projecting cells localizes to the motor cortex and both areas are co-entrained during movement execution (Gao *et al.*, 2018), we focused our experiments on the characterization of the motor cortical subpopulation. In a first step of understanding brain-wide effects of motor cortical DCN-projecting cells on the systems level, we determined the downstream projection targets of this cell population. Therefore, we apply a sparse labeling approach by injecting a small volume of 30µl of AAVretro encoding Cre to the DCN of WT mice and co-injecting Cre-dependent GFP virus in the motor cortex. We combined this sparse labeling approach with 2P-fMOST imaging to allow brain-wide single axon tracing. This technique allows the whole brain atlas registration and micrometer-precise reconstruction of the axonal branching of the motor cortical neurons that innervate the CN. (Xiong *et al.*, 2014; Guo *et al.*, 2017*a*; Muñoz-castañeda *et al.*, 2020)(Figure 2A-B). In total, we reconstructed 15 cerebro-cerebellar projection neurons and their downstream projection targets (Figure 2C,D). In addition, we identified the downstream projection targets by using a similar AAVretro based and Cre encoding viral labeling approach with which we conditionally express tdtomato in DCN-projecting motor cortical cells (Figure 2E,F). We report ipsilateral orbitofrontal and sensory cortex as well as long-range cortical projection targets. As subcortical projection targets we identified the putamen, the zona incerta, the thalamus, the red nucleus, the superior colliculus, the pontine nucleus as well as brainstem nuclei. All fibers run along the pyramidal tract down into the spine, which identifies them as a subclass of cortico-spinal neurons (CSNs). In the DCN we found the bottom of ipsilateral anterior interposed

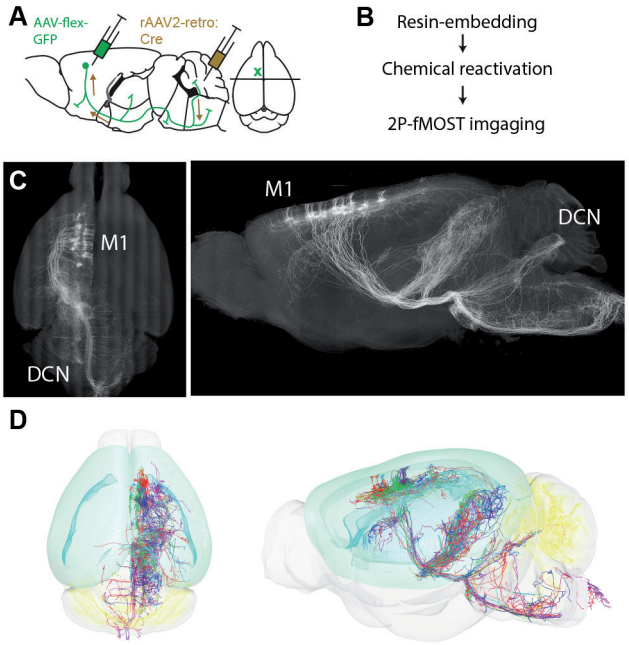

Figure 2A-D. Projection trajectory of cerebro-cerebellar projecting cells. (**A**) The viral labelling strategy for single-axon reconstructions is based on delivery of retro-Cre to the DCN and flexed-GFP to the motor cortex. (**B**) Pipeline describing the processing of tissue samples for two-photon fluorescence micro-optical sectioning tomography (2P-fMOST). (**C**) High-resolution 2P-fMOST based images of whole-brain projection pattern of cerebro-cerebellar projecting cells. (**D**) Single axon tracing and whole brain reconstruction of cerebro-cerebellar projection trajectory.

nucleus and fastigial nucleus as the main target of cerebro-cerebellar projecting cells (Figure 2 E, F and G). To understand the neurotransmitter identity of this cell type we used an immunostaining against vesicular glutamate transporter type 1 (vGluT1). We found that CSN axon terminals express vGluT1, indicating the glutamatergic nature of these synapses (Figure 2H).

In a next step we showed the connectivity of motor cortex and CN at the physiological level by testing whether stimulation of DCN-projecting CSNs modulates the neuronal activity patterns of DCN neurons. Therefore, we used optical stimulation of DCN-projecting CSNs in combination with multi-unit recordings of DCN neurons in awake, head-fixed mice. We express ChR2 in DCN-projecting cells by delivery of AAVretro encoding Cre to the DCN in Ai32 mice. We prepared the mice with a Clear Skull Cap, which allowed us to photoactivate DCN-projecting CSNs in the motor cortex through the intact skull (Figure 3A). In parallel we used silicone probes to record multi-unit neuronal activity from DCN neurons. We found that activation of DCN-projecting cells in the motor cortex with a 50 Hz optical stimulus at 470nm resulted in diverse modulation patterns of the

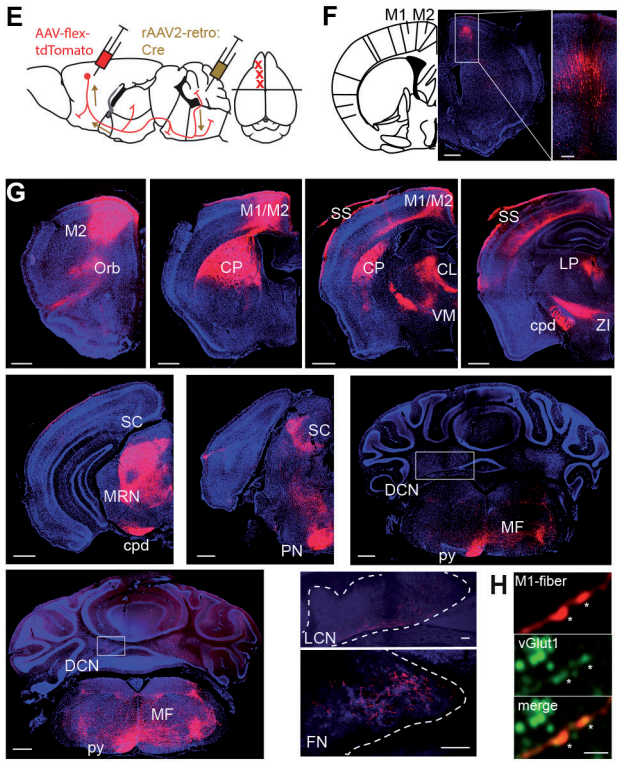

Figure 2E-H. Projection trajectory of cerebro-cerebellar projecting cells. (**E**) Viral labelling strategy for identification of downstream projection targets. Somata of cerebro-cerebellar projecting cells that localize to motor corex (**F**). (**G**) Downstream projection targets of cerebro-cerebellar cells that innervate orbitofrontal cortex (Orb), primary and secondary motor cortex (M1 and M2, respectively), sensory cortex (SS), caudate putamen (CP), centro-lateral thalamus (CL), ventro-medial thalamus (VM), lateral pole (LP), zona incerta (ZI), midbrain reticular formation (MRN), superior colliculus (SC), pontine nuclei (PN), brain stem reticular formation (MRF) and deep cerebellar nuclei (DCN). In the DCN the main targets are the bottom of interposed nucleus and fastigial nucleus (FN). (**H**) Immunostaining of motor cortical fibers shows that they stain positive for vesicular glutamate transporter 1 (vGlut1). Scale bars 500µm and 10µm in inlay.

neural activity in DCN neurons. A proportion of 30% of DCN neurons (32/107 cells Figure 3B,D) responded with increasing firing rates and an average facilitation of 17.0 +/- 1.5Hz (Figure 3E,F), while 7% of DCN neurons (8/107, Figure 3C,D) responded with decreasing firing rates that had an average suppression of 20.2 +/- 3.7Hz (Figure 3G,H).

In general CSNs in L5 of the motor cortex form a well described cell population with well characterized cell morphology, defined input-output embedding in brain circuits and distinct genetic profiles (Harris & Shepherd, 2015; Economo *et al.*, 2018; Winnubst *et al.*, 2019; Muñoz-castañeda *et al.*, 2020). To understand how DCN-projecting CSNs fit into the framework of L5 projection neuron characteristics, we need to understand which proportion of the CSN population they form and whether they are distinct from

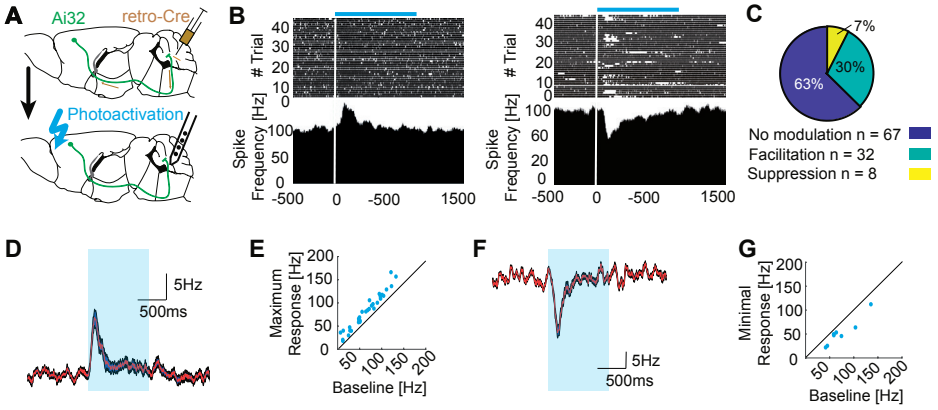

Figure 3. Optical stimulation of cerebro-cerebellar cells evokes response in DCN *in-vivo*. (**A**) Scheme showing injection strategy to label cerebro-cerebellar cells in Ai32 mice that were prepared with a clear skull cap. (**B**) Peristimulus-time-histogram (PSTH) of a representative DCN cell that facilitates and a representative DCN cell that supresses internal spike patterns after optical stimulation of cerebro-cerebellar projecting cells. Upper part of PSTH shows spiking pattern of DCN cells where every row represents a single trial. The lower part of the PSTH represents the average spiking frequency across trials. (**C**) Fraction of DCN cells that show no modulation, facilitate or suppress their spike patterns upon optical stimulation. (**D**) Average change in firing frequency in DCN cells that facilitate their spike response upon cortical cell stimulation. In (**E**) the maximal response of all facilitating cells is quantified. (**F**) The average decrease in firing frequency in DCN cells that suppress their firing pattern after cortical stimulation is depicted. In (**G**) the minimal reponses of all suppressive cells are depicted.

other projection-target specific CSN subpopulations such as the reticular formation-projecting CSNs (MRF-projecting CSNs). We delivered AAVretro expressing RFP to the DCN and AAVretro expressing GFP to the pontine nuclei (PN) to label DCN-projecting and the full population of CSNs, respectively (Figure 4A, B). We found that DCN-projecting CSNs form 3.0 +/- 1.0% of PN-projecting CSNs, while PN-projecting cells are 10.0 +/- 1.5 times more abundant than DCN-projecting cells (Figure 4C, PN: 1149 +/- 104.4 cells, DCN: 95.8 +/- 23.3 cells, PN+DCN: 36.5 +/- 12.1 cells, n = 4). Next, we focused on the potential differences between the DCN-projecting and MRF-projecting CSNs. Hereto we injected AAVretro expressing RFP to the DCN and AAVretro expressing GFP to the MRF and found that DCN- and MRF-projecting CSN subpopulations are distinct and non-overlapping (Figure 4C, MRF: 252.2 +/- 34.5 cells, DCN: 86.0 +/- 22.1 cells, 3 +/- 1.0% of MRF-projecting cells innervate DCN, 9.6 +/- 2.3% of DCN innervate MRF, n = 5).

To characterize the CN-projecting CSN in more detail, we compared the genetic profile of CSN populations with MRF-projecting and PN-projecting CSNs. Therefore, we used the above-described viral injection strategy to label PN- or MRF-projecting CSNs with GFP as well as DCN-projecting CSNs with RFP (Figure 4D). To isolate the individual cell populations, we prepared in-vitro brain slices from motor cortex and manually collect the fluorescence labelled CSNs with a low-resistance glass pipette (Figure 4D) (8-10

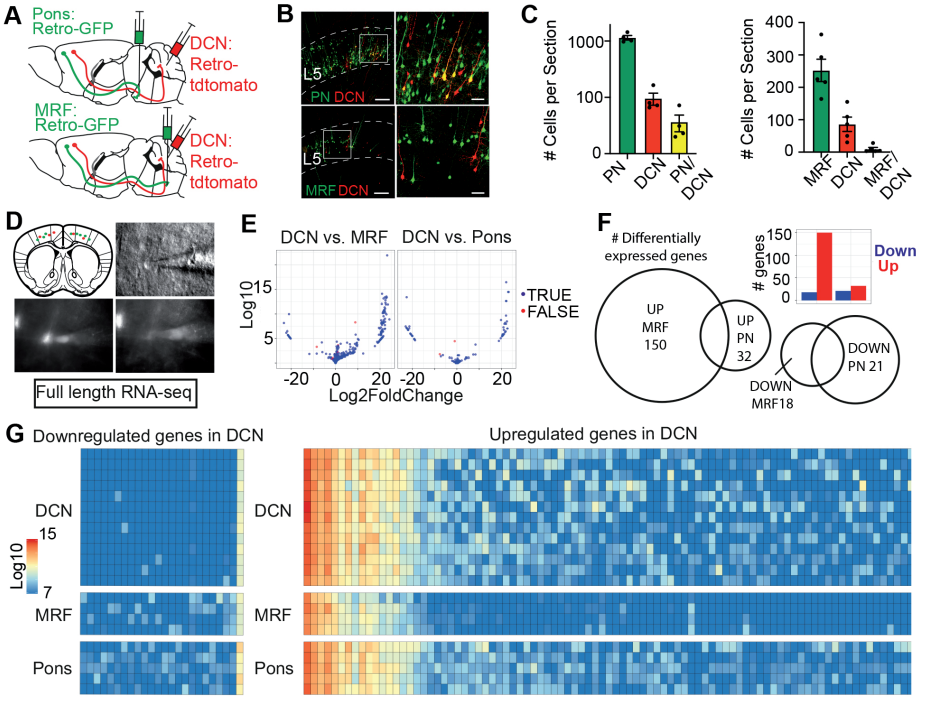

Figure 4. DCN-projecting neurons form a distinct subpopulation of Cortico-spinal neurons (CSN). (**A**) Illustration depicting the injection strategy to label DCN-projecting CSN with RFP and Reticular formation projecting (MRF) CSNs as well as Pontine nucleus (PN) projecting CSNs with GFP. (**B**) Images showing layer 5 (L5) of motor cortex in which PN- and MRF-projecting CSNs are labelled with GFP (green) and DCN-projecting CSNs are labelled with RFP (red). (**C**) Quantification of PN-, MRF- and DCN-projecting CSNs as well as the overlapping CSN population that projects to both downstream targets. (**D**) Illustration that depicts fluorescent cell collection strategy in an in-vitro brain slice, that is used to isolate cell samples for RNA-sequencing. (**E**) Log-Log plot that illustrates the signal range of differentially expressed genes between the PN and DCN as well as between the MRF and DCN groups. (**F**) Bar diagram that shows the number of differentially expressed genes. The Venn diagram illustrates the relation between the differentially expressed genes that were upregulated and downregulated for both PN and MRF samples when compared with the DCN samples. (**G**) Heatmaps illustrate the signal ranges of the genes that are differentially expressed between the PN- and DCN-projecting as well as the MRF- and DCN-projecting cell populations. Scale bar is 200µm. Scale bar in the inlay is 50µm.

neurons per sample). We prepared DNA libraries according to the Smart-seq2 method (Picelli *et al.*, 2013) and sequenced the samples on the Illumina HiSeq2500 platform. After sequencing the transcriptomes of all three populations, we compared the profile of DCN-projecting CSNs with the one of PN-projecting and MRF-projecting CSNs. We determined the differentially expressed genes by comparing the signal ranges of genes expressed in the DCN-projecting population and the PN- or MRF-projecting groups (Figure 4E). When we compared differentially expressed genes in DCN-projecting cells versus PN-projecting cells we found 32 genes upregulated and 21 genes downregulated, suggesting high similarity in the genetic profile of both groups (Figure 4D,F; DEseq2 with ashr fold change shrinkage estimator, n = 13 and n = 5, respectively). When we compare

the DCN-projecting population with the MRF-projecting population we found that 150 genes were upregulated in the DCN-projecting group while 18 genes were downregulated, indicative of distinct differences between both DCN- and MRF-projecting subpopulations (Figure 4E,F; DEseq2 with ashr fold change shrinkage estimator, n = 13 and n = 4, respectively). Interestingly, the most differentially expressed gene was the Sodium Voltage-Gated Channel Beta Subunit and found in the MRF-projecting comparison ($p<0.0000001$, DEseq2 with ashr fold change shrinkage estimator).

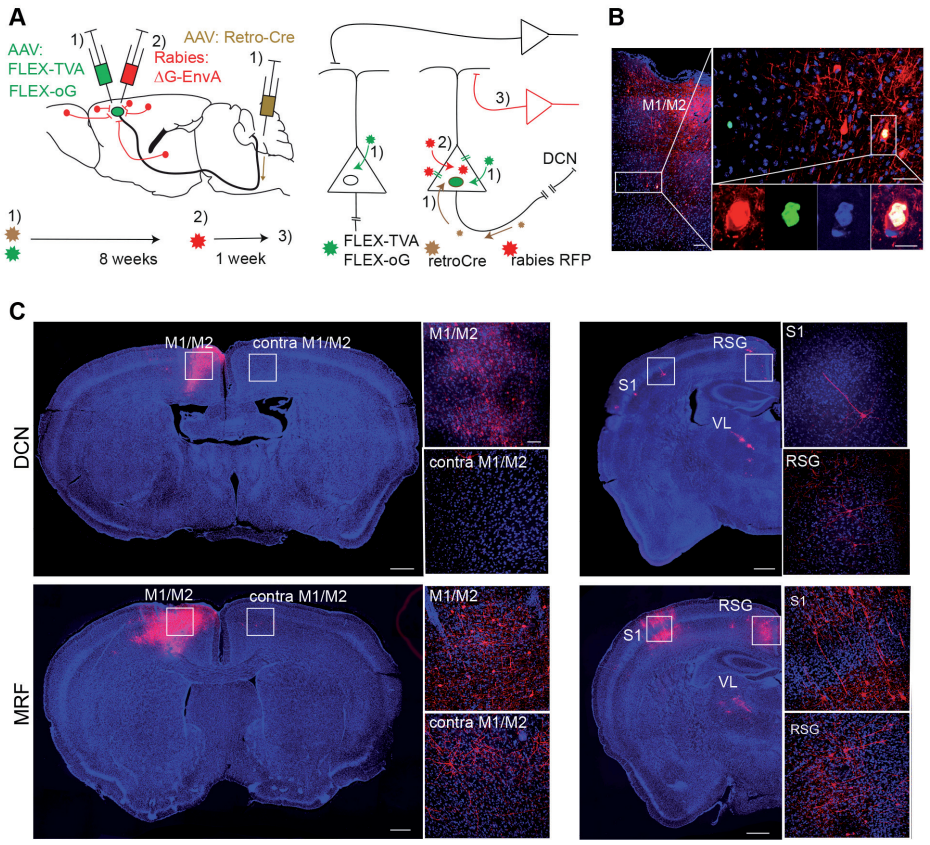

Figure 5A-C. Trans-Synaptic Rabies-Mediated Input-Output Mapping Reveals Inputs to DCN- and MRF-projecting CSNs. (**A**) Schematic for rabies tracing, shown for DCN-projecting CSNs. Left, injection strategy that isolates inputs to DCN-projecting CSN subpopulation by delivery of retro-Cre expressing AAV to the DCN and a mix of conditionally expressed TVA-GFP and optimized rabies glycoprotein-GFP (oG) to unilateral motor cortex. After 8 weeks of incubation EnvA-pseudotyped, G-deleted, mCherry-expressing rabies virus (Rabies ΔG-EnvA) was delivered to motor cortex and labels inputs to TVA-expressing starter cells (right). (**B**) Starter cells for DCN- and MRF-projecting CSNs localize to motor cortex and express both TVA-GFP and Rabies-mCherry. (**C**) Coronal sections depict inputs to DCN- and MRF projecting CSNs from primary and secondary motor cortex (M1/M2), contralateral motor cortex (contra M1/M2), ipsilateral sensory cortex (S1) and retrosplenial cortex (RSG).

As CSNs are characterized by distinct embedding in anatomical brain circuits (Luo *et al.*, 2019; Muñoz-castañeda *et al.*, 2020), we investigated whether DCN-projecting CSNs and other CSN subpopulations have distinctive afferents. Based on the diverse transcriptomic profile of DCN- and MRF-projecting CSNs, we used MRF-projecting CSNs as a reference population and applied trans-synaptic rabies-mediated input-output mapping (Figure 5A). In one set of mice we injected AAVretro encoding Cre in DCN and conditionally expressed the avian viral receptor TVA and optimized G in the somata of CSNs in the motor cortex. In another set of mice we placed the AAVretro injection in the MRF but kept the motor cortical injections similar. Subsequent infection with rabies-virus gives rise to DCN- and MRF-projecting starter neurons and their mono-synaptically connected input neurons (Figure 5B, C). On average we quantify 11.1 +/- 2.6 starter cells for DCN-projecting CSNs and 60.0 +/- 16.7 starter cells for MRF-projecting CSNs that localize to the motor cortex (Figure 5D, inlay). Our rabies-tracing data reveal that DCN-projecting and MRF-projecting CSNs receive inputs from 14 brain areas (Figure 5C,D; Supplementary table 1, n = 9 and n = 3, respectively). We showed that rabies infection was specific to TVA-positive cells, as rabies virus infection in non-TVA positive tissue yielded no rabies labeled cells (Supplementary Figure 2A,B). When we grouped inputs to local and long-range cortical as well as subcortical areas, the rabies tracing data

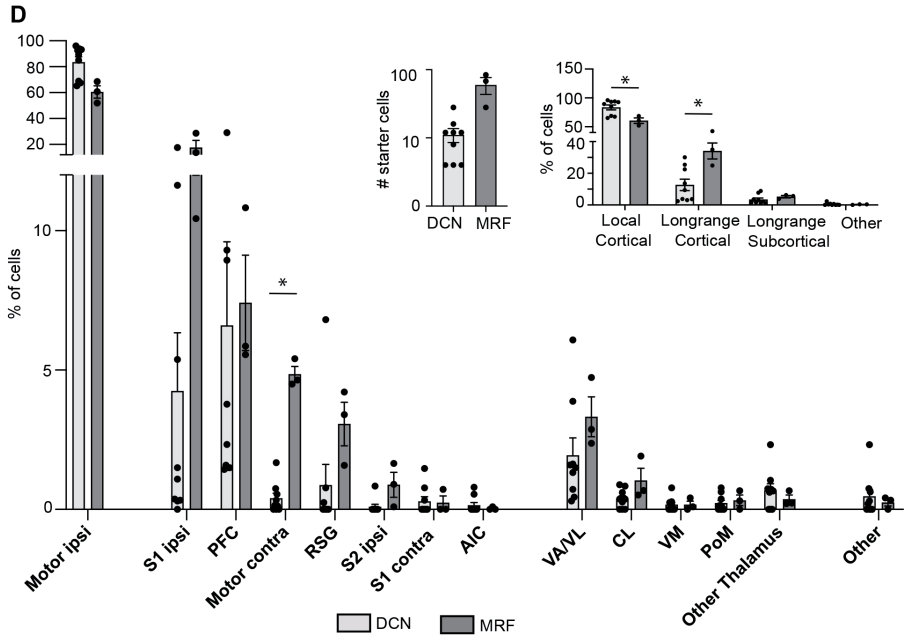

Figure 5D. Trans-Synaptic Rabies-Mediated Input-Output Mapping Reveals Inputs to DCN- and MRF-projecting CSNs. (**D**) Quantification of inputs to DCN- and MRF-projecting CSNs across brain areas. The inlays depict the number of starter cells as well as the distribution of inputs to local cortical, longrange cortical or subcortical or other brain areas. * p-value < 0.05.

shows that DCN-projecting CSNs receive a higher proportion of their inputs from local networks when compared to MRF-projecting CSNs (Figure 5C, D; DCN: 83.5 +/- 4.2%, MRF 60.5 +/- 4.8%, p = 0.0160, n = 9 and 3 respectively, Multiple t-test with Holm-Sidak correction). In addition it stands out that MRF-projecting CSNs integrate information from various long-range cortical input areas in addition to their local inputs, while DCN-projecting CSNs are minimally embedded in these long-range circuits (Figure 5C,D; DCN: 12.6 +/- 3.6%, MRF 34.1 +/- 5.0%, p = 0.0115, n = 9 and 3 respectively, Multiple t-test with Holm-Sidak correction). Here, the most prominent difference we find is that unlike CN, MRF-projecting CSNs also receive contralateral motor cortex inputs (Figure 5C,D; DCN: 0.4 +/- 0.2%, MRF: 4.8 +/- 0.3%, p < 0.0001, n = 9 and 3 respectively, Multiple t-test with Holm-Sidak correction).

DISCUSSION

Here, we characterize a novel type of corticospinal neuron that forms a direct and unilateral connection to the fastigial nucleus in the cerebellum. We use retrograde tracing to identify cerebro-cerebellar projecting cells in L5 of the cortex of mice and rhesus monkey. In addition, we apply anatomical input-output circuit mapping by using single axon tracing and trans-synaptic rabies labelling strategies to identify downstream projection targets and upstream input areas, respectively. Apart from the cerebellar nuclei as additional downstream target, the downstream projection pattern of this L5 cell population compares to the general population of CSN. In contrast, the rabies tracing reveals that DCN-projecting CSN are differentially embedded in sensorimotor brain circuits, as they receive most of their inputs from local motor cortical networks and minimal inputs from long-range cortical areas such as sensory cortex and contra lateral motor cortex. Furthermore, viral tracing as wells as RNA-sequencing based genetic profiling reveal that DCN-projecting CSNs form a subpopulation of the general CSN population, while they stay distinct from other CSN subpopulations such as the MRF-projecting subpopulation.

We want to highlight the cross-species presence of this novel cerebellar-projecting class of CSNs. In addition to the data presented in this paper, cerebro-cerebellar projecting cells have been detected in kittens (Tolbert & Panneton, 1983; Panneton & Tolbert, 1984), in zebra finches and in rats (Wild & Williams, 2000). However, most of these anatomical tracing papers are based on anterograde tracer injections to the motor cortex and the sparse detection of axonal fibers in the DCN. Our experiments show, that due to the distribution of this cell population across the full anterior-posterior axis of the motor cortex, a retrograde labelling approach is required to label the full cell population and the corresponding innervation pattern in the DCN. Here, we apply a viral labelling ap-

proach that profits from the recent development of genetically modified adenoviruses with enhanced retrograde transport rate (Tervo *et al.*, 2016). Nevertheless, the absolute number of cerebro-cerebellar projecting cells remains dependent on the efficiency of viral labelling techniques and can only be estimated from the present datasets. Interestingly, cerebro-cerebellar CSNs in kittens were only transiently present during the early stages of postnatal development (Tolbert & Panneton, 1983; Panneton & Tolbert, 1984; Tolbert, 1987), while our viral approach labels them in the adult cortices of mice and rhesus monkey (Figure 1 H,I). We want to highlight that our data in combination with the detection of sparse labelling of fibers in the DCN after BDA injection to the motor cortex in Macaca mulatta (Yamamoto *et al.*, 2019) are suggestive of the presence of cerebellar-projecting CSN, not only in mice and rhesus monkey, but also in other human apes as well as in humans.

Previous rabies tracing experiments show that the most prominent long-range input areas to PT neurons in motor cortex: ipsilateral sensory cortex, retrosplenial cortex and contra lateral motor cortex in combination with the corresponding thalamic targets such as VL, PoM and VM (Zhang *et al.*, 2016; Luo *et al.*, 2019; Muñoz-castañeda *et al.*, 2020). This inputome is also resembled by our rabies tracing data that labels the inputs specific to PN- and MRF-projecting CSNs. In contrast, DCN-projecting CSNs are differentially embedded in the brain circuitry as they receive less information from long-range cortical input areas while they are mainly embedded in local motor cortical networks. This suggests that DCN-projecting neurons process and integrate local motor cortical information and send an efference copy of local motor cortical activity patterns to their downstream targets including the fastigial nucleus in the DCN.

Furthermore, the direct and unilateral nature of this pathway contrasts the contra laterality of the cerebro-cerebellar communication via the pontine pathway. For conventional cerebro-cerebellar communication the cortex sends projections to the pontine nuclei, which in turn send mossy fibers to the contralateral cerebellar cortex (Cicirata *et al.*, 2004; Proville *et al.*, 2014; Biswas *et al.*, 2019; Henschke & Pakan, 2020). From the cerebellar cortex in turn, Purkinje cells send a hugely converging and integrated signal to the cerebellar nuclei (Person & Raman, 2011). In fact, cerebro-cerebellar communication via the classic ponto-cerebellar pathway requires the relay via multiple synapses and results in a hugely integrated signal that deviates from the original cortical signals. In contrast, this cerebro-cerebellar pathway sends a direct efference copy of cortical activity patterns to the ipsilateral fastigial nucleus, which suggests a more efficient and specific route for the communication between cortex and cerebellar nuclei. How the pathways converge and how the cerebellar nuclei integrate both streams of information remains open for discussion. It is possible to speculate about a relevance of this pathway

for guiding the laterality during movement execution and/or an error correction function in which the integrated signal from the cerebellar cortex can be compared to the time-locked motor cortical output signals that are send to brainstem nuclei and spine.

Future experiments will show how cerebro-cerebellar projecting cells are involved in the functional network that guides the learning and execution of skilled movements. It remains an open question how DCN-projecting CSNs modulate their activity patterns during the execution of movements and how that consequently affects spiking patterns in the DCN. Here, the comparison of other CSNs subpopulations will show how region-specific CSNs are engaged during distinct steps of movement execution and how direct cerebro-cerebellar communication shapes motor skills. The data presented in this paper provide a first anatomical framework to advance future studies that illuminate the function of this novel cerebro-cerebellar pathway.

METHODS

Animals

All experiments were performed in accordance with the European Communities Council Directive. All animal protocols were approved by the Dutch national experimental animal committee (DEC). Wild-type C57BL/6J (No. 000664) and transgenic Ai32 (No. 024109) mice were purchased from the Jackson Laboratory. The genotype was tested by PCR reaction using toe-tissue gathered at postnatal day 7-10. The mice used in this study were 6-30 weeks old and individually housed in a 12-hours light/dark cycle with ad libitum access to water and food.

Viral vectors

For the viral labeling of cerebro-cerebellar projecting cells we used the following viral vectors: retro-AAV2-CAG-Cre, retro-AAV2-GFP, retro-AAV2-tdTomato, AAV1-Flex-Tdtomato, AAV9-Flex-GFP. In addition we used Choleratoxin B (CTB, 1:10000) as a retrograde tracer. For the rabies tracing we combined the retro-Cre injection strategy with co-injection of AAV9-FLEX-H2B-GFP-2A-oG and AAV-Ef1A-DIO-HTB as well as co-injection of Rabies-deletedG-CMV-EnvA-mCherry and CTB. All viral constructs were purchased from Addgene. A summary of all injection strategies including viruses and injection volumes can be found in **Supplementary Table 1**. For the labeling of cerebro-cerebellar projections in rhesus monkey a 1:1 mix of biotinylated dextran amide (BDA) and CTB was used.

Surgeries

For all surgeries mice were anaesthetized with isoflurane (5% in 0.5L/min O_2 during the induction and 1.5% in 0.5L/min O_2 for maintainance). The skull of all mice was fixed on a stereotaxic surgical plate (David Kopf Instruments), the body temperature was maintained at 37 °C and the eyes were covered with Dura Tears (Alcon Laboratories). For the local pain treatment we applied Lidocain (2.5mg/ml) to the skulp. Buprenorphine (50µg/kg bodyweight) was applied in the beginning of the surgery for analgesia.

Stereotaxic delivery of viral vectors

After the removal of the hair on the scalp, the skin above the skull was opened. Subsequently, bregma and lambda were leveled and small craniotomies were established above the injection sites. For all injections a glass capillary was filled with viral vectors and lowered to the corresponding coordintes in the mouse brain. For injections to the hindbrain the following stereotaxic coordinates were measured relative to lambda, midline and the dura (x, y, z; in mm): -0.7, -2.7, -2.3 for fastigial nucleus (FN), -1.5, -2.7, -2.2 for interposed nucleus (IntP), -0.4, -0.4, -5.5 for pontine nuclei (PN) and -0.7, -2.6, -4.3 for midbrain reticular formation (MRF). For injections to the forebrain the coordinates were measured relative to bregma, midline and the dura (x, y, z; in mm): -1.2, 0, -0.8; -1.2, +1, -0.8; -1.7, +2.5, -0.8 for motor cortex. A summary of all injection strategies including viruses, injection volumes and coordinates can be found in **Supplementary Table 1**. Depending on the experimental strategy the brains were injected uni- or bilaterally (see **Supplementary Table 1**). After surgery the skin was sutured and animals recovered for at least 2 days.

Clear Skull preparation and Craniotomy

For the photostimulation and in-vivo electrophysiology experiments the previously injected Ai32 (**see Supplementary Table 1**) mice were prepared with a clear-skull cap and a headbar (Guo *et al.*, 2014; Gao *et al.*, 2018). In short, the skin above the dorsal surface of the skull was removed and a thin layer of cyanoacrylate adhesive (Krazy Glue, Elmer's Products) was applied to the skull. The skull was thinned at the following coordinates relative to bregma, midline and the dura (x, y, z; in mm): -/+1.2, 0, -0.8; -/+1.2, +1, -0.8; -/+1.7, +2.5, -0.8 for motor cortex. A custom made headbar was placed between lambda and bregma and cemented on the skull with the use of clear dental acrylic cement (Lang Dental Jet Repair Acrylic, L-type Clear Cement). A thin layer of clear dental cement was distributed across the frontal surface of the skull and covered by a thin layer of clear transparent nail polish (2B colours). After incubation for 6-8 weeks, a craniotomy of approximately 3 mm length was placed above the FN and IntP for in-vivo recordings. For constructing the recording chamber a thin layer of Optibond All-in one (Kerr) was

distributed on the surrounding skull. The chamber was build with the use of Charisma (Heraeus Kulzer) and sealed with Picodent twinsil after surgery and recording.

In-vivo electrophysiology and Photostimulation

For in-vivo recordings we used a multichannel acquisition system (64 channels ASSY 77H-H2, Cambridge Neuro Tech). We recorded DCN neurons at a depth of 2.0-2.7mm from the cerebellar surface for at least 50 trials with optogenetic stimulation. The recordings were amplified and digitized on an Intan RHD2000 Evaluation System (Intan Technology). All recordings were sampled at 20 kHz, notch-filtered at 50 Hz and further analyzed with custom-written Matlab codes. For photostimulation at 470 nm, we applied 50 Hz light pulses at a 50/50 duty cycle and light powers ranging between 5-10 mW on the Clear Skull Cap of awake mice. The light was controlled by a high-power light driver (DC2100, Thorlabs) and delivered by an optical fiber (200 µm diameter, 0.22 NA, Thorlabs).

In-vivo Electrophysiology Data Analysis

For the analysis of multichannel recordings we used JRCLUST spike sorting software (Jun *et al.*, 2017). We calculated peristimulus time histograms (PSTHs) of well-isolated units by superimposing optogenetic trigger-aligned responses of DCN cells and averaged them in a shifting window (50 ms window size, 5 ms increment). The baseline firing frequency was calculated as the mean frequency in the first 1000 ms before the optogenetic stimulus. To calculate changes in firing rate upon optogenetic stimulation, we substracted the baseline firing frequency from the spike rates during the response window of 1000 ms after the optogenetic stimulus onset. We considered cells with average firing rate changes of more than three SDs of the baseline frequency as modulatory in response to the optogenetic stimulus. We linearly fitted the PSTH of the spike frequency during the response onset to identify the direction of the modulation and identified linear fits with positive slopes as facilitating spike rates and negative slopes as suppressing spike rates.

iDisco+ Brain Clearing Procedure

For the idisco clearing we followed the protocole published earlier (Renier *et al.*, 2014). In a first step, the brain was dehydrated by 1h incubation steps in methanol solutions (20%, 40%, 60%, 80% and 100%) and overnight in 1/2 mix of methanol dichloromethane. Next we applied a bleaching step in 5% H_2O_2 in 90% methanol at 4°C over night. After re-hydration, the brain was incubated in blocking solution for 2 days at 37°C. Afterwards the brain was incubated for 1 week at 37°C in 4ml primary antibody solution that contained PTwH incubation medium (PBS, 0.2% Tween-20, 100µg/10ml Heparin, 5% DMSO, 3% Normal Donkey Serum) and anti-GFP antibody (35, Abcam,) in a dilution of 1:1000.

The incubation with primary antibody was repeated 2x for a week. After washing, the brain was incubated for 1 week in 4ml secondary antibody solution that contained anti-rabbit Cy5 (4) diluted in PTwH (1:750). All antibody containing solutions were filtered at 0.2µm and Amphotericin (10µl/ml) was added every second day to prevent fungal growth. All antibody incubation steps were perfomed at 37°C. After washing, the final tissue clearing step followed at room temperature. The brain was dehydrated by 1h incubation steps in methanol solutions (20%, 40%, 60%, 80% and 100%) and overnight in 1/2 mix of methanol/dichloromethane. The following day, the brains were placed in dichloromethane (2 times 20 minutes) and final clearing was achieved by storage in benzylether.

Light-sheet imaging

Whole brains (partially the cerebellum was removed) were imaged on a light-sheet microscope (Ultramicroscope II, LaVision Biotec) with a Neo sCmos camera (Andor, 2560 x 2160 pixels). The samples were imaged with a double-sided illumination and a sheet Na of 0.148348, which results in a 5 µm thick lightsheet. We used a step-size of 2.5 µm in line with a horizontal focusing lightsheet imaging method. The effective magnification for all images was 1.36x (zoombody*objective plus dipping lens = 0.63x * 2.152x). For the illumination we used the Coherent OBIS 488-50 LX Laser with a 525/50nm filter for the autofluorescent channel and the Coherent OBIS 647-120 LX with the 676/29 filter for the fluorescent channel.

Image Processing and Clearmap Analysis Pipeline

All cellbodies were manually mapped as spots with the use of Imaris software (Bitplane, http://www.bitplane.com/imaris/imaris). A 3D reconstruction of the location of the cell bodies was used as an input file for the automated cell detection and registration pipeline ClearMap (Renier *et al.*, n.d.). In short, the ClearMap platform registers the brain to a reference atlas, detects the location of cells, maps them to the reference atlas and generates heatmaps of the cell locations as well as statistical analysis.

RNA sequencing

Following 3-6 weeks of incubation after viral injection, isoflurane-anesthetized mice were decapitated, their brains were quickly removed and placed into ice-cold slicing medium containing (in mM): 93 NMDG, 93 HCl, 2.5 KCl, 1.2 $NaHPO_4$, 30 $NaHCO_3$, 25 Glucose, 20 HEPES, 5 Na-ascorbate, 3 Na-pyruvate, 2 Thiourea, 10 $MgSO_4$, 0.5 $CaCl_2$, 5 N-acetyl-L-Cysteine (osmolarity 310 ± 5; bubbled with 95% O_2 / 5% CO_2). Next, 200 µm thick coronal slices were cut using a Leica vibratome (VT1000S). For the recovery, brain slices were incubated for 5 min in slicing medium at 34±1˚C and subsequently for ~40 min in artifical cerebrospinal fluid (ACSF; containing in mM: 124 NaCl, 2.5 KCl, 1.25 Na_2HPO_4, 2

$MgSO_4$, 2 $CaCl_2$, 26 $NaHCO_3$, and 20 D–glucose, osmolarity 310±5; bubbled with 95% O_2 / 5% CO_2) at 34±1 ˚C. After recovery brain slices were stored at room temperature until the cell collection started. For the cell collection we used a low-resistance patch pipette of 1.3MΩ that was filled with a minimal volume of intracellular solution containing RNAse inhibitor (in mM: 124 K-Gluconate, 9 KCl, 10 KOH, 4 NaCl, 10 HEPES, 28.5 Sucrose, 4 Na_2ATP, 0.4 Na_3GTP (pH 7.25-7.35; osmolarity 295 ± 5)). The patch pipette was localized in close proximity to the fluorescently labelled cells and under pressure was used to suck the cells into the pipette. When the cell collection was finished we used over pressure to empty the content of the patch pipette into a lysis solution (in PBS: 0.2% Triton, 5% RNAse Inhibitor). In total we collected 9-18 cells per sample and stored the sample at -80°C.

Sequencing libraries were prepared from these samples using the Smart-seq2 cDNA preparation protocol [Picelli, 2013] followed by Nextera DNA XT library preparation (Illumina, South Canada). Subsequently, sequencing was performed on HiSeq 2500 instruments (Illumina, San Diego, CA, USA). Approximately 20 million single reads of 50 base pairs in length were generated per sample.

Adapter and adenosine homo-polymer (poly A) sequences were removed from the reads using AdapterTrimmer (https://github.com/erasmus-center-for-biomics/AdapterTrimmer). The remainders were mapped to the mouse GRCm38 reference genome using HISAT2 (version 2.1.0) (Kim *et al.*, 2015). Gene expression was quantified using HTseq-count (version 0.11.2) based on the Ensembl 96 transcript annotation.

Immunohistochemistry and Image Acquisition

For histology the mice were perfused with 4% paraformaldehyde (PFA, in 0.1 M phosphate buffer (PB) at pH 7.3), post-fixed in PFA for 2 hours and stored in 10% sucrose overnight. After removal of the dura, the brains were embeded in a 12% gelatine and 10% sucros solution and incubated in 10% formaline and 30% sucrose solution for 3h. Afterwards the brains were stored in 30% sucrose. The brains were cut in slices of 50µm thickness on a cryotome (SM2000R, Leica) and stored in 0.1 M PB. Before antibody treatment slices were blocked for 2h at RT (10% normal horse serum (NHS) and 0.5% Triton-X100 in PBS). Primary antibodies were incubated overnight at 4°C (2% NHS and 0.5% Triton-X100 in PBS) and secondary antibodies were incubated for 4h at RT. Brain slices were rinsed and mounted in Vectashield (Vector Laboratories). The following primary antibodies were used for fluorescent stainings: anti-RFP (rabbit, 1:2000, Rockland), anti-vGlut1 (guinea pig, 1:2000, MilliPore Bioscience), anti-CTB (goat, 1:15000, List labs). The following secondary antibodies were used: anti-guineapig-A405 (1:400, Jackson Immunoresearch), anti-rabbit-Cy3 (1:400, Jackson Immunoresearch), anti-goat-Cy5 (1:400, Jackson Im-

munoresearch). For the background staining of cell nuclei, all sections were incubated for with DAPI (300nM). For light-microscopy stainings of CTB in rhesus monkey, the slices were incubated for 20 min in 3% H2O2 (in PBS) to remove endogenous peroxidase activity of blood. We used anti-CTB (goat, 1:15000, List labs) primary antibody and anti-goat-biotinylated secondary antibody (1:200, Vector). After washing, the sections were incubated in Avidin-Biotine complex (1:200 Avidine and Biotine in PBS, Vector) for 1.5 hours at RT and subsequently stained with 3,3'-Diaminobenzidine (DAB, 75mg/ml stock, 1:300, Sigma).

The fluorescent overview images were acquired with a 10x objective on a fluorescent scanner (Axio Imager 2, Zeiss). The confocal images were acquired on a LSM 700 microscope (Zeiss) and the use of 20x as well as 63x objectives with numerical apertures of 0.3 and 1.4, respectively. Lightmicroscopic images were acquired on a Nanozoomer (2.0-RS, Hamamatsu) with a 40x objective. Histological images were processed with ImageJ software packages.

Single-Axon Tracing data

For the single-axon tracing experiments, mice were perfused and their brains were stored in PFA. The histological tissue processing and imaging as well as the single axon tracing and reconstruction followed the pipeline published previously (Xiong *et al.*, 2014; Guo *et al.*, 2017*a*).

Statistics

For statistical analysis all data are represented as mean +/- standard error of the mean (SEM). To test for differentially expressed genes of the RNA-sequencing dataset we used the DEseq2 analysis package with ashr fold change shrinkage estimator (Love *et al.*, 2014; Stephens, 2017). For the analysis of the rabies data we used multiple t-tests with Holm-Sidak correction of the GraphPad PRISM software package.

SUPPLEMENTARY MATERIAL

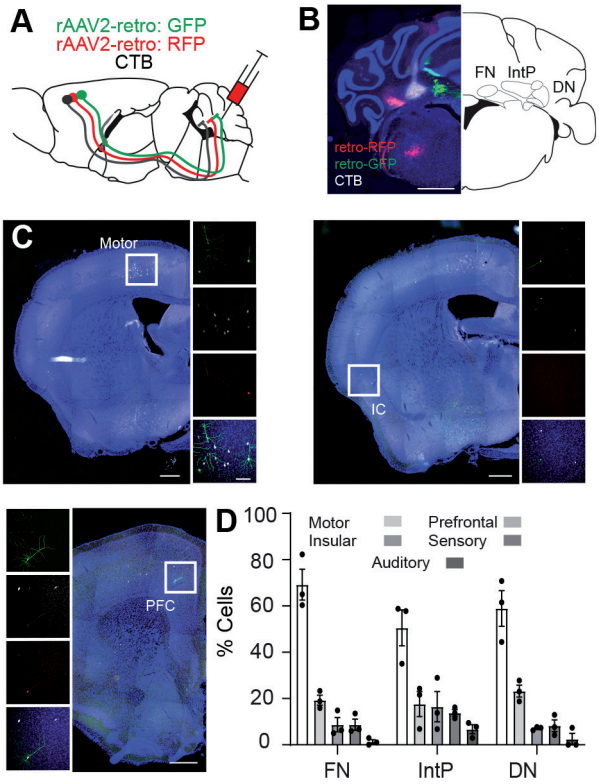

Supplementary Figure 1. Cerebellar nuclei specific distribution of cortical cells. (**A**) Scheme illustrating the simultaneous delivery of retrograde tracers such as retro-GFP, retro-RFP and CTB to fastigial (FN), interposed (IntP) and dentate nucleus (DN) in the deep cerebellar nuclei (**B**). (**C**) Images illustrating the distribution of labelled cells in the motor cortex (Motor), insular cortex (IC) and prefrontal cortex (PFC) after subnuclei specific injection in the cerebellar nuclei. (**D**) Distribution of cortical cells dependent on their innervation pattern in the DCN. Scale bars are 500µm. Scale bars in inlays are 100µm.

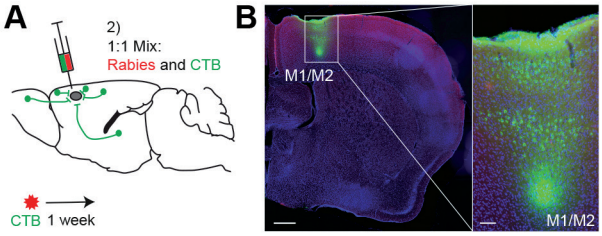

Supplementary Figure 2. Rabies tracing is dependent on TVA-expression in DCN-projecting cells. (**A**) Scheme showing co-injection of CTB and Rabies-ΔG-EnvA-mCherry to the motor cortex. (**B**) Image shows that in absence of TVA/oG Rabies-ΔG-EnvA-mCherry is not infectious, while motor cortical cells are labelled by CTB. The scale bar is 500µm and 100µm in the inlay.

Supplementary Table S1

Experiment	Brain Region	Mouse Line	Virus	Plasmid	Titer [molecules/ml]	Coordinates (from Bregma; x,y,z)	Volume [nl]
Fig. 1 A-D	FN + IntP (unilateral)	WT	retro_AAV2_CAG_GFP retro_AAV2_CAG_RFP	addgene#37825 addgene#59462	7x10^12 1.01x10^12	2 spots: -0.7, -2.7, -2.4; -1.5, -2.7, -2.3	60-150
Fig. 1 E-G	FN + IntP (bilaterally)	Ai32	Retro_AAV2_CAG_Cre	Custom made	1.1x10^12	2 spots: -0.7, -2.7, -2.4; -1.5, -2.7, -2.3	60-150
Fig. 1 H-I							
Fig. 2 A-D	FN (unilateral)	WT	Retro_AAV2_CAG_Cre	Custom made	1.1x10^12	1 spot:-0.7, -2.7, -2.4	10
	Motor cortex (ipsilateral)		AAV9_CAG_Flex_GFP		3.7x10^12	3 spots: 1, 0, -0.7; 1, 1, -0.7; 1.5, 2.5, -0.7	50
Fig. 2 E-G	FN (unilateral)	WT	Retro_AAV2_CAG_Cre	Custom made	1.1x10^12	1 spot:-0.7, -2.7, -2.4	60
	Motor cortex (ipsilateral)		AAV9_CAG_Flex_RFP			3 spots: 1, 0, -0.7; 1, 1, -0.7; 1.5, 2.5, -0.7	150
Fig. 3 A	Fn+IntP (bilaterally)	Ai32	Retro_AAV2_CAG_Cre	Custom made	1.1x10^12	2 spots: -0.7, -2.7, -2.4; -1.5, -2.7, -2.3	60-150
Fig. 4 A	FN + IntP (unilateral)	WT	retro_AAV2_CAG_RFP	addgene#59462	1.01x10^12	2 spots: -0.7, -2.7, -2.4; -1.5, -2.7, -2.3	60
	MRF, unilateral)		retro_AAV2_CAG_GFP	addgene#37825	7x10^12	1 spot: -0.75, -2.6, -4.3	60
	PN (unilateral)		retro_AAV2_CAG_GFP	addgene#37825	7x10^12	1 spot: -0.4, -0.4, -5.5	60
Fig 5 A	FN + IntP (unilateral)	WT	Retro_AAV2_CAG_Cre	Custom made	7x10^12	2 spots: -0.7, -2.7, -2.4; -1.5, -2.7, -2.3	120
	MRF (unilateral)		Retro_AAV2_CAG_Cre	Custom made	7x10^12	1 spot: -0.75, -2.6, -4.3	60
	PN (unilateral)		Retro_AAV2_CAG_Cre	Custom made	7x10^12	1 spot: -0.4, -0.4, -5.5	60
	Motor Cortex (ipsilateral)		AAV9-FLEX-H2B-GFP-2A-oG/ AAV1-Ef1A-DIO-HTB	addgene#: 44187/salk vectore core	1.82x10^11/ 7.19x10^12	1 spot: 1, 1, -0.7	200
	Motor Cortex (ipsilateral)		Rabies-deletedG-CMV-EnvA-mCherry/ CTB	Salk vector core	1.11x10^9/ 1:10000 dilution	1 spot: 1, 1, -0.7	200

Every END is just a new BEGINNING.

—Marianne Williamson

Chapter 8

Discussion

SYNOPSIS ON KEY DISCOVERIES IN THE THALAMIC SYSTEM

The generally accepted concept of first and higher order thalamic nuclei that are innervated by synapses with driving or modulatory properties has been established by Murray Sherman and collegues in the 70s (Sherman & Guillery, 1998, 2006; Murray Sherman, 2001; Theyel *et al.*, 2009; Sherman, 2012; Kyuyoung & Huguenard, 2014). Originally, the description of X- and Y-cells in the lateral geniculate nucleus of the cat gave rise to the concept of core- and matrix-type cell classes in the thalamus, respectively (Murray Sherman *et al.*, 1976; Friedlander *et al.*, 1979; Sur *et al.*, 1982, 1984). Here, the identification of cell-type specific and topographically organized thalamo-cortical connectivity and projection patterns in the visual thalamus suggested the presence of a well organized cortico-thalamo-cortical brain circuitry (Sur, M.; Sherman, 1982; Humphrey *et al.*, 1985*a*, 1985*b*; Tamamaki *et al.*, 1995; Viaene *et al.*, 2011). In line with this original subcategorization into core- and matrix-type thalamic nuclei, the discovery of 'driver' and 'modulator' like synapses in the visual thalamus allowed a further refinement of the above described concept into first- and higher-order thalamic nuclei (Hoogland *et al.*, 1991; Godwin *et al.*, 1996; Turner & Salt, 1998; Sherman & Guillery, 1998; Rouiller & Welker, 2001; Reichova & Sherman, 2004; Bickford *et al.*, 2015). The connectivity between first and higher order thalamic nuclei suggested that cortico-cortical communication is mediated via a stopover in the thalamus (Guillery & Sherman, 2002; Theyel *et al.*, 2010; Sherman & Guillery, 2011). Furthermore the discovery of the t-type calcium channel allowed the identification of burst and tonic spike modes within the thalamus (Jahnsen & Llinas, 1984*a*, 1984*b*; Lu *et al.*, 1992; Godwin *et al.*, 1996; Llinás *et al.*, 2005) that can be inter-switched dependent on inputs from modulatory and/or driver synapses.

THE CORTICAL DRIVER SYNAPSE AS A MODEL FOR SYNAPTIC TRANSMISSION

The essential scientific discoveries that I described above defined our current understanding of how cortico-thalamo-cortical communication works. From these original studies in the visual thalamus (Sur, M.; Sherman, 1982; Humphrey *et al.*, 1985*b*, 1985*a*; Raznahan *et al.*, 2011), the concept of first- and higher order thalamic nuclei was extended to other sensory modalities such as the proprioceptive system (Ahissar *et al.*, 2000; Guillery & Sherman, 2002; Reichova & Sherman, 2004; Groh *et al.*, 2008; Mease *et al.*, 2014, 2016; Seol & Kuner, 2015). In fact, for the proprioceptive system, the anatomy of the sub-cortical driver-like input has been described in great detail (Williams *et al.*, 1994; Veinante & Deschênes, 1999; Ahissar *et al.*, 2000; Pierret *et al.*, 2000). Furthermore, the modulatory feedback from cortical layer 6 is characterized (Reichova & Sherman, 2004;

Mease *et al.*, 2014) and - last but not least - the cortical driver-like feedback from cortical layer 5 in PoM is also described (Groh *et al.*, 2008; Seol & Kuner, 2015). The structure and function of presynaptic and postsynaptic proteins are mainly studied in synapses in which the anatomical wiring of the brain provides unique monosynaptic connectivity (Dondzillo *et al.*, 2010; Schulz Mendoza *et al.*, 2014; Körber *et al.*, 2015). However, the high release probability, fast synaptic recovery and large volume of VL cortical driver synapses in the thalamus makes them a suitable model to study synaptic transmission. In **Chapter 2** we use single-synapse electrical stimulation of cortical driver synapses as a model to study the role of the presynaptic scaffolding protein Bassoon in neurotransmitter release. The properties of the cortical driver synapse in the POm (as described in Groh et al., 2008, Seol and Kuner, 2015 as well as in Chapter 2), suggest the presence of a large pool of releasable vesicles that is depleted by a single action potential. In more detail, the average readily releasable pool contains ~64 synaptic vesicles from which 80 percent are released upon the first stimulus, while the recovery to 80% of the first response takes ~500ms. These characteristics give cortical driver synapses the optimal properties to function as a low-pass-filter in the cortico-thalamo-cortical system as discussed in **Chapter 4** and **5** for subcortical, cerebello-thalamic driver synapses. Nevertheless, it remains a challenge to compare the synaptic properties of the cortical driver in POm with the subcortical driver-like input from the cerebellum to VL (see **Chapter 4** and **5**) as the use of optogenetics as well as the approach to activate the full population of cerebellar fibers limits the possibility to calculate the readily releasable pool on the level of the individual synaptic connection (see 'Methodological Discourse on Fiber Population Stimulation in Neuronal Tissue' in this discussion).

CROSS-MODALITY CONVERGENCE IN THE THALAMIC ORGANIZATION

In **Chapter 3** of this thesis we cross the boundaries between the sensory and the motor domain within the thalamic system. We provide a summary and prospective review of the anatomical converge of sensory streams with cerebellar pathways, which provides a perspective on sensori-motor convergence and integration that is centered around the thalamic nuclei and extra-thalamic pre-inhibitory structures that send afferents to thalamic nuclei. This provides a detailed background discussion that combines **Chapter 2** as well as **Chapter 4** and **5** and identifies hot spots for cross-level integration. Apart from the cerebro-cerebellar convergence found in pre-thalamic inhibitory regions such as the APT and ZI, I want to highlight that the POm itself is another spot for cross-level sensory-motor integration within the thalamic system. Even though this higher-order nucleus of the proprioceptive system is receiving a minor amount of cerebellar inputs, it

receives inputs from both sensory (as described in **Chapter 2**) and motor cortical areas (Yamawaki & Shepherd, 2015; Jeong *et al.*, 2016). Furthermore, it does project to both sensory and motor cortices (Deschênes *et al.*, 1998; Meyer *et al.*, 2010; Ohno *et al.*, 2012; Hooks *et al.*, 2013). With these properties the POm is the only thalamic nucleus in which inputs and outputs from and to sensory as well as motor cortices exist.

EXTENDING THE CONCEPT OF DRIVERS AND MODULATORS TO THE MOTOR DOMAIN

As described in the first paragraph of the discussion, the general principles for thalamo-cortical communication has been established for the visual and the proprioceptive system (Godwin *et al.*, 1996; Turner & Salt, 1998; Reichova & Sherman, 2004; Groh *et al.*, 2008; Mease *et al.*, 2016). However extending this knowledge into the motor domain is crucial as cerebello-thalamo-cortical communication forms a pathway essential for motor control and motor planning (Schiemann *et al.*, 2015; Gao *et al.*, 2018; Sauerbrei *et al.*, 2020). Even though the cerebellar afferents to the thalamus have been described histologically and by in-vivo recordings (Angaut *et al.*, 1985; Sawyer *et al.*, 1994*a*, 1994*b*; Teune *et al.*, 2000; Proville *et al.*, 2014), a detailed description of their properties across thalamic nuclei and their integration with feedback form the cortex is lacking (Yamawaki & Shepherd, 2015; Jeong *et al.*, 2016). The work described in **Chapters 3, 4** and **5** of this thesis extends the concept of higher- and first order thalamic nuclei into the motor domain. In **Chapter 4** we focus on the anatomical and physiological description of the cerebellar driver input into the thalamus and in **Chapter 5** we follow-up on this work to further establish how modulatory feedback from motor cortical layer 6 shifts the thalamic response mode from bursty to tonic spiking patterns. In **Chapter 4** we find that VL is formed by a mix of core- and matrix type neurons and VM as well as CL are formed by matrix-type neurons (see introduction for an explanation of core- and matrix type neurons). Previous data has shown that core-type neurons in VL send focal projections to middle and output layers in motor cortex (Kuramoto *et al.*, 2009), while VM neurons distribute their axonal projections across various cortical areas and to the striatum (Kuramoto *et al.*, 2015). In addition, RNA-sequencing shows that the genetic profile of VL clusters with the one of first-order nuclei, while VM clusters with second-order nuclei and CL clusters with intra-laminar nuclei (Phillips *et al.*, 2019). In line with these data, **Chapter 4** suggests that for the cerebellar streams within the motor system VL forms the first-order and VM forms the higher-order nucleus for thalamo-cortical communication, while CL and CM form intra-laminar nuclei (see also Sherman et al 2013, the neuroscientist). As higher order thalamic nuclei receive driver-like feedback from cortical layer V, the investigation of motor cortical feedback from layer 5 to the motor thalamus is

essential for a final characterization. Here, in-vitro circuit-mapping experiments have shown that inputs from anterio-lateral motor cortical layer 5 evoke large amplitude responses in the lateral portion of VM, but not the VL (Yamawaki & Shepherd, 2015; Guo *et al.*, 2018). In line with these results, future studies need to investigate the feedback from layer V of motor cortex to understand how cortical driver-type inputs that come from the motor cortex integrate with subcortical driver-type inputs from the cerebellar nuclei (Yamawaki & Shepherd, 2015; Jeong *et al.*, 2016; Guo *et al.*, 2018; Winnubst *et al.*, 2019).

TEMPORAL CODING IN MOTOR THALAMUS

It still remains an open and controversial question how the high frequency spiking pattern of the cerebellar nuclei are processed in downstream targets such as the red nucleus, the reticular formation as well as the thalamic nuclei. Contrastingly, the spontaneous spiking rates in the CN have frequencies that range between 30 and 140 Hz (Hoebeek *et al.*, 2010), while the thalamic spiking patterns have low frequencies between 5 and 20 Hz (Baker, 1971; Sawyer *et al.*, 1994*b*).

For a discussion of the thalamic low-pass filtering function, I first want to describe the modulation of cerebellar nuclei neuron spiking pattern during movement execution in more detail (Hoebeek *et al.*, 2010; Sarnaik & Raman, 2018). For instance, during natural running on a treadmill the CN firing rate rises above 100 Hz during the lift of the paw and decreases sharply during the 100 ms before paw movement (Sarnaik & Raman, 2018). Also during saccadic eye-movements in monkeys the actual movement aligns to CN spiking patterns (Ohmae *et al.*, 2013). Finally, after Pavlovian eye-blink conditioning in mice the spiking rate of interposed nucleus neurons increases during the conditioned response, but decreases right before the initiation of the eyelid movement (Ten Brinke et al., 2017). These intrinsically high spiking patterns are remarkable and striking at the same time as 73 percent of the synaptic input to CN neurons comes from hundreds of converging purkinje cells that convey prominent inhibitory signals via their GABAergic connections (Palkovits *et al.*, 1977; Gauck & Jaeger, 2000; Person & Raman, 2011). Interestingly, following activation of the purkinje cell inputs to the cerebellar nuclei or inhibitory current injections neurons in the CN can respond with a depolarization of the membrane potential and consequently the firing of a ‘rebound’ burst of action potentials (Llinás & Muehlethaler, 1988; Aizenman & Linden, 1999; Hoebeek *et al.*, 2010). It is important to understand that the synchronicity of cerebellar nuclei spiking and their pauses is essential for downstream signal transfer where inputs from several cerebellar nuclei neurons converge. But if and how the firing frequency of cerebellar nuclei neurons can be modulated and/or even synchronized remains an open question. Within the

cerebellar cortex, there is a high chance that inputs from parallel fibers and climbing fibers which modulate simple spike frequency and generate complex spikes, respectively, mediate the generation of pauses in cerebellar nuclei spiking as well as the generation of rebound spikes (Hoebeek *et al.*, 2005, 2010; Person & Raman, 2011; Herzfeld *et al.*, 2015; Ten Brinke *et al.*, 2017). Here, the complex spike - relayed via climbing fibers that arise from the inferior olive - has the power to synchronize the simple spike patterns across cerebellar modules that align in the parasagittal plane of the cerebellar cortex (de Zeeuw *et al.*, 1988; Sugihara *et al.*, 1999; Schmolesky *et al.*, 2002; Apps & Hawkes, 2009). Here, cerebellar models suggest that the degree of purkinje cell spiking synchronicity determines the firing rate of CN neurons (Person & Raman, 2011). Furthermore, stimulation of the inferior olive results in poststimulus pauses in CN spiking patterns (Hoebeek *et al.*, 2010; Blenkinsop & Lang, 2011; Tang *et al.*, 2016) and an increase in the poststimulus spiking frequency (Hoebeek *et al.*, 2010). In this context, it is important to realize that pause length and the occurrence of rebound spikes are no hard values but grade along a continuum of periods with lower frequency that include pauses in spiking as well as periods with high spiking rates (Bengtsson *et al.*, 2011; Blenkinsop & Lang, 2011), that even correlate with behaviour (Ohmae *et al.*, 2013; Sarnaik & Raman, 2018). But, whether the complex spike that is distributed across Purkinje cells in a cerebellar module has the power to time-lock Purkinje cell spiking and translate all the way down to synchronized facilitation/inhibition in CN neuron spiking patterns (Blenkinsop & Lang, 2011; Tang *et al.*, 2016; Yarden-Rabinowitz & Yarom, 2017) remains under debate.

The highly irregular CN spike rates are translated in downstream target areas such as the thalamus. As described above, cerebellar spiking rates shift to phases of high and low frequency with pauses during movement (Ohmae *et al.*, 2013; Ten Brinke *et al.*, 2017; Sarnaik & Raman, 2018), while thalamic spiking ranges between 5-20 Hz and is intermingle with bursting discharges (Whitmire *et al.*, n.d.; Baker, 1971; Vitek *et al.*, 1994; Raeva *et al.*, 1999; Ahissar *et al.*, 2000; Proville *et al.*, 2014). These differences in spiking properties suggest a low-pass filtering function for cerebellar synapses and/or thalamic neurons. The high-release probability of the cerebellar synapses in the thalamus suggests that cerebellar synapses deplete, which in turn blocks or attenuates the transfer of information between VL and motor cortex (**Chapter 4** and **5**, Figure 1). From this perspective, spike coding from thalamus to motor cortex is depending on recovery from synaptic depression during a pause or a period of low-frequency CN spiking. The transfer of cerebellar information from thalamus to cortex is attenuated during high-frequency CN activity, but can be relayed after the induction of initial spikes and/or rebound spikes that follow a pause or low frequency activity in CN spiking. Within this concept, the movement related occurance of low frequency CN spiking patterns or pauses would be more essential for thalamo-cortical spike transfer than cerebellar rebound spiking, as

the pause itself results in the recharging of cerebellar synapses in the thalamus. In Chapter 4 and 5, we use optogenetic stimulation to synchronously activate cerebellar fibers that converge on a single thalamic neuron. Whether this activation pattern resembles in-vivo like properties remains controversial, as it remains an open question whether this level of synchronicity is also resembled in CN spiking patterns during behaviour (see discussion above).

In addition to the properties of cerebellar synapses in the thalamus, the transfer of cerebellar information to the motor cortex is dictated by the state of the thalamic membrane potential (Jahnsen & Llinas, 1984*b*; Mccormick & Bal, 1997). Our findings suggest that repetitive stimulation of M1 L6 fibers modulates the thalamic membrane potential and affects the availability of t-type calcium channels (**Chapter 5**). At depolarized potentials t-type calcium channels are inactivated, while hyperpolarized potentials de-inactivate them and drive thalamic cells to fire the characteristic low threshold calcium spike (LTS) and a burst of action potentials (Jahnsen and Llinas, 1984a, 1984b). The degree of t-type channel de-inactivation is time- and voltage-dependent and determines the number of spikes transferred within a burst (Jahnsen & Llinas, 1984*b*; Mease *et al.*, 2017) and thereby the quality and timing of thalamic spiking (Wolfart *et al.*, 2005; Mease *et al.*, 2014). In this context, it is important to notice that high cerebellar spiking rates above 100 Hz are likely to induce minimal responses in thalamic neurons, when compared with lower frequency results in relatively more hyperpolarized potentials. Furthermore, cortical feedback from M1 L6 neurons mono-synaptically innervates excitatory neurons in VL as well as inhibitory neurons in the reticular thalamic nucleus (RTN), which provides feed-forward inhibition to thalamo-cortical relay neurons (Yamawaki & Shepherd, 2015). The depressing short-term release dynamics of RTN synapses in the thalamus shift the balance between excitation and inhibition induced by M1 L6 towards depolarized membrane potentials (Crandall *et al.*, 2015).

From the combination of our knowledge on cerebellar spiking patters, the depletion of cerebellar synapses in the thalamus (**Chapter 4** and **5**) as well as the potential dependence of thalamic spiking output (**Chapter 5**), we could speculate that the sparse thalamic spiking patterns during movement execution (Baker, 1971; Vitek *et al.*, 1994; Raeva *et al.*, 1999) could be explained by the following processes: firstly due to the tonic firing of CN neurons, the synapses are likely to be depressed at rest, which only provides a tonically low depolarizing drive to the thalamus. Secondly, a period of cerebellar silence or low cerebellar spiking rates would allow cerebellar synapses to re-charge while providing no depolarizing drive to the thalamic potential. Together these two phases would reactivate large proportions of t-type calcium channels, which – thirdly - would allow the thalamus to respond with spike output once the silent cerebellar period

would be ended by a rebound spike and/or a new phase with high cerebellar spike rates would start (Hoebeek *et al.*, 2010; Sarnaik & Raman, 2018). Whether the debated rebound spiking of CN neurons following a climbing fiber-mediated pause provides a significant contribution remains controversial (Gauck & Jaeger, 2000; Alviña *et al.*, 2008; Hoebeek *et al.*, 2010; Bengtsson *et al.*, 2011; Person & Raman, 2011; Dykstra *et al.*, 2016; Sarnaik & Raman, 2018). Within the above described concept of cerebello-thalamic spike transfer, high cerebellar firing frequency patterns that are intermixed with pauses and/or low spike rate phases are essential, while rebound spikes would only amplify the effect thereof via an increased spike number after the pause. Still, the properties that we describe in **Chapter 4** and **5** indicate that VL neurons translate the high-frequency cerebellar spiking pattern into a temporally sparse and potentially movement related code, which may serve to fine-tune the processing in motor cortex.

CEREBRO-CEREBELLAR COMMUNICATION VIA A SHORTCUT?

In contrast to **Chapter 3, 4,** and **5** - which focus on the communication between the cerebellum, the thalamus and the cortex - **Chapter 7** focuses on the communication from the cortex to the cerebellum. This is particularly interesting as the communication in the brain is organized in loops in which the cerebellum, the thalamus and the cortex are interconnected. Conventional cerebello-thalamo-cortical communication is organized in the following way: cerebellar nuclei – contralateral thalamus – cortex – pontine nuclei – contralateral cerebellar cortex and nuclei. 'What wires together fires together' proves true as recent work shows that both cerebellar nuclei and cerebral cortex are co-entrained (Soteropoulos & Baker, 2006; Proville *et al.*, 2014; Gao *et al.*, 2018; Wagner *et al.*, 2019; Lindeman *et al.*, 2020). Behavioural, physiological and anatomical work shows that both the motor cortex and the cerebellar nuclei show preparatory activity during motor task that is co-dependent in a closed loop (Gao *et al.*, 2018). In contrast to the 'conventional' cerebro-cerebellar loop described above, the connection described in **Chapter 7** provides a new aspect to cerebro-cerebellar connectivity as it wires as follows: cerebellar nuclei – contralateral thalamus – cortex – ipsilateral cerebellar nuclei. This communication is not only faster but it also skips the signal integration processes in the cerebellar cortex. We hypothesize that this connection allows the motor cortex to send an efference copy to the cerebellar nuclei that informs the cerebellar system about ongoing motor execution and planning in the cortex. Future experiments will need to monitor the activity of cerebro-cerebellar projecting cells in the motor cortex, the insular cortex as well as the prefrontal cortex during behaviour and evaluate their effect on ongoing cerebellar activity. Whether this specific cerebro-cerebellar projecting cell population is co-entrained in the cerebro-cerebellar loop remains an open question.

METHODOLOGICAL DISCOURSE ON FIBER POPULATION STIMULATION IN NEURONAL TISSUE

While performing the experiments for **Chapters 2, 4, 5, 6** and **7**, I came across several ways to activate neuronal fibers in the mouse brain. The stimulation techniques used here range from the specific electrical stimulation of a single synapse (**Chapter 2**), optical stimulation of fiber populations in an in-vitro slice of the thalamus or cortex (**Chapter 4, 5** and **6**) as well as optical stimulation of cell populations in the intact brain system (**Chapter 7**). From a historical perspective, electrical stimulation in brain slices or the living brain system has been used to identify neuronal connectivity and synaptic properties in diverse neuronal systems. Fast electrical stimulation pulses in the microseconds range allow high-frequency stimulation trains with low temporal jitter that can go up to hundreds of Hertz. However, the placement of electrical stimulation electrodes in fiber bundles of the in-vitro or in-vivo preparation suffers from a low spatial specificity as it will activate all axons that pass through the electrical field of the electrode. Nevertheless, the use of electrical stimulation in brain tissue has dominated the neurosciences as well as the thalamo-cortical field as the identification of synaptic input properties was investigated with electrical stimulation techniques (Sawyer *et al.*, 1994*b*; Godwin *et al.*, 1996; Turner & Salt, 1998; Reichova & Sherman, 2004; Groh *et al.*, 2008; Pelzer *et al.*, 2017).

The pioneering of optogenetics, developed into the game changer of brain stimulation as it allows the activation of specific neuronal subpopulations and axonal fiber bundles while it is combinable with genetic tools and tuneable by optical manipulations (Harz & Hegemann, 1991; Gunaydin *et al.*, 2010; Zhang *et al.*, 2011; Klapoetke *et al.*, 2014; Schneider *et al.*, 2015; Deisseroth & Hegemann, 2017). Nevertheless, the available optogentic tools suffer from slow channel opening and closing kinetics (on- and off- kinetics) that apply an upper limit to the sustainability of high stimulation frequencies. As an example Klapoetke et al demonstrate that 2 ms light pulses result in risetimes of 3.5 ms for Channelrhodopsin and 8 ms for Chrimson as well as channel closing rates of 9.5 ms and 20 ms, respectively (Klapoetke et al., 2014, Supplementary Figure 3). Furthermore, the photocycle of opsins such as Channelrhodopsin and Chrimson determines the recovery of the peak photocurrent and thus the applicable stimulation frequencies. In more detail, the absorption of a photon triggers the isomerization and conformational changes of the retinal which induces the transition into the dark state in which the opsin remains inactivated and unexcitable (Stehfest & Hegemann, 2010; Schneider *et al.*, 2015). This is particularly critical for the stimulation of axonal fibers in in-vitro as well as in-vivo preparations, as the number of opsins within the relatively small surface of axons is lower than in the membrane of the soma. The transition of a high proportion

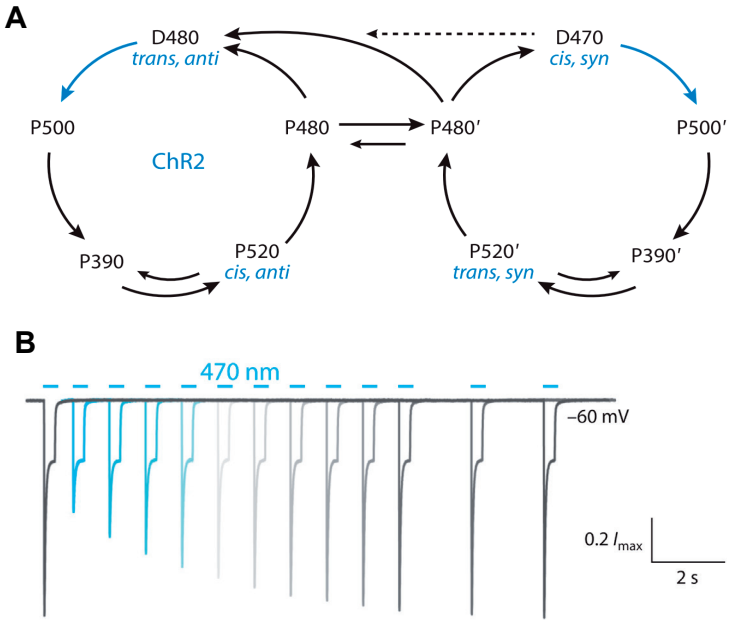

Figure 1. Photocycle model of Channelrhodopsin. (**A**) Photocycle model for Channelrhodopsin that implies photoactivation of the two dark states D480 and D470 with distinct retinal configurations (cis and trans). The light activation is indicated by blue arrows and the transition between both photocycles occurs in the presence of photointermediates P480 and P480'. (**B**) The recovery of the Channelrhodpsin photocurrents depends on the time interval between two light stimulation periods. This is the time that the Channelrhodopsin molecules require for conformational changes that allow them to transition from the dark state back to an excitable state. Adapted from (Schneider *et al.*, 2015).

of opsins to the dark state can easily result in the loss of axons during higher frequency activation patterns. Therefore, the optical stimulation parameters such as stimulation intensity or duration as well as experimental conditions such as the expression level of the corresponding opsin need to be carefully tested and evaluated. In **Chapter 4** and **5** we use optical stimulation frequencies of up to 50 Hz for Channelrhodopsin expressing cerebellar fibers and 20 Hz for ChrimsonR expressing motor cortical fibers, which – considering the on- and off- kinetics of the opsins - are at the upper limit suitable. To assure that the opsin expression levels and stimulation parameters allow the successful stimulation at these frequencies, we measured the photocurrent and channel closing rate in the Channelrhodopsin expressing CN somata as well as the ChrimsonR expressing M1 somata (**Chapter 5**, Figure 5 and 6). We find that the photocurrents gated by both opsins are unattenuated and suggest that the spike probabilities of both CN and M1-L6 neurons did not decrease during 50 Hz and 20 Hz optical stimulation. Especially for the Channelrhodopsin activation at 50 Hz, our experimental design profits from the short stimulation pulses of 1 ms that allow the fast recovery of the opsin from the dark cycle. These carefully titrated control experiments allow us to work at the upper edge

of stimulation frequency that the current optogenetic tools allow and provided us with the unique chance to stimulate cell-specific fiber bundles at physiologically relevant frequency ranges that could only be achieved with electrical stimulation for unspecific fiber bundles.

ABERRANT AXONAL CONNECTIVITY IN THE CORTEX CAN INDUCE EPILEPTIC SEIZURES

As introduced and summarized in **Chapter 6**, exogeneous expression of the dominant RHEB1p.P37L mutant induces mTOR pathway hyperactivity and spontaneous tonic-clonic seizures. A detailed analysis of the phenotype inducing brain malfunction shows that it is not the cortical malformation but aberrant axonal connectivity and vesicle release generated during cortical development that induces epilepsy. In the context of this thesis, **Chapter 6** highlights how we can use our basic knowledge on how the brain works in the healthy condition to understand the origins of brain malfunctions that cause clinical phenotypes such as epileptic seizures. I want to speculate about the effects of the identified hyperconnectivity on the systems level of brain function and the potential effect thereof on the cortico-thalamo-cortical loops described in **Chapter 1, 2, 3, 4** and **5**. The results in **Chapter 6**, show that in the RHEB1p.P37L mutant situation the axonal innervation to the contralateral sensory cortex is denser, which is accompanied by a synaptic hyperconnectivity to both L2/3 and L5. Whether this hyperconnectivity is due to an increase in the hardwiring of axonal connections and/or an increase in the number of release sides in the contralateral cortex remains controversial. In anyway, the resulting hyperexcitation is likely to induce the increased excitability and spiking of sensory neurons which transfer their output to interconnected downstream targets. As introduced in **Chapter 1** and described in **Chapter 2,** neurons in sensory cortex send projections to downstream thalamic targets such as the POm and the RTN, which in turn re-connect with the cortex by forming the cortico-thalamo-cortical loop. This closed-loop brain circuitry, is a potent circuit for the generation of seizures as any imbalance applied to this brain system can result in the generation of oscillations between the cortex and the thalamus – forming the base for epileptic phenotypes (Paz *et al.*, 2011, 2012). Here, it is important to understand that the resulting epileptic disease phenotype is a secondary consequence that can be induced by diverse primary events such as a mutation that offsets the thalamic and/or cerebral cortical excitation-inhibition balance or a stroke (Paz *et al.*, 2010, 2011, 2012; Kros *et al.*, 2015; Paz & Huguenard, 2015). With this knowledge in mind, it is easy to speculate that the hyperconnectivity and hyperexcitation of cortical neurons in the RHEB1p.37L mutant could be relayed down to the thalamus and induce reverberating network oscillations by inducing unbalanced

shifts in cortico-thalamo-cortical communication. Interestingly, blocking the synaptic vesicle release with Tetanus toxin prenatally and/or after the development of seizures in the RHEB1p.P37 mutant rescues the epileptic phenotype and normalizes the intrinsic excitability of the non-targeted contralateral cells in sensory cortex (**Chapter 6**). These data suggest, that once the excitation/inhibition imbalance in the cortex is reversed, the epileptic phenotype vanishes. Whether the epileptic phenotype can be traced back to reverberating oscillations via the cortico-thalamo-cortical loop could be proven by monitoring thalamic activity during the seizure.

Appendix

REFERENCES

Abs E, Goorden SMI, Schreiber J, Overwater IE, Hoogeveen-Westerveld M, Bruinsma CF, Aganović E, Borgesius NZ, Nellist M, Elgersma Y. 2013. TORC1-dependent epilepsy caused by acute biallelic Tsc1 deletion in adult mice. *Ann Neurol* **74**:569–79.

Ahissar E, Sosnik R & Haidarliu S (2000). Transformation from temporal to rate coding in a somatosensory thalamocortical pathway. Nature 406, 302–306.

Aizenman CD & Linden DJ (1999). Regulation of the rebound depolarization and spontaneous firing patterns of deep nuclear neurons in slices of rat cerebellum. J Neurophysiol 82, 1697–1709.

Albus JS (1971). A theory of cerebellar function. Math Biosci 10, 25–61.

Alloway KD (2008). Information processing streams in rodent barrel cortex: The differential functions of barrel and septal circuits. Cereb Cortex 18, 979–989.

Alloway KD, Smith JB & Beauchemin KJ (2010). Quantitative analysis of the bilateral brainstem projections from the whisker and forepaw regions in rat primary motor cortex. J Comp Neurol 518, 4546–4566.

Altrock WD et al. (2003). Functional inactivation of a fraction of excitatory synapses in mice deficient for the active zone protein bassoon. Neuron 37, 787–800.

Alviña K, Walter JT, Kohn A, Ellis-Davies G & Khodakhah K (2008). Questioning the role of rebound firing in the cerebellum. Nat Neurosci 11, 1256–1258.

Angaut P & Cicirata F (1988). The dentatorubral projection in the rat: An autoradiographic study. Behav Brain Res 28, 71–73.

Angaut P, Cicirate F & Serapide F (1985). Topographic organization of the cerebellothalamic projections in the rat. An autoradiographic study. Neuroscience.

Antziferova LI, Orlovsky GN & Pavlova GA (1980). Activity of Neurons of Cerebellar Nuclei During Fictitious Scratch Reflex in the Cat I Fastigial Nucleus. Brain Res 200, 239–248.

Apps R & Hawkes R (2009). Cerebellar cortical organization: a one-map hypothesis. Nat Rev Neurosci 10, 670–681.

Arber S (2017). Organization and function of neuronal circuits controlling movement. EMBO Mol Med 9, 281–284.

Arber S & Costa RM (2018). Connecting neuronal circuits for movement. Science (80-) 360, 1403–1404.

Armstrong BYDM & Edgley SA (1984). Discharges of Nucleus Interpositus Neurones During Locomotion in the Cat. J Physiol 351, 411–432.

Aronoff R, Matyas F, Mateo C, Ciron C, Schneider B & Petersen CCH (2010a). Long-range connectivity of mouse primary somatosensory barrel cortex. Eur J Neurosci 31, 2221–2233.

Aronoff R, Matyas F, Mateo C, Ciron C, Schneider B & Petersen CCH (2010b). Long-range connectivity of mouse primary somatosensory barrel cortex. Eur J Neurosci 31, 2221–2233.

Asanuma C, Thach WT & Jones EG (1983). Distribution of cerebellar terminations and their relation to other afferent terminations in the ventral lateral thalamic region of the monkey. Brain Res Rev 5, 237–265.

Aumann TD (2002). Cerebello-thalamic synapses and motor adaptation. Cerebellum 1, 69–77.

Aumann TD & Horne MK (1996a). Ramification and termination of single axons in the cerebellothalamic pathway of the rat. J Comp Neurol 376, 420–430.

Aumann TD & Horne MK (1996b). A comparison of the ultrastructure of synapses in the cerebello-rubral and cerebello-thalamic pathways in the rat. Neurosci Lett 211, 175–178.

Aumann TD & Horne MK (1999a). Ultrastructural change at rat cerebellothalamic synapses associated with volitional motor adaptation. J Comp Neurol 409, 71–84.

Aumann TD & Horne MK (1999b). Ultrastructural change at rat cerebellothalamic synapses associated with volitional motor adaptation. J Comp Neurol 409, 71–84.

Aumann TD, Rawson J a, Finkelstein DI & Horne MK (1994). Projections from the lateral and interposed cerebellar nuclei to the thalamus of the rat: a light and electron microscopic study using single and double anterograde labelling. J Comp Neurol 349, 165–181.

Aumann TD, Redman SJ & Horne MK (2000). Long-term potentiation across rat cerebello-thalamic synapses in vitro. Neurosci Lett 287, 151–155.

Bai X, Ma D, Liu A, Shen X, Wang QJ, Liu Y, Jiang Y. 2007. Rheb activates mTOR by antagonizing its endogenous inhibitor, FKBP38. *Science* **318**:977–80.

Baker MA (1971). SPONTANEOUS AND EVOKED ACTIVITY OF NEURONES IN THE SOMATOSENSORY THALAMUS OF THE WAKING CAT BY. J Physiol 217, 359–379.

Banker G, Goslin K. 1988. Developments in neuronal cell culture. *Nature*

Barkovich AJ, Guerrini R, Kuzniecky RI, Jackson GD, Dobyns WB. 2012. A developmental and genetic classification for malformations of cortical development: Update 2012. *Brain*.

Barthó P, Freund TF & Acsady L (2002). Selective GABAergic innervation of thalamic nuclei from zona incerta. Eur J Neurosci 16, 999–1014.

Bartho P, Slezia A, Varga V, Bokor H, Pinault D, Buzsaki G & Acsady L (2007). Cortical Control of Zona Incerta. J Neurosci 27, 1670–1681.

Bava A, Cicirata F, Giuffrida R, Licciardello S & Panto MR (1986). Electrophysiologic properties and nature of ventrolateral thalamic nucleus neurons reactive to converging inputs of paleo- and neocerebellar origin. Exp Neurol 91, 1–12.

Bava A, Manzoni T & Urbano A (1967). Effects of fastigial stimulation on thalamic neurones belonging to the diffuse projection system. Brain Res 4, 378–380.

Becker MI & Person AL (2019). Cerebellar Control of Reach Kinematics for Endpoint Precision. Neuron 103, 335-348.e5.

Beloozerova IN, Sirota MG & Swadlow HA (2003). Activity of Different Classes of Neurons of the Motor Cortex during Locomotion. J Neurosci 23, 1087–1097.

Bengtsson F, Ekerot CF & Jörntell H (2011). In vivo analysis of inhibitory synaptic inputs and rebounds in deep cerebellar nuclear neurons. PLoS One 6, 1–12.

Bentivoglio M & Kuypers H (1982). Divergent Axon Collaterals from Rat Cerebellar Nuclei to Diencephalon, Mesencephalon, Medulla Oblongata and Cervical Cord. Exp Brain Res339–356.

Berendse, H.W., and Groenewegen, H.J. (1991). Restricted cortical termination fields of the midline and intralaminar thalamic nuclei in the rat. Neuroscience 42, 73-102.

Berkley KJ (1983). Spatial Relationships Between the Terminations of Somatic Sensory Motor Pathways i n the Rostral Brainstem of Cats and Monkeys . 11 . Cerebellar Projections Compared With Those of the Ascending Somatic Sensory Pathways i n Lateral Diencephalon. J Comp Neurol 251, 229–251.

Bhaskar PT, Hay N. 2007. The Two TORCs and Akt. *Dev Cell*.

Bickford, M.E. (2015). Thalamic Circuit Diversity: Modulation of the Driver/Modulator Framework. Frontiers in neural circuits 9, 86.

Bickford ME, Zhou N, Krahe TE, Govindaiah G & Guido W (2015). Retinal and Tectal " Driver-Like " Inputs Converge in the Shell of the Mouse Dorsal Lateral Geniculate Nucleus. 35, 10523–10534.

Binder DK, Croll SD, Gall CM, Scharfman HE. 2001. BDNF and epilepsy: Too much of a good thing? *Trends Neurosci*.

Biswas MS, Luo Y, Sarpong GA & Sugihara I (2019). Divergent projections of single ponto-

cerebellar axons to multiple cerebellar lobules in the mouse. J Comp Neurol 527, 1966–1985.

Blenkinsop TA & Lang EJ (2011). Synaptic action of the olivocerebellar system on cerebellar nuclear spike activity. J Neurosci 31, 14708–14720.

Bodor AL, Giber K, Rovó Z, Ulbert I & Acsády L (2008). Structural correlates of efficient GABAergic transmission in the basal ganglia-thalamus pathway. J Neurosci 28, 3090–3102.

Bodranghien, F., Bastian, A., Casali, C., Hallett, M., Louis, E.D., Manto, M., Marien, P., Nowak, D.A., Schmahmann, J.D., Serrao, M., et al. (2016). Consensus Paper: Revisiting the Symptoms and Signs of Cerebellar Syndrome. Cerebellum 15, 369-391.

Bokor H, Frère SGA, Eyre MD, Slézia A, Ulbert I, Lüthi A & Acsády L (2005). Selective GABAergic control of higher-order thalamic relays. Neuron 45, 929–940.

Bortone DS, Olsen SR & Scanziani M (2014). Translaminar inhibitory cells recruited by layer 6 corticothalamic neurons suppress visual cortex. Neuron 82, 474–485.

Bosman LWJ, Houweling AR, Owens CB, Tanke N, Shevchouk OT, Rahmati N, Teunissen WHT, Ju C, Gong W, Koekkoek SKE & De Zeeuw CI (2011). Anatomical Pathways Involved in Generating and Sensing Rhythmic Whisker Movements. Front Integr Neurosci 5, 1–28.

Bosman LWJ, Koekkoek SKE, Shapiro J, Rijken BFM, Zandstra F, van der Ende B, Owens CB, Potters J-W, de Gruijl JR, Ruigrok TJH & De Zeeuw CI (2010). Encoding of whisker input by cerebellar Purkinje cells. J Physiol 588, 3757–3783.

Bourassa J, Pinault D & Deschênes M (1995). Corticothalamic projections from the cortical barrel field to the somatosensory thalamus in rats: a single-fibre study using biocytin as an anterograde tracer. Eur J Neurosci 7, 19–30.

Bouvier J, Caggiano V, Leiras R, Caldeira V, Bellardita C, Balueva K, Fuchs A & Kiehn O (2015). Descending Command Neurons in the Brainstem that Halt Locomotion. Cell 163, 1191–1203.

Brecht M, Schneider M, Sakmann B & Margrie TW (2004). Whisker movements evoked by stimulation of single pyramidal cells in rat motor cortex. Nature 427, 704–710.

Ten Brinke MM, Heiney SA, Wang X, Proietti-Onori M, Boele HJ, Bakermans J, Medina JF, Gao Z & De Zeeuw CI (2017). Dynamic modulation of activity in cerebellar nuclei neurons during pavlovian eyeblink conditioning in mice. Elife 6, 1–27.

Brooks JX, Carriot J & Cullen KE (2015). Learning to expect the unexpected: rapid updating in primate cerebellum during voluntary self-motion. Nat Neurosci 18, 1310–1317.

Budnik V, Ruiz-Cañada C, Wendler F. 2016. Extracellular vesicles round off communication in the nervous system. *Nat Rev Neurosci* **17**:160–172.

Buee, J., Deniau, J.M., and Chevalier, G. (1986). Nigral modulation of cerebello-thalamocortical transmission in the ventral medial thalamic nucleus. Experimental brain research 65, 241-244.

Cadusseau J & Roger M (1991). Cortical and Subcortical Connections of the Pars Compacta of the Anterior Pretectal Nucleus in the Rat. Neurosci Res 12, 83–100.

Capelli P, Pivetta C, Esposito MS & Arber S (2017). Locomotor speed control circuits in the caudal brainstem. Nature 551, 373–377.

Cases-Langhoff C, Voss B, Garner A, Appeltauer U, Takei K, Kindler S, Vehs RW, De Camilli P, Gundelfinger ED & Garner CC (1996). Piccolo, a novel 420 kDa protein associated with the presynaptic cytomatrix. Eur J Cell Biol 69, 214–223.

Chabrol FP, Arenz A, Wiechert MT, Margrie TW & Digregorio DA (2015). Synaptic diversity enables temporal coding of coincident multisensory inputs in single neurons. Nat Neurosci; DOI: 10.1038/nn.3974.

Chassoux F, Landre E, Rodrigo S, Beuvon F, Turak B, Semah F, Devaux B. 2008. Intralesional

recordings and epileptogenic zone in focal polymicrogyria. *Epilepsia* **49**:51–64.

Chauvière L, Rafrafi N, Thinus-Blanc C, Bartolomei F, Esclapez M, Bernard C. 2009. Early deficits in spatial memory and theta rhythm in experimental temporal lobe epilepsy. *J Neurosci* **29**:5402–5410.

Chazeron IDE, Raboisson P & Dallel R (2004). Organization of Diencephalic Projections from the Spinal Trigeminal Nucleus Oralis : An Anterograde Tracing Study in the Rat. Neuroscience 127, 921–928.

Chen CH, Fremont R, Arteaga-Bracho EE & Khodakhah K (2014). Short Latency cerebellar modulation of the basal ganglia. Nat Publ Gr 17, 1767–1775.

Chen S, Augustine GJ & Chadderton P (2016). The cerebellum linearly encodes whisker position during voluntary movement. Elife 5, 1–16.

Chen T-W, Li N, Daie K & Svoboda K (2017). A Map of Anticipatory Activity in Mouse Motor Cortex. Neuron 94, 866-879.e4.

Chevassus-au-Louis N, Baraban SC, Gaíarsa J-L, Ben-Ari Y. 1999. Cortical Malformations and Epilepsy: New Insights from Animal Models. *Epilepsia* **40**:811–821.

Chiaia NL, Rhoades RW, Bennett-clarke CA, Fish SE & Killackey HP (1991a). Thalamic Processing of Vibrissal Information in the Rat . I . Afferent Input to the Medial Ventral Posterior and Posterior Nuclei. J Cell Biol.

Chiaia NL, Rhoades RW, Fish SE & Killackey HP (1991b). Thalamic Processing of Vibrissal Information in the Rat : 11 . Morphological and Functional Properties of Medial Ventral Posterior Nucleus and Posterior Nucleus Neurons. J Comp Neurol.

Choi Y-J, Di Nardo A, Kramvis I, Meikle L, Kwiatkowski DJ, Sahin M, He X. 2008. Tuberous sclerosis complex proteins control axon formation. *Genes Dev* **22**:2485–95.

Chung, S., Li, X., and Nelson, S.B. (2002). Short-term depression at thalamocortical synapses contributes to rapid adaptation of cortical sensory responses in vivo. Neuron 34, 437-446.

Ciceri G, Dehorter N, Sols I, Huang ZJ, Maravall M, Marín O. 2013. Lineage-specific laminar organization of cortical GABAergic interneurons. *Nat Neurosci* **16**:1199–1210.

Cicirata F, Serapide MF, Parenti R, Pant?? MR, Zappal?? A, Nicotra A & Cicero D (2004). The basilar pontine nuclei and the nucleus reticularis tegmenti pontis subserve distinct cerebrocerebellar pathways. Prog Brain Res 148, 261–282.

Clascá F, Rubio-Garrido P & Jabaudon D (2012). Unveiling the diversity of thalamocortical neuron subtypes. Eur J Neurosci 35, 1524–1532.

Cohen, D., Chambers, W.W., and Sprague, J.M. (1958). Experimental study of the efferent projections from the cerebellar nuclei to the brainstem of the cat. The Journal of comparative neurology 109, 233-259.

Cohen JD, Hirata A & Castro-alamancos MA (2008). Vibrissa Sensation in Superior Colliculus : Wide-Field Sensitivity and State-Dependent Cortical Feedback. J Neurosci 28, 11205–11220.

Comoli E, Coizet V, Boyes J, Bolam JP, Canteras NS, Quirk RH, Overton PG & Redgrave P (2003). A direct projection from superior colliculus to substantia nigra for detecting salient visual events. Nat Neurosci 6, 974–980.

Constantinople CM & Bruno RM (2013). Deep Cortical Layers Are Activated Directly by Thalamus. Science (80-); DOI: 10.1126/science.1236425.

Crandall SR, Cruikshank SJ & Connors BW (2015a). A Corticothalamic Switch: Controlling the Thalamus with Dynamic Synapses. Neuron 86, 768–782.

Crandall SR, Cruikshank SJ, Connors BW, Crandall SR, Cruikshank SJ & Connors BW (2015b). Article A Corticothalamic Switch : Controlling the Thalamus with Dynamic Synapses Article A Corticothalamic Switch : Controlling the Thalamus with Dynamic Synapses. Neuron1–15.

Crino PB. 2011. MTOR: A pathogenic signaling pathway in developmental brain malformations. *Trends Mol Med* **17**:734–742.

Crochet S & Petersen CCH (2006). Correlating whisker behavior with membrane potential in barrel cortex of awake mice. Nat Neurosci 9, 608–610.

Cruikshank SJ, Ahmed OJ, Stevens TR, Patrick SL, Gonzalez AN, Elmaleh M & Connors BW (2012). Thalamic control of layer 1 circuits in prefrontal cortex. J Neurosci 32, 17813–17823.

Cruikshank SJ, Lewis TJ & Connors BW (2007). Synaptic basis for intense thalamocortical activation of feedforward inhibitory cells in neocortex. 10, 462–468.

Daniel, H., Billard, J.M., Angaut, P., and Batini, C. (1987). The interposito-rubrospinal system. Anatomical tracing of a motor control pathway in the rat. Neuroscience research 5, 87-112.

Davydova D, Marini C, King C, Klueva J, Bischof F, Romorini S, Altrock WD, Montenegro-venegas C, Heine M, Schneider R, Schroeder MS, Henneberger C, Rusakov DA, Gundelfinger ED & Fe (2014). Bassoon Specifically Controls Presynaptic P/Q-type Ca2+ Channels via RIM-Binding Protein. Neuron 82, 181–194.

Deisseroth K & Hegemann P (2017). The form and function of channelrhodopsin. Science (80-); DOI: 10.1126/science.aan5544.

Deschênes M, Veinante P & Zhang ZW (1998). The organization of corticothalamic projections: Reciprocity versus parity. Brain Res Rev 28, 286–308.

Deschenes, M., Bourassa, J., Doan, V.D., and Parent, A. (1996a). A single-cell study of the axonal projections arising from the posterior intralaminar thalamic nuclei in the rat. The European journal of neuroscience 8, 329-343.

Deschenes, M., Bourassa, J., and Parent, A. (1996b). Striatal and cortical projections of single neurons from the central lateral thalamic nucleus in the rat. Neuroscience 72, 679-687.

De Zeeuw, C.I., Hoebeek, F.E., Bosman, L.W., Schonewille, M., Witter, L., and Koekkoek, S.K. (2011). Spatiotemporal firing patterns in the cerebellum. Nature reviews Neuroscience 12, 327-344.

Dieck S, Sanmartí-vila L, Langnaese K, Richter K, Kindler S, Soyke A, Wex H, Smalla K, Kämpf U, Fränzer J, Stumm M, Garner CC & Gundelfinger ED (1998). Bassoon, a Novel Zinc-finger CAG/Glutamine-repeat Protein Selectively Localized at the Active Zone of Presynaptic Nerve Terminals. J Cell Biol 142, 499–509.

Dondzillo A, Sätzler K, Horstmann H, Altrock WD, Gundelfinger ED & Kuner T (2010). Targeted three-dimensional immunohistochemistry reveals localization of presynaptic proteins Bassoon and Piccolo in the rat calyx of Held before and after the onset of hearing. J Comp Neurol 518, 1008–1029.

Douglas RJ & Martin KAC (2004). Neuronal Circuits of the Neocortex. Annu Rev Neurosci 27, 419–451.

Dufner Almeida LG, Nanhoe S, Zonta A, Hosseinzadeh M, Kom-Gortat R, Elfferich P, Schaaf G, Kenter A, Kümmel D, Migone N, Povey S, Ekong R, Nellist M. 2019. Comparison of the functional and structural characteristics of rare TSC2 variants with clinical and genetic findings. *Hum Mutat* humu.23963.

Dumas DB, Gornati S V., Adolfs Y, Shimogori T, Pasterkamp RJ & Hoebeek FE (2019). Anatomical development of the cerebellothalamic tract in embryonic mice. bioRxiv1–47.

Dykstra S, Engbers JDT, Bartoletti TM & Turner RW (2016). Determinants of rebound burst responses in rat cerebellar nuclear neurons to physiological stimuli. J Physiol 594, 985–1003.

Eccles BYJC, Llinas R & Sasaki K (1966). The excitatory synaptic action of climbing fibres on the Purkinje cells of the cerebellum. J Physiol 182, 268–296.

Economo M, Viswanathan S, Tasic B, Bas E, Winnubst J, Menon V, Graybuck LT, Nguyen TN, Wang L, Gerfen CR, Chandrashekar J, Zeng H, Looger LL & Svoboda K (2017). Distinct descending motor cortex pathways and their roles in movement. bioRxiv229260.

Economo MN, Viswanathan S, Tasic B, Bas E, Winnubst J, Menon V, Graybuck LT, Nguyen TN, Smith KA, Yao Z, Wang L, Gerfen CR, Chandrashekar J, Zeng H, Looger LL & Svoboda K (2018). Distinct descending motor cortex pathways and their roles in movement. Nature 563, 79–84.

Elsayed GF, Lara AH, Kaufman MT, Churchland MM & Cunningham JP (2016). Reorganization between preparatory and movement population responses in motor cortex. Nat Commun 7, 1–15.

Esposito MS, Capelli P & Arber S (2014). Brainstem nucleus MdV mediates skilled forelimb motor tasks. Nature 508, 351–356.

Fader CM, Sánchez DG, Mestre MB, Colombo MI. 2009. TI-VAMP/VAMP7 and VAMP3/cellubrevin: two v-SNARE proteins involved in specific steps of the autophagy/multivesicular body pathways. *Biochim Biophys Acta - Mol Cell Res* **1793**:1901–1916.

Fame RM, MacDonald JL, Macklis JD. 2011. Development, specification, and diversity of callosal projection neurons. *Trends Neurosci*.

Felsen G & Mainen ZF (2008). Neural Substrates of Sensory-Guided Locomotor Decisions in the Rat Superior Colliculus. Neuron 60, 137–148.

Fenster SD, Chung WJ, Zhai R, Cases-Langhoff C, Voss B, Garner a M, Kaempf U, Kindler S, Gundelfinger ED & Garner CC (2000). Piccolo, a presynaptic zinc finger protein structurally related to bassoon. Neuron 25, 203–214.

Fenlon LR, Suárez R, Richards LJ. 2017. The anatomy, organisation and development of contralateral callosal projections of the mouse somatosensory cortex. *Brain Neurosci Adv* **1**:239821281769488.

Ferreira, T.A., Blackman, A.V., Oyrer, J., Jayabal, S., Chung, A.J., Watt, A.J., Sjostrom, P.J., and van Meyel, D.J. (2014). Neuronal morphometry directly from bitmap images. Nature methods 11, 982-984.

Foster GA, Sizer AR, Rees H & Roberts MHT (1989). Afferent projections to the rostral anterior pretectal nucleus of the rat: a possible role in the processing of noxious stimuli. Neuroscience 29, 685–694.

Franklin, K., and Paxinos, G. (2001). The mouse brain in stereotactic coordinates, Compact, 2nd edn (cademic Press).

Friedlander MJ, Lin CS & Sherman SM (1979). Structure of physiologically identified X and Y cells in the cat's lateral geniculate nucleus. Science (80-) 204, 1114–1117.

Fujita H, Kodama T & Du Lac S (2020). Modular output circuits of the fastigial nucleus for diverse motor and nonmotor functions of the cerebellar vermis. Elife 9, 1–91.

Gaisano HY, Sheu L, Foskett JK, Trimble WS. 1994. Tetanus toxin light chain cleaves a vesicle-associated membrane protein (VAMP) isoform 2 in rat pancreatic zymogen granules and inhibits enzyme secretion. *J Biol Chem* **269**:17062–17066.

Galiñanes GL, Bonardi C & Huber D (2018). Directional Reaching for Water as a Cortex-Dependent Behavioral Framework for Mice. Cell Rep 22, 2767–2783.

Galliano E, Gao Z, Schonewille M, Todorov B, Simons E, Pop AS, D'Angelo E, Van Den Maagdenberg AMJM, Hoebeek FE & De Zeeuw CI (2013). Silencing the Majority of Cerebellar Granule Cells Uncovers Their Essential Role in Motor Learning and Consolidation. Cell Rep 3, 1239–1251.

Gambino F, Pagès S, Kehayas V, Baptista D, Tatti R, Carleton A & Holtmaat A (2014). Sensory-evoked LTP driven by dendritic plateau potentials in vivo. Nature; DOI: 10.1038/nature13664.

Gao Z, van Beugen BJ & De Zeeuw CI (2012). Distributed synergistic plasticity and cerebellar learning. Nat Rev Neurosci 13, 619–635.

Gao Z, Davis C, Thomas AM, Economo MN, Abrego AM, Svoboda K, Zeeuw CI De & Li N (2018). A cortico-cerebellar loop for motor planning. Nature 563, 113–116.

Gao Z, Proietti-Onori M, Lin Z, ten Brinke MM, Boele HJ, Potters JW, Ruigrok TJH, Hoebeek FE & De Zeeuw CI (2016). Excitatory Cerebellar Nucleocortical Circuit Provides Internal Amplification during Associative Conditioning. Neuron 89, 645–657.

Garwicz M & Andersson G (1992). Spread of synaptic activity along parallel fibres in cat cerebellar anterior lobe. Exp Brain Res 88, 615–622.

Gauck V & Jaeger D (2000). The control of rate and timing of spikes in the deep cerebellar nuclei by inhibition. J Neurosci 20, 3006–3016.

Geinisman, Y. (1993). Perforated axospinous synapses with multiple, completely partitioned transmission zones: probable structural intermediates in synaptic plasticity. Hippocampus 3, 417-433.

Giber K, Diana M a, M Plattner V, Dugué GP, Bokor H, Rousseau C V, Maglóczky Z, Havas L, Hangya B, Wildner H, Zeilhofer HU, Dieudonné S & Acsády L (2015). A subcortical inhibitory signal for behavioral arrest in the thalamus. Nat Neurosci; DOI: 10.1038/nn.3951.

Giber K, Slezia A, Bokor H, Bodor AL, Ludanyi A, Katona I & Acsády L (2008). Heterogeneous Output Pathways Link the Anterior Pretectal Nucleus With the Zona Incerta and the Thalamus in Rat. J Comp Neurol 506, 122–140.

Godwin DW, Vaughan JW & Sherman SM (1996). Metabotropic glutamate receptors switch visual response mode of lateral geniculate nucleus cells from burst to tonic. J Neurophysiol 76, 1800–1816.

Goldberg, J.H., Farries, M.A., and Fee, M.S. (2013). Basal ganglia output to the thalamus: still a paradox. Trends in neurosciences 36, 695-705.

Gong S, Doughty M, Harbaugh CR, Cummins A, Hatten ME, Heintz N & Gerfen CR (2007). Targeting Cre Recombinase to Specific Neuron Populations with Bacterial Artificial Chromosome Constructs. 27, 9817–9823.

Gong X, Zhang L, Huang T, Lin T V., Miyares L, Wen J, Hsieh L, Bordey A. 2015. Activating the translational repressor 4E-BP or reducing S6K-GSK3β activity prevents accelerated axon growth induced by hyperactive mTOR *in vivo*. *Hum Mol Genet* **24**:5746–5758.

Goorden SMI, Abs E, Bruinsma CF, Riemslagh FW, van Woerden GM, Elgersma Y. 2015. Intact neuronal function in Rheb1 mutant mice: implications for TORC1-based treatments. *Hum Mol Genet* **24**:3390–8.

Gornati S V., Schäfer CB, Eelkman Rooda OHJ, Nigg AL, De Zeeuw CI & Hoebeek FE (2018). Differentiating Cerebellar Impact on Thalamic Nuclei. Cell Rep2690–2704.

Groenewoud MJ, Goorden SMI, Kassies J, Pellis-van Berkel W, Lamb RF, Elgersma Y, Zwartkruis FJT. 2013. Mammalian target of rapamycin complex I (mTORC1) activity in ras homologue enriched in brain (Rheb)-deficient mouse embryonic fibroblasts. *PLoS One* **8**:e81649.

Groh A, Bokor H, Mease R a, Plattner VM, Hangya B, Stroh A, Deschenes M & Acsády L (2013). Convergence of Cortical and Sensory Driver Inputs on Single Thalamocortical Cells. Cereb Cortex.

Groh A, de Kock CPJ, Wimmer VC, Sakmann B & Kuner T (2008). Driver or coincidence detector: modal switch of a corticothalamic giant synapse controlled by spontaneous activity and short-term depression. J Neurosci 28, 9652–9663.

Guillery RW & Sherman SM (2002). Thalamic relay functions and their role in corticocortical communication: Generalizations from the visual system. Neuron 33, 163–175.

Gummadavelli, A., Motelow, J.E., Smith, N., Zhan, Q., Schiff, N.D., and Blumenfeld, H. (2015). Thalamic stimulation to improve level of

consciousness after seizures: evaluation of electrophysiology and behavior. Epilepsia 56, 114-124.

Gunaydin L a, Yizhar O, Berndt A, Sohal VS, Deisseroth K & Hegemann P (2010). Ultrafast optogenetic control. Nat Neurosci 13, 387–392.

Gundelfinger ED & Fejtova A (2012). Molecular organization and plasticity of the cytomatrix at the active zone. Curr Opin Neurobiol 22, 423–430.

Guo C, Peng J, Zhang Y, Li A, Li Y, Yuan J, Xu X, Ren M, Gong H & Chen S (2017a). Single-axon level morphological analysis of corticofugal projection neurons in mouse barrel field. Sci Rep 7, 1–9.

Guo JZ, Graves AR, Guo WW, Zheng J, Lee A, Rodríguez-Gonzá Lez J, Li N, Macklin JJ, Phillips JW, Mensh BD, Branson K & Hantman AW (2015). Cortex commands the performance of skilled movement. Elife 4, 1–18.

Guo K, Yamawaki N, Svoboda K & Shepherd GMG (2018). Anterolateral motor cortex connects with a medial subdivision of ventromedial thalamus through cell-type-specific circuits, forming an excitatory thalamo-cortico-thalamic loop via layer 1 apical tuft dendrites of layer 5B pyramidal tract type neurons Sec. ; DOI: 10.1523/JNEUROSCI.1333-18.2018.

Guo Z, Li N, Huber D, Ophir E, Gutnisky D, Ting J, Feng G & Svoboda K (2014). Flow of cortical activity underlying a tactile decision in mice. Neuron 81, 179–194.

Guo Z V., Inagaki HK, Daie K, Druckmann S, Gerfen CR & Svoboda K (2017b). Maintenance of persistent activity in a frontal thalamocortical loop. Nature 545, 181–186.

Guy N, Chalus M, Dallel R & Voisin DL (2005). Both oral and caudal parts of the spinal trigeminal nucleus project to the somatosensory thalamus in the rat. Eur J Neurosci 21, 741–754.

Gwyn DG & Flumerfelt BA (1974). A comparison of the distribution of cortical and cerebellar afferents in the red nucleus of the rat. Brain Res 69, 130–135.

Halassa MM & Acsády L (2016). Thalamic Inhibition : Diverse Sources , Diverse Scales. Trends Neurosci 39, 680–693.

Hallermann S, Fejtova A, Schmidt H, Weyhersmüller A, Silver RA, Gundelfinger ED & Eilers J (2010). Bassoon speeds vesicle reloading at a central excitatory synapse. Neuron 68, 710–723.

Hanai S, Sukigara S, Dai H, Owa T, Horike S ichi, Otsuki T, Saito T, Nakagawa E, Ikegaya N, Kaido T, Sato N, Takahashi A, Sugai K, Saito Y, Sasaki M, Hoshino M, Goto Y ichi, Koizumi S, Itoh M. 2017. Pathologic Active mTOR Mutation in Brain Malformation with Intractable Epilepsy Leads to Cell-Autonomous Migration Delay. *Am J Pathol* **187**:1177–1185.

Hansel C, Linden DJ & D'Angelo E (2001). Beyond parallel fiber LTD: The diversity of synaptic and non-synaptic plasticity in the cerebellum. Nat Neurosci 4, 467–475.

Harris KD & Shepherd GMG (2015). review The neocortical circuit : themes and variations.

Haroian, A.J., Massopust, L.C., and Young, P.A. (1981). Cerebellothalamic projections in the rat: an autoradiographic and degeneration study. The Journal of comparative neurology 197, 217-236.

Harz H & Hegemann P (1991). Rhodopsin-regulated calcium currents in Chlamydomonas. Nature 351, 489–491.

Häusser M & Clark BA (1997). Tonic synaptic inhibition modulates neuronal output pattern and spatiotemporal synaptic integration. Neuron 19, 665–678.

Heise CE & Mitrofanis J (2006). Evidence for a Glutamatergic Projection from the Zona Incerta to the Basal. J Comp Neurol 495, 482–495.

Henschke JU & Pakan JMP (2020). Disynaptic cerebrocerebellar pathways originating from multiple functionally distinct cortical areas. Elife 9, 1–27.

Herkenham, M. (1979). The afferent and efferent connections of the ventromedial thalamic nucleus in the rat. The Journal of comparative neurology 183, 487-517.

Herkenham, M. (1980). Laminar organization of thalamic projections to the rat neocortex. Science 207, 532-535.

Herzfeld DJ, Kojima Y, Soetedjo R & Shadmehr R (2015). Encoding of action by the Purkinje cells of the cerebellum. Nature 526, 439–441.

Hoebeek, F.E., Khosrovani, S., Witter, L., and De Zeeuw, C.I. (2008). Purkinje cell input to cerebellar nuclei in tottering: ultrastructure and physiology. Cerebellum 7, 547-558.

Hoebeek FE, Stahl JS, Van Alphen a. M, Schonewille M, Luo C, Rutteman M, Van Den Maagdenberg a. MJM, Molenaar PC, Goossens HHLM, Frens M a. & De Zeeuw CI (2005). Increased noise level of Purkinje cell activities minimizes impact of their modulation during sensorimotor control. Neuron 45, 953–965.

Hoebeek FE, Witter L, Ruigrok TJH & De Zeeuw CI (2010). Differential olivo-cerebellar cortical control of rebound activity in the cerebellar nuclei. Proc Natl Acad Sci U S A 107, 8410–8415.

Hoffer ZS, Arantes HB, Roth RL & Alloway KD (2005). Functional circuits mediating sensorimotor integration: Quantitative comparisons of projections from rodent barrel cortex to primary motor cortex, neostriatum, superior colliculus, and the pons. J Comp Neurol 488, 82–100.

Hoogland PV, Wouterlood FG, Welker E & Van der Loos H (1991). Ultrastructure of giant and small thalamic terminals of cortical origin: a study of the projections from the barrel cortex in mice using Phaseolus vulgaris leuco-agglutinin (PHA-L). Eperimental Brain Res 87, 159–172.

Hooks BM (2016). Sensorimotor Convergence in Circuitry of the Motor Cortex. Neurosci1–13.

Hooks BM, Hires SA, Zhang YX, Huber D, Petreanu L, Svoboda K & Shepherd GMG (2011). Laminar analysis of excitatory local circuits in vibrissal motor and sensory cortical areas. PLoS Biol; DOI: 10.1371/journal.pbio.1000572.

Hooks BM, Lin XJY, Guo C & Svoboda K (2015). Dual-Channel Circuit Mapping Reveals Sensorimotor Convergence in the Primary Motor Cortex. 35, 4418–4426.

Hooks BM, Mao T, Gutnisky D a, Yamawaki N, Svoboda K & Shepherd GMG (2013). Organization of cortical and thalamic input to pyramidal neurons in mouse motor cortex. J Neurosci 33, 748–760.

Houck BD & Person AL (2015). Cerebellar premotor output neurons collateralize to innervate the cerebellar cortex. J Comp Neurol; DOI: 10.1002/cne.23787.

Hsieh LS, Wen JH, Claycomb K, Huang Y, Harrsch FA, Naegele JR, Hyder F, Buchanan GF, Bordey A. 2016. Convulsive seizures from experimental focal cortical dysplasia occur independently of cell misplacement. *Nat Commun* **7**:11753.

Huang CC, Sugino K, Shima Y, Guo C, Bai S, Mensh BD, Nelson SB & Hantman AW (2013). Convergence of pontine and proprioceptive streams onto multimodal cerebellar granule cells. Elife 2013, 1–17.

Huguenard JR & McCormick DA (2007). Thalamic synchrony and dynamic regulation of global forebrain oscillations. Trends Neurosci 30, 350–356.

Humphrey AL, Sur M, Uhlrich DJ & Sherman SM (1985a). Termination patterns of individual X- and Y-cell axons in the visual cortex of the cat: Projections to area 18, to the 17/18 border region, and to both areas 17 and 18. J Comp Neurol 233, 190–212.

Humphrey AL, Sur M, Uhlrich DJ & Sherman SM (1985b). Projection patterns of individual X- and Y-cell axons from the lateral geniculate nucleus to cortical area 17 in the cat. J Comp Neurol 233, 159–189.

Hwang XK, Bertolero MA, Liu XWB & Esposito XMD (2017). The Human Thalamus Is an Integrative Hub for Functional Brain Networks. J Neurosci 37, 5594–5607.

Iino Y, Sawada T, Yamaguchi K, Tajiri M, Ishii S, Kasai H & Yagishita S (2020). Dopamine D2 receptors in discrimination learning and spine enlargement. Nature 579, 555–560.

Ishikawa T, Shimuta M, Häusser M & Ha M (2015). Multimodal sensory integration in single cerebellar granule cells in vivo. Elife 4, e12916.

Jahnsen BYH & Llinas R (1984a). Ionic Basis for the Electroresponsiveness and Oscillatory properties of guinea-pig thalamic neurones in vitro. J Physiol 349, 227–247.

Jahnsen BYH & Llinas R (1984b). Electrophysiological properties of guinea-pig thalamic neurones: An in-vitro study. J Physiol 349, 205–226.

Jahnsen H & Llinás R (1984). Electrophysiological properties of guinea???pig thalamic neurones: an in vitro study. J Physiol 349, 205–226.

Jeong M, Kim Y, Kim J, Ferrante DD, Mitra PP, Osten P & Kim D (2016). Comparative three-dimensional connectome map of motor cortical projections in the mouse brain. Sci Rep1–14.

Jones EG (1998). Viewpoint: The core and matrix of thalamic organization. Neuroscience 85, 331–345.

Jones EG (2007). The Thalamus.

Jones, E.G., and Hendry, S.H. (1989). Differential Calcium Binding Protein Immunoreactivity Distinguishes Classes of Relay Neurons in Monkey Thalamic Nuclei. The European journal of neuroscience 1, 222-246.

Jörntell H & Ekerot CF (1999). Topographical organization of projections to cat motor cortex from nucleus interpositus anterior and forelimb skin. J Physiol 514, 551–566.

Jun JJ et al. (2017). Fully integrated silicon probes for high-density recording of neural activity. Nature 551, 232–236.

Juric-Sekhar G, Hevner RF. 2019. Malformations of Cerebral Cortex Development: Molecules and Mechanisms. *Annu Rev Pathol Mech Dis* **14**:293–318.

Kandel ER, Schwartz JH, Jessell TM, Siegelbaum SA & Hudspeth AJ (2012). Principles of Neural Science.

Kane N, Acharya J, Benickzy S, Caboclo L, Finnigan S, Kaplan PW, Shibasaki H, Pressler R, van Putten MJAM. 2017. A revised glossary of terms most commonly used by clinical electroencephalographers and updated proposal for the report format of the EEG findings. Revision 2017. *Clin Neurophysiol Pract* **2**:170–185.

Kaneko T (2013). Local connections of excitatory neurons in motor-associated cortical areas of the rat. Front Neural Circuits 7, 75.

Kebschull JM, Richman EB, Ringach N, Friedmann D, Albarran E, Kolluru SS, Jones RC, Allen WE, Wang Y, Cho SW, Zhou H, Ding JB, Chang HY, Deisseroth K, Quake SR & Luo L (2020). Cerebellar nuclei evolved by repeatedly duplicating a conserved cell-type set. Science;

Koene LMC, van Grondelle SE, Proietti Onori M, Wallaard I, Kooijman NHRM, van Oort A, Schreiber J, Elgersma Y. 2019. Effects of antiepileptic drugs in a new TSC/mTOR-dependent epilepsy mouse model. *Ann Clin Transl Neurol* **6**:1273–1291.

Kool MJ, Proietti Onori M, Borgesius NZ, van de Bree JE, Elgersma-Hooisma M, Nio E, Bezstarosti K, Buitendijk GHS, Aghadavoud Jolfaei M, Demmers JAA, Elgersma Y, van Woerden GM. 2019. CAMK2-dependent signaling in neurons is essential for survival. *J Neurosci* 1341–18.

Kelly, L.R., Li, J., Carden, W.B., and Bickford, M.E. (2003). Ultrastructure and synaptic targets of tectothalamic terminals in the cat lateral posterior nucleus. The Journal of comparative neurology 464, 472-486.

Kha HT, Finkelstein DI, Pow DV, Lawrence AJ & Horne MK (2000). Study of projections from the entopeduncular nucleus to the

thalamus of the rat. J Comp Neurol 426, 366–377.

Killackey HP & Erzurumlu RS (1981). Trigeminal Projections to the Superior Colliculus of the Rat. J Comp Neurol 242, 221–242.

Killackey HP & Sherman SM (2003). Corticothalamic projections from the rat primary somatosensory cortex. J Neurosci 23, 7381–7384.

Kim D, Langmead B & Salzberg SL (2015). HISAT: A fast spliced aligner with low memory requirements. Nat Methods 12, 357–360.

Kim TH, Zhang Y, Lecoq J, Jung JC, Li J, Zeng H, Niell CM & Schnitzer MJ (2016). Long-Term Optical Access to an Estimated One Million Neurons in the Live Mouse Cortex. Cell Rep 17, 3385–3394.

Kita T, Shigematsu N & Kita H (2016). Intralaminar and tectal projections to the subthalamus in the rat. Eur J Neurosci 44, 2899–2908.

Klapoetke NC et al. (2014). Independent optical excitation of distinct neural populations. Nat Methods 11, 338–346.

de Kock CPJ & Sakmann B (2009). Spiking in primary somatosensory cortex during natural whisking in awake head-restrained rats is cell-type specific. Proc Natl Acad Sci U S A 106, 16446–16450.

Komiyama T, Sato TR, Oconnor DH, Zhang YX, Huber D, Hooks BM, Gabitto M & Svoboda K (2010). Learning-related fine-scale specificity imaged in motor cortex circuits of behaving mice. Nature 464, 1182–1186.

Körber C, Horstmann H, Venkataramani V, Herrmannsdörfer F, Kremer T, Kaiser M, Schwenger DB, Ahmed S, Dean C, Dresbach T & Kuner T (2015). Modulation of Presynaptic Release Probability by the Vertebrate-Specific Protein Mover. Neuron1–13.

Kros L, Eelkman Rooda OHJ, Spanke JK, Alva P, Van Dongen MN, Karapatis A, Tolner EA, Strydis C, Davey N, Winkelman BHJ, Negrello M, Serdijn WA, Steuber V, Van Den Maagdenberg AMJM, De Zeeuw CI & Hoebeek FE (2015). Cerebellar output controls generalized spike-and-wave discharge occurrence. Ann Neurol 77, 1027–1049.

Krueger DA, Sadhwani A, Byars AW, de Vries PJ, Franz DN, Whittemore VH, Filip-Dhima R, Murray D, Kapur K, Sahin M. 2017. Everolimus for treatment of tuberous sclerosis complex-associated neuropsychiatric disorders. *Ann Clin Transl Neurol* **4**:877–887.

Kuramoto E, Fujiyama F, Nakamura KC, Tanaka Y, Hioki H & Kaneko T (2011). Complementary distribution of glutamatergic cerebellar and GABAergic basal ganglia afferents to the rat motor thalamic nuclei. Eur J Neurosci 33, 95–109.

Kuramoto E, Furuta T, Nakamura KC, Unzai T, Hioki H & Kaneko T (2009a). Two types of thalamocortical projections from the motor thalamic nuclei of the rat: a single neuron-tracing study using viral vectors. Cereb Cortex 19, 2065–2077.

Kuramoto E, Furuta T, Nakamura KC, Unzai T, Hioki H & Kaneko T (2009b). Two types of thalamocortical projections from the motor thalamic nuclei of the rat: A single neuron-tracing study using viral vectors. Cereb Cortex 19, 2065–2077.

Kuramoto E, Ohno S, Furuta T, Unzai T, Tanaka YR, Hioki H & Kaneko T (2013). Ventral Medial Nucleus Neurons Send Thalamocortical Afferents More Widely and More Preferentially to Layer 1 than Neurons of the Ventral Anterior-Ventral Lateral Nuclear Complex in the Rat. Cereb Cortex1–15.

Kuramoto E, Ohno S, Furuta T, Unzai T, Tanaka YR, Hioki H & Kaneko T (2015). Ventral medial nucleus neurons send thalamocortical afferents more widely and more preferentially to layer 1 than neurons of the ventral anterior-ventral lateral nuclear complex in the rat. Cereb Cortex 25, 221–235.

Kyuyoung CL & Huguenard JR (2014). Modulation of short-term plasticity in the corticothalamic circuit by group III metabotropic glutamate receptors. J Neurosci 34, 675–687.

Lamarre Y, Filion M & Cordeau JP (1971). Neuronal discharges of the ventrolateral nucleus of

the thalamus during sleep and wakefulness in the cat I. Spontaneous activity. Exp Brain Res 12, 480–498.

Landisman CE & Connors BW (2007). VPM and PoM nuclei of the rat somatosensory thalamus: intrinsic neuronal properties and corticothalamic feedback. Cereb Cortex 17, 2853–2865.

Landisman CE, Long MA, Beierlein M, Deans MR, Paul DL & Connors BW (2002). Electrical synapses in the thalamic reticular nucleus. J Neurosci 22, 1002–1009.

Laplante M, Sabatini DM. 2012. mTOR Signaling. *Cold Spring Harb Perspect Biol* **4**:a011593-.

Lara AH, Cunningham JP & Churchland MM (2018). Different population dynamics in the supplementary motor area and motor cortex during reaching. Nat Commun;

Lavalle P, Urbain N, Dufresne C, Bokor H & Desche M (2005). Feedforward Inhibitory Control of Sensory Information in Higher-Order Thalamic Nuclei. J Neurosci 25, 7489–7498.

Lee J, Wang W & Sabatini BL (2020). Anatomically segregated basal ganglia pathways allow parallel behavioral modulation. Nat Neurosci

Leergaard TB, Alloway KD, Mutic JJ & Bjaalie JG (2000). Three-dimensional topography of corticopontine projections from rat barrel cortex: correlations with corticostriatal organization. J Neurosci 20, 8474–8484.

Leergaard TB, Alloway KD, Pham TAT, Bolstad I, Hoffer ZS, Pettersen C & Bjaalie JG (2004). Three-dimensional topography of corticopontine projections from rat sensorimotor cortex: Comparisons with corticostriatal projections reveal diverse integrative organization. J Comp Neurol 478, 306–322.

Lemon RN (2008). Descending Pathways in Motor Control. Annu Rev Neurosci 31, 195–218.

Leventer RJ, Guerrini R, Dobyns WB. 2008. Malformations of cortical development and epilepsy. *Dialogues Clin Neurosci*.

Leventer RJ, Phelan EM, Coleman LT, Kean MJ, Jackson GD, Harvey AS. 1999. Clinical and imaging features of cortical malformations in childhood. *Neurology* **53**:715–22.

Levy S, Lavzin M, Benisty H, Ghanayim A, Dubin U, Achvat S, Brosh Z, Aeed F, Mensh BD, Schiller Y, Meir R, Barak O, Talmon R, Hantman AW & Schiller J (2020). Cell-Type-Specific Outcome Representation in the Primary Motor Cortex. Neuron 107, 954-971.e9.

Li J, Guido W & Bickford ME (2003). Two distinct types of corticothalamic EPSPs and their contribution to short-term synaptic plasticity. J Neurophysiol 90, 3429–3440.

Li Y, Inoki K, Guan K-L. 2004. Biochemical and Functional Characterizations of Small GTPase Rheb and TSC2 GAP Activity. *Mol Cell Biol* **24**:7965–7975.

Li N, Chen T-W, Guo Z V., Gerfen CR & Svoboda K (2015). A motor cortex circuit for motor planning and movement. Nature 519, 51–56.

Li N, Daie K, Svoboda K & Druckmann S (2016). Robust neuronal dynamics in premotor cortex during motor planning. Nature 537, 122–122.

Liang H, Paxinos G, Watson C & Smi- PÁGADÁÁCQLÁ (2012). The red nucleus and the rubrospinal projection in the mouse. Brain Struct Funct 217, 221–232.

Liao C-C, Chen R-F, Lai W-S, Lin RCS & Yen C-T (2010). Distribution of large terminal inputs from the primary and secondary somatosensory cortices to the dorsal thalamus in the rodent. J Comp Neurol 518, 2592–2611.

Lim JS, Kim W, Kang H-C, Kim SH, Park AH, Park EK, Cho Y-W, Kim S, Kim HM, Kim JA, Kim J, Rhee H, Kang S-G, Kim HD, Kim D, Kim D-S, Lee JH. 2015. Brain somatic mutations in MTOR cause focal cortical dysplasia type II leading to intractable epilepsy. *Nat Med* **21**:395–400.

Lindeman S, Hong S, Kros L, Mejias JF, Romano V, Oostenveld R, Negrello M, Bosman LWJ & de Zeeuw CI (2020). Cerebellar purkinje cells can differentially modulate coherence between sensory and motor cortex

depending on region and behavior. Proc Natl Acad Sci U S A

Llinás R & Muehlethaler M (1988). Electrophysiology of guinea-pig cerebellar nuclear cells in the in-vitro brain stem-cerebellar preparation. J Physiol 404, 241–258.

Llinás R, Urbano FJ, Leznik E, Ramírez RR & van Marle HJF (2005). Rhythmic and dysrhythmic thalamocortical dynamics: GABA systems and the edge effect. Trends Neurosci 28, 325–333.

Love MI, Huber W & Anders S (2014). Moderated estimation of fold change and dispersion for RNA-seq data with DESeq2. Genome Biol 15, 1–21.

Lu SM, Guido W & Sherman SM (1992). Effects of membrane voltage on receptive field properties of lateral geniculate neurons in the cat: Contributions of the low-threshold Ca2+ conductance. J Neurophysiol 68, 2185–2198.

Luo P, Li A, Zheng Y, Han Y, Tian J, Xu Z, Gong H & Li X (2019). Whole brain mapping of long-range direct input to glutamatergic and GABAergic neurons in motor cortex. Front Neuroanat 13, 1–13.

Liu, X.B., Munoz, A., and Jones, E.G. (1998). Changes in subcellular localization of metabotropic glutamate receptor subtypes during postnatal development of mouse thalamus. The Journal of comparative neurology 395, 450-465.

Manto, M., Bower, J.M., Conforto, A.B., Delgado-Garcia, J.M., da Guarda, S.N., Gerwig, M., Habas, C., Hagura, N., Ivry, R.B., Marien, P., et al. (2012). Consensus paper: roles of the cerebellum in motor control--the diversity of ideas on cerebellar involvement in movement. Cerebellum 11, 457-487.

Major P, Rakowski S, Simon M V., Cheng ML, Eskandar E, Baron J, Leeman BA, Frosch MP, Thiele EA. 2009. Are cortical tubers epileptogenic? Evidence from electrocorticography. *Epilepsia* **50**:147–154. doi:10.1111/j.1528-1167.2008.01814.x

Manning BD, Cantley LC. 2003. Rheb fills a GAP between TSC and TOR. *Trends Biochem Sci*.

Marlinski V, Nilaweera WU, Zelenin P V., Sirota MG & Beloozerova IN (2012). Signals from the ventrolateral thalamus to the motor cortex during locomotion. J Neurophysiol 107, 455–472.

Masterson, S.P., Li, J., and Bickford, M.E. (2009). Synaptic organization of the tectorecipient zone of the rat lateral posterior nucleus. The Journal of comparative neurology 515, 647-663.

Marr BYD (1969). The Theory of cerebellar cortex. J Physiol437–470.

Matsuda T, Cepko CL. 2007. Controlled expression of transgenes introduced by in vivo electroporation. *Proc Natl Acad Sci U S A* **104**:1027–32.

Matyas F, Sreenivasan V, Marbach F, Wacongne C, Barsy B, Mateo C, Aronoff R & Petersen CCH (2010). Motor control by sensory cortex. Science 330, 1240–1243.

May PJ, Sun W & Hall WC (1997). Reciprocal connections between the zona incerta and the pretectum and superior colliculus of the cat. Neuroscience 77, 1091–1114.

Mccormick DA & Bal T (1997). SLEEP AND AROUSAL : Thalamocortical Mechanisms. Annu Rev Neurosci185–215.

Mease R a, Krieger P & Groh A (2014a). Cortical control of adaptation and sensory relay mode in the thalamus. Proc Natl Acad Sci U S A 111, 6798–6803.

Mease RA, Krieger P & Groh A (2014b). Cortical control of adaptation and sensory relay mode in the thalamus. ; DOI: 10.1073/pnas.1318665111.

Mease RA, Kuner T, Fairhall AL & Groh A (2017). Multiplexed Spike Coding and Adaptation in the Thalamus. Cell Rep 19, 1130–1140.

Mease RA, Metz M & Groh A (2016a). Cortical Sensory Responses Are Enhanced by the Higher-Order Thalamus. Cell Rep 14, 208–215.

Mease RA, Sumser A, Sakmann B & Groh A (2016b). Corticothalamic Spike Transfer via the L5B-POm Pathway in vivo. Cereb Cortex1–15.

Meyer HS, Wimmer VC, Oberlaender M, De Kock CPJ, Sakmann B & Helmstaedter M (2010). Number and laminar distribution of neurons in a thalamocortical projection column of rat vibrissal cortex. Cereb Cortex 20, 2277–2286.

Miller, J.W., Gray, B.C., and Bardgett, M.E. (1992). Characterization of cholinergic regulation of seizures by the midline thalamus. Neuropharmacology 31, 349-356.

Milikovsky DZ, Weissberg I, Kamintsky L, Lippmann K, Schefenbauer O, Frigerio F, Rizzi M, Sheintuch L, Zelig D, Ofer J, Vezzani A, Friedman A. 2017. Electrocorticographic dynamics as a novel biomarker in five models of epileptogenesis. *J Neurosci* **37**:4450–4461.

Mitrofanis J (2005). Some certainty for the "zone of uncertainty"? Exploring the function of the zona incerta. Neuroscience 130, 1–15.

Mitrofanis J & Mikuletic L (1999). Organisation of the cortical projection to the zona incerta of the thalamus. J Comp Neurol 412, 173–185.

Miyashita E, Keller A & Asanuma H (1994). Input-output organization of the rat vibrissal motor cortex. Exp Brain Res 99, 223–232.

Moffat JJ, Ka M, Jung EM, Kim WY. 2015. Genes and brain malformations associated with abnormal neuron positioning. *Mol Brain* **8**:1–12. doi:10.1186/s13041-015-0164-4

Nie D, Di Nardo A, Han JM, Baharanyi H, Kramvis I, Huynh T, Dabora S, Codeluppi S, Pandolfi PP, Pasquale EB, Sahin M. 2010. Tsc2-Rheb signaling regulates EphA-mediated axon guidance. *Nat Neurosci* **13**:163–72.

Molinari HH, Schultze KE & Strominger NL (1996). Gracile , Cuneate , and Spinal Trigeminal Projections to Inferior Olive in Rat and Monkey. J Comp Neurol 375, 467–480.

Monconduit, L., and Villanueva, L. (2005). The lateral ventromedial thalamic nucleus spreads nociceptive signals from the whole body surface to layer I of the frontal cortex. The European journal of neuroscience 21, 3395-3402.

Morandell K & Huber D (2017). The role of forelimb motor cortex areas in goal directed action in mice. Sci Rep 7, 1–14.

Moruzzi G (1950). Effects at different frequencies of cerebellar stimulation upon postural tonus and myotatic reflexes. Electroencephalogr Clin Neurophysiol 2, 463–469.

Mukherjee K, Yang X, Gerber SH, Kwon H-B, Ho A, Castillo PE, Liu X & Südhof TC (2010). Piccolo and bassoon maintain synaptic vesicle clustering without directly participating in vesicle exocytosis. Proc Natl Acad Sci U S A 107, 6504–6509.

Muñoz-castañeda R, Zingg B, Matho KS, Wang Q, Foster NN, Narasimhan A, Li A, Hirokawa KE, Bannerjee S, Korobkova L, Park CS, Park Y, Michael S, Chon U, Wheeler DW, Li X, Wang Y & Kelly K (2020). Cellular Anatomy of the Mouse Primary Motor Cortex. BioRxiv1–66.

Murray PD, Masri R & Keller A (2010). Abnormal Anterior Pretectal Nucleus Activity Contributes to Central Pain Syndrome. J Neurophysiol 103, 3044–3053.

Murray Sherman S (2001). Tonic and burst firing: Dual modes of thalamocortical relay. Trends Neurosci 24, 122–126.

Murray Sherman S, Wilson JR, Kaas JH & Webb S V. (1976). X- and Y-cells in the dorsal lateral geniculate nucleus of the owl monkey (Aotus trivirgatus). Science (80-) 192, 475–476.

Nicolelis MAL, Chapin JK & Lin RCS (1992). Somatotopic maps within the zona incerta relay parallel GABAergic somatosensory pathways to the neocortex, superior colliculus, and brainstem. Brain Res 577, 134–141.

Nicolelis MAL, Chapin JK & Lin RCS (1995). Development of direct GABAergic projections from the zona incerta to the somatosensory cortex of the rat. Neuroscience 65, 609–631.

Oberlaender M, De Kock CPJ, Bruno RM, Ramirez A, Meyer HS, Dercksen VJ, Helmstaedter M & Sakmann B (2012). Cell type-specific three-dimensional structure of thalamocortical circuits in a column of rat vibrissal cortex. Cereb Cortex 22, 2375–2391.

Ohmae S, Uematsu A & Tanaka M (2013). Temporally Specific Sensory Signals for the Detection of Stimulus Omission in the Primate Deep Cerebellar Nuclei. 33, 15432–15441.

Ohno S, Kuramoto E, Furuta T, Hioki H, Tanaka YR, Fujiyama F, Sonomura T, Uemura M, Sugiyama K & Kaneko T (2012). A morphological analysis of thalamocortical axon fibers of rat posterior thalamic nuclei: A single neuron tracing study with viral vectors. Cereb Cortex 22, 2840–2857.

Olsen SR, Bortone DS, Adesnik H & Scanziani M (2012a). Gain control by layer six in cortical circuits of vision. Nature 483, 47–52.

Olsen SR, Bortone DS, Adesnik H & Scanziani M (2012b). Gain control by layer six in cortical circuits of vision. Nature 483, 47–54.

Overwater IE, Rietman AB, Bindels-De Heus K, Looman CWN, Rizopoulos D, Sibindi TM, Cherian PJ, Jansen FE, Moll HA, Elgersma Y, De Wit MCY. 2016. Sirolimus for epilepsy in children with tuberous sclerosis complex. *Neurology* **87**:1011–1018.

Overwater Iris E., Rietman AB, Mous SE, Bindels-De Heus K, Rizopoulos D, Ten Hoopen LW, Van Der Vaart T, Jansen FE, Elgersma Y, Moll HA, De Wit MCY. 2019. A randomized controlled trial with everolimus for IQ and autism in tuberous sclerosis complex. *Neurology* **93**:E200–E209.

Overwater Iris E, Rietman AB, van Eeghen AM, de Wit MCY. 2019. Everolimus for the treatment of refractory seizures associated with tuberous sclerosis complex (TSC): current perspectives. *Ther Clin Risk Manag* **15**:951–955. doi:10.2147/TCRM.S145630

Park SM, Lim JS, Ramakrishina S, Kim SH, Kim WK, Lee JHJ, Kang H-C, Reiter JF, Kim DS, Kim H (Henry), Lee JHJ. 2018. Brain somatic mutations in MTOR disrupt neuronal ciliogenesis, leading to focal cortical dyslamination. *Neuron* **99**:1–15.

Palkovits M, Mezey E, Hámori J & Szentágothai J (1977). Quantitative histological analysis of the cerebellar nuclei in the cat. I. Numerical data on cells and on synapses. Exp brain Res 28, 189–209.

Pananceau M & Rispal-Padel L (2000). Functional plasticity in the interposito-thalamocortical pathway during conditioning. Role of the interstimulus interval. Exp Brain Res 132, 314–327.

Panneton WM & Tolbert DL (1984). The Collateral Origin of a Transient Cerebrocerebellar Pathway in Kittens . A Study Using Fluorescent Double-Labeling Techniques. 14, 247–254.

Parmar N, Tamanoi F. 2010. Rheb G-proteins and the activation of mTORC1The Enzymes. Academic Press. pp. 39–56.

Patel B, Patel J, Cho J-H, Manne S, Bonala S, Henske E, Roegiers F, Markiewski M, Karbowniczek M. 2015. Exosomes mediate the acquisition of the disease phenotypes by cells with normal genome in tuberous sclerosis complex. *Oncogene* 1–10.

Patel N, Jankovic J & Hallett M (2014). Sensory aspects of movement disorders. Lancet Neurol 13, 100–112.

Paxinos G & Franklin KBJ (2001). The Mouse Brain in Stereotaxic Coordinates.

Paz JT, Bryant AS, Peng K, Fenno L, Yizhar O, Frankel WN, Deisseroth K & Huguenard JR (2011). A new mode of corticothalamic transmission revealed in the Gria4(-/-) model of absence epilepsy. Nat Neurosci 14, 1167–1173.

Paz JT, Christian C a, Parada I, Prince D a & Huguenard JR (2010). Focal cortical infarcts alter intrinsic excitability and synaptic excitation in the reticular thalamic nucleus. J Neurosci 30, 5465–5479.

Paz JT, Davidson TJ, Frechette ES, Delord B, Parada I, Peng K, Deisseroth K & Huguenard JR (2012). Closed-loop optogenetic control of thalamus as a tool for i

znterrupting seizures after cortical injury. Nat Neurosci1–10.

Paz JT & Huguenard JR (2015). Microcircuits and their interactions in epilepsy: is the focus out of focus? Nat Neurosci 18, 351–359.

Pearson KG & Gordon EG (2013). Spinal Reflexes. In Principles of Neural Science, pp. 790–811.

Pelzer P, Horstmann H & Kuner T (2017a). Ultrastructural and functional properties of a giant synapse driving the piriform cortex to mediodorsal thalamus projection. Front Synaptic Neurosci 9, 1–11.

Peng H, Xie P, Liu L, Kuang X, ... & Zeng H (2020). Brain-wide single neuron reconstruction reveals morphological diversity in molecularly defined striatal, thalamic, cortical and claustral neuron types. bioRxiv.

Person AL & Raman IM (2011a). Purkinje neuron synchrony elicits time-locked spiking in the cerebellar nuclei. Nature 481, 502–505.

Person AL & Raman IM (2011b). Purkinje neuron synchrony elicits time-locked spiking in the cerebellar nuclei. Nature 481, 502–505.

Peter, S., Ten Brinke, M.M., Stedehouder, J., Reinelt, C.M., Wu, B., Zhou, H., Zhou, K., Boele, H.J., Kushner, S.A., Lee, M.G., et al. (2016). Dysfunctional cerebellar Purkinje cells contribute to autism-like behaviour in Shank2-deficient mice. Nature communications 7, 12627.

Peters AJ, Chen SX & Komiyama T (2014). Emergence of reproducible spatiotemporal activity during motor learning. Nature 510, 263–267.

Peters AJ, Lee J, Hedrick NG, O'neil K & Komiyama T (2017). Reorganization of corticospinal output during motor learning. Nat Neurosci 20, 1133–1141.

Petreanu L, Mao T, Sternson SM & Svoboda K (2009). The subcellular organization of neocortical excitatory connections. Nature 457, 1142–1145.

Phillips AJW, Schulmann A, Hara E, Liu C & Brenda C (2017). A topographic axis of transcriptional identity in thalamus. bioRxiv1–27.

Phillips JW, Schulmann A, Hara E, Winnubst J, Liu C, Valakh V, Wang L, Shields BC, Korff W, Chandrashekar J, Lemire AL, Mensh B, Dudman JT, Nelson SB & Hantman AW (2019). A repeated molecular architecture across thalamic pathways. Nat Neurosci 22, 1925–1935.

Picelli S, Björklund ÅK, Faridani OR, Sagasser S, Winberg G & Sandberg R (2013). Smart-seq2 for sensitive full-length transcriptome profiling in single cells. Nat Methods 10, 1096–1100.

Pierret T, Lavallée P & Deschênes M (2000). Parallel streams for the relay of vibrissal information through thalamic barreloids. J Neurosci 20, 7455–7462.

Pijpers A, Voogd J & Ruigrok TJH (2005). Topography of olivo-cortico-nuclear modules in the intermediate cerebellum of the rat. J Comp Neurol 492, 193–213.

Pita-Almenar JD, Yu D, Lu H-C & Beierlein M (2014). Mechanisms Underlying Desynchronization of Cholinergic-Evoked Thalamic Network Activity. J Neurosci 34, 14463–14474.

Popa D, Spolidoro M, Proville RD, Guyon N, Belliveau L & Léna C (2013). Functional role of the cerebellum in gamma-band synchronization of the sensory and motor cortices. J Neurosci 33, 6552–6556.

Proville RD, Spolidoro M, Guyon N, Dugué GP, Selimi F, Isope P, Popa D & Léna C (2014). Cerebellum involvement in cortical sensorimotor circuits for the control of voluntary movements. Nat Neurosci 17, 1233–1239.

Raeva S, Vainberg N & Dubinin V (1999). Analysis of spontaneous activity patterns of human thalamic ventrolateral neurons and their modifications due to functional brain changes. Neuroscience 88, 365–376.

Raman IM & Bean BP (1999). Ionic currents underlying spontaneous action potentials in isolated cerebellar Purkinje neurons. J Neurosci 19, 1663–1674.

Raman IM, Gustafson AE & Padgett D (2000). Ionic currents and spontaneous firing in neu-

rons isolated from the cerebellar nuclei. J Neurosci 20, 9004–9016.

Ramanathan D, Conner JM & Tuszynski MH (2006). A form of motor cortical plasticity that correlates with recovery of function after brain injury. Proc Natl Acad Sci U S A 103, 11370–11375.

Ramnani N (2006). The primate cortico-cerebellar system: anatomy and function. Nat Rev Neurosci 7, 511–522.

Ransdell JL & Nerbonne JM (2018). Voltage-gated sodium currents in cerebellar Purkinje neurons: functional and molecular diversity. Cell Mol Life Sci 75, 3495–3505.

Raymond JL, Lisberger SG & Mauk MD (1996). The cerebellum: a neuronal learning machine? Science 272, 1126–1131.

Raznahan A, Shaw P, Lalonde F, Stockman M, Wallace GL, Greenstein D, Clasen L, Gogtay N & Giedd JN (2011). How does your cortex grow? J Neurosci 31, 7174–7177.

Rees H & Roberts MHT (1993). The anterior pretectal nucleus: a proposed role in sensory processing. Pain 53, 121–135.

Reichova I (2004). Somatosensory Corticothalamic Projections: Distinguishing Drivers From Modulators. J Neurophysiol 92, 2185–2197.

Reichova I & Sherman SM (2004). Somatosensory corticothalamic projections: distinguishing drivers from modulators. J Neurophysiol 92, 2185–2197.

Reijnders MRFRF, Kousi M, Van Woerden GMM, Klein M, Bralten J, Mancini GMSMS, Van Essen T, Proietti-Onori M, Smeets EEJEJ, Van Gastel M, Stegmann APAPA, Stevens SJCJC, Lelieveld SHH, Gilissen C, Pfundt R, Tan PLL, Kleefstra T, Franke B, Elgersma Y, Katsanis N, Brunner HGG. 2017. Variation in a range of mTOR-related genes associates with intracranial volume and intellectual disability. *Nat Commun* **8**:1052.

Renier N, Adams EL, Kirst C, Dulac C, Osten P, Tessier-lavigne M, Renier N, Adams EL, Kirst C, Wu Z, Azevedo R, Kohl J, Autry AE, Kadiri L, Venkataraju KU, Zhou Y,

Renier N, Adams EL, Kirst C, Wu Z, Azevedo R, Kohl J, Autry AE, Kadiri L, Umadevi Venkataraju K, Zhou Y, Wang VX, Tang CY, Olsen O, Dulac C, Osten P & Tessier-Lavigne M (2016). Mapping of Brain Activity by Automated Volume Analysis of Immediate Early Genes. Cell 165, 1789–1802.

Renier N, Wu Z, Simon DJ, Yang J, Ariel P & Tessier-Lavigne M (2014). IDISCO: A simple, rapid method to immunolabel large tissue samples for volume imaging. Cell 159, 896–910.

Represa A. 2019. Why Malformations of Cortical Development Cause Epilepsy. *Front Neurosci* **13**:250.

Ribierre T, Deleuze C, Bacq A, Baldassari S, Marsan E, Chipaux M, Muraca G, Roussel D, Navarro V, Leguern E, Miles R, Baulac S. 2018. Second-hit mosaic mutation in mTORC1 repressor DEPDC5 causes focal cortical dysplasia-associated epilepsy. *J Clin Invest* **128**:2452–2458.

Rispal-Padel L, Harnois C & Troiani D (1987). Converging cerebellofugal inputs to the thalamus - I. Mapping of monosynaptic field potentials in the ventrolateral nucleus of the thalamus. Exp Brain Res 68, 47–58.

Rispal-Padel L & Latreille J (1974). The organization of projections from the cerebellar nuclei to the contralateral motor cortex in the cat. Exp Brain Res 19, 36–60.

Rispal-Padel L, Massion J & Grangetto A (1973). Relations between the ventrolateral thalamic nucleus and motor cortex and their possible role in the central organization of motor control. Brain Res 60, 1–20.

Rispal-Padel, L., and Grangetto, A. (1977). The cerebello-thalamo-cortical pathway. Topographical investigation at the unitary level in the cat. Experimental brain research 28, 101-123.

Roger M & Cadusseau J (1985). Afferents to the zona incerta in the rat: A combined retrograde and anterograde study. J Comp Neurol 241, 480–492.

Rollenhagen, A., and Lubke, J.H. (2006). The morphology of excitatory central synapses: from structure to function. Cell and tissue research 326, 221-237.

Rouiller EM & Welker E (2001). A comparative analysis of the morphology of corticothalamic projections in mammals. Brain Res Bull 53, 727–741.

Rovó Z, Ulbert I & Acsády L (2012). Drivers of the primate thalamus. J Neurosci 32, 17894–17908.

Rubio-Garrido, P., Perez-de-Manzo, F., Porrero, C., Galazo, M.J., and Clasca, F. (2009). Thalamic input to distal apical dendrites in neocortical layer 1 is massive and highly convergent. Cerebral cortex 19, 2380-2395.

Ruder L, Schina R, Kanodia H, Valencia-Garcia S, Pivetta C & Arber S (2021). A functional map for diverse forelimb actions within brainstem circuitry. Nature1–6.

Ruder L, Takeoka A & Arber S (2016). Long-Distance Descending Spinal Neurons Ensure Quadrupedal Locomotor Stability. Neuron 92, 1063–1078.

Ruigrok TJH & Voogd J (2000). Organization of projections from the inferior olive to the cerebellar nuclei in the rat. J Comp Neurol 426, 209–228.

Sabatini DM. 2017. Twenty-five years of mTOR: Uncovering the link from nutrients to growth. *Proc Natl Acad Sci U S A*.

Saito T, Nakatsuji N. 2001. Efficient gene transfer into the embryonic mouse brain using in vivo electroporation. *Dev Biol* **240**:237–46.

Sakata HS, Ishijma T & Toyoda Y (1966). SINGLE UNIT STDIES ON VENTROLATERAL NCLES OF THE THALAMS IN CAT: ITS RELATION TO THE CEREBELLM, MOTOR CORTEX AND BASAL GANGLIA. Jpn J Physiol 16, 42–60.

Sarnaik R & Raman IM (2018). Control of voluntary and optogenetically perturbed locomotion by spike rate and timing of neurons of the mouse cerebellar nuclei. Elife 7, 1–31.

Sasaki K, Kawaguchi S, Matsuda Y & Mizuno N (1972). Electrophysiological studies on cerebello-cerebral projections in the cat. Exp Brain Res 16, 75–88.

Sauerbrei BA, Guo JZ, Cohen JD, Mischiati M, Guo W, Kabra M, Verma N, Mensh B, Branson K & Hantman AW (2020). Cortical pattern generation during dexterous movement is input-driven. Nature 577, 386–391.

Sawyer SF, Tepper JM & Groves PM (1994a). Cerebellar-responsive neurons in the thalamic ventroanterior-ventrolateral complex of rats: light and electron microscopy. Neuroscience 63, 725–745.

Sawyer SF, Young SJ, Groves PM & Tepper JM (1994b). Cerebellar-responsive neurons in the thalamic ventroanterior-ventrolateral complex of rats: in vivo electrophysiology. Neuroscience 63, 711–724.

Saxton RA, Sabatini DM. 2017. mTOR Signaling in Growth, Metabolism, and Disease. *Cell*.

Scalia F & Arango V (1979). Topographic organization of the projections of the retina to the pretectal region in the rat. J Comp Neurol 186, 271–292.

Schiavo GG, Benfenati F, Poulain B, Rossetto O, De Laureto PP, Dasgupta BR, Montecucco C. 1992. Tetanus and botulinum-B neurotoxins block neurotransmitter release by proteolytic cleavage of synaptobrevin. *Nature* **359**:832–835.

Schiemann J, Puggioni P, Dacre J, Pelko M, Domanski A, VanRossum MCW & Duguid I (2015). Cellular Mechanisms Underlying Behavioral State-Dependent Bidirectional Modulation of Motor Cortex Output. Cell Rep 11, 1319–1330.

Schmitz SK, Hjorth JJJJ, Joemai RMS, Wijntjes R, Eijgenraam S, de Bruijn P, Georgiou C, de Jong APH, van Ooyen A, Verhage M, Cornelisse LN, Toonen RF, Veldkamp W. 2011. Automated analysis of neuronal morphology, synapse number and synaptic recruitment. *J Neurosci Methods* **195**:185–193.

Schmolesky MT, Weber JT, De Zeeuw CI & Hansel C (2002). The making of a complex spike: Ionic composition and plasticity. Ann N Y Acad Sci 978, 359–390.

Schneggenburger R, Meyer AC & Neher E (1999). Released Fraction and Total Size of a Pool of Immediately Available Transmitter Quanta at a Calyx Synapse. 23, 399–409.

Schneider F, Grimm C & Hegemann P (2015). Biophysics of Channelrhodopsin. Annu Rev Biophys 44, 167–186.

Schoch S & Gundelfinger ED (2006). Molecular organization of the presynaptic active zone. Cell Tissue Res 326, 379–391.

Schulz Mendoza A, Jing Z, Mar J, Wetzel F, Dresbach T, Strenzke N, Wichmann C & Moser T (2014). Bassoon-disruption slows vesicle replenishment and induces homeostatic plasticity at a CNS synapse. EMBO J 33, 512–527.

Schwenger DB & Kuner T (2010). Acute genetic perturbation of exocyst function in the rat calyx of Held impedes structural maturation, but spares synaptic transmission. Eur J Neurosci 32, 974–984.

Seol M & Kuner T (2015). Ionotropic glutamate receptor GluA4 and T-type calcium channel Ca v 3 . 1 subunits control key aspects of synaptic transmission at the mouse L5B-POm giant synapse. 42, 3033–3044.

Sherman S & Guillery RW (2006). Exploring the thalamus and its role in cortical function.

Sherman SM (2012). Thalamocortical interactions. Curr Opin Neurobiol 22, 575–579.

Sherman SM & Guillery RW (1998). On the actions that one nerve cell can have on another: distinguishing “drivers” from “modulators”. Proc Natl Acad Sci U S A 95, 7121–7126.

Sherman SM & Guillery RW (2002). The role of the thalamus in the flow of information to the cortex. Philos Trans R Soc B Biol Sci 357, 1695–1708.

Sherman SM & Guillery RW (2011). Distinct functions for direct and transthalamic corticocortical connections. J Neurophysiol 106, 1068–1077.

Sherman, S.M. (2014). The function of metabotropic glutamate receptors in thalamus and cortex. The Neuroscientist : a review journal bringing neurobiology, neurology and psychiatry 20, 136-149.

Shimojo M, Courchet J, Pieraut S, Torabi-Rander N, Sando R, Polleux F, Maximov A. 2015. SNAREs Controlling Vesicular Release of BDNF and Development of Callosal Axons. *Cell Rep* **11**:1054–1066.

Shinoda Y (1985). Synaptic Organization of the Cerebello-Thalamo-Cerebral Pathway in the Cat. Projection of Individual Cerebellar Nuclei to Single Pyramidal Tract Neurons in Areas 4 and 6. Neurosci Res.

Sillitoe R V., Chung SH, Fritschy JM, Hoy M & Hawkes R (2008). Golgi cell dendrites are restricted by purkinje cell stripe boundaries in the adult mouse cerebellar cortex. J Neurosci 28, 2820–2826.

Simpson JI, Wylie DR & De Zeeuw CI (1996). On climbing fiber signals and their consequence(s). Behav Brain Sci 19, 384–398.

Simpson K, Wang YUE & Lin RCS (2008). Patterns of Convergence in Rat Zona Incerta from the Trigeminal Nuclear Complex : Light and Electron Microscopic Study. J Comp Neurol 507, 1521–1541.

Smith JB, Watson GDR, Alloway KD, Schwarz C & Chakrabarti S (2015). Corticofugal projection patterns of whisker sensorimotor cortex to the sensory trigeminal nuclei. Front Neural Circuits 9, 1–14.

Soetedjo R, Kojima Y & Fuchs AF (2008). Complex spike activity in the oculomotor vermis of the cerebellum: A vectorial error signal for saccade motor learning? J Neurophysiol 100, 1949–1966.

Sosnik R, Haidarliu S & Ahissar E (2001). Temporal Frequency of Whisker Movement . I . Representations in Brain Stem and Thalamus. J Neurophysiol339–353.

Soteropoulos DS & Baker SN (2006). Corticocerebellar coherence during a precision grip task in the monkey. J Neurophysiol 95, 1194–1206.

Sreenivasan V, Esmaeili V, Kiritani T, Galan K, Crochet S & Petersen CCH (2016). Movement

Initiation Signals in Mouse Whisker Motor Cortex. Neuron 92, 1368–1382.

Sreenivasan V, Karmakar K, Rijli FM & Petersen CCH (2015). Parallel pathways from motor and somatosensory cortex for controlling whisker movements in mice. Eur J Neurosci 41, 354–367.

Stehfest K & Hegemann P (2010). Evolution of the channelrhodopsin photocycle model. ChemPhysChem 11, 1120–1126.

Stephens M (2017). False discovery rates: A new deal. Biostatistics 18, 275–294.

Steriade, M. (1995). Two channels in the cerebellothalamocortical system. The Journal of comparative neurology 354, 57-70.

Steriade, M., Apostol, V., and Oakson, G. (1971). Control of unitary activities in cerebellothalamic pathway during wakefulness and synchronized sleep. Journal of neurophysiology 34, 389-413.

Stoodley, C.J., D'Mello, A.M., Ellegood, J., Jakkamsetti, V., Liu, P., Nebel, M.B.,

Gibson, J.M., Kelly, E., Meng, F., Cano, C.A., et al. (2017). Altered cerebellar connectivity in autism and cerebellar-mediated rescue of autism-related behaviors in mice. Nature neuroscience 20, 1744-1751.

Südhof TC (2012). The presynaptic active zone. Neuron 75, 11–25.

Sugihara I, Wu HS & Shinoda Y (1999). Morphology of single olivocerebellar axons labeled with biotinylated dextran amine in the rat. J Comp Neurol 414, 131–148.

Sugimoto T, Mizuno N & Uchida K (1982). Distribution of cerebellar fiber terminals in the midbrain visuomotor areas: An autoradiographic study in the cat. Brain Res 238, 353–370.

Sur, M.; Sherman M (1982). Retinogeniculate Terminations in Cats: Morphological Differences between X and Y Cell Axons. Science (80-) 218, 389–391.

Sur M, Humphrey AL & Sherman SM (1982). Monocular deprivation affects X- and Y-cell retinogeniculate terminations in cats. Nature 300, 183–185.

Sur M, Weller RE & Sherman SM (1984). Development of X- and Y-cell retinogeniculate terminations in kittens. Nature 310, 246–249.

Suter XBA & Shepherd GMG (2015). Reciprocal Interareal Connections to Corticospinal Neurons in Mouse M1 and S2. J Neurosci 35, 2959–2974.

Suzuki L, Coulon P, Sabel-Goedknegt EH & Ruigrok TJH (2012). Organization of Cerebral Projections to Identified Cerebellar Zones in the Posterior Cerebellum of the Rat. J Neurosci 32, 10854–10869.

Svoboda K & Li N (2017a). Neural mechanisms of movement planning: motor cortex and beyond. Curr Opin Neurobiol 49, 33–41.

Svoboda K & Li N (2017b). Neural mechanisms of movement planning: motor cortex and beyond. Curr Opin Neurobiol 49, 33–41.

Swenson R, Kosinski R & Castro A (1984). Topography of spinal, dorsal column nuclear, and spinal trigeminal projections to the pontine gray in rats. J Comp Neurol 222, 301–311.

Takao-Rikitsu E, Mochida S, Inoue E, Deguchi-Tawarada M, Inoue M, Ohtsuka T & Takai Y (2004). Physical and functional interaction of the active zone proteins, CAST, RIM1, and Bassoon, in neurotransmitter release. J Cell Biol 164, 301–311.

Tamamaki N, Uhlrich DJ & Sherman SM (1995). Morphology of physiologically identified retinal X and Y axons in the cat's thalamus and midbrain as revealed by intraaxonal injection of biocytin. J Comp Neurol 354, 583–607.

Tang T, Suh CY, Blenkinsop TA & Lang EJ (2016). Synchrony is Key: Complex Spike Inhibition of the Deep Cerebellar Nuclei. Cerebellum 15, 10–13.

Tang W, Ehrlich I, Wolff SBE, Michalski A-M, Wölfl S, Hasan MT, Lüthi A & Sprengel R (2009). Faithful expression of multiple proteins via 2A-peptide self-processing: a versatile and reliable method for manipulating brain circuits. J Neurosci 29, 8621–8629.

Tennant KA, Adkins DL, Donlan NA, Asay AL, Thomas N, Kleim JA & Jones TA (2011). The organization of the forelimb representation of the C57BL/6 mouse motor cortex as defined by intracortical microstimulation and cytoarchitecture. Cereb Cortex 21, 865–876.

Terenzi MG, Zagon A & Roberts MHT (1995). Efferent connections from the anterior pretectal nucleus to the diencephalon and mesencephalon in the rat. Brain Res 701, 183–191.

Tervo DGR, Hwang BY, Viswanathan S, Gaj T, Lavzin M, Ritola KD, Lindo S, Michael S, Kuleshova E, Ojala D, Huang CC, Gerfen CR, Schiller J, Dudman JT, Hantman AW, Looger LL, Schaffer D V. & Karpova AY (2016). A Designer AAV Variant Permits Efficient Retrograde Access to Projection Neurons. Neuron 92, 372–382.

Teune TM, van der Burg J, van der Moer J, Voogd J & Ruigrok TJ (2000). Topography of cerebellar nuclear projections to the brain stem in the rat. Prog Brain Res 124, 141–172.

Theyel BB, Llano DA & Sherman SM (2009). The corticothalamocortical circuit drives higher-order cortex in the mouse. Nat Neurosci 13, 84–88.

Theyel BB, Llano DA & Sherman SM (2010). The corticothalamocortical circuit drives higher-order cortex in the mouse. Nat Neurosci 13, 84–88.

Ting JT, Daigle TL, Chen Q, Feng G. 2014. Acute brain slice methods for adult and aging animals: Application of targeted patch clamp analysis and optogenetics. *Methods Mol Biol* **1183**:221–242.

Tolbert DL (1987). Intrinsically directed pruning as a mechanism regulating the elimination of transient collateral pathways. 33, 11–21.

Tolbert DL & Panneton WM (1983). Transient cerebrocerebellar projections in kittens: Postnatal development and topography. J Comp Neurol 221, 216–228.

Trageser JC & Keller A (2004). Reducing the Uncertainty : Gating of Peripheral Inputs by Zona Incerta. 24, 8911–8915.

Turner JP & Salt TE (1998). Characterization of sensory and corticothalamic excitatory inputs to rat thalamocortical neurones in vitro. J Physiol 510, 829–843.

Tsai PT, Greene-Colozzi E, Goto J, Anderl S, Kwiatkowski DJ, Sahin M. 2013. Prenatal rapamycin results in early and late behavioral abnormalities in wildtype C57BL/6 mice. *Behav Genet* **43**:51–9.

Tsai, P.T., Hull, C., Chu, Y., Greene-Colozzi, E., Sadowski, A.R., Leech, J.M., Steinberg, J., Crawley, J.N., Regehr, W.G., and Sahin, M. (2012). Autistic-like behaviour and cerebellar dysfunction in Purkinje cell Tsc1 mutant mice. Nature 488, 647-651.

Uno M, Yoshida M & Hirota I (1970). The mode of cerebello-thalamic relay transmission investigated with intracellular recording from cells of the ventrolateral nucleus of cat's thalamus. Exp brain Res 10, 121–139.

Urbain N & Deschênes M (2007). Motor cortex gates vibrissal responses in a thalamocortical projection pathway. Neuron 56, 714–725.

Uusisaari M & Knöpfel T (2010). GlyT2+ neurons in the lateral cerebellar nucleus. Cerebellum 9, 42–55.

Uusisaari M & Knöpfel T (2011). Functional Classification of Neurons in the Mouse Lateral Cerebellar Nuclei. Cerebellum 10, 637–646.

Uusisaari M, Obata K, Kno T & Morphological T (2007). Morphological and Electrophysiological Properties of GABAergic and Non-GABAergic Cells in the Deep Cerebellar Nuclei. J Neurophysiol 97, 901–911.

Van Slegtenhorst M, Nellist M, Nagelkerken B, Cheadle J, Snell R, Van Den Ouweland A, Reuser A, Sampson J, Halley D, Van Der Sluijs P. 1998. Interaction between hamartin and tuberin, the TSC1 and TSC2 gene products. *Hum Mol Genet* **7**:1053–1057.

Veinante P & Deschênes M (1999). Single- and multi-whisker channels in the ascending projections from the principal trigeminal

nucleus in the rat. J Neurosci 19, 5085–5095.

Veinante P, Jacquin MF, Desche M, Giffard L & Giffard R (2000a). Thalamic Projections From the Whisker- Sensitive Regions of the Spinal Trigeminal Complex in the Rat. J Comp Neurol 420, 233–243.

Veinante P, Lavallée P & Deschênes M (2000b). Corticothalamic projections from layer 5 of the vibrissal barrel cortex in the rat. J Comp Neurol 424, 197–204.

Viaene a. N, Petrof I & Sherman SM (2011a). Properties of the thalamic projection from the posterior medial nucleus to primary and secondary somatosensory cortices in the mouse. Proc Natl Acad Sci 108, 18156–18161.

Viaene AN, Petrof I & Sherman SM (2011b). Properties of the thalamic projection from the posterior medial nucleus to primary and secondary somatosensory cortices in the mouse. Proc Natl Acad Sci U S A 108, 18156–18161.

Viaene AN, Petrof I & Sherman SM (2013). Activation requirements for metabotropic glutamate receptors. Neurosci Lett 541, 67–72.

Vitek JL, Ashe J, DeLong MR & Alexander GE (1994). Physiologic properties and somatotopic organization of the primate motor thalamus. J Neurophysiol 71, 1498–1513.

Wagner MJ, Kim TH, Kadmon J, Nguyen ND, Ganguli S, Schnitzer MJ & Luo L (2019). Shared Cortex-Cerebellum Dynamics in the Execution and Learning of a Motor Task. Cell 177, 669-682.e24.

Waites CL, Leal-Ortiz S a, Okerlund N, Dalke H, Fejtova A, Altrock WD, Gundelfinger ED & Garner CC (2013). Bassoon and Piccolo maintain synapse integrity by regulating protein ubiquitination and degradation. EMBO J 32, 954–969.

Waldron HA & Gwyn DG (1969). Descending Nerve Tracts in the Spinal Cord of the R a t. J Comp Neurol 137, 143–153.

Wanaverbecq N, Bodor L, Bokor H, Slezia A, Lüthi A & Acsády L (2008). Contrasting the Functional Properties of GABAergic Axon Terminals with Single and Multiple Synapses in the Thalamus. J Neurosci 28, 11848–11861.

Wang C-L, Zhang L, Zhou Y, Zhou J, Yang X-J, Duan S, Xiong Z-Q, Ding Y-Q. 2007. Activity-dependent development of callosal projections in the somatosensory cortex. *J Neurosci* **27**:11334–42.

Wang, S.S., Kloth, A.D., and Badura, A. (2014). The cerebellum, sensitive periods, and autism. Neuron 83, 518-532.

Wang X, Hu B, Zieba A, Neumann NG, Kasper-Sonnenberg M, Honsbein A, Hultqvist G, Conze T, Witt W, Limbach C, Geitmann M, Danielson H, Kolarow R, Niemann G, Lessmann V & Kilimann MW (2009). A protein interaction node at the neurotransmitter release site: domains of Aczonin/Piccolo, Bassoon, CAST, and rim converge on the N-terminal domain of Munc13-1. J Neurosci 29, 12584–12596.

Wang VX, Tang CY & Olsen O (n.d.). Mapping of Brain Activity by Automated Volume Analysis of Immediate Early Genes Resource Mapping of Brain Activity by Automated Volume Analysis of Immediate Early Genes. Cell 165, 1789–1802.

Wang X, Kibschull M, Laue MM, Lichte B, Petraschparwez E, Kilimann MW, Chemie P, Anatomie I, Bochum R & Bochum D- (1999). Aczonin , a 550-kD Putative Scaffolding Protein of Presynaptic Active Binds Profilin. J Cell Biol 147, 151–162.

Wang X, Liu Y, Li X, Zhang Z, Yang H, Zhang Y, Williams PR, Alwahab NSA, Kapur K, Yu B, Zhang Y, Chen M, Ding H, Gerfen CR, Wang KH & He Z (2017). Deconstruction of Corticospinal Circuits for Goal-Directed Motor Skills. Cell 171, 440-455.e14.

Wang X, Yu S yang, Ren Z, De Zeeuw CI & Gao Z (2020). A FN-MdV pathway and its role in cerebellar multimodular control of sensorimotor behavior. Nat Commun; DOI: 10.1038/s41467-020-19960-x.

Watson GDR, Smith JB & Alloway KD (2015). The Zona Incerta Regulates Communication between the Superior Colliculus and the Posteromedial Thalamus: Implications for Thalamic Interactions with the Dorsolateral Striatum. J Neurosci 35, 9463–9476.

Way SW, Rozas NS, Wu HC, Mckenna J, Reith RM, Hashmi SS, Dash PK, Gambello MJ. 2012. The differential effects of prenatal and/or postnatal rapamycin on neurodevelopmental defects and cognition in a neuroglial mouse model of tuberous sclerosis complex. *Hum Mol Genet* **21**:3226–3236.

Weiler N, Wood L, Yu J, Solla SA & Gordon MG (2009). Top-down laminar organization of the excitatory netwrok in motor cortex. Nat Neurosci 11, 360–366.

Welker C (1974). Receptive Fields of Barrels in the Somatosensory Neocortex of the Rat ' 52. Brain Res173–189.

Westby GWM, Collinson C & Dean P (1993). Excitatory Drive from Deep Cerebellar Neurons to the Superior Colliculus in the Rat: an Electrophysiological Mapping Study. Eur J Neurosci 5, 1378–1388.

Weyand TG, Boudreaux M, Guido W, Tsanov M, Chah E, Wright N, Vann SD, Reilly R, Jonathan T, Aggleton JP, Mara SMO, Alitto HJ, Iv BDM, Rathbun DL & Usrey WM (2000). Burst and Tonic Response Modes in Thalamic Neurons During Sleep and Wakefulness. J Neurophysiol1107–1118.

Whitmire CJ, Waiblinger C, Schwarz C & Stanley GB (2016). Information Coding through Adaptive Gating of Synchronized Thalamic Bursting. Cell Rep 14, 1–13.

Whitmire CJ, Waiblinger C, Schwarz C & Stanley GB (n.d.). Information Coding through Adaptive Gating of Synchronized Thalamic Bursting.

Wild JM & Williams MN (2000). A direct cerebrocerebellar projection in adult birds and rats. Neuroscience 96, 333–339.

Williams MN, Zahm DS & Jacquin MF (1994a). Differential Foci and Synaptic Organization of the Principal and Spinal Trigeminal Projections to the Thalamus in the Rat. Eur J Neurosci 6, 429–453.

Williams MN, Zahrn DS & Jacquin MF (1994b). Differential Foci and Synaptic Organization of the Principal and Spinal Trigeminal Projections to the Thalamus in the Rat. Eur J Neurosci 6, 429–453.

Williams RW & Herrup K (1988). The Control of Neuron Number. Annu Rev Neurosci 11, 423–453.

Wimmer VC, Bruno RM, De Kock CPJ, Kuner T & Sakmann B (2010). Dimensions of a projection column and architecture of VPM and POm axons in rat vibrissal cortex. Cereb Cortex 20, 2265–2276.

Wimmer VC, Nevian T & Kuner T (2004). Targeted in vivo expression of proteins in the calyx of Held. Pflugers Arch 449, 319–333.

Winnubst J et al. (2019). Reconstruction of 1,000 Projection Neurons Reveals New Cell Types and Organization of Long-Range Connectivity in the Mouse Brain. Cell 179, 268-281.e13.

Wolfart J, Debay D, Masson G Le, Destexhe A & Bal T (2005). Synaptic background activity controls spike transfer from thalamus to cortex. 8, 1760–1767.

Wong M, Roper SN. 2016. Genetic animal models of malformations of cortical development and epilepsy. *J Neurosci Methods*.

Yan L, Findlay GM, Jones R, Procter J, Cao Y, Lamb RF. 2006. Hyperactivation of mammalian target of rapamycin (mTOR) signaling by a gain-of-function mutant of the Rheb GTPase. *J Biol Chem* **281**:19793–19797.

Woolsey TA & Van der Loos H (1970). The structural organization of layer IV in the somatosensory region (S I) of mouse cerebral cortex. The description of a cortical field composed of discrete cytoarchitectonic units. Brain Res 17, 205–242.

Wulff P, Schonewille M, Renzi M, Viltono L, Sassoè-Pognetto M, Badura A, Gao Z, Hoebeek FE, Van Dorp S, Wisden W, Farrant M & De Zeeuw CI (2009). Synaptic inhibition of Purkinje cells mediates consolidation of

vestibulo-cerebellar motor learning. Nat Neurosci 12, 1042–1049.

Xiong H, Zhou Z, Zhu M, Lv X, Li A, Li S, Li L, Yang T, Wang S, Yang Z, Xu T, Luo Q, Gong H & Zeng S (2014). Chemical reactivation of quenched fluorescent protein molecules enables resin-embedded fluorescence microimaging. Nat Commun 5, 1–9.

Yamamoto T, Hayashi T, Murata Y, Ose T & Higo N (2019). Premotor Cortical-Cerebellar Reorganization in a Macaque Model of Primary Motor Cortical Lesion and Recovery. J Neurosci 39, 8484–8496.

Yamawaki N & Shepherd GMG (2015). Synaptic Circuit Organization of Motor Corticothalamic Neurons. J Neurosci 35, 2293–2307.

Yarden-Rabinowitz Y & Yarom Y (2017). In vivo analysis of synaptic activity in cerebellar nuclei neurons unravels the efficacy of excitatory inputs. J Physiol 595, 5945–5963.

Yatim N, Billig I, Compoint C, Buisseret P & Buisseret-Delmas C (1996). Trigeminocerebellar and trigemino-olivary projections in rats. Neurosci Res 25, 267–283.

Yezierski RP (1982). Spinomesencephalic tract: Projections from the lumbosacral spinal cord of the rat, cat, and monkey. J Comp Neurol 267, 131–146.

Yoshida A, Sessle BJ, Dostrovsky JO & Chiang CY (1992). Trigeminal and dorsal column nuclei projections to the anterior pretectal nucleus in the rat. Brain Res 590, 81–94.

Yu CR, Power J, Barnea G, O'Donnell S, Brown HEV, Osborne J, Axel R, Gogos JA. 2004. Spontaneous neural activity is required for the establishment and maintenance of the olfactory sensory map. *Neuron* **42**:553–566.

De Zeeuw CI, Hoebeek FE, Bosman LWJ, Schonewille M, Witter L & Koekkoek SK (2011). Spatiotemporal firing patterns in the cerebellum. Nat Rev Neurosci 12, 327–344.

de Zeeuw CI, Holstege JC, Calkoen F, Ruigrok TJH & Voogd J (1988). A new combination of WGA-HRP anterograde tracing and GABA immunocytochemistry applied to afferents of the cat inferior olive at the ultrastructural level. Brain Res 447, 369–375.

Zhang F, Vierock J, Yizhar O, Fenno LE, Tsunoda S, Kianianmomeni A, Prigge M, Berndt A, Cushman J, Polle J, Magnuson J, Hegemann P & Deisseroth K (2011). The microbial opsin family of optogenetic tools. Cell 147, 1446–1457.

Zhang S, Xu M, Chang WC, Ma C, Hoang Do JP, Jeong D, Lei T, Fan JL & Dan Y (2016). Organization of long-range inputs and outputs of frontal cortex for top-down control. Nat Neurosci 19, 1733–1742.

Zikopoulos, B., and Barbas, H. (2007). Parallel driving and modulatory pathways link the prefrontal cortex and thalamus. PloS one 2, e848.

Zikopoulos, B., and Barbas, H. (2012). Pathways for emotions and attention converge on the thalamic reticular nucleus in primates. The Journal of neuroscience : the official journal of the Society for Neuroscience 32, 5338-5350.

SUMMARY

This dissertation focuses on describing the anatomical and functional characteristics of selected pathways that wire the cerebellum, the thalamus, the sensory cortex and the motor cortex. We zoom in on individual hot spots of synaptic connectivity and describe the anatomical and physiological characteristics that shape the function of the pathway in the bigger network of hardwired brain routes. After an introduction of the important brain areas in **Chapter 1**, we describe the physiological properties of cortical driver synapses in sensory thalamus and characterize their properties in absence of the presynaptic scaffolding protein Bassoon (**Chapter 2**). Here, we find faster synaptic depletion in absence of Bassoon, which suggests a role of this presynaptic protein for the reloading of synaptic vesicles during sustained synaptic transmission. After this initial chapter on the properties of a single synapse in the thalamus, **Chapter 3 to 5** are centered around describing the anatomical and physiological characteristics of cortical and cerebellar inputs to the thalamus on the microcircuit level. Precisely, in **Chapter 3** we evaluate the convergence pattern of primary sensory cortex and the cerebellar output nuclei in a prospective review and suggest extra-thalamic areas such as the zona incerta, superior colliculus and anterior pretectal area as comparators for sensory and cerebellar information. In **Chapter 4,** we describe the cerebellar input in the individual motor thalamic nuclei and find an increased density and size of the cerebellar synapse as well as an enhanced charge transfer and action potential firing in ventro-lateral nucleus when compared to ventro-medial and centro-lateral nucleus. These data establish that the cerebellar impact on the individual nuclei of the motor thalamus differ depending on the characteristics of the cerebellar synapse. **Chapter 5** shows that the in **Chapter 4** described cerebellar input converges with modulatory feedback from motor cortical layer 6 in ventro-lateral nucleus. Furthermore, we show that the thalamo-cortical spike transfer can be facilitated by both pauses in cerebellar activation as well as a shift in the membrane potential via the inputs from motor cortex. In summary of **Chapter 4 and 5**, we use anatomical tools in combination with single and dual color optical stimulation to extend the thalamic concept of drivers and modulators to the motor domain. After describing connectivity patterns in the healthy mouse brain (**Chapter 2 to 5**), we show how aberrant axonal connectivity can result in disease phenotypes (**Chapter 6**). In **Chapter 6**, we describe how hyperactivity of the mTOR signaling pathway, due to a dominant-active mutation in the *RHEB1* gene (*RHEB1p.Pro37Leu*), induces enhanced axonal connectivity and hyperexcitability of distally connected neurons. Blocking synaptic release from *RHEB1p.Pro37Leu* neurons reverses the epileptic phenotype. This suggests that hyperactivation of the mTOR pathway induces connectivity abnormalities on the circuit level which in turn causes epileptic seizures. In **Chapter 7** we focus on the communication between the cortex and the cerebellum and characterize a novel

subpopulation of corticospinal neuron in the motor cortex that forms a direct connection to the cerebellar nuclei. More specifically, we define the anatomical input-output pattern that embeds it in the brain circuitry and describe the physiological properties as well as the genetic profile.

SAMENVATTING

Dit proefschrift richt zich op het beschrijven van de anatomische en functionele kenmerken van geselecteerde paden die het cerebellum, de thalamus, de sensorische cortex en de motorische cortex bedraden. We zoomen in op individuele hotspots van synaptische connectiviteit en beschrijven de anatomische en fysiologische kenmerken die de functie van een specifiek pad in het grotere netwerk van vastgenestelde hersenroutes bepalen. Na een introductie van de belangrijke hersengebieden in **Hoofdstuk 1** beschrijven we de fysiologische eigenschappen van corticale aandrijfsynapsen in sensorische thalamus en karakteriseren we hun eigenschappen in afwezigheid van het presynaptische structuur-eiwit Bassoon (**Hoofdstuk 2**). Hier vinden we snellere synaptische uitputting in afwezigheid van Bassoon, wat suggereert dat dit presynaptische eiwit een rol speelt bij het herladen van synaptische vesicles tijdens aanhoudende synaptische transmissie. Na dit eerste hoofdstuk over de eigenschappen van een enkele synaps in de thalamus, zijn Hoofdstuk 3 tot en met 5 gecentreerd rond het beschrijven van de anatomische en fysiologische kenmerken van corticale en cerebellaire inputs naar de thalamus op microcircuit niveau. In **Hoofdstuk 3** evalueren we het convergentiepatroon van de primaire sensorische cortex en de cerebellaire outputkernen in een prospectieve review en suggereren we extra-thalamische gebieden zoals de zona incerta, superieure colliculus en anterieur pretectaal gebied als vergelijkers voor sensorische en cerebellaire informatie. In **Hoofdstuk 4** beschrijven we de cerebellaire input in de individuele motorische thalamuskernen en vinden we een grotere dichtheid en afmeting van de cerebellaire synaps, evenals een verbeterde ladingsoverdracht en verhoogd actiepotentiaal signalen afgeven in de ventro-laterale kern in vergelijking met ventro-mediale en centro-laterale kern. Deze gegevens stellen vast dat de cerebellaire impact op de individuele kernen van de motorische thalamus verschillend is, afhankelijk van de kenmerken van de cerebellaire synaps. **Hoofdstuk 5** laat zien dat de in Hoofdstuk 4 beschreven cerebellaire input convergeert met modulerende feedback van motorcorticale laag 6 in de ventro-laterale nucleus. Verder laten we zien dat de thalamo-corticale spike-overdracht kan worden vergemakkelijkt door zowel pauzes in cerebellaire activering als een verschuiving in de membraanpotentiaal via de input van de motorische cortex. Hoofdstuk 4 en 5 samengevat; we gebruiken anatomische hulpmiddelen in combinatie met optische stimulatie met enkele en dubbele kleuren om het thalamische concept van drivers en modulatoren uit te breiden naar het motorische domein. Na het beschrijven van connectiviteitspatronen in het gezonde muizenbrein (Hoofdstuk 2 tot 5) laten we zien hoe afwijkende axonale connectiviteit kan resulteren in ziektefenotypes (**Hoofdstuk 6**). In Hoofdstuk 6 beschrijven we hoe hyperactiviteit van de mTOR signaalroute, als gevolg van een dominant-actieve mutatie in het RHEB1 gen (RHEB1p.Pro37Leu), een verbeterde axonale connectiviteit en hyperexciteerbaarheid van distaal verbonden neuronen induceert. Het

blokkeren van synaptische afgifte van RHEB1p.Pro37Leu-neuronen keert het epileptische fenotype om. Dit suggereert dat hyperactivering van de mTOR-route afwijkingen in de connectiviteit op circuitniveau induceert, wat op zijn beurt epileptische aanvallen veroorzaakt. In **Hoofdstuk 7** richten we ons op de communicatie tussen de cortex en het cerebellum en karakteriseren we een nieuwe subpopulatie van corticospinale neuronen in de motorische cortex die een directe verbinding vormt met de cerebellaire kernen. Meer specifiek definiëren we het anatomische input-outputpatroon dat dit pad in het hersencircuit integreert. Verder beschrijven we zowel de fysiologische eigenschappen als het genetische profiel.

CURRICULUM VITAE

Personal details

Name:	Carmen Bianca Schäfer
Nationality:	German
Place of birth:	Brackenheim, Germany
Date of birth:	24th October 1988

Education

Jan 2015 – Sep 2021	Erasmus University Rotterdam, The Netherlands Erasmus Medical Center, Department of Neuroscience PhD Program
Sept. 2011 – Mar 2014	University of Heidelberg, Germany Master of Molecular Biosciences, Major Neuroscience
Sept. 2012 – Dec. 2012	University of Toronto, The Hospital for Sick Children, Canada Internship
Sept. 2008 – Jul. 2011	University of Heidelberg, Germany Bachelor of Science in Biology
Aug. 2010 – Jan. 2011	University of Copenhagen, Denmark ERASMUS program
Sept. 2005 – Jun. 2008	Commercial High School Gustav-von-Schmoller Schule Heilbronn, Germany

Teaching

Jan 2015 – Sep 2021	Assisting in the supervision of bachelor students of laboratory research, and a neuroscience master student

PHD PORTFOLIO

Conferences and Schools

2015, 11th December	E-phys-Brain Conference, 11th December 2015, Erasmus MC, Rotterdam, the Netherlands
2016, 19-20th May	Barrel Cortex Function, VU University Amsterdam, the Netherlands
2016, 12-16th November	Society for Neuroscience, Convention Center San Diego, USA
2017, 26-28th June	Procedural Learning Summer School, Amsterdam, the Netherlands
2018, 7-11th July	11th FENS Forum of Neuroscience, Berlin, Germany
2018, 11-15th December	School of Brain Cells & Circuits "Camillo Golgi", Erice, Italy Poster Prize Winner
2019, 24th January	BIG Biomedical Sciences Theme Day Speaker
2019, 24th June – 12th July	Computational Neuroscience School, Okinawa Institute of Science and Technology, Okinawa, Japan
2019, 7th Oct – 11th Oct	Optical Control of brain functioning with optogenetics and wave front shaping

Grants

2019, 5th June	Stichting Erasmus Trustfonds, Research and Education Projects

LIST OF PUBLICATIONS

This thesis:

Schäfer CB, Fejtova A, Körber C, Herrmannsdörfer F, Gundelfinger ED & Kuner T. Synaptic Release in Bassoon Deficient Thalamic Giant Synapses. *In preparation*

Schäfer CB & Hoebeek FE (2018). Convergence of Primary Sensory Cortex and Cerebellar Nuclei Pathways in the Whisker System. *Neuroscience* 368, 229–239.

Gornati S V.*, **Schäfer CB***, Eelkman Rooda OHJ, Nigg AL, De Zeeuw CI & Hoebeek FE (2018). Differentiating Cerebellar Impact on Thalamic Nuclei. *Cell Rep* 23, 2690–2704.

Onori MP, Koene LMC*, **Schäfer CB***, Nellist M, de Brito van Velze M, Gao Z, Elgersma Y & van Woerden GM (2020). RHEB/mTOR-hyperactivity causing cortical malformations drives seizures through increased axonal connectivity. *Plos Biology* 5, 1-34

Schäfer CB, Gao Z, De Zeeuw CI & Hoebeek FE (2021). Temporal dynamics of the cerebello-cortical convergence in ventro-lateral motor thalamus. *J Physiol* 599, 2055–2073.

Schäfer CB, Li A, van Hoogstraten B, Bouwen B, Hasanbegovic H, Flierman N, Adolfs Y, Pasterkamp J, van IJcken Wilfried Fj, De Zeeuw C, Hoebeek FE, Zhenyu G. A Novel Subtype of Cerebro-Spinal Projection Neuron that Innervates Cerebellar Nuclei. *In preparation*

* contributed equally

Other Publications:

Schäfer CB, Morgan BR, Ye AX, Taylor MJ & Doesburg SM (2014). Oscillations, networks, and their development: MEG connectivity changes with age. *Hum Brain Mapp* 35, 5249–5261.

Ye AX, Leung RC, **Schäfer CB**, Taylor MJ & Doesburg SM (2014). Atypical resting synchrony in autism spectrum disorder. *Hum Brain Mapp* 6066, 6049–6066.

ACKNOWLEDGEMENTS

Wow! I am done! It is Unbelievable!

Definitely the last years have been a long and stormy journey with several setbacks and many moments of deep frustration! I mean this PhD has been more than challenging. Yes – working in Science definitely requires a high tolerance for frailure and miss success. BUT it is worth it. There is nothing better than the feeling that one of your ideas finally works and you actually discovered something new. Nobody else ever saw that before. Even nicer is the task of puzzling around a new finding and developing it into a story. It is a free and creative process that requires a lot of flexibility. Just keep on trying new techniques on old and/or new questions or reshape the way that you raise your questions. Just run another pilot. It never gets boring. Now in the end of this PhD period I think I learned a shit load about science, perspectives and finally we created all the stories and papers that are printed in this book.

Of course, I never would have succeeded in all of this without the wonderful people that I have in my life. I mean yeah, I also had to learn Dutch and to integrate into the Netherlands. A challenge in itself. Therefore, I wanna thank all the people that supported me during the last years!

Freek. Thanks a lot for all your support especially during the first period of my PhD. I think you are a great mentor with fantastic teaching skills. I remember hours that were spend on journal clubs. We discussed papers into the tiniest little detail just so that we learn the specifics of the techniques and the impact that has on the field. You definitely spend hours on rephrasing and commenting on our manuscripts, just to refine them and make them even better. I don't know many people that have so much patience for their students. I also really respect your drive for science and your hard-working attitude. Niet lullen maar putzen. And then after all these years of hard work you finally got this great opportunity to become full Professor in Utrecht. Fantastic! I really wish you all the Best for setting up your lab over there.

Chris. - Bingo - is what you said. I remember that time quite clearly: I was running out of money to finish up my PhD and then I asked you whether we could write a grant together to fix that problem. You were in for that! You got that sparkle in your eyes, started to talk about all the scientific spin off we will get from this and that this will have to work. It sounded quite convincing, I have to say. And then we got the money! Bingo. I am really thankful for your support during that time, because I learned a great deal from it. Running a science department with several research groups takes a lot of

responsibility, I really respect that! Thanks for your support and thanks for giving me all these possibilities here in Rotterdam.

Gao. You have scope, the right perspective, and the capability to get it done. You are full of bubbling and sparkling new ideas that are most of the time covered in hard logic. Working with you is quite inspiring and I am lucky that you have been my mentor in the last years. I mean, if you say something I really have to listen! That is not always easy because 8 out of 10 times my ideas will be shut down right away. However, the 2 ideas that are left are definitely worth working with as we never go for a low hanging fruit. That makes all the difference between a good and a bad story! I have learned a great deal from you and I start understanding what it means to be that Rock in Science. I really respect your working attitude and dedication. We never give up and if experiments don't work we have to either try harder or come up with something smarter. There has also been a time when I have been without funding and without working group. I really wanna thank you for your support during this period of my PhD and for finally taking me into your lab when all the problems were solved. I don't think I would have made it without that! Seriously! So, thanks a lot for being my mentor, for being this inspiring scientist and for having my back whenever necessary!

I also wanna thank all the members of my committee: **Christiaan, Gerard, Aleksandra, Geeske, Tom** and **Thomas.** Thanks for all your feedback and support.

And then there are all the people in the department that have already left or that joined some time ago. **Saša, Negah, Oscar, Francois, Bibi, Dick, Bastian, Bas, Joshua, Martijn, Sadaf, Devika** and **Lieke.** Thanks for being great colleagues and for creating a nice atmosphere in the department. **Simo,** thanks for the crazy times we shared. Thanks for your support in times of trouble. **Sashini** thanks for all the dinner times we had. **Farnaz** I think we even started within the same month at the EMC. Can't believe that. There were plenty of nights out, dinners and parties! Just keep on changing your haircut and stay yourself. Thanks. **Aaron and Ursula** Also we know each other since quite a long time. We spend many evenings playing games and watching Ghibli movies! It has been fun! Thanks for everything! **Lisanne** and **Lukas** – thanks for the most recent Borrelmania!.

Importantly, I wanna thank our technicians that work in the heart of our department – the Histolab! **Elize,** I think without your effort to maintain the equipment, order all the labstuff that we need and - of course - your indepth knowledge on ANY KIND of staining, antibody or histological technique our Histolab would literally fall apart! It doesn't really matter what kind of question we have, we can drop it in your office and you will always take the time to answer it or to fix the problem. You are also a great collegue that

always has an open ear to listen to the newest problem, complains and you are always supportive and patient. I can always rely on you and I really appreciate and respect that! Thanks for being there!! **Erika,** definitely you are the most talkative person in the heart of our Histolab. I mean no matter what kind of new story, it can't get pas you. Thanks for listening to all the complains, stories and problems of everybody. Thanks for being supportive in times of trouble and helping me to learn Dutch! Thanks for all the Gezelligheid next to the coffee machine. **Mandy,** I think you are one of the most organized persons within our department. Thanks a lot for your support in the lab and for taking care of all the animal business! YES - I really think without the help of **Elize, Erika and Mandy** I wouldn't have been able to finish my PhD in this life! You guys helped to mount millions of sections and perfused hundreds of brains for me! Thanks for everything!

Youri, also you have been very supportive during our little collaboration on the iDISCO project! Thanks for imaging all these brains for me, aligning them to the mouse atlas, setting up the analysis pipeline and listening to all the problems that came along during that time!

My students: **Valentina, Renske, Margherita and Meryem.** Thanks to all of you! It has been great how all of you contributed to the work in this thesis. I am quite proud on having worked with you. All of you are so different. I always tried to be a good, patient and stimulating mentor but let's be honest I also learned a lot from all of you! You taught me what it needs to be an understanding and motivating teacher that can stimulate enthusiasm for science in other people. Thanks.

Sander How is the life over there on your tropical island? I guess there is only one right answer: GOOD ☺ Yes, we had a lot of fun times together. I remember loads of drumming and jam sessions. Playing table soccer in the hallway and many borrels. Also, thanks a lot for hosting me in Okinawa and – yes – there is not much better than snorkling and diving trips over there. Please don't loose your silly humour and always stay yourself! Thanks Dude!

Vincenzo Mamma mia!! My Italian neighbour! Damn it – it have been several years. Also we have had a shit load of fun together. I remember hours of playing table soccer and table tennis! We have been to the FENS and the Gordon conferences together and had plenty inside-out science discussion. You are not only hard working and passionate about science but also one of the Borrel maniacs in the department. Work hard – Play hard. ☺ . Over time we became friends and I really like having you around in the department. You were always there!! We shared all the frustrations in good and bad times. Thanks for all your perspectives and support!

Martina, we always had a really good click and in the end we became friends ☺ I think you are a really good scientist and I really enjoyed working in a project with you! We form a great TEAM. Apart from working together I of course also enjoyed our movie nights, bike trips and 'social distance walks'. It was great to be your paranymph and I really wish you ALL the best in the Big Apple. See you soon!

Zhong - my most recent lab neighbour, just keep on coding! **Mimo** – ja, usually our humour escalates quickly. Let's keep it like that. Also, just keep wearing two different kind of socks. That is quite funny!

Anne, you joined our lab and in no time the atmosphere was flooded with jokes, singing and bubbles full of silliness. Awesome ☺. Not only that, but if it comes down to business you never miss to make the point. It is really great to have you around!

Xiaolu My dear office, lab and PhD mate. It has been quite some time that we worked together in the lab and I literally always enjoyed our in-depth science discussion and vivid conversations! I really appreciate your flexibility and openness if it comes to sharing equipment, technical advice or solving any other upcoming problem. Your helpfulness is beyond scope, which makes it really pleasant to work in a team with you! I also don't know how many times you had the patience to listen to all my stories, complains and you even managed my occasional singing in the office. Thanks for all the silliness in between ☺ and thanks for being a friend that always has my back!

Hana, *'I can't Expresso how much you Bean for me'!* You wanted a LAME quote for the acknowledgement. Here you go. I did my best! Because - Yes - you really are the BARISTA in our Coffee Corner. Hard Rock Heavy Metal! Hana always knows her shit. It is true. You know how to crack code, you make things work and usually you never give up. No challenge is to much for you. Thanks for all your support, Dad jokes and coffee insights! Thanks for helping me to learn Dutch and thanks for being there in Good and Bad times!

RVC Libanon. My Volleyball Club! Where would I be without RVC Libanon? We have spent so many hours training and playing in that sportshal. I remember so many nice parties that were organized and of course all the borrels that we celebrated. Thanks to all the teammates – I mean **Nienke, Lotte, Lotte Clara, Aniek, Ilse, Anne, Naomi, Inge** and **Martijn.** Thanks to all the other Club mates **Renske, Caro, Suus, Loes, Lies, Monique, Emma, Eliane, Annemieke** and all the other people that I didn't mention now. Thanks for all the great nights out. Thanks for the gezelligheid!!

Groep Spanje! Nicole, Stefanie, Julie and Esther. Yes, these were the good old times! Most of us were Single and we went on beach volleyball vacation in Spain ☺ Hahaha great times with a lot of Sun. We also had loads of BBQs, game nights, festivals and of course borrels with Libanon. We also ate a lot of Nachos and drank a lot of Corona beers. You guys were always there, right from the beginning! You helped me to learn Dutch and to settle up in Rotterdam. You listened to all my complaints, also in times of trouble! Thanks for all of that!! **Esther,** thanks for everything! I always appreciated your honest opinion! **Julie,** thanks for all the gezelligheid! I wish you and Cas all the Best in Limburg. **Stefanie** you really helped a lot with learning Dutch! Thanks for listening. I wish you the best for all the steps that are ahead of you. **Nicole,** thanks for all the gezelligheid and the support. Thanks for all the game and dinner nights. By now most of us have partners and/or even kids. How and when did that happen? I don't know, the time went by too quickly. Now, many moved to different cities and our lifes developed in many different directions. In any way, thanks for everything! Thanks for the gezelligheid, Thanks for the friendship!

Nora and Daan It was great to share the house with you guys! Nora you were an awesome roommate. Hahaha You brought me back to salsa dancing. Loads of salsa dance parties and nights out! Just keep on surfing Girl! Thanks for all the Gezelligheid at home!

Jessica and Koen. Jajajaja…Wat zeg je over Brabanders…. Dat is een gezellig volkje. It didn't take a long time and we became friends. Plenty of laughing, singing and even dancing :P Damn it, it is cozy at home when you guys are there. Thanks for your support, thanks for listening and of course thanks for all the laughter!!!

Denise Danke für deine starke Meinung und deine Unterstützung! Wir sehen uns bald wieder!

Pepe Good old times! Danke für all deine Unterstützung in den letzten Jahren!

Saskia Meine Liebste! Ja was würde ich ohne dich nur machen. Es ist viel passiert in den letzten Jahren und du warst immer da. Vielen Dank fürs Zuhören, für deine Unterstützung und für deine Freundschaft!!

Michel Jij snapt mij! Wij kunnen heerlijk samen lachen en al ons passies delen. Jij bent een ongeloofelijk mens en ik heb ontzettend veel geluk met jou! Ik hou van jou. Dankjewel voor al jouw ondersteuning!!

Andreas und Anja Ja, auch ihr seid immer für mich da. Vielen Dank für all die Unterstützung in den letzten Jahren.

Mama und Papa! Ich wüsste nicht was ich ohne Euch machen würde. Ihr seid immer für mich da und stärkt mir meinen Rücken. Ohne euch hätte ich meine Dokterarbeit sicherlich nicht abschliessen können. Ihr habt mir beigebracht, dass man für die wichtigen Dinge im Leben kämpfen muss und ohne Disziplin oder Durchsetzungsvermögen nicht weiter kommt. Papa am Ende haben wir sogar zusammen an ein paar Projekten gearbeitet. Danke dafür. Ich habe alles von Euch gelernt und Euch viel zu verdanken. Danke für eure Unterstützung! Danke für Alles!